

**THERMOELECTRIC PROPERTIES AT HIGH TEMPERATURE
OF CuFeO_2 DELAFOSSITE COMPOUND DOPED
WITH Pt, Al, Sn AND Pb**



**A THESIS SUBMITTED IN FULFILLMENT
OF THE REQUIREMENT FOR THE DEGREE OF
DOCTOR OF PHILOSOPHY IN APPLIED PHYSICS
FACULTY OF SCIENCE
KING MONGKUT'S INSTITUTE OF TECHNOLOGY LADKRABANG
2011
KMITL-2011-SC-D-030-025**

This material is reserved for educational use only, not allowed for commercial use.

Forbidden to modify the content, and cite the document when use.

สมบัติเทอร์โมอิเล็กทริกที่อุณหภูมิสูงของสารประกอบ CuFeO_2 เดลาฟอสไซต์
เจือ Pt, Al, Sn และ Pb

**THERMOELECTRIC PROPERTIES AT HIGH TEMPERATURE
OF CuFeO_2 DELAFOSSITE COMPOUND DOPED
WITH Pt, Al, Sn AND Pb**



วิทยานิพนธ์นี้สำหรับการศึกษาตามหลักสูตรปรัชญาดุษฎีบัณฑิต
สาขาฟิสิกส์ประยุกต์
คณะวิทยาศาสตร์
สถาบันเทคโนโลยีพระจอมเกล้าเจ้าคุณทหารลาดกระบัง
พ.ศ. 2554

KMITL-2011-SC-D-030-025

This material is reserved for educational use only, not allowed for commercial use.

Forbidden to modify the content, and cite the document when use.



COPYRIGHT 2011

FACULTY OF SCIENCE

KING MONGKUT'S INSTITUTE OF TECHNOLOGY LADKRABANG

This material is reserved for educational use only, not allowed for commercial use.

Forbidden to modify the content, and cite the document when use.

| | |
|-----------------------------|---|
| หัวข้อวิทยานิพนธ์ | สมบัติเทอร์โมอิเล็กทริกที่อุณหภูมิสูงของสารประกอบ CuFeO_2 เคลือบไอโซโทป Pt, Al, Sn และ Pb |
| นักศึกษา | นายเชรชฐา รัตนพันธ์ |
| รหัสประจำตัว | 52650101 |
| ปริญญา | ปรัชญาคุษฎีบัณฑิต |
| สาขาวิชา | ฟิสิกส์ประยุกต์ |
| พ.ศ. | 2554 |
| อาจารย์ที่ปรึกษาวิทยานิพนธ์ | รศ.ดร.อารีย์ วิเชียรฉาย |

บทคัดย่อ

วิทยานิพนธ์นี้มีจุดประสงค์เพื่อศึกษาสมบัติเทอร์โมอิเล็กทริกของสารประกอบ CuFeO_2 ประเภท Delafossite และปรับปรุงสมบัติเทอร์โมอิเล็กทริกให้ดีขึ้นด้วยการเจือ Pt, Al, Sn และ Pb อะตอม ใช้วิธีไฟไนต์เอลิเมนต์คำนวณศักย์ไฟฟ้าบนโมเดลของโมดูลเทอร์โมอิเล็กทริก และประดิษฐ์ต้นแบบโมดูลเทอร์โมอิเล็กทริกเพื่อวัดค่าต่างศักย์ไฟฟ้า กระแสไฟฟ้า และกำลังไฟฟ้าที่ผันได้จากความแตกต่างความร้อน ในงานวิจัยนี้ได้สังเคราะห์สารประกอบขึ้น 5 ตัวอย่างได้แก่ CuFeO_2 , $\text{Cu}_{1-x}\text{Pt}_x\text{FeO}_2$, $\text{CuFe}_{0.5}\text{Al}_{0.5}\text{O}_2$, $\text{CuFe}_{1-x}\text{Sn}_x\text{O}_2$, และ $\text{CuFe}_{1-x}\text{Pb}_x\text{O}_2$ ($x=0.01, 0.03$ และ 0.05) โดยวิธีปฏิบัติที่แท้จริง จากนั้นนำสารตัวอย่างไปวัดสมบัติเทอร์โมอิเล็กทริก (สัมประสิทธิ์ซีเบค สภาพนำไฟฟ้า และสภาพนำความร้อน) ในช่วงอุณหภูมิสูง ตั้งแต่อุณหภูมิห้องจนถึง 960K เพื่อนำผลมาวิเคราะห์ในการปรับปรุงสมบัติเทอร์โมอิเล็กทริกของสาร CuFeO_2 ให้ดีขึ้น ผลที่ได้พบว่าสาร CuFeO_2 เป็นสารกึ่งตัวนำไฟฟ้าชนิดบวก และมีค่าสัมประสิทธิ์ซีเบค สภาพนำไฟฟ้า สภาพนำความร้อน และค่า ZT เป็น $300 \mu\text{V/K}$, 13 S/cm , 3.5 W/m-K และ 0.03 ตามลำดับที่อุณหภูมิ 960K และผลจากการวัดพบว่า CuFeO_2 สามารถปรับปรุงสมบัติให้ดีขึ้นได้ โดยค่าสภาพนำไฟฟ้าสามารถเพิ่มขึ้นได้โดยการแทนที่ไอออน Pt^{2+} ลงในตำแหน่ง Cu^{2+} ดังในสาร $\text{Cu}_{0.95}\text{Pt}_{0.05}\text{FeO}_2$ สามารถเพิ่มความนำไฟฟ้าเป็น 23 S/cm สูงกว่า CuFeO_2 เป็น 10 เท่า สำหรับค่าซีเบคสามารถเพิ่มขึ้นได้โดยการแทนที่ไอออน Sn^{2+} จำนวนเล็กน้อยลงในตำแหน่ง Fe^{2+} ดังในสาร $\text{CuFe}_{0.99}\text{Sn}_{0.01}\text{O}_2$ สามารถเพิ่มค่าซีเบคขึ้น $370 \mu\text{V/K}$ สูงกว่า CuFeO_2 ส่วนค่าสภาพนำความร้อนสามารถลดลงได้โดยการแทนที่อะตอมที่มีน้ำหนักมาก เช่น Sn (118.69 g) หรือ Pb (207.19 g) ลงในตำแหน่ง Fe^{2+} ดังในสาร $\text{CuFe}_{0.99}\text{Sn}_{0.01}\text{O}_2$, $\text{CuFe}_{0.97}\text{Pb}_{0.03}\text{O}_2$ และ $\text{CuFe}_{0.95}\text{Pb}_{0.05}\text{O}_2$ สามารถลดค่าสภาพนำความร้อนลงเป็น 1 W/m-K ลดลง 3.5 เท่าจาก CuFeO_2 ส่วนการเปลี่ยนชนิดตัวนำของ CuFeO_2 จากบวกเป็นลบนั้น สามารถเปลี่ยนได้โดยการแทนที่ไอออน Pb^{2+} ลงในตำแหน่ง Fe^{2+} ดังในสาร $\text{CuFe}_{1-x}\text{Pb}_x\text{O}_2$ ซึ่งแสดงการนำไฟฟ้าชนิดลบ สำหรับงานวิจัยนี้สารตัวอย่างที่ให้ค่า ZT สูงสุด คือ $\text{CuFe}_{0.95}\text{Sn}_{0.05}\text{O}_2$ ซึ่งมีค่า 0.1 ที่ 970 K สูงเป็น 4 เท่าจาก CuFeO_2 สำหรับการคำนวณไฟไนต์เอลิเมนต์นั้นพบว่าโมดูลเทอร์โมอิเล็กทริกที่มี 2 ขา จะให้ค่าศักย์ไฟฟ้ามากกว่า 1 ขา 2 เท่า ส่วนต้นแบบโมดูลเทอร์โมอิเล็กทริกได้ประดิษฐ์จาก $P\text{-Cu}_{0.95}\text{Pt}_{0.05}\text{FeO}_2$ และ $N\text{-CuFe}_{0.95}\text{Pb}_{0.05}\text{O}_2$ นั้น โมดูล 4 ขา ให้กำลังไฟฟ้า 2.5 mW และกระแสไฟฟ้า $0.035 \mu\text{A}$ ที่ความต่างอุณหภูมิ 160K ซึ่งสูง 10 และ 6 เท่าตามลำดับจากโมดูล 2 ขา ดังนั้นงานวิจัยนี้จึงสรุปได้ว่าสาร CuFeO_2 สามารถปรับปรุงสมบัติเทอร์โมอิเล็กทริกที่อุณหภูมิสูงให้ดีขึ้นได้

คำสำคัญ : เทอร์โมอิเล็กทริก; CuFeO_2 ; เคลือบไอโซโทป; สัมประสิทธิ์ซีเบค; วิธีไฟไนต์เอลิเมนต์

This material is reserved for educational use only, not allowed for commercial use.

Forbidden to modify the content, and cite the document when use.

| | |
|-----------------------|---|
| Thesis Title | Thermoelectric properties at high temperature of CuFeO ₂ Delafossite compound doped with Pt, Al, Sn and Pb |
| Student | Mr.Chesta Ruttanapun |
| Student ID | 52650101 |
| Degree | Doctor of Philosophy |
| Program | Applied Physics |
| Year | 2011 |
| Thesis Advisor | Assoc. Prof. Dr. Aree Wichainchai |

ABSTRACT

This dissertation aims to investigate thermoelectric properties of the CuFeO₂ delafossite compound, to improve the properties by substituting the Pt, Al, Sn and Pb atom, to use the Finite Element technique to compute the output voltage on the thermoelectric models, and to invent the prototype of thermoelectric modules to measure the output electric voltage, current and power. This research, the CuFeO₂, Cu_{1-x}Pt_xFeO₂, CuFe_{0.5}Al_{0.5}O₂, CuFe_{1-x}Sn_xO₂, and CuFe_{1-x}Pb_xO₂ (x=0.01, 0.03 and 0.05) samples were synthesized by solid-state reaction. Then, all samples were measured the thermoelectric properties (Seebeck coefficient, electrical and thermal properties) from room temperature to 960 K. The results of thermoelectric properties of all samples were used for analyzing to improve the properties of the CuFeO₂ compound. The measurement results of the CuFeO₂ sample at 960K are 300 μV/K, 13 S/cm, 3.5 W/m-K and 0.03 for the Seebeck coefficient, electric conductivity, thermal conductivity and ZT value, respectively. In addition, the results of the substituted samples show that the properties of the CuFeO₂ can be improved. The electrical conductivity can be increased by the Pt¹⁺-substituted into the Cu¹⁺ sites as the Cu_{0.95}Pt_{0.05}FeO₂ sample containing 23 S/cm as high as the CuFeO₂ in 10 times. The Seebeck coefficient can be increased by the small amount Sn²⁺-substituted into the Fe³⁺ sites as the CuFe_{0.99}Sn_{0.01}O₂ containing 370 μV/K as high as the CuFeO₂. The thermal conductivity can be decreased by substitution the large atomic weight of the Sn or Pb atoms into the Fe³⁺ sites as the CuFe_{0.99}Sn_{0.01}O₂, CuFe_{0.97}Pb_{0.03}O₂, and CuFe_{0.95}Pb_{0.05}O₂ samples containing approximately 1 W/m-K as low as the CuFeO₂ in 3.5 times. The n-type of the CuFeO₂ can be produced by the Pb⁴⁺-substituted into the Fe³⁺ sites as the CuFe_{1-x}Pb_xO₂ sample playing n-type conductor. The maximum ZT of this work is 0.1 of the CuFe_{0.95}Sn_{0.05}O₂ at 970 K which is higher than 4 times of the CuFeO₂. The Finite Element analysis was applied on the model of CuFe_{0.5}Al_{0.5}O₂ thermoelectric module as the results corresponding to the experimental results. In the preliminary prototype of the p-Cu_{0.95}Pt_{0.05}FeO₂ and n-CuFe_{0.95}Pb_{0.05}O₂ thermoelectric modules, the output values of electric power, electric current and voltage are 2.5 nW, 0.035 μA and 80 mV, respectively, on the 4 legs of thermoelectric module at temperature difference 160 K. This research can be concluded that the CuFeO₂ Delafossite compound can be improved to good thermoelectric properties at high temperature.

Keywords: Thermoelectric; CuFeO₂; Delafossite; Seebeck coefficient; Finite Element analysis.

This material is reserved for educational use only, not allowed for commercial use.

Forbidden to modify the content, and cite the document when use.

ACNOWLEDGEMENT

(กิตติกรรมประกาศ)

วิทยานิพนธ์ฉบับนี้เกิดขึ้นได้โดยได้รับความกรุณาจาก ดร.วิโรจน์ ตันตราภรณ์ ที่ได้ให้ คำบรรยาย หลักคิด คำแนะนำ ตลอดจนบทความของท่าน สร้างแรงบันดาลใจนำมาสู่ความสำเร็จที่เกิดขึ้นใน วิทยานิพนธ์ฉบับนี้

ความสำเร็จของวิทยานิพนธ์ฉบับนี้ได้รับความกรุณาอาจารย์ที่ปรึกษา รศ.ดร.อารีย์ วิเชียรฉาย ที่ ปรึกษาหัวข้องานวิจัย ให้คำชี้แนะและช่วยแก้ปัญหา จนทำให้งานวิจัยสำเร็จลุล่วงเป็นอย่างดี

ขอขอบพระคุณ รศ.ดร.ฐิตินัย แก้วแดง รศ.ดร.วราวุฒิ เถลัดดา รศ.ดร.อารีย์ วิเชียรฉาย รศ.ดร.วิทยา อมรกิจบำรุง และ อ.ดร.ประธาน บุรณศิริ ที่ร่วมเป็นคณะกรรมการสอบวิทยานิพนธ์

ขอขอบพระคุณ รศ.ดร. วิทยา อมรกิจบำรุง นายกสมาคมสมาคมฟิสิกส์ไทย, ประธานและ ผู้อำนวยการศูนย์วิจัยนาโนเทคโนโลยีบูรณาการ ภาควิชาฟิสิกส์ และหัวหน้าภาควิชาฟิสิกส์ คณะวิทยาศาสตร์ มหาวิทยาลัยขอนแก่น ที่กรุณาเสียสละเวลาเดินทางมาจากขอนแก่นเพื่อสอบเค้าโครง วิทยานิพนธ์และสอบวิทยานิพนธ์ขั้นสุดท้าย

ขอขอบคุณ ว่าที่ดร.สมภพ ถมโพธิ์ นักศึกษาภาควิชาเคมี คณะวิทยาศาสตร์ จุฬาลงกรณ์ มหาวิทยาลัย ว่าที่ดร. อภิรักษ์ ภูษิตระกูล อ.ดร. ทีปานีส ชาชิโย ภาควิชาฟิสิกส์ คณะวิทยาศาสตร์ มหาวิทยาลัยขอนแก่น ผศ.ดร.บรรจง บุญชม สาขาวิชาเคมี สถาบันเทคโนโลยีพระจอมเกล้าเจ้าคุณทหาร ลาดกระบัง สำหรับคำแนะนำดี ๆ เกี่ยวกับการเขียนบทความ

The authors would like to thank Priv.-Doz. Dr. rer. nat. habil. Dipl.-Phys. Siegfried Fritzsche Institute of Theoretical Physics, Leipzig University, Faculty of Physics and Geosciences, Postfach 100920, D-04009 Leipzig, Germany for language editors to improve the article.

ขอขอบคุณ ว่าที่ดร.วุฒิสักดิ์ ประชามอญ ภาควิชาฟิสิกส์ คณะวิทยาศาสตร์ มหาวิทยาลัย อุบลราชธานี ที่ช่วยวิเคราะห์ XRD ทุกตัวอย่าง ทำให้งานวิจัยนี้สำเร็จลุล่วง และได้มีผลงานตีพิมพ์ใน วารสารวิชาการระดับนานาชาติอันเป็นที่ยอมรับในสาขา

ขอขอบคุณ อ.ดร.เอนก เจริญภักดี คณบดีคณะวิทยาศาสตร์และเทคโนโลยี มหาวิทยาลัย เทคโนโลยีราชมงคล (มทร.) สุวรรณภูมิ ผศ.ดร.ทศวรรษ สีตะวัน ศูนย์วิจัยเทอร์โมอิเล็กทรอนิกส์ คณะวิทยาศาสตร์และเทคโนโลยี มหาวิทยาลัยราชภัฏสกลนคร และอ.ดร. อนุชา แสงไธสง ภาควิชาฟิสิกส์ คณะวิทยาศาสตร์ มหาวิทยาลัยอุบลราชธานี ที่ให้ความอนุเคราะห์ทบทวนเนื้อหางานวิจัยก่อนส่งตีพิมพ์

ขอขอบคุณ ผศ.ดร.รุ่งนภา นิยมพันธ์ และ ผศ.ดร.อนุสร นิยมพันธ์ ภาควิชาฟิสิกส์ คณะวิทยาศาสตร์ มหาวิทยาลัยอุบลราชธานี ที่อนุเคราะห์เครื่อง XRD และการวัดสารตัวอย่าง

ขอขอบคุณ สาขาวิชาฟิสิกส์ และ อ.ดร.วรการ นียากร หัวหน้าภาควิชาฟิสิกส์ คณะวิทยาศาสตร์ สถาบันเทคโนโลยีพระจอมเกล้าเจ้าคุณทหารลาดกระบัง ที่อนุเคราะห์สารเคมี $PtCl_2$ และ อ.ดร.วิรัตน์ เจริญบุญ วิทยาลัยนาโนเทคโนโลยีพระจอมเกล้าลาดกระบัง ที่อนุเคราะห์สารเคมี $SnCl_2$

ขอขอบคุณ นายครรชิต สิงห์สุข และนายสุริยา ศรีชัย ศูนย์วิจัยเทอร์โมอิเล็กทริก คณะวิทยาศาสตร์และเทคโนโลยี มหาวิทยาลัยราชภัฏสกลนคร ที่เป็นผู้ช่วยในการประดิษฐ์ต้นแบบเทอร์โมอิเล็กทริก

ขอขอบคุณ ผศ.ดร.สมชาย เกียรติกมลชัย ภาควิชาฟิสิกส์ คณะวิทยาศาสตร์ จุฬาลงกรณ์มหาวิทยาลัย ที่อนุเคราะห์เครื่องมือทดสอบการวัดค่าสัมประสิทธิ์ซีเบคเบื้องต้น

ขอขอบคุณ ผศ.ดร.เสน่ห์ ทองรินทร์ ภาควิชาภาษาอังกฤษ คณะศิลปศาสตร์ มหาวิทยาลัยธรรมศาสตร์ และ อ.ดร.พัชรี เมืองนาคิน สาขาวิชาศิลปศาสตร์ประยุกต์ คณะครุศาสตร์อุตสาหกรรม สถาบันเทคโนโลยีพระจอมเกล้าเจ้าคุณทหารลาดกระบัง ที่สอนการเขียนบทความตีพิมพ์ในระดับนานาชาติจนสามารถตีพิมพ์ลงวารสารนานาชาติชั้นนำได้

วิทยานิพนธ์นี้ “ได้รับทุนสนับสนุนการทำวิทยานิพนธ์จากสถาบันเทคโนโลยีพระจอมเกล้าเจ้าคุณทหารลาดกระบัง” สำหรับจัดพิมพ์รูปเล่ม

สุดท้ายต้องขอขอบคุณว่าที่ภรรยาของข้าพเจ้า คุณปิยธาริน วรสินวัฒนา ที่เป็นเสมือนคู่คิด ให้กำลังใจและเป็นผู้ช่วยเหลืออยู่เบื้องหลังตลอดเวลา

สำหรับคุณงามความดีอันใดที่เกิดจากวิทยานิพนธ์ฉบับนี้ ข้าพเจ้าขอมอบให้กับบิดามารดาญาติพี่น้อง ทุกคนที่เป็นกำลังใจ ตลอดจนจนครุอาจารย์ที่เคารพทุกท่านที่ได้ประสาทวิชาความรู้และถ่ายทอดประสบการณ์ที่ดีให้แก่ข้าพเจ้า

เชรชฐา รัตนพันธ์

2 กันยายน 2554

TABLE OF CONTENTS

| | PAGE |
|---|-------|
| THAI ABSTRACT..... | I |
| ENGLISH ABSTRACT..... | II |
| ACKNOWLEDGEMENT..... | III |
| TABLE OF CONTENTS..... | IV |
| LIST OF FIGURES..... | XI |
| LIST OF NATATIONS..... | XVIII |
| CHAPTER 1 INTRODUCTION | 1 |
| 1.1 BACKGROUND..... | 1 |
| 1.2 STATEMENT AND SIGNIFICANCE OF THE PROBLEMS..... | 6 |
| 1.3 OBJECTIVE OF THESIS..... | 7 |
| 1.4 OVERVIEW OF THESIS..... | 8 |
| CHAPTER 2 OVERREVIEW OF THERMOELECTRICITY AND DELAFOSSITE STRUCTURE | 9 |
| 2.1 THERMOELECTRIC ENERGY CONVERSION..... | 9 |
| 2.1.1 SEEBECK EFFECT..... | 9 |
| 2.1.2 PELTIER EFFECT..... | 10 |
| 2.2 THERMOELECTRIC FIGURE OF MERIT..... | 11 |
| 2.3 OPTIMIZING THERMOELECTRIC EFFICIENCY..... | 13 |
| 2.4 THERMOELECTRIC PROPERTIES..... | 14 |
| 2.4.1 SEEBECK COEFFICIENT RELATION..... | 14 |
| 2.4.2 ELECTRICAL CONDUCTIVITY RELATION..... | 17 |
| 2.4.3 THERMAL CONDUCTIVITY RELATION..... | 18 |
| 2.4.4 RELATION OF ENERGY GAP AND OPERATING TEMPERATURE..... | 19 |
| 2.5 DELAFOSSITE STRUCTURE | 19 |
| 2.5.1 CuFeO ₂ | 21 |
| 2.5.2 Cu _{1-x} Pt _x FeO ₂ | 21 |
| 2.5.3 CuFe _{1-x} Al _x O ₂ | 22 |
| 2.5.4 CuFe _{1-x} Sn _x O ₂ | 22 |
| 2.5.5 CuFe _{1-x} Pb _x O ₂ | 22 |

This material is reserved for educational use only, not allowed for commercial use.

Forbidden to modify the content, and cite the document when use.

| | |
|---|----|
| CHAPTER 3 RESEARCH METHODOLOGY AND MATERIAL CHARACTERIZATION..... | 23 |
| 3.1 EXPERIMENTAL PROCEDURE..... | 23 |
| 3.2 RESEARCH MATERIALS AND TOOLS..... | 24 |
| 3.2.1 EXPERIMENT TOOLS..... | 24 |
| 3.2.2 STARTING POWDERS..... | 26 |
| 3.2.3 ANALYTICAL PROCEDURE..... | 26 |
| 3.3 SAMPLE CHARACTERIZATION | 27 |
| 3.3.1 X-RAY DIFFRACTION ANALYSIS..... | 28 |
| 3.3.2 SEEBECK COEFFICIENT AND ELECTRICAL CONDUCTIVITY..... | 29 |
| 3.3.2.1 SEEBECK COEFFICIENT..... | 31 |
| 3.3.2.2 ELECTRICAL CONDUCTIVITY..... | 32 |
| 3.3.3 THERMAL CONDUCTIVITY..... | 33 |
| 3.3.3.1 THERMAL DIFFUSIVITY MEASUREMENT | 34 |
| 3.3.3.2 HEAT CAPACITY MEASUREMENT..... | 36 |
| 3.3.3.3 SAMPLE DENSITY | 37 |
| 3.3.4 UV-VIS-NIR SCANNING SPECTROPHOTOMETER..... | 37 |
| 3.3.4.1 ABSORPTION COEFFICIENT..... | 37 |
| 3.3.4.2 ABSORPTION MEASUREMENTS..... | 39 |
| 3.3.5 THERMAL ANALYSIS | 40 |
| 3.3.5.1 DIFFERENCE THERMAL ANALYSIS (DTA)..... | 40 |
| 3.3.5.2 THERMOGRAVIMETRIC METHOD (TG)..... | 40 |
| CHAPTER 4 EXPERIMENTA RESULTS..... | 41 |
| 4.1 THERMOELECTRIC PROPERTIES AT HIGH TEMPERATURE OF CuFeO_2 | 41 |
| 4.1.1 INTRODUCTION..... | 41 |
| 4.1.2 EXPERIMENTAL PROCEDURE..... | 41 |
| 4.1.3 RESULTS AND DISCUSSION..... | 42 |
| 4.1.3.1 X-RAY DIFFRACTION..... | 42 |
| 4.1.3.2 DENSITY..... | 43 |
| 4.1.3.3 SCANNING ELECTRON MICROSCOPE..... | 43 |
| 4.1.3.4 THERMOGRAVIMETRIC AND DIFFERENTIAL THERMAL..... | 46 |
| 4.1.3.5 SEEBECK COEFFICIENT..... | 47 |
| 4.1.3.6 THE HEIKES FORMULA..... | 47 |

| | |
|---|----|
| 4.1.3.7 ELECTRICAL CONDUCTIVITY..... | 48 |
| 4.1.3.8 THERMAL CONDUCTIVITY | 49 |
| 4.1.3.9 DIMENSIONLESS OF FIGURE OF MERIT..... | 51 |
| 4.1.3.10 ACTIVATION ENERGY..... | 52 |
| 4.1.3.10.1 ACTIVATION ENERGY OF PRODUCTION OF FREE CARRIERS..... | 52 |
| 4.1.3.10.2 ACTIVATION ENERGY OF CARRIER CONDUCTION..... | 53 |
| 4.1.3.10.3 ACTIVATION ENERGY OF CARRIER MOBILITY ... | 54 |
| 4.1.3.11 THE UMKLAPP RELATION..... | 56 |
| 4.1.3.12 OPTICAL PROPERTIES..... | 57 |
| 4.1.3.13 THE RELATION OF ENERGY GAP WITH TEMPERATURE..... | 60 |
| 4.1.3.14 ENERGY DIAGRAM..... | 61 |
| 4.1.3.15 RELATION OF MELTING POINT WITH ENERGY GAP..... | 61 |
| 4.1.4 SUMMARIES..... | 63 |
| 4.2 THERMOELECTRIC PROPERTIES AT HIGH TEMPERATURE OF $\text{Cu}_{1-x}\text{Pt}_x\text{FeO}_2$ | 64 |
| 4.2.1 INTRODUCTION..... | 64 |
| 4.2.2 EXPERIMENTAL PROCEDURE..... | 64 |
| 4.2.3 RESULTS AND DISCUSSION..... | 65 |
| 4.2.3.1 X-RAY DIFFRACTION..... | 65 |
| 4.2.3.2 DENSITY..... | 66 |
| 4.2.3.3 SCANNING ELECTRON MICROSCOPE..... | 67 |
| 4.2.3.4 SEEBECK COEFFICIENT..... | 68 |
| 4.2.3.5 THE HEIKES FORMULA..... | 69 |
| 4.2.3.6 ELECTRICAL CONDUCTIVITY..... | 69 |
| 4.2.3.7 POWER FACTOR..... | 73 |
| 4.2.3.8 THERMAL CONDUCTIVITY..... | 74 |
| 4.2.3.9 DIMENSIONLESS OF FIGURE OF MERIT (ZT)..... | 76 |
| 4.2.3.10 ACTIVATION ENERGY..... | 77 |
| 4.2.3.10.1 ACTIVATION ENERGY OF PRODUCTION OF FREE CARRIERS..... | 77 |
| 4.2.3.10.2 ACTIVATION ENERGY OF CARRIER | |

| | |
|--|-----|
| CONDUCTION..... | 78 |
| 4.2.3.10.3 ACTIVATION ENERGY OF CARRIER MOBILITY ... | 79 |
| 4.2.3.11 UMKLAPP RELATION..... | 80 |
| 4.2.3.12 OPTICAL PROPERTIES..... | 81 |
| 4.2.3.13 THE RELATION OF ENERGY GAP WITH TEMPERATURE..... | 83 |
| 4.2.3.14 ENERGY DIAGRAM..... | 84 |
| 4.2.3.15 RELATION OF MELTING POINT WITH ENERGY GAP..... | 85 |
| 4.2.4 SUMMARIES..... | 86 |
| 4.3 THERMOELECTRIC PROPERTIES AT HIGH TEMPERATURE OF $\text{CuFe}_{1-x}\text{Al}_x\text{O}_2$.. | 88 |
| 4.3.1 INTRODUCTION..... | 88 |
| 4.3.2 EXPERIMENTAL PROCEDURE..... | 88 |
| 4.3.3 RESULTS AND DISCUSSION..... | 89 |
| 4.3.3.1 X-RAY DIFFRACTION..... | 89 |
| 4.3.3.2 DENSITY..... | 90 |
| 4.3.3.3 SCANNING ELECTRON MICROSCOPE..... | 91 |
| 4.3.3.4 SEEBECK COEFFICIENT..... | 92 |
| 4.3.3.5 EXTENSIONS HEIKES FORMULA..... | 93 |
| 4.3.3.6 ELECTRICAL CONDUCTIVITY..... | 95 |
| 4.3.3.7 THERMAL CONDUCTIVITY..... | 96 |
| 4.3.3.8 POWER FACTOR AND DIMENSIONLESS OF FIGURE OF MERIT | 98 |
| 4.3.3.9 ACTIVATION ENERGY..... | 100 |
| 4.3.3.9.1 ACTIVATION ENERGY OF PRODUCTION OF FREE CARRIERS..... | 100 |
| 4.3.3.9.2 ACTIVATION ENERGY OF CARRIER CONDUCTION | 101 |
| 4.3.3.9.3 ACTIVATION ENERGY OF CARRIER MOBILITY.... | 102 |
| 4.3.3.10 OPTICAL PROPERTIES..... | 103 |
| 4.3.3.11 RELATION OF ENERGY GAP WITH TEMPERATURE | 105 |
| 4.3.3.12 ENERGY DIAGRAM..... | 105 |
| 4.3.3.13 RELATION OF MELTING POINT WITH ENERGY GAP..... | 107 |
| 4.3.4 SUMMARIES..... | 108 |
| 4.4 FINITE ELEMENT ANALYSIS OF $\text{CuFe}_{0.5}\text{Al}_{0.5}\text{O}_2$ | 110 |

| | |
|---|-----|
| 4.4.1 INTRODUCTION..... | 110 |
| 4.4.2 EXPERIMENTAL PROCEDURE..... | 110 |
| 4.4.3 THERMOELECTRIC PROPERTIES..... | 112 |
| 4.4.4 FINITE ELEMENT ANALYSIS..... | 114 |
| 4.4.4.1 GOVERNING EQUATION..... | 114 |
| 4.4.4.2 FINITE ELEMENT EQUATION..... | 115 |
| 4.4.4.3 THERMOELECTRIC 1 BAR | 117 |
| 4.4.4.3.1 GEOMETRY DOMAIN | 117 |
| 4.4.4.3.2 BOUNDARY CONDITION..... | 117 |
| 4.4.4.3.3 MATERIAL PROPERTIES | 118 |
| 4.4.4.3.4 FINITE ELEMENT RESULTS | 118 |
| 4.4.4.4 THERMOELECTRIC 1 MODULE..... | 119 |
| 4.4.4.4.1 GEOMETRY AND FINITE ELEMENT DOMAIN..... | 120 |
| 4.4.4.4.2 BOUNDARY CONDITIONS..... | 120 |
| 4.4.4.4.3 MATERIAL PROPERTIES | 121 |
| 4.4.4.4.4 FINITE ELEMENT RESULTS..... | 121 |
| 4.4.5 SUMMARIES..... | 122 |
| 4.5 THERMOELECTRIC PROPERTIES AT HIGH TEMPERATURE | |
| OF $\text{CuFe}_{1-x}\text{Sn}_x\text{O}_2$ | 123 |
| 4.5.1 INTRODUCTION..... | 123 |
| 4.5.2 EXPERIMENTAL PROCEDURE..... | 123 |
| 4.5.3 RESULTS AND DISCUSSION..... | 124 |
| 4.5.3.1 X-RAY DIFFRACTION..... | 124 |
| 4.5.3.2 DENSITY..... | 125 |
| 4.5.3.3 SCANNING ELECTRON MICROSCOPE..... | 125 |
| 4.5.3.4 SEEBECK COEFFICIENT..... | 126 |
| 4.5.3.5 EXTENSIONS HEIKES FORMULA..... | 128 |
| 4.5.3.6 ELECTRICAL CONDUCTIVITY..... | 129 |
| 4.5.3.7 POWER FACTOR..... | 130 |
| 4.5.3.8 ACTIVATION ENERGY..... | 131 |
| 4.5.3.8.1 ACTIVATION ENERGY OF PRODUCTION OF FREE | |

| | |
|--|-----|
| CARRIERS..... | 131 |
| 4.5.3.8.2 ACTIVATION ENERGY OF CARRIER CONDUCTION..... | 132 |
| 4.5.3.8.3 ACTIVATION ENERGY OF CARRIER MOBILITY..... | 133 |
| 4.5.3.9 THERMAL CONDUCTIVITY..... | 134 |
| 4.5.3.10 DIMENSIONLESS OF FIGURE OF MERIT | 135 |
| 4.5.4 SUMMARIES..... | 136 |
| 4.6 THERMOELECTRIC PROPERTIES AT HIGH TEMPERATURE OF CuFe _{1-x} Pb _x O ₂ | 138 |
| 4.6.1 INTRODUCTION..... | 138 |
| 4.6.2 EXPERIMENTAL PROCEDURE..... | 138 |
| 4.6.3 RESULTS AND DISCUSSION..... | 139 |
| 4.6.3.1 X-RAY DIFFRACTION..... | 139 |
| 4.6.3.2 DENSITY..... | 140 |
| 4.6.3.3 SCANNING ELECTRON MICROSCOPE..... | 141 |
| 4.6.3.4 SEEBECK COEFFICIENT..... | 143 |
| 4.6.3.5 EXTENSIONS HEIKES FORMULA..... | 144 |
| 4.6.3.6 ELECTRICAL CONDUCTIVITY..... | 145 |
| 4.6.3.7 THERMAL CONDUCTIVITY..... | 146 |
| 4.6.3.8 DIMENSIONLESS OF FIGURE OF MERIT (<i>ZT</i>)..... | 148 |
| 4.6.4 SUMMARIES..... | 147 |
| 4.7 PROTOTYPE OF THERMOELECTRIC MODULE OF <i>p</i> -Cu _{0.95} Pt _{0.05} FeO ₂ AND <i>n</i> -CuFe _{0.95} Pb _{0.05} O ₂ | 150 |
| 4.7.1 INTRODUCTION..... | 150 |
| 4.7.2 GEOMETRY OF MODULES..... | 150 |
| 4.7.3 THE INVENTION PROCESS OF THERMOELECTRIC MODULES..... | 151 |
| 4.7.4 MEASUREMENT PROCEDURE | 154 |
| 4.7.5 MEASUREMENT RESULTS | 155 |
| 4.7.5.1 OUTPUT ELECTRICAL VOLTAGE AND CURRENT | 155 |
| 4.7.5.2 OUTPUT POWER | 157 |
| 4.7.6 SUMMARIES..... | 160 |
| CHAPTER 5 RESULTS AND DISCUSSION..... | 161 |

| | |
|--|-----|
| 5.1 DISCUSSION IN SEPARATE RESULTS | 161 |
| 5.2 SUMMARIES..... | 165 |
| CHAPTER 6 CONCLUSION AND SUGGESTION..... | 166 |
| 6.1 CONCLUSION | 167 |
| 6.2 SUGGESTION AND FUTURE WORK..... | 167 |
| REFERENCES..... | 168 |
| APPENDICES..... | 173 |
| A: PUBLICATION IN INTERNATIONAL JOURNALS..... | 174 |
| A.1: THERMOELECTRIC PROPERTIES OF $\text{Cu}_{1-x}\text{Pt}_x\text{FeO}_2$ ($0 \leq x \leq 0.05$) DELAFOSSITE-TYPE TRANSITION OXIDE..... | 175 |
| A.2: THEORETICAL STUDY OF ELECTRONIC STRUCTURE AND THERMOELECTRIC PROPERTIES OF DOPED CuAlO_2 | 183 |
| B: NATIONAL AND INTERNATIONAL PROCEEDING..... | 188 |
| B.1: SYNTHESIS AND THERMOELECTRIC PROPERTIES OF P-TYPE CuFeO_2 DELAFOSSITE-TYPE OXIDE..... | 189 |
| B.2: SYNTHESIS AND THERMOELECTRIC, ELECTRICAL AND OPTICAL PROPERTIES OF P-TYPE CuAlO_2 DELAFOSSITE..... | 193 |
| B.3: SYNTHESIS, THERMOELECTRIC PROPERTIES OF $\text{CuFe}_{0.5}\text{Al}_{0.5}\text{O}_2$ DELAFOSSITE AND FINITE ELEMENT COMPUTING FOR POWER GENERATOR ON ITS MODULE..... | 204 |
| B.4: PREPARATION AND COMPARISON OF THERMOELECTRIC PROPERTIES OF CuFeO_2 , CuAlO_2 AND $\text{CuFe}_{0.5}\text{Al}_{0.5}\text{O}_2$ DELAFOSSITE STRUCTURE..... | 209 |
| C: INVITATING EMAIL FROM THE INTERNATIONAL CENTRE OF DIFFRACTION..... | 211 |
| D: CRYSTALLOGRAPHIC REFERENCE..... | 216 |
| D.1: CuFeO_2 : ICSD#10-075-2146..... | 217 |
| D.2: CuO : JCPDS#05-0661..... | 219 |
| D.3: Fe_2O_3 : JCPDS#07-0322..... | 220 |
| D.4: CuAlO_2 : JCPDS# 35-1401..... | 221 |

LIST OF FIGURES

| | PAGE |
|-------------------|--|
| FIGURE 1.1 | (A) Thermoelectric power generator (B) Thermoelectric cooler (C) Thermoelectric module 1 |
| FIGURE 1.2 | The application of thermoelectric devices..... 1 |
| FIGURE 1.3 | The thermoelectric properties of Bi_2Te_3 (A) Seebeck coefficient (B) The electrical conductivity (C) The thermal conductivity..... 2 |
| FIGURE 1.4 | (A) The conventional thermoelectric materials (B) The ZT of conventional thermoelectric materials..... 3 |
| FIGURE 1.5 | The alternately stacking octahedral layers of delafossite and Na_xCoO_2 compound..... 3 |
| FIGURE 1.6 | (A) The crystal field effect to splitting 3d energy state into two state of t_{2g} and e_g . (B) The degeneracy of low spin state of Na_xCoO_2 for the Co^{3+} ($3d^6$), $g_3=1$ and Co^{4+} ($3d^5$), $g_3=6$ 4 |
| FIGURE 1.7 | The experimental results of thermoelectric power of the $\text{Na}_{0.5}\text{CoO}_2$ by Plewa and Ohtaki, and The CuCrO_2 delafossite doped Mg by Y. Ono..... 5 |
| FIGURE 1.8 | (A) The model of module (B) The Finite element meshes (C) The temperature and (D) The voltage distribution..... 5 |
| FIGURE 1.9 | The relation of energy gap with temperature of thermoelectric materials in constant $E_g = 4k_B T$ 6 |
| FIGURE 2.1 | The conversion of temperature differences directly into electric potential.... 10 |
| FIGURE 2.2 | The heat is released or absorbed at the junction of two dissimilar materials, when the current is applied..... 10 |
| FIGURE 2.3 | A one-leg device of thermoelectric generator with n- type materials..... 12 |
| FIGURE 2.4 | A thermoelectric generator with n- and p-type materials connected..... 13 |
| FIGURE 2.5 | The S , $\sigma (=1/\rho)$, κ_e , κ_l and ZT as a function of the carrier concentration..... 13 |
| FIGURE 2.6 | (A) The CuFeO_2 delafossite structure. (B) The rhombohedral primitive cell. (C) The hexagonal unit cell. (D) The alternative stacking layers of O-A-O dumbbell and octahedral layer..... 19 |
| FIGURE 2.7 | The CuFeO_2 delafossite structure..... 21 |
| FIGURE 3.1 | The agate mortar..... 24 |
| FIGURE 3.2 | The hydraulic pressure..... 24 |
| FIGURE 3.3 | The alumina crucible..... 25 |
| FIGURE 3.4 | The sintering furnace..... 25 |

This material is reserved for educational use only, not allowed for commercial use.

Forbidden to modify the content, and cite the document when use.

| | | |
|--------------------|--|----|
| FIGURE 3.5 | The pelleting mould for pellet sample and bar sample..... | 26 |
| FIGURE 3.6 | Bragg reflection..... | 28 |
| FIGURE 3.7 | Powder x-ray diffraction (XRD) of PHILIPS model: X' Pert MPD..... | 29 |
| FIGURE 3.8 | The configuration of ZEM-2 the Seebeck coefficient measuring system..... | 30 |
| FIGURE 3.9 | (A) System inside the furnace, (B) The sample operation..... | 30 |
| FIGURE 3.10 | The diagram to measure Seebeck coefficient..... | 31 |
| FIGURE 3.11 | The diagram to measure electric resistivity..... | 32 |
| FIGURE 3.12 | System of measuring thermal conductivity in a model TC-7000 of the ULVAC-RIKO..... | 34 |
| FIGURE 3.13 | The diagram to measure thermal conductivity..... | 35 |
| FIGURE 3.14 | The temperature vs. time measurement curve by the laser flash technique.... | 35 |
| FIGURE 3.15 | The diagram to measure heat capacity..... | 36 |
| FIGURE 3.16 | The diagram of UV-VIS-NIR scanning spectrophotometer..... | 39 |
| FIGURE 4.1 | The pellets of the CuFeO ₂ sinter sample..... | 42 |
| FIGURE 4.2 | The XRD patterns of the CuFeO ₂ sinter sample..... | 42 |
| FIGURE 4.3 | The microstructure and the morphology of the CuFeO ₂ sinter sample..... | 43 |
| FIGURE 4.4 | The Energy-Dispersive X-ray spectroscopy of the CuFeO ₂ sinter sample..... | 45 |
| FIGURE 4.5 | The TG-DTG curve of the CuFeO ₂ sinter sample..... | 46 |
| FIGURE 4.6 | The temperature dependence of Seebeck coefficient of the CuFeO ₂ sinter sample comparing with other compounds..... | 47 |
| FIGURE 4.7 | The temperature dependence of electrical conductivity coefficient of the CuFeO ₂ sinter sample comparing with other compounds..... | 49 |
| FIGURE 4.8 | The temperature dependence of thermal conductivity of the CuFeO ₂ sinter sample comparing with other compounds..... | 50 |
| FIGURE 4.9 | The temperature dependence of ZT of the CuFeO ₂ sintering sample comparing with other compounds..... | 52 |
| FIGURE 4.10 | The Seebeck coefficient (S) vs. 1000/T curve | 53 |
| FIGURE 4.11 | The curve of log σ vs. 1000/T of CuFeO ₂ sintering sample..... | 54 |
| FIGURE 4.12 | The thermal conductivity vs. 1000/T curve | 56 |
| FIGURE 4.13 | Absorbance spectrum of the CuFeO ₂ sample at room temperature..... | 58 |
| FIGURE 4.14 | (A) Direct optical gap of the CuFeO ₂ sample (B) Indirect optical gap of the CuFeO ₂ sample..... | 59 |
| FIGURE 4.15 | Temperature dependence of the direct band gap (E_g) of the CuFeO ₂ sample..... | 60 |
| FIGURE 4.16 | The energy level diagram of the CuFeO ₂ delafossite (not exact to the scale).. | 61 |
| FIGURE 4.17 | The relation curve of energy gap and temperature..... | 62 |

| | | |
|--------------------|---|----|
| FIGURE 4.18 | The pellet and bar of the $\text{Cu}_{1-x}\text{Pt}_x\text{FeO}_2$ samples..... | 65 |
| FIGURE 4.19 | The XRD patterns of the CuFeO_2 and the $\text{Cu}_{1-x}\text{Pt}_x\text{FeO}_2$ samples with Pt content of the $x = 0.01, 0.03$ and 0.05 | 65 |
| FIGURE 4.20 | The lattice parameters as a function of the Pt concentration in x content of the $\text{Cu}_{1-x}\text{Pt}_x\text{FeO}_2$ ($x=0, 0.01, 0.03$ and 0.05) samples..... | 66 |
| FIGURE 4.21 | The microstructure on cutting surface of the $\text{Cu}_{1-x}\text{Pt}_x\text{FeO}_2$ samples..... | 67 |
| FIGURE 4.22 | The Seebeck coefficient of the $\text{Cu}_{1-x}\text{Pt}_x\text{FeO}_2$ ($x=0, 0.01, 0.03$, and 0.05) samples vs. the temperature..... | 68 |
| FIGURE 4.23 | The electrical conductivity of the $\text{Cu}_{1-x}\text{Pt}_x\text{FeO}_2$ ($x=0, 0.01, 0.03$, and 0.05) samples vs. the temperature..... | 70 |
| FIGURE 4.24 | The activation energy (E_σ) as a function of the Pt substitution in x content... | 72 |
| FIGURE 4.25 | The $\log \sigma$ vs. $1/T^{1/4}$ curve | 73 |
| FIGURE 4.26 | The power factor of the $\text{Cu}_{1-x}\text{Pt}_x\text{FeO}_2$ ($x = 0, 0.01, 0.03$ and 0.05) samples vs. the temperature..... | 74 |
| FIGURE 4.27 | The thermal conductivity of the $\text{Cu}_{1-x}\text{Pt}_x\text{FeO}_2$ ($x = 0, 0.01, 0.03$ and 0.05) samples vs. the temperature..... | 75 |
| FIGURE 4.28 | The ZT value of the $\text{Cu}_{1-x}\text{Pt}_x\text{FeO}_2$ ($x = 0.01, 0.03$ and 0.05) samples vs. the temperature..... | 77 |
| FIGURE 4.29 | The Seebeck coefficient vs. $1000/T$ curve | 78 |
| FIGURE 4.30 | The $\log \sigma$ vs. $1000/T$ curve | 79 |
| FIGURE 4.31 | The thermal conductivity vs. $1000/T$ curve | 80 |
| FIGURE 4.32 | The absorption spectra of the $\text{Cu}_{1-x}\text{Pt}_x\text{FeO}_2$ ($x = 0.01, 0.03$ and 0.05) samples..... | 81 |
| FIGURE 4.33 | The direct optical gap of the $\text{Cu}_{1-x}\text{Pt}_x\text{FeO}_2$ ($x = 0.01, 0.03$ and 0.05) samples..... | 82 |
| FIGURE 4.34 | The indirect optical gap of the $\text{Cu}_{1-x}\text{Pt}_x\text{FeO}_2$ ($x = 0.01, 0.03$ and 0.05) samples..... | 83 |
| FIGURE 4.35 | The temperature dependence of the direct band gap of the $\text{Cu}_{1-x}\text{Pt}_x\text{FeO}_2$ samples..... | 84 |
| FIGURE 4.36 | The energy level diagram of the $\text{Cu}_{1-x}\text{Pt}_x\text{FeO}_2$ delafossite (not exact to the scale)..... | 85 |
| FIGURE 4.37 | The relation curve of energy gap and temperature..... | 86 |
| FIGURE 4.38 | The pellet and bar samples of the CuFeO_2 , the $\text{CuFe}_{0.5}\text{Al}_{0.5}\text{O}_2$ and the CuAlO_2 samples..... | 88 |
| FIGURE 4.39 | The XRD patterns of the sinter samples of the $\text{CuFe}_{0.5}\text{Al}_{0.5}\text{O}_2$, the CuFeO_2 , and the CuAlO_2 | 89 |

| | | |
|--------------------|---|-----|
| FIGURE 4.40 | The lattice parameters of the sintered samples of the $\text{CuFe}_{0.5}\text{Al}_{0.5}\text{O}_2$, the CuFeO_2 , and the CuAlO_2 | 90 |
| FIGURE 4.41 | The microstructure and morphology of the CuFeO_2 , the $\text{CuFe}_{0.5}\text{Al}_{0.5}\text{O}_2$ and the CuAlO_2 samples..... | 92 |
| FIGURE 4.42 | The Seebeck coefficient of the CuFeO_2 , the $\text{CuFe}_{0.5}\text{Al}_{0.5}\text{O}_2$, and the CuAlO_2 samples vs. the temperature..... | 93 |
| FIGURE 4.43 | The degeneracy of high spin state of the CuFeO_2 delafossite..... | 94 |
| FIGURE 4.44 | The electrical conductivity the $\text{CuFe}_{0.5}\text{Al}_{0.5}\text{O}_2$, the CuFeO_2 , and the CuAlO_2 samples vs. the temperature..... | 95 |
| FIGURE 4.45 | The $\log \sigma$ vs. $1/T^{1/4}$ curves..... | 96 |
| FIGURE 4.46 | The thermal conductivity of the $\text{CuFe}_{0.5}\text{Al}_{0.5}\text{O}_2$, the CuFeO_2 and the CuAlO_2 samples vs. the temperature. | 97 |
| FIGURE 4.47 | The power factor of the $\text{CuFe}_{0.5}\text{Al}_{0.5}\text{O}_2$, the CuFeO_2 and the CuAlO_2 samples vs. the temperature..... | 98 |
| FIGURE 4.48 | The dimensionless Figure of Merit (ZT) of the CuFeO_2 , the CuAlO_2 , and the $\text{CuFe}_{0.5}\text{Al}_{0.5}\text{O}_2$ samples vs. temperature..... | 99 |
| FIGURE 4.49 | The Seebeck coefficient vs. $1000/T$ curve..... | 100 |
| FIGURE 4.50 | The $\log \sigma$ vs. $1000/T$ curve..... | 102 |
| FIGURE 4.51 | Absorbance spectrum of the CuFeO_2 , the CuAlO_2 , and the $\text{CuFe}_{0.5}\text{Al}_{0.5}\text{O}_2$ samples at room temperature..... | 103 |
| FIGURE 4.52 | (A) Indirect and (B) Direct energy gap of the $\text{CuFe}_{0.5}\text{Al}_{0.5}\text{O}_2$, the CuFeO_2 and the CuAlO_2 samples..... | 104 |
| FIGURE 4.53 | The temperature dependence of the direct band gap of the $\text{CuFe}_{0.5}\text{Al}_{0.5}\text{O}_2$, the CuFeO_2 and the CuAlO_2 delafossite..... | 105 |
| FIGURE 4.54 | The energy level diagram of the (A) CuFeO_2 , (B) $\text{CuFe}_{0.5}\text{Al}_{0.5}\text{O}_2$, and (C) CuAlO_2 delafossite (not exact to the scale)..... | 107 |
| FIGURE 4.55 | The relation curve of the energy gap and the temperature..... | 108 |
| FIGURE 4.56 | The single bar of $\text{CuFe}_{0.5}\text{Al}_{0.5}\text{O}_2$ sample in dimension $4.2 \times 2.5 \times 20 \text{ mm}^3$ | 110 |
| FIGURE 4.57 | (A) The test kid for measuring samples of the thermoelectric generator. (B) The applying temperature difference on the sample bar. | 111 |
| FIGURE 4.58 | The output voltage of the $\text{CuFe}_{0.5}\text{Al}_{0.5}\text{O}_2$ bar after applied the temperature difference..... | 111 |
| FIGURE 4.59 | The properties of (A) Seebeck coefficient (B) electrical conductivity and (C) thermal conductivity of the $\text{CuFe}_{0.5}\text{Al}_{0.5}\text{O}_2$ samples..... | 113 |
| FIGURE 4.60 | (A) The thermoelectric bar. (B) The Finite element model. And (C) The Finite element mesh..... | 117 |

| | | |
|--------------------|--|-----|
| FIGURE 4.61 | (A) The Finite element model (B) Voltage and (C) Temperature distribution..... | 118 |
| FIGURE 4.62 | The output voltage of the $\text{CuFe}_{0.5}\text{Al}_{0.5}\text{O}_2$ bar on measurement, and the Finite Element computing..... | 119 |
| FIGURE 4.63 | The model of thermoelectric module..... | 119 |
| FIGURE 4.64 | (A) The Finite element model of the thermoelectric module and (C) The Finite element mesh of the thermoelectric module..... | 120 |
| FIGURE 4.65 | (A) The Finite element mesh (B) Voltage and (C) Temperature distribution..... | 121 |
| FIGURE 4.66 | The output voltage of the single bar and the modules thermoelectric..... | 122 |
| FIGURE 4.67 | The specimen of the $\text{CuFe}_{1-x}\text{Sn}_x\text{O}_2$ samples..... | 123 |
| FIGURE 4.68 | The XRD patterns of the CuFeO_2 and the $\text{CuFe}_{1-x}\text{Sn}_x\text{O}_2$ samples with the Sn content of the $x = 0.01, 0.03$ and 0.05 | 124 |
| FIGURE 4.69 | The lattice parameters as a function of the Sn concentration in the x content of the $\text{CuFe}_{1-x}\text{Sn}_x\text{O}_2$ ($x=0, 0.01, 0.03,$ and 0.05) samples..... | 125 |
| FIGURE 4.70 | The microstructure on surface of the $\text{CuFe}_{1-x}\text{Sn}_x\text{O}_2$ sinter samples..... | 126 |
| FIGURE 4.71 | The Seebeck coefficient of the $\text{CuFe}_{1-x}\text{Sn}_x\text{O}_2$ ($x=0, 0.01, 0.03,$ and 0.05) samples vs. the temperature..... | 127 |
| FIGURE 4.72 | The electrical conductivity of the $\text{CuFe}_{1-x}\text{Sn}_x\text{O}_2$ ($x=0, 0.01, 0.03,$ and 0.05) samples vs. the temperature..... | 130 |
| FIGURE 4.73 | The power factor of the $\text{CuFe}_{1-x}\text{Sn}_x\text{O}_2$ ($x=0, 0.01, 0.03,$ and 0.05) samples vs. the temperature..... | 131 |
| FIGURE 4.74 | The Seebeck coefficient (S) vs. temperature and $1000/T$ curve | 132 |
| FIGURE 4.75 | The $\log \sigma$ vs. $1000/T$ curve | 133 |
| FIGURE 4.76 | The thermal conductivity of the $\text{CuFe}_{1-x}\text{Sn}_x\text{O}_2$ ($x=0, 0.01, 0.03,$ and 0.05) samples vs. the temperature..... | 134 |
| FIGURE 4.77 | The ZT value of the $\text{CuFe}_{1-x}\text{Sn}_x\text{O}_2$ ($x=0, 0.01, 0.03,$ and 0.05) samples vs. temperature..... | 136 |
| FIGURE 4.78 | The pellet and bar samples of the $\text{CuFe}_{1-x}\text{Pb}_x\text{O}_2$ | 138 |
| FIGURE 4.79 | The XRD patterns of the CuFeO_2 and the $\text{CuFe}_{1-x}\text{Pb}_x\text{O}_2$ samples with Pb content of $x = 0.01, 0.03$ and 0.05 | 139 |
| FIGURE 4.80 | The lattice parameters as a function of the Pb concentration in the x content of the $\text{CuFe}_{1-x}\text{Pb}_x\text{O}_2$ ($x=0, 0.01, 0.03,$ and 0.05) samples..... | 140 |
| FIGURE 4.81 | The Energy-Dispersive X-ray spectroscopy of sinter sample (A) the CuFeO_2 , (B) $\text{CuFe}_{1-x}\text{Pb}_x\text{O}_2$ for $x=0.03$ and (C) $\text{CuFe}_{1-x}\text{Pb}_x\text{O}_2$ for $x=0.05$ | 143 |

| | | |
|--------------------|---|-----|
| FIGURE 4.82 | The Seebeck coefficient of the $\text{CuFe}_{1-x}\text{Pb}_x\text{O}_2$ ($x=0, 0.01, 0.03, \text{ and } 0.05$) samples vs. the temperature..... | 144 |
| FIGURE 4.83 | The electrical conductivity the $\text{CuFe}_{1-x}\text{Pb}_x\text{O}_2$ ($x=0, 0.01, 0.03, \text{ and } 0.05$) samples vs. the temperature..... | 146 |
| FIGURE 4.84 | The thermal conductivity of the $\text{CuFe}_{1-x}\text{Pb}_x\text{O}_2$ ($x=0, 0.03, \text{ and } 0.05$) samples vs. the temperature..... | 147 |
| FIGURE 4.85 | The ZT value of the $\text{CuFe}_{1-x}\text{Pb}_x\text{O}_2$ ($x=0, 0.03, \text{ and } 0.05$) samples vs. temperature..... | 148 |
| FIGURE 4.86 | The model of thermoelectric module..... | 150 |
| FIGURE 4.87 | The prototypes of thermoelectric module..... | 151 |
| FIGURE 4.88 | The specimens of the $\text{Cu}_{0.95}\text{Pt}_{0.05}\text{FeO}_2$ and the $\text{CuFe}_{0.95}\text{Pb}_{0.05}\text{O}_2$ samples..... | 151 |
| FIGURE 4.89 | The copper straps contacted on the top surface of alumina plate..... | 152 |
| FIGURE 4.90 | (A) The 1 couple of the n-p leg module and (B) the 2 couples of the n-p leg module..... | 152 |
| FIGURE 4.91 | The copper strap on (A) The 1 couple of n-leg and p-leg and (B) the 2 couples of n-leg and p-leg..... | 153 |
| FIGURE 4.92 | (A) The connection of the copper wires, and (B) The topping of the alumina plate..... | 153 |
| FIGURE 4.93 | (A) The thermoelectric modules. (B) Thermoelectric module of 1 couple p-leg and n-leg and (C) The thermoelectric module of 2 couples p-legs and n-legs..... | 154 |
| FIGURE 4.94 | The setting measurement of output power of the thermoelectric module.... | 155 |
| FIGURE 4.95 | The output of electrical voltage of the thermoelectric modules with temperature difference..... | 156 |
| FIGURE 4.96 | The output of electrical current of thermoelectric modules with temperature difference..... | 157 |
| FIGURE 4.97 | The Output power of the thermoelectric modules with temperature difference..... | 158 |
| FIGURE 4.98 | The output voltage of the thermoelectric modules with output current..... | 159 |
| FIGURE 4.99 | The output power of the thermoelectric modules with output current..... | 159 |
| FIGURE 5.1 | The Seebeck coefficient of the $\text{Cu}_{0.95}\text{Pt}_{0.05}\text{FeO}_2$, $\text{CuFe}_{0.5}\text{A}_{0.5}\text{O}_2$, $\text{CuFe}_{1-x}\text{Sn}_x\text{O}_2$ ($x=0.01, 0.03, \text{ and } 0.05$) samples and the CuFeO_2 sample-based..... | 162 |
| FIGURE 5.2 | The electrical conductivity of the $\text{Cu}_{0.95}\text{Pt}_{0.05}\text{FeO}_2$, $\text{CuFe}_{0.5}\text{A}_{0.5}\text{O}_2$, $\text{CuFe}_{0.95}\text{Sn}_{0.05}\text{O}_2$ samples and the CuFeO_2 sample-based..... | 163 |

- FIGURE 5.3** The thermal conductivity of the $\text{Cu}_{0.95}\text{Pt}_{0.05}\text{FeO}_2$, $\text{CuFe}_{0.5}\text{A}_{0.5}\text{O}_2$, $\text{CuFe}_{1-x}\text{Sn}_x\text{O}_2$ ($x=0.01, 0.03, \text{ and } 0.05$), $\text{CuFe}_{1-x}\text{Pb}_x\text{O}_2$ ($x=0.03 \text{ and } 0.05$) samples and the CuFeO_2 sample-based..... 164
- FIGURE 5.4** The ZT value of the $\text{Cu}_{0.95}\text{Pt}_{0.05}\text{FeO}_2$, $\text{CuFe}_{0.5}\text{A}_{0.5}\text{O}_2$, $\text{CuFe}_{0.95}\text{Sn}_{0.05}\text{O}_2$, $\text{CuFe}_{0.95}\text{Pb}_{0.05}\text{O}_2$ and the CuFeO_2 sample-based..... 165



LIST OF NOTATIONS

| | |
|----------------|--|
| A | The cross-sectional area of bulk sample. |
| C_p | The heat capacity. |
| D | The atomic density. |
| D_r | The ratio of bulk density to theoretical density. |
| E | The electric field. |
| E_F | The Fermi energy level. |
| E_g | The energy band gap. |
| $E_g(T)$ | The band gap at temperature T K. |
| $E_g(0)$ | The band gap at temperature 0 K. |
| E_G | The optimal energy gap. |
| E_u | The activation energy for carrier mobility. |
| E_σ | The activation energy for carrier conduction. |
| E_s | The activation energy for production of free carrier. |
| E_x | The electric field strength in x-component. |
| E_o | The maximum value of electric field strength. |
| I | The electric current. |
| I_e | The intensity of electric field. |
| $I_e(\lambda)$ | The intensity of light transmitted at wavelength λ . |
| $I_o(\lambda)$ | The intensity of light incident at wavelength λ . |
| I_{out} | The output of electrical current. |
| J | The electrical current density. |
| L | The thickness the bulk sample. |
| L_d | The orbital degeneracy. |
| L_o | The Lorenz factor. |
| M | The average atomic mass. |
| N | The number of particle. |
| N_D | The doping density (or the hole carriers density). |
| N_T | The effective density of states of charge carrier |
| N_v | The effective density of state. |
| OD | The optical density. |
| P_{out} | The electrical power output. |

| | |
|-------------------|--|
| PF | The power factor. |
| Q | The heat absorption energy. |
| Q_{in} | The thermal power input. |
| R | The electrical resistance. |
| R_{ref} | The reference resistor. |
| R_{load} | The resistance of load. |
| S | The Seebeck coefficient. |
| S_d | The spin degeneracy. |
| T | The temperature. |
| ΔT | The temperature gradient. |
| T_C | The temperature at cold site. |
| T_H | The temperature at hot site. |
| T^e | The nodal unknown of temperature on element e. |
| T_h | The operation temperature. |
| T_m | The melting temperature. |
| V | The volume of bulk sample. |
| ΔV | The potential difference. |
| V_{out} | The output of electrical voltage. |
| W | The characteristic penetration depth. |
| Z | The Figure of Merit. |
| ZT | The dimensionless of Figure of Merit. |
| a | The thermal diffusivity. |
| a_{ab} | The optical absorbance. |
| $a_{ab}(\lambda)$ | The absorbance of wavelength at λ . |
| d | The sample density. |
| d_l | The lattice plane distance. |
| d_x | The theoretically density. |
| e | The electronic charge constant. |
| f | The Fermi function. |
| g | The degeneracy of system. |
| $h\nu$ | The photon energy. |
| i_h | The thickness of bulk sample. |
| k_B | The Boltzmann's constant. |

| | |
|-----------------------|--|
| m | The weight of bulk sample. |
| n | The carrier concentration. |
| $n(\varepsilon)$ | The carrier density as a function of energy. |
| q | The heat flux. |
| r | The specific resistance. |
| t | The time. |
| x | The ration of difference carrier with total atom site. |
| Π | The Peltier coefficient. |
| Ξ | The transport distribution. |
| α | The absorption coefficient. |
| δ | The proportionality constant of the Umklapp. |
| ε | The energy. |
| η | The efficiency of thermoelectric generator. |
| φ | The electric potential. |
| φ^e | The nodal unknown of the potential on element e. |
| κ | The thermal conductivity. |
| κ_e | The electronic part of thermal conductivity. |
| κ_l | The lattice part of thermal conductivity. |
| κ_u | The Umklapp phonon thermal conductivity. |
| λ | The wavelength of light. |
| μ | The mobility of carriers. |
| μ_c | The Chemical potential. |
| μ_o | The mobility constant. |
| $\mu(\varepsilon)$ | The carrier mobility as a function of energy. |
| θ | The Bragg's angle. |
| ρ | The electrical resistivity. |
| σ | The electrical conductivity. |
| $\sigma(\varepsilon)$ | The electronic conductivity as a function of energy. |
| σ_s | The system entropy. |
| ω | The angular frequency. |

CHAPTER 1

INTRODUCTION

1.1 BACKGROUND

Today, thermoelectric materials [1–3] have been displayed their potential as alternative sources of energy. The thermoelectric effect refers to a phenomenon whereby a temperature gradient is converted directly into electrical current and vice versa. Furthermore, thermoelectric generator can be used to converting waste heat to produce by various sources to electrical power. **Figure 1.1** displays the thermoelectric module, and its power greater and cooler. The reverse effect can be practiced in thermoelectric coolers of refrigerators and other cooling systems. Other applications, it can use in application of detectors and sensors. **Figure 1.2** shows the application of thermoelectric.

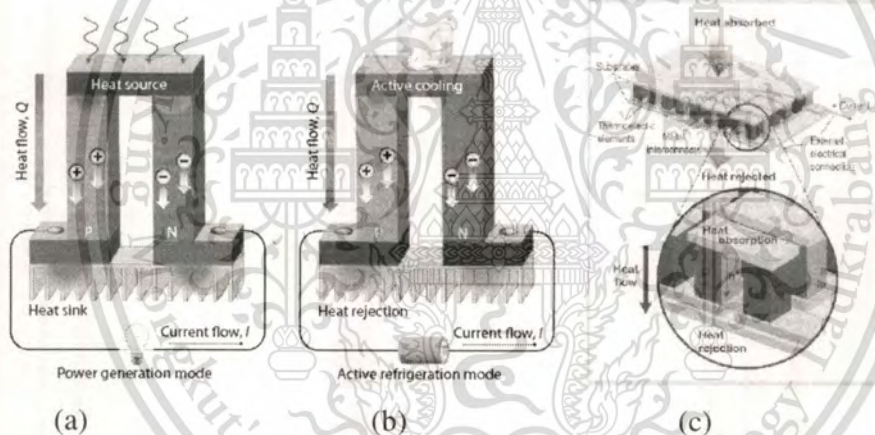


Figure 1.1 (a) Thermoelectric power generator (b) Thermoelectric cooler (c) Thermoelectric power module [4, 5].

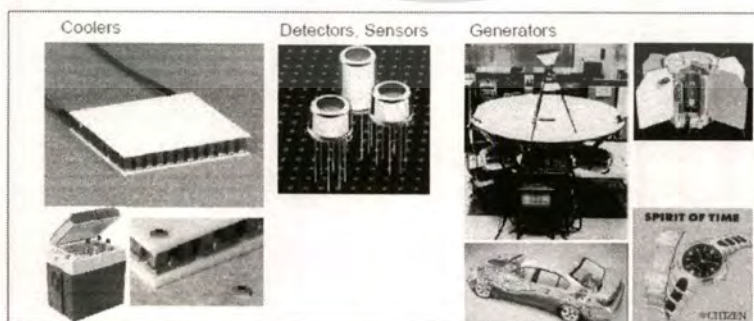


Figure 1.2 The application of thermoelectric device.

This material is reserved for educational use only, not allowed for commercial use.

Forbidden to modify the content, and cite the document when use.

These conversion mechanisms have advantages of not having moving parts. The performance of the thermoelectric material is determined by the dimensionless Figure of Merit, $ZT = \sigma S^2 T / \kappa$, where T is the absolute temperature, S is the Seebeck coefficient, σ and κ are the electrical and thermal conductivity, respectively [3, 6, 7]. Ideally, the ZT value approaches its optimum value when σ and S are maximized, and κ is as small as possible. As the equation suggests, the efficiency is increased at high temperature.

The conventional thermoelectric materials, such as Bi_2Te_3 and PbTe [7], show high thermoelectric properties and high ZT value. The thermoelectric properties of the Bi_2Te_3 [8] are shown in Figure 1.3 and the ZT of Bi_2Te_3 and PbTe is shown in Figure 1.4 (b). However, the Bi_2Te_3 easily decompose, oxidize or melt at high temperatures in air [9] as shown in Figure 1.4 (a). In fact, heavy metals in Bi-Te and Pb-Te are costly and toxic [7]. This may result in a limited use in practical applications of thermoelectric power generation. Hence, the development of oxide materials with both high performance and environmentally stable at high temperature is crucial for practical applications. Recently, thermoelectric properties of oxide materials have been shown conversion efficiency close to that of conventional semi-metallic materials as shown in Figure 1.4 (b). For example, thermoelectric voltage and direct current conductivity of transition-metal oxides such as NiO , NaCo_2O_4 and $\text{Ca}_3\text{Co}_4\text{O}_9$ have been reported to be large at high temperature conditions [7-11]. In addition, CuFeO_2 , which is low-cost and non-toxic, compound of delafossite structure has been reported to exhibit a large value of S ($544 \mu\text{V/K}$) and PF ($0.44 \times 10^{-4} \text{ W/mK}^2$) [12].

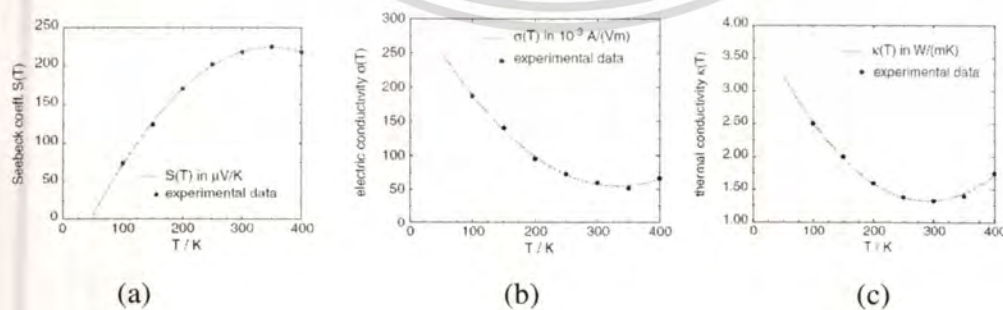


Figure 1.3 Thermoelectric properties of Bi_2Te_3 (a) Seebeck coefficient (b) The electrical conductivity (c) The thermal conductivity[8].

This material is reserved for educational use only, not allowed for commercial use.

Forbidden to modify the content, and cite the document when use.

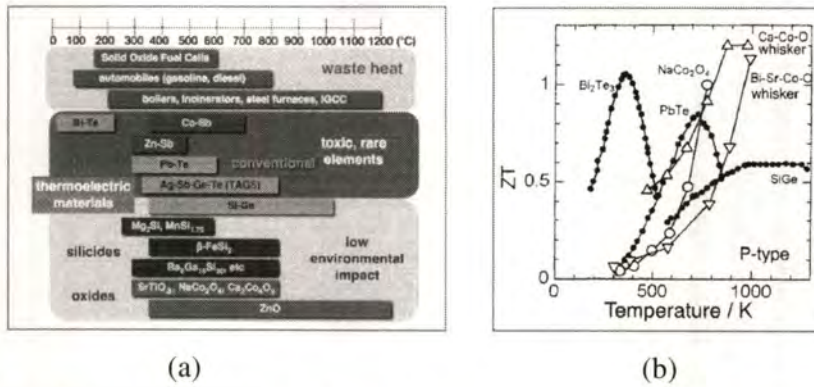


Figure 1.4 (a) The conventional thermoelectric materials (b) The ZT of conventional thermoelectric materials.

Moreover, many studies have reported that CuFeO_2 delafossite has a ZT value approximately 0.04 at 960 K [13]. Other studies report that the ZT value of CuFeO_2 was improved by doping trivalent and divalent metal such as Ni, Mg, Co and Ti [13-15]. However, upon doping the ZT was increased by less than 0.05 at 960 K. Recently, many studies have report that the Ag cations can be doped into the Cu-based delafossite such as $\text{Cu}_{1-x}\text{Ag}_x\text{RhO}_2$ [16], $\text{Cu}_{1-x}\text{Ag}_x\text{CrO}_2$ [17], and $\text{Cu}_{1-x}\text{Ag}_x\text{AlO}_2$ [18], causing the ZT value to improve slightly. This reason points out that the delafossite oxide-compound is candidate for thermoelectric materials and can improve its properties for high performance of thermoelectric device.

The Seebeck coefficient (S) is expressed by the electric field (E) of material, which occurs due to the diffusion of charge carriers from hot end to cool end, producing by temperature gradient (∇T) as expressed by $S = E / |\nabla T|$ [19, 20]. The S value of semiconductor has been proposed by Heikes [20], which equals to the entropy per site, as expressed by:

$$S = -\frac{k_B}{e} \ln \left[\frac{x}{(1-x)} \right]; \text{ where } x \text{ is the ration of difference carrier with total atom site, } e \text{ is the}$$

electronic charge, and k_B is the Boltzmann's constant.

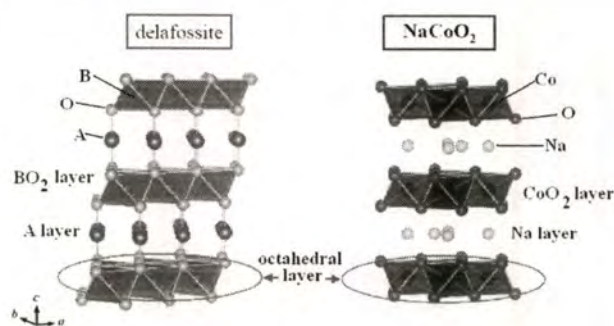


Figure 1.5 The alternately stacking octahedral layers of delafossite and Na_xCoO_2 . This material is reserved for educational use only, not allowed for commercial use.

In addition, Meakawa, Koshibae and Terasaki [21 - 24] have been succeeded to predict the limit highest of S value on the Na_xCoO_2 transition-metal oxide compound at the

high temperature by extended the Heikes formula as relation by $S = -\frac{k_B}{e} \ln \left[\frac{g_3}{g_4} \left(\frac{x}{1-x} \right) \right]$;

where the g_3 and g_4 are degeneracy of spin and orbital carrier. The Na_xCoO_2 compound has Na and CoO_6 octahedral layers alternately stacking along the c-axis that show in **Figure 1.5**.

The transition octahedral oxide of CoO_6 layer displays degeneracy of electronic state of Co^{3+} and Co^{4+} ions during to crystal field effect to splitting 3d energy state into two state of t_{2g} and e_g respectively as shown in **Figure 1.6** (a). Also, the Co^{3+} has $g_3=1$ from the spin degeneracy of $S_d=1$ and orbital degeneracy of $L_d=1$, and the Co^{4+} has $g_3=6$ from the spin degeneracy of $S_d=2$ and orbital degeneracy of $L_d=3$, as shown in **Figure 1.6** (b). The maximum limit of Seebeck value for low spin of Na_xCoO_2 in $x=0.5$, which has the ration $\text{Co}^{4+} : \text{Co}^{3+}=1:1$, is obtained $154 \mu\text{V/K}$. This results correspond with experiment by Plewa[25] and Ohtaki [26] which display saturation value at $150 \mu\text{V/K}$ at temperature above 800 K as shown in **Figure 1.7**.

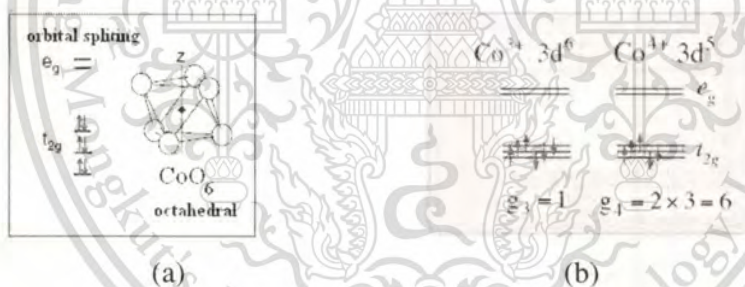


Figure 1.6 (a) The crystal field effect to splitting 3d energy state into two state of t_{2g} and e_g . (b) The degeneracy of low spin state of Na_xCoO_2 for the $\text{Co}^{3+}(3d^6)$, $g_3=1$ and $\text{Co}^{4+}(3d^5)$, $g_3=6$.

Moreover, delafossite compound contains the octahedral oxide layer similar to the NaCoO_2 compound as shown in **Figure 1.5**. The delafossite compound contains transition octahedral oxide layer corresponding to the Na_xCoO_4 . Therefore, the extended Heikes formula can be used to predict the maximum of the Seebeck value of delafossite compound at high temperature. There are many compounds in a delafossite group such as CuFeO_2 , CuCoO_2 , PdCoO_2 , PtCoO_2 [13–15,] and CuCrO_2 [27] etc. T. Nozaki et. al. [14] have reported that the CuFeO_2 doped Rh can predict Seebeck coefficient at high temperature by using the

extended Heikes formula. Y. Ono et. al. [27] has displayed the CuCrO_2 has high Seebeck value than the NaCoO_2 compound as shown in **Figure 1.7**.

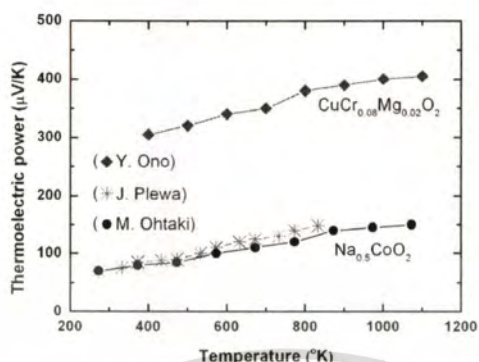


Figure 1.7 The experimental results of thermoelectric power of the $\text{Na}_{0.5}\text{CoO}_2$ by Plewa [25] and Ohtaki [26], and The CuCrO_2 delafossite doped Mg by Y. Ono [27].

The Finite Element technique has been used to compute the thermoelectric device. Ebling et al. [28] have applied the Finite Element technique to calculate thermoelectric power generator module. **Figure 1.8** shows the example model of finite element mesh model of thermoelectric module and the voltage and temperature distribution. The Finite Element analysis is used to solve of two couple equations of the thermoelectric effect of heat transfer and electric current density phenomena. The governing equations are governed by couple equation of heat transfer and continuity of current density [29]. The constitutive equations of heat flux and current density are inserted into the 2 couple field equation. The final finite element equations are solved by the Galerkin weighting scheme. The unknown of temperature and voltage are obtained from solving the finite element equations.

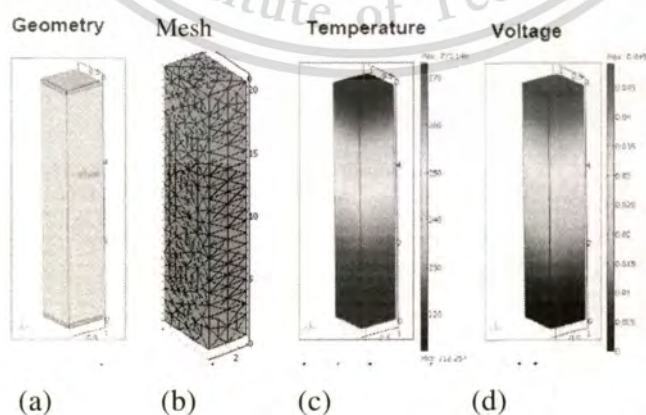


Figure 1.8 (a) The model of module (b) The Finite element meshes (c) The temperature and (d) The voltage distribution [28].

This material is reserved for educational use only, not allowed for commercial use.

Forbidden to modify the content, and cite the document when use.

In improving thermoelectric performance, Rowe [30] has reported that the energy gap of materials is must larger than $4k_B T$; where k_B is the Boltzmann's constant and T is the absolute temperature. Schwartz et. al. [31] has discussed in relation of energy gap and melting point for high thermoelectric material as relating to $E_G = 4k_B T_h$; where E_G is the optimum energy gap, k_B is the Boltzmann's constant and T_h is the operation temperature.

In addition, they have reported that the E_G of the Bi_2Te_3 (0.13eV)[31] is closely to the constant of $4k_B T_h$ at temperature 400 K which is the highest of the ZT value (~ 1) as shown in **Figure 1.9**. Another, the SiGe has the highest ZT (~ 1) at 1200 K with E_g 0.43 eV corresponding to the relation of $E_G = 4k_B T_h = 0.413$ eV at $T_h = 1200\text{K}$ as shown in **Figure 1.9**. Moreover, the PbSe, ZnSb, Sb_2Te_3 , and PbTe [31] have the highest ZT with the E_G closely to $4k_B T_h$ constant at temperatures 300, 700, 900, and 1080 K, respectively.

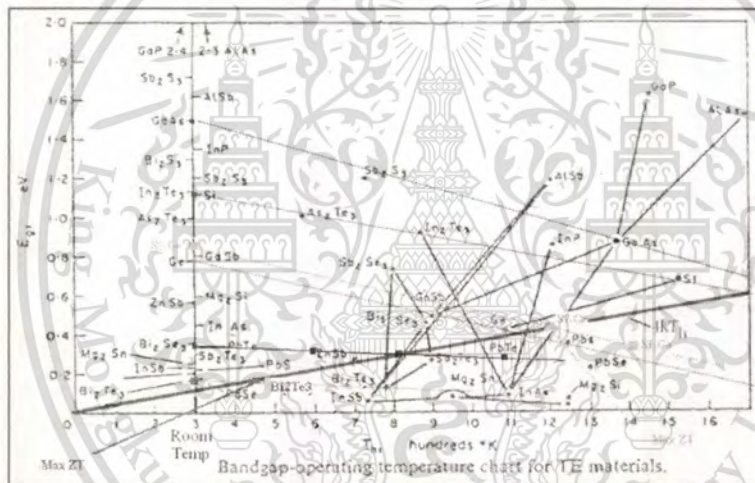


Figure 1.9 The relation of energy gap with temperature of thermoelectric materials in constant $E_G = 4k_B T$ [31].

1.2 STATEMENT AND SIGNIFICANCE OF THE PROBLEMS

Nowadays, thermoelectric materials have been displayed their potential as alternative sources of energy. The thermoelectric effect refers to a phenomenon whereby a temperature gradient is converted directly into electrical current and vice versa. In addition, thermoelectric generators can be used to convert waste heat to produce electrical power. The reverse effect can be practiced in thermoelectric coolers of refrigerators and other cooling systems.

The thermoelectric properties of low-cost oxide materials such as NaCo_2O_4 and $\text{Ca}_3\text{Co}_4\text{O}_9$ have been reported to have a converse efficiency close to that of state-of-the-art

This material is reserved for educational use only, not allowed for commercial use.

Forbidden to modify the content, and cite the document when use.

materials, Bi_2Te_3 and PbTe . In addition, the low-cost oxide materials of CuFeO_2 delafossite structure compound have been reported the Seebeck coefficient at high temperature increasing as increasing the temperature and also have been reported to be an interesting material for enhancement thermoelectric properties and used for thermoelectric device at high temperatures.

This thesis aims to improve the thermoelectric properties of CuFeO_2 delafossite oxide for using at high temperatures doping Pt, Al, Sn and Pb atom in the CuFeO_2 compound. Moreover, the numerical Finite Element technique is used to study the output voltage of thermoelectric modules. Finally, the thermoelectric modules are built for investigating the output electrical power, current, and power.

1.3 OBJECTIVE OF THESIS

The goals of this thesis are as follow:

- 1) to investigate thermoelectric properties of CuFeO_2 delafossite oxide compounds,
- 2) to improve thermoelectric properties of the CuFeO_2 compound by:
 - ❖ 2.1) doping PtCl_2 powder (oxidation state 1^+) for substituted Pt^{1+} cations into Cu^{1+} sites of the CuFeO_2 compound as chemical formula $\text{Cu}_{1-x}\text{Pt}_x\text{FeO}_2$,
 - ❖ 2.2) doping Al_2O_3 powder (oxidation state 3^+) for substituted Al^{3+} cations into Fe^{3+} sites of the CuFeO_2 compound as chemical formula $\text{CuFe}_{1-x}\text{Al}_x\text{O}_2$,
 - ❖ 2.3) doping SnCl_2 powder (oxidation state 2^+) for substituted Sn^{2+} cations into Fe^{3+} sites of the CuFeO_2 compound as chemical formula $\text{CuFe}_{1-x}\text{Sn}_x\text{O}_2$,
 - ❖ 2.4) doping PbO_2 powder (oxidation state 4^+) for substituted Pb^{4+} cations into Fe^{3+} sites of the CuFeO_2 compound as chemical formula $\text{CuFe}_{1-x}\text{Pb}_x\text{O}_2$,
- 3) to use numerical technique of Finite Element method to compute output voltage of thermoelectric module,
- 4) to invent prototype of thermoelectric modules for measurement their outputs electric voltage, current, and power.

This material is reserved for educational use only, not allowed for commercial use.

Forbidden to modify the content, and cite the document when use.

1.4 OVERVIEW OF THESIS

The thesis is structure in six main parts and four appendixes. First part interludes a general overview about the introduction of thesis. Second part describes the research on the overview of the thermoelectricity and delafossite structure. Third part is related to the research methodology and material characterization. Fourth part gathers the experimental results, discussion and conclusion. The more detailed below is described the content each chapter:

Chapter 1 Introduction,

Chapter 2 Overview of thermoelectricity and delafossite structure,

Chapter 3 Research methodology and material characterization,

Chapter 4 Experimental results,

Chapter 5 Results and discussion,

Chapter 6 Conclusion and suggestion.

In addition, first appendix adds the article which is published in intentional journal occurring from work of this thesis. Second appendix contains the proceeding which is published from work of this thesis. Third appendix report the invitation mail of ICCD and the final shows the crystallographic reference. The more detailed below is described the content each appendix:

Appendix A: Publication in international journals,

Appendix B: National and international proceeding

Appendix C: Invitation mail from the international centre of diffraction

Appendix D: Crystallographic reference

CHAPTER 2

OVERREVIEW OF THERMOELECTRICITY AND DELAFOSSITE STRUCTURE

This chapter concerned with the description of thermoelectric effect and structure of delafossite compound. The component of this chapter consists of:

1. Thermoelectric energy conversion,
2. Thermoelectric figure of merit,
3. Optimizing thermoelectric efficiency,
4. Thermoelectric properties,
5. Delafossite structure.

The detail of each section is described below.

2.1 THERMOELECTRIC ENERGY CONVERSION

The thermoelectric effect refers to phenomenon of the direct conversion of temperature gradient to electricity and vice versa [1-4, 29, 30, 34]. Furthermore, thermoelectric generators can be used to convert vest heat generated by various sources to electric power. For indirect effect, thermoelectric coolers can be used to make refrigerators and other cooling systems. The thermoelectric power generation is referred to the Seebeck effect and the thermoelectric cooling device is mentioned to the Peltier effect. The two basic phenomena of Seebeck and Peltier effect will be describe.

2.1.1 SEEBECK EFFECT

The Seebeck effect (S) [29, 30, 34] is a phenomenon that potential difference (ΔV) is induced in proportion to applied temperature gradient (ΔT) as shown in **Figure 2.1**. The S relation is expressed as:

$$S = \frac{\Delta V}{\Delta T} \quad (2.1),$$

where S is the Seebeck coefficient (thermoelectric power, or thermopower).

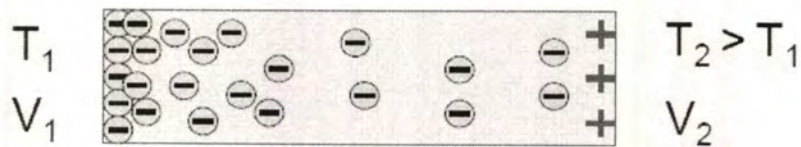


Figure 2.1 The conversion of temperature differences directly into electric potential.

For semiconductor material, the positive Seebeck coefficient represents p-type of semiconductor, and the negative Seebeck coefficient represents n-type of semiconductor conductor.

2.1.2 PELTIER EFFECT

The Peltier effect [29, 30, 34] is a phenomenon that the heat absorption or emission (Q) is induced at the junctions to the leads by the applied electrical current (I) as shown in **Figure 2.2**. The Peltier effect is the reverse process to the Seebeck effect. The Q , expressed as:

$$Q = \Pi I \quad (2.2),$$

where Π is the Peltier coefficient.

According to the Onsager relation, the S and Q are satisfying the relation of $\Pi = ST$.

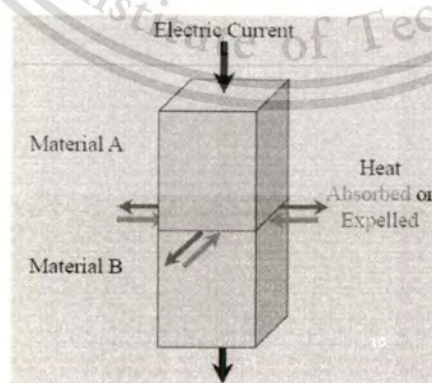


Figure 2.2 The heat is released or absorbed at the junction of two dissimilar materials, when the current is applied.

2.2 THERMOELECTRIC FIGURE OF MERIT

In the case of a thermoelectric generator, the efficiency (η) [30, 34] of a device is defined by the ration between the output of electrical power generated by the materials (P_{in}) with the input of thermal flux through the device (Q_{out}). The efficiency is expressed as:

$$\eta = \frac{P_{out}}{Q_{in}} \quad (2.3),$$

where η is the efficiency of thermoelectric generator,

P_{out} is the electrical power generated output,

Q_{in} is the thermal flux input.

First case for determining of efficiency, a simple n-type bar model of thermoelectric generator is considered as shown in **Figure 2.3**. The efficiency conversion is related by the energy balance of the system with expressed [30, 34] by:

$$\eta = \frac{R_{load} I^2}{\kappa \Delta T - ST_C I - \frac{1}{2} R I^2} \quad (2.4),$$

Where R_{load} is the resistance of the load,

R is the resistance of the bar,

I is electric current,

κ is the thermal conductivity,

S is Seebeck coefficient,

ΔT is the temperature gradient ($T_H - T_C$),

T_H is the temperature at hot source,

T_C is the temperature at heat sink.

For optimizing η with respect to R_{load} the maximum efficient is gained:

$$\eta_{max} = \frac{T_H - T_C}{T_H} \frac{\sqrt{1 + ZT_M} - 1}{\sqrt{1 + ZT_M} + \frac{T_H}{T_C}} \quad (2.5),$$

where $T_M = \frac{T_H + T_C}{2}$, $Z = \frac{S^2}{\rho\kappa}$ and $ZT_M = \frac{S^2}{\rho\kappa} \left(\frac{T_H + T_C}{2} \right)$ with ρ is the electrical resistivity.



Figure 2.3 A one-leg device of thermoelectric generator with n- type materials.

The Z is called the Figure of Merit of the thermoelectric materials and the ZT is called the dimensionless of Figure of Merit of the thermoelectric materials. From the relation of efficiency conversion, the optimizing of η is obtained by the large of ZT . Therefore, the efficiency of thermoelectric generator is strongly depend on the tree parameters of the materials consisting of the Seebeck coefficient (S), the electrical resistivity (ρ) and the thermal conductivity (κ),

For the cast of a thermoelectric generator with both n- and p-type materials as shown in **Figure 2.4**, the maximum efficient (η) [30, 34] is express:

$$\eta_{max} = \frac{T_H - T_C}{T_H} \frac{\sqrt{1 + Z_{np}T_M} - 1}{\sqrt{1 + Z_{np}T_M} + \frac{T_H}{T_C}} \quad (2.6),$$

where $Z_{np} = \frac{(S_p - S_n)^2}{[(\rho_p\kappa_p)^{1/2} + (\rho_n\kappa_n)^{1/2}]^2} \approx \frac{Z_n + Z_p}{2}$.

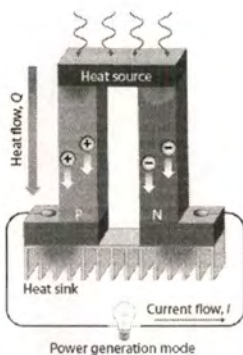


Figure 2.4 A thermoelectric generator with n- and p-type materials connected.

2.3 OPTIMIZING THERMOELECTRIC EFFICIENCY

The dimensionless Figure of Merit of the thermoelectric materials (ZT) [30, 34] is given:

$$ZT = \frac{S^2}{\rho\kappa} T = \frac{S^2}{\rho(\kappa_e + \kappa_l)} T \quad (2.7),$$

where κ_e is the electronic part of thermal conductivity,

κ_l is the lattice part of thermal conductivity.

The maximize ZT is obtained with a large Seebeck coefficient (S), small thermal conductivity (κ) and small electrical resistivity (ρ). The parameter of thermoelectric properties as a function of electronic part is shown in **Figure 2.5**.

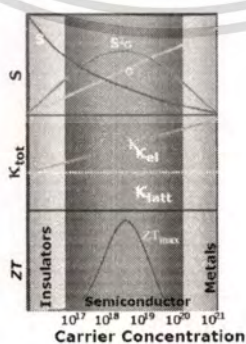


Figure 2.5 The S , $\sigma (=1/\rho)$, κ_e , κ_l and ZT as a function of the carrier concentration.

From the **Figure 2.5**, the parameter of the S , σ (electrical conductivity), and κ_e are strongly inter-dependent with electric mechanism. Another, the κ_l is controlled by lattice phonon mechanism. Also, the κ_l can be minimized due to independent from the other parameter. The maximum value of the $S^2\sigma$ and ZT can be obtained from materials of semiconductor as carries density closely to $10^{18} - 10^{19} \text{ cm}^{-3}$.

2.4 THERMOELECTRIC PROPERTIES

This section deals with the properties of thermoelectric as consisting of the Seebeck coefficient, electrical conductivity, thermal conductivity, and Figure of Merit (ZT) relation. The detail of each parameter is described as below.

2.4.1 SEEBECK COEFFICIENT RELATION

In the case of metals [30, 34], the Seebeck coefficient is related:

$$S = \frac{\pi^2 k_B^2 T}{3e} \left[\frac{\partial \ln \sigma(\varepsilon)}{\partial \varepsilon} \right]_{\varepsilon=E_F} \quad (2.8),$$

where $\sigma(\varepsilon) = en(\varepsilon)\mu(\varepsilon)$ is the electronic conductivity,

$n(\varepsilon)$ is the carrier density,

$\mu(\varepsilon)$ is the carrier mobility

k_B is the Boltzmann's constant,

e is the electronic charge constant,

ε is the energy,

E_F is the Fermi energy level.

In the case of semiconductor materials [34], the Seebeck coefficient is related as:

$$S = \frac{k_B}{e} \frac{E_g}{k_B T} \quad (2.9),$$

Where E_g is the band gap.

In the case of strongly correlation in oxide materials which is strong correlation effects between the charge carriers, the Seebeck coefficient can be derived from the Hubbard model with using the narrow bands of Kubo formalism [21, 34, 35] as expressed:

$$S = -\frac{S^{(2)}/S^{(1)}}{eT} + \frac{\mu_c}{eT} \quad (2.10),$$

$$\text{with } S^{(1)} = \int_{-\infty}^{\infty} \Xi(\varepsilon)(\varepsilon) \left(-\frac{\partial f(\varepsilon)}{\partial \varepsilon} \right) d\varepsilon,$$

$$S^{(2)} = \int_{-\infty}^{\infty} \Xi(\varepsilon) \left(-\frac{\partial f(\varepsilon)}{\partial \varepsilon} \right) d\varepsilon.$$

where ε is the energy,

μ_c is the Chemical potential,

e is the electronic charge,

T is the temperature,

f is the Fermi function,

Ξ is the transport distribution.

The $S^{(1)}$ is depended on the energy and transport distribution and the $S^{(2)}$ is depended on the transport distribution only. In the high temperature with $T \rightarrow \infty$, the S [21, 34, 35] is obtained:

$$S = \frac{\mu_c}{eT} = -\frac{1}{|e|} \left(\frac{\partial \sigma_s}{\partial N} \right) = -\frac{k_B}{|e|} \left(\frac{\partial \ln g}{\partial N} \right) \quad (2.11),$$

where σ_s is the system entropy ($\sigma_s = k_B \ln g$),

N is the number of particle,

g is the degeneracy of the system.

In above equation, the Seebeck coefficient (S) is considered in case of the entropy per carrier of system. For the case of the strongly correlation, the mixing of the entropy will effect to

large Seebeck coefficient at high T . For consider the case of spinless fermions, the Heikes formula [21, 34, 35] is obtained:

$$S = \frac{\mu_c}{eT} = -\frac{k_B}{|e|} \ln\left(\frac{x}{1-x}\right) \quad (2.12),$$

where x is the carrier density or the ration of difference carrier with total atom site.

For the case of the entropy in strongly correlation between the spins and orbitals degeneracy, the Seebeck coefficient at T is considered in the system of the mixed-valent cation of the $M^{(n)+}/M^{(n+1)+}$ spin values, where n is ion state. Also, the extension of Heikes formula [21, 34, 35] is obtained:

$$S = \frac{\mu_c}{eT} = -\frac{k_B}{|e|} \ln\left(\frac{g^{(n)+} x}{g^{(n+1)+} (1-x)}\right) \quad (2.13),$$

where $g^{(n)+}$ is the spin and orbital degeneracies associated with $M^{(n)+}$ spin,
 $g^{(n+1)+}$ is the spin and orbital degeneracies associated with $M^{(n+1)+}$ spin.

For the example in applying of the equation (2.13), Meagawa [21] proposes that high Seebeck value of the Na_xCoO_2 compound effects from the strong correlation of spin and orbital in Co^{3+} and Co^{4+} ions.

The low spin state of the Na_xCoO_2 electronic configuration of:

- the $\text{Co}^{3+}(3d^6)$ ion is 6 in the t_{2g} state $[(t_{2g})^6]$ and is 0 in the e_g state $[(e_g)^0]$,
- the $\text{Co}^{4+}(3d^5)$ ion is 5 in the t_{2g} state $[(t_{2g})^5]$ and is 0 in the e_g state $[(e_g)^0]$.

Also, the Co^{3+} has $g_3=1$ from $(S_d L_d)$:

- the spin degeneracy of the $S_d=1$,
- the orbital degeneracy of the $L_d=1$.

The Co^{4+} has $g_3=6$ from $(S_d L_d)$:

- the spin degeneracy of the $S_d=2$,
- the orbital degeneracy of the $L_d= 3$.

Therefore, the maximum limit of Sebeck value by using the extended Heikes formula at the high temperature for low spin of the Na_xCoO_2 [25, 26] compound in $x=0.5$ with the rasion $\text{Co}^{4+} : \text{Co}^{3+}=1:1$, is obtained 154 uV/K.

2.4.2 ELECTRICAL CONDUCTIVITY RELATION

The relation of electrical conductivity (σ) [35] is given by the equation:

$$\sigma = en\mu \quad (2.14),$$

where e is the carrier charge,

n is the carrier concentration,

μ is the mobility of carriers.

For the electronic transport in semiconductor, the charge carriers must be excited to free carriers, and then they move by hopping mobility mechanism. The electrical conductivity for semiconductor is described [35] by the relation:

$$\sigma = eN_T \exp\left(-\frac{E_F - E_v}{k_B T}\right) \mu_o \exp\left(-\frac{E_u}{k_B T}\right) \quad (2.15),$$

where N_T is the effective density of states of charge carrier,

μ_o is the mobility constant,

E_u is the activation energy for carrier mobility,

k_B is the Boltzmann's constant,

e is the electronic charge constant,

E_v is the energy of the valance-band edge,

E_F is the Fermi energy level,

T is the absolute temperature.

2.4.3 THERMAL CONDUCTIVITY RELATION

The total thermal conductivity (κ) [1-4, 29, 30, 34] is consisted of 2 parts of the electronic part and the lattice part as expressed:

$$\kappa = \kappa_e + \kappa_l \quad (2.16),$$

where κ_e is the electronic part of thermal conductivity,

κ_l is the lattice part of thermal conductivity.

The electronic part of thermal conductivity (κ_e) [1-4, 29, 30, 34] is expressed by the Wiedemann-Franz law in relation:

$$\kappa_e = \left(\frac{\pi^2 k_B^2}{3e} \right) \sigma T = L_o \sigma T \quad (2.17),$$

where L_o is the Lorenz factor ($2.45 \times 10^{-8} \text{ W}\cdot\Omega/\text{K}^2$),

σ is electrical conductivity,

T is the absolute temperature.

The lattice part of thermal conductivity (κ_l) is considered in the term of phonon mechanism. The Umklapp scattering contribution[31] in the phonon scattering process is expressed by the equation:

$$\kappa_u = \delta [(T_m)^{3/2} M^{(-7/6)} D^{2/3}] T^{(-1)} \quad (2.18),$$

where κ_u is the Umklapp phonon thermal conductivity,

δ is the proportionality constant,

T_m is the melting temperature,

M is the average atomic mass,

D is the atomic density,

T is the operation temperature.

2.4.4 RELATION OF ENERGY GAP AND OPERATING TEMPERATURE

For application of thermoelectric at high temperature, the relation between energy gap and temperature for optimal operating for the best thermoelectric materials, Schwartz et. al. [31] have suggested in the relation:

$$E_G = 4k_B T_h \quad (2.19),$$

where E_G is the optimal energy gap,

k_B is the Boltzmann's constant,

T_h is the operation temperature.

For the best ZT value, Schwartz et. al. [31] has suggested that the value of the T_h is used in the relation:

$$T_h = 0.9T_m \quad (2.20),$$

where T_h is the operation temperature.

T_m is the melting point of materials.

2.5 DELAFOSSITE STRUCTURE

Delafossite compounds are classified in a group of ternary oxides whose chemical formula is $A^+B^{III}O_2$ [36, 37]. Its structure is formed by alternative stacking layers of O-A-O dumbbell and BO_2 edge-shared octahedral along with the c-axis as shown in **Figure 2.6**. The A^+ cation is linearly connection with O^{2-} anion in c-axis. The $[BO_2]^-$ octahedral-shaped are formed by charring of edge BO_2 . The trivalent B^{3+} ions occupy in the middle of the octahedral block.

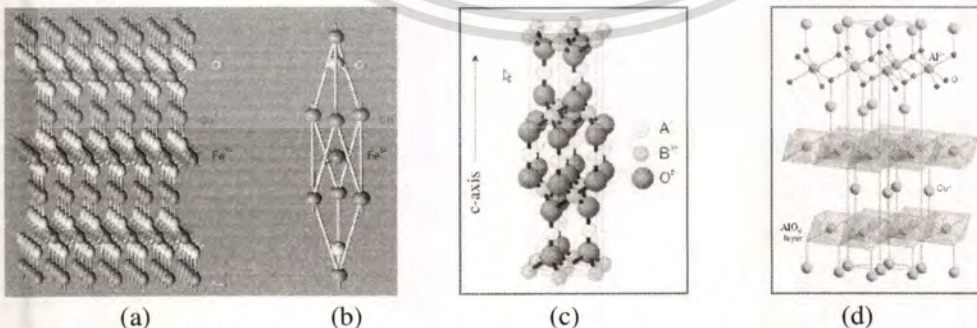


Figure 2.6 (a) The $CuFeO_2$ delafossite structure. (b) The rhombohedral primitive cell. (c) The hexagonal unit cell. (d) The alternative stacking layers of O-A-O dumbbell and octahedral layer.

The delafossite crystal has a unit cell structure of hexagonal (space group: R3m) and a primitive structure of rhombohedral.

The A-site cations are composed of Cu, Ag, Pd, or Pt transition-metal ions maintained in a monovalent state. The properties of delafossite are strongly dependent on which types of A-site cations being used. The Cu^+ and Ag^+ (d^{10} ions) cations are responsible for semiconducting behaviors, while Pt^+ and Pd^+ (d^9 ions) cations give rise to electrical conductivity.

The B-site cations mostly consist of 4 groups of:

- (1) the trivalent transition metals (Cr, Mn, Fe, Co, Ni, Rh),
- (2) the group III metal elements (Sc, Y, La),
- (3) the group 13 metal elements (Al, Ga, In, Tl), or
- (4) the rare earths (Pr, Nd, Sm, Eu).

There are many compounds in a delafossite group such as CuFeO_2 , CuCoO_2 , PdCoO_2 and PtCoO_2 etc. [36–38]. The delafossite structure and rhombohedral primitive cell structure of CuFeO_2 are shown in **Figure 2.6**.

The Cu-based and Ag-based delafossite such as CuFeO_2 or AgCoO_2 clearly display semiconducting behavior [37, 38], while the Pd-based and Pt-based delafossite such as PdCoO_2 or PtCoO_2 are metallic conductors [37, 38].

The example compounds in Cu-based of B-site for 4 groups are shown below:

- (1) the trivalent transition metals such as CuCrO_2 , CuMnO_2 , CuFeO_2 , CuCoO_2 , CuNiO_2 , and CuRhO_2 ,
- (2) the group III metal elements such as CuScO_2 , CuYO_2 , and CuLaO_2 ,
- (3) the group 13 metal elements such as CuAlO_2 , CuGaO_2 , CuInO_2 , and CuTlO_2 ,
- (4) the rare earths such as CuPrO_2 , CuNdO_2 , CuSmO_2 , and CuEuO_2 .

This research focus on CuFeO_2 compound because its Seebeck coefficient contains high value at high temperature and increases as increasing the temperature. The research is aimed to improve the thermoelectric properties of the CuFeO_2 compound at high temperatures by doping Pt, Al, Sn and Pb atom in the CuFeO_2 compound by synthesizing $\text{Cu}_{1-x}\text{Pt}_x\text{FeO}_2$, $\text{CuFe}_{1-x}\text{Al}_x\text{O}_2$,

$\text{CuFe}_{1-x}\text{Sn}_x\text{O}_2$ and $\text{CuFe}_{1-x}\text{Pb}_x\text{O}_2$ compound, respectively. In improvement, the CuFeO_2 , $\text{Cu}_{1-x}\text{Pt}_x\text{FeO}_2$, $\text{CuFe}_{1-x}\text{Al}_x\text{O}_2$, $\text{CuFe}_{1-x}\text{Sn}_x\text{O}_2$ and $\text{CuFe}_{1-x}\text{Pb}_x\text{O}_2$ compounds have been synthesis in this thesis to investigate the thermoelectric properties. The detail of the lattice structure of each compound is described below.

2.5.1 CuFeO_2

The CuFeO_2 delafossite compounds are classified as a ternary oxides group with chemical formula is $\text{Cu}^+\text{Fe}^{3+}\text{O}_2$ [7, 8]. Its structure is formed by alternative stacking layers of O-Cu-O dumbbell-like and FeO_2 edge-shared octahedral along with the c-axis as shown in **Figure 2.7**. The Cu^+ cation is linearly connection with O^{2-} anion in c-axis. The $[\text{FeO}_2]^-$ octahedral-shaped are formed by charring of edge FeO_2 . The trivalent Fe^{3+} ions occupy in the middle of the octahedral block. The Cu-site is in the transition-metal ions maintained of a monovalent state and The Fe-site is in trivalent transition metals.

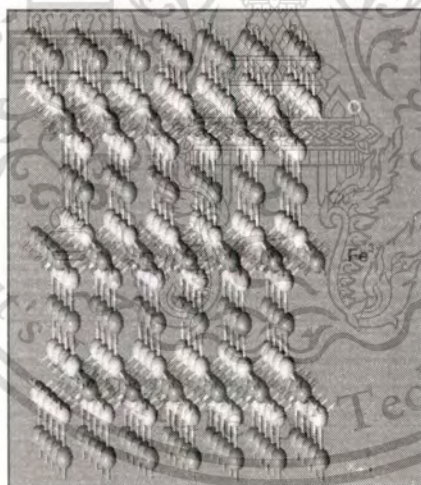


Figure 2.7 The CuFeO_2 delafossite structure.

2.5.2 $\text{Cu}_{1-x}\text{Pt}_x\text{FeO}_2$

The $\text{Cu}_{1-x}\text{Pt}_x\text{FeO}_2$ compounds have been synthesis by substitution Pt^{1+} cation into the Cu-site of the CuFeO_2 compound. The obtained $\text{Cu}_{1-x}\text{Pt}_x\text{FeO}_2$ compound exhibits a group of the delafossite. This compound is modified from the PtCoO_2 delafossite compound as the metallic

conductor [13]. Also, the Pt atom can substitute into the CuFeO_2 compound. The partial Pt atoms are substitution at the Cu site.

2.5.3 $\text{CuFe}_{1-x}\text{Al}_x\text{O}_2$

The $\text{CuFe}_{1-x}\text{Al}_x\text{O}_2$ compounds have been synthesis by substitution Al^{3+} cation into the Fe-site of the CuFeO_2 compound. The obtained $\text{CuFe}_{1-x}\text{Al}_x\text{O}_2$ compound displays a group of the delafossite. This compound is modified from the CuAlO_2 delafossite compound as showing the thermoelectric materials [40, 51]. Also, the Al atom can substitute into the CuFeO_2 compound. The 50% of Al atoms are substitution at the Fe site.

2.5.4 $\text{CuFe}_{1-x}\text{Sn}_x\text{O}_2$

The $\text{CuFe}_{1-x}\text{Sn}_x\text{O}_2$ compounds have been synthesis by substitution Sn^{2+} cation into the Fe-site of the CuFeO_2 compound. The obtained $\text{CuFe}_{1-x}\text{Sn}_x\text{O}_2$ compound displays a group of the delafossite. This compound is modified from the $\text{AgIn}_{1-x}\text{Sn}_x\text{O}_2$ delafossite compound as showing the thermoelectric materials [52]. Also, the Sn^{2+} cation can substitute into the CuFeO_2 compound with display p-type conductor. Clearly, the partial Sn atoms are substitution at the Fe site.

2.5.5 $\text{CuFe}_{1-x}\text{Pb}_x\text{O}_2$

The $\text{CuFe}_{1-x}\text{Pb}_x\text{O}_2$ compounds have been synthesis by substitution Pb^{4+} cation into the Fe-site of the CuFeO_2 compound. The obtained $\text{CuFe}_{1-x}\text{Pb}_x\text{O}_2$ compound displays a group of the delafossite. This compound is modified from the AgInO_2 compound doped Sn^{4+} as showing the n-type thermoelectric materials [52]. Also, the Pb^{4+} cation can substitute into the CuFeO_2 compound with display n-type conductor. Clearly, the partial Pb atoms are substitution at the Fe site.

CHAPTER 3

RESEARCH METHODOLOGY AND MATERIAL CHARACTERIZATION

This chapter deals with the material and method of experiment and measurement using in this thesis. The section of this chapter consists of:

1. Experimental procedure
2. Research materials and tools
3. Analytical procedure
4. Sample characterizations

The detail of each section is described below.

3.1 EXPERIMENTAL PROCEDURE

The studied samples were prepared by a conventional direct solid-state reaction. The process to prepare of bulk samples are as follow:

- 1) The starting power was measure mass in ration of molar in chemical formula.
- 2) The starting materials of stoichiometric amounts of high-purity powders were sufficiently mixed and ground in an agate mortar to ensure homogeneity.
- 3) A homogenous mixture was obtained and cool pressed into pellets of 12 mm diameter with 2.5 mm thickness by hydraulic pressure.
- 4) The resulting pellets were sintered by performed inside alumina boat in furnace at 1050 °C in air for 15 - 25 hours.
- 5) After heat treatment, the sintered pellets were rapidly quenched to room temperature.
- 6) The heated pellets were repeatedly subjected to grounding, pelleting, firing, and phased identifying procedures for several times until the pure phase of specimen samples were obtained.

3.2 RESEARCH MATERIALS AND TOOLS

3.2.1 EXPERIMENT TOOLS

The tools for using in the experiment of this thesis compost of:

- Agate mortar.

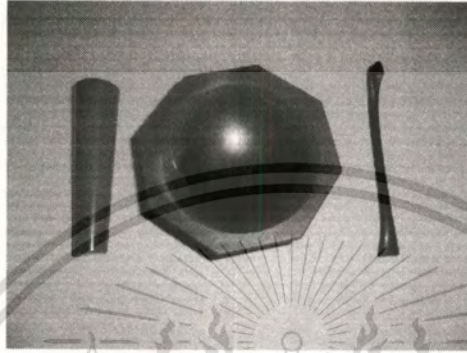


Figure 3.1 The agate mortar.

- Hydraulic pressure.



Figure 3.2 The hydraulic pressure.

This material is reserved for educational use only, not allowed for commercial use.

Forbidden to modify the content, and cite the document when use.

- Alumina crucible.

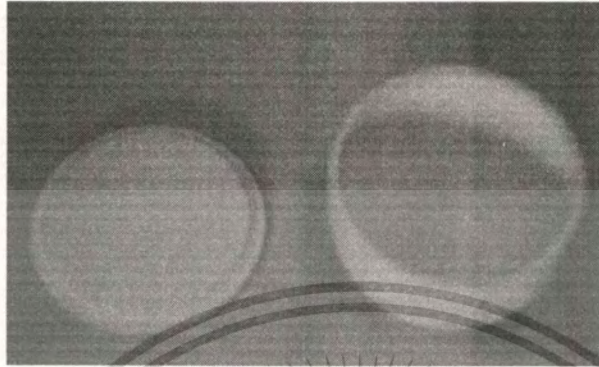


Figure 3.3 The alumina crucible.

- Sintering furnace.



Figure 3.4 The sintering furnace.

- Pelleting mould.



Figure 3.5 The pelleting mould for pellet sample and bar sample.

3.2.2 STARTING POWDERS

The starting materials for preparing bulk samples in this research consist of:

- 1) CuO (Merk, 99.98%).
- 2) Fe₂O₃ (Sigma-Aldrich, Inc., 99%).
- 3) PtCl₂ (Sigma-Aldrich, Inc., 98%).
- 4) Al₂O₃ (Fluke; 99.99%).
- 5) PbO₂ (Sigma-Aldrich, Inc., 99%).
- 6) SnCl₂ (Sigma-Aldrich, Inc., 99%).

3.2.3 ANALYTICAL PROCEDURE

This research, the sinter samples were analyzed crystal phase by using the XRD, thermal decomposition using TG/DTG, morphology using SEM, thermal properties using by ZEM-2 and laser-flash and optical properties using UV-VIS-NIR scanning. The procedure to analyze the samples is displayed below.

This material is reserved for educational use only, not allowed for commercial use.

Forbidden to modify the content, and cite the document when use.

- 1) The crystallography of samples was determined by the powder x-ray diffraction (XRD) of PHILIPS model: X' Pert MPD analysis using Cu K α radiation with $2\theta = 10^\circ$ to 80° with 0.02 steps.
- 2) The lattice parameter was determined by the Rietveld refinement program, X'Pert High Score Plus V2.0a.
- 3) The decomposition analysis of the samples was analyzed using thermogravimetric method (TG) by the Pyris Diamond TG/DTG (Perkin Elmer Instrument) under air atmosphere.
- 4) The particle size and morphology of the samples were observed by scanning electron microscope (SEM) using the JEOL model: JSM-5410.
- 5) The Seebeck coefficient and electrical conductivity were simultaneously measured on the $4.2 \times 2.5 \times 20 \text{ mm}^3$ sample bar using the ULVAC-RIKO ZEM-2 thermoelectric property measurement system under a low-pressure helium atmosphere.
- 6) The thermal conductivity was determined from thermal diffusivity and specific heat on pellets of 12 mm diameter with thickness 1.6 mm by the ULVAC SINKU RIKO Inc. model: TC-7000 laser-flash method in a N₂ atmosphere.
- 7) The absorbance was measured by a UV-VIS-NIR scanning spectrophotometer (Shimadzu UV-3101PC) in the wide wavelength of range 200 to 2500 nm at room temperature.

3.3 SAMPLE CHARACTERIZATION

The prepared samples were characterized to confirm of the improvement the thermoelectric properties of the CuFeO₂ compound at high temperature. The characterization of samples in this research is as follow:

1. X-ray diffraction analysis
2. Seebeck coefficient and Electrical conductivity
3. Thermal conductivity
4. UV-Vis-Nir scanning spectrophotometer
5. Thermal analysis.

The detail of each topic is described below.

3.3.1 X-RAY DIFFRACTION ANALYSIS

X-ray Diffraction (XRD) is a technique of characterizing for crystalline materials. It gives information on structures, phases, preferred crystal orientations (texture) and other structural parameters such as average grain size, crystallinity, strain and crystal defects. Crystal of materials consists of a periodic arrangement of atoms or molecules that form a crystal lattice. There are several lattice planes in crystal. The distance between parallel lattice planes is the lattice plane distance (d). In natural, the crystalline consists of regular array atoms, ions or molecules within inter-atomic spacing of the order of 10 pm. The wavelengths of X-ray ($\lambda = 0.02 - 11 \text{ nm}$) is in around 2 to 5 orders of magnitude smaller than inter-atomic spacing. For the diffraction condition, the wavelength of the incident light has the same order of magnitude as the spacing of grating. Also, the diffraction condition can occur in the crystal of materials from the wavelengths of x-ray region. The condition of the refraction in lattice crystal by x-ray is governed by the Bragg's Law [41] as shown in **Figure 3.6** relating of Bragg's equation as following:

$$2d_i \sin\theta = n\lambda \quad (3.1),$$

where $2d_i \sin\theta$ is the path difference,

d_i is the lattice plane distance,

λ is the x-ray wavelengths,

θ is the Bragg's angle,

n is 1, 2, 3, ... reflection order.

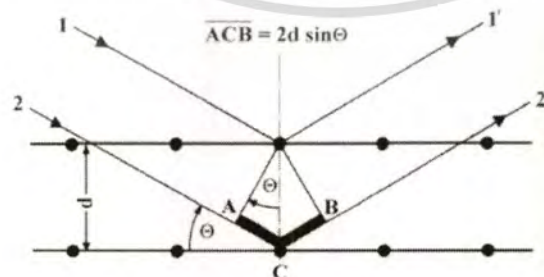


Figure 3.6 Bragg reflection.

The present work, the X-Ray Diffraction Analysis was operated on a powder x-ray diffraction (XRD) of PHILIPS model: X' Pert MPD analysis using Cu $K\alpha$ radiation source as shown in **Figure 3.7**. The x-ray diffraction pattern of an unknown specimen is compared with reference patterns from the database of the International Centre for Diffraction Data (ICDD).

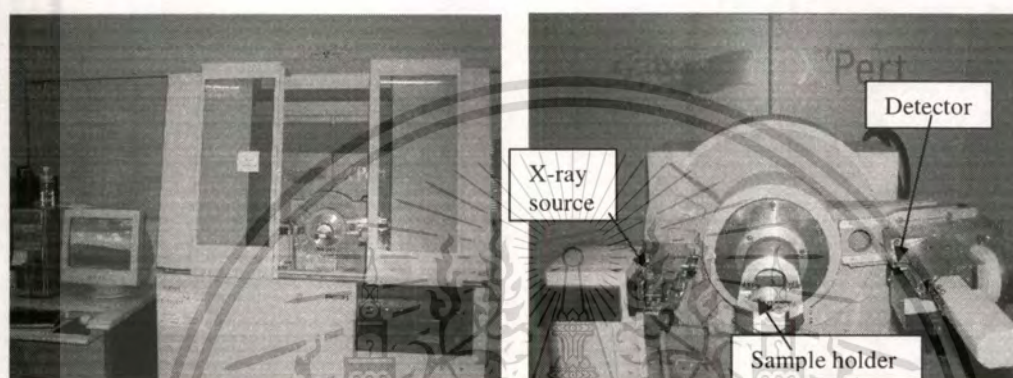


Figure 3.7 Powder x-ray diffraction (XRD) of PHILIPS model: X' Pert MPD.

3.3.2 SEEBECK COEFFICIENT AND ELECTRICAL CONDUCTIVITY

The Seebeck coefficient and electrical conductivity were simultaneously measured on the Seebeck coefficient measuring system in a model ZEM-2 of the ULVAC-RIKO, Inc, Yokohama, Japan. The measurement was performed in temperature range from room temperature to 800 C within a system of low pressure helium gas atmosphere. This system measures the electromotive force and electrical ductility of thermoelectric materials. The **Figure 3.8** and **Figure 3.9** show configuration of ZEM-2 the Seebeck coefficient measuring system.

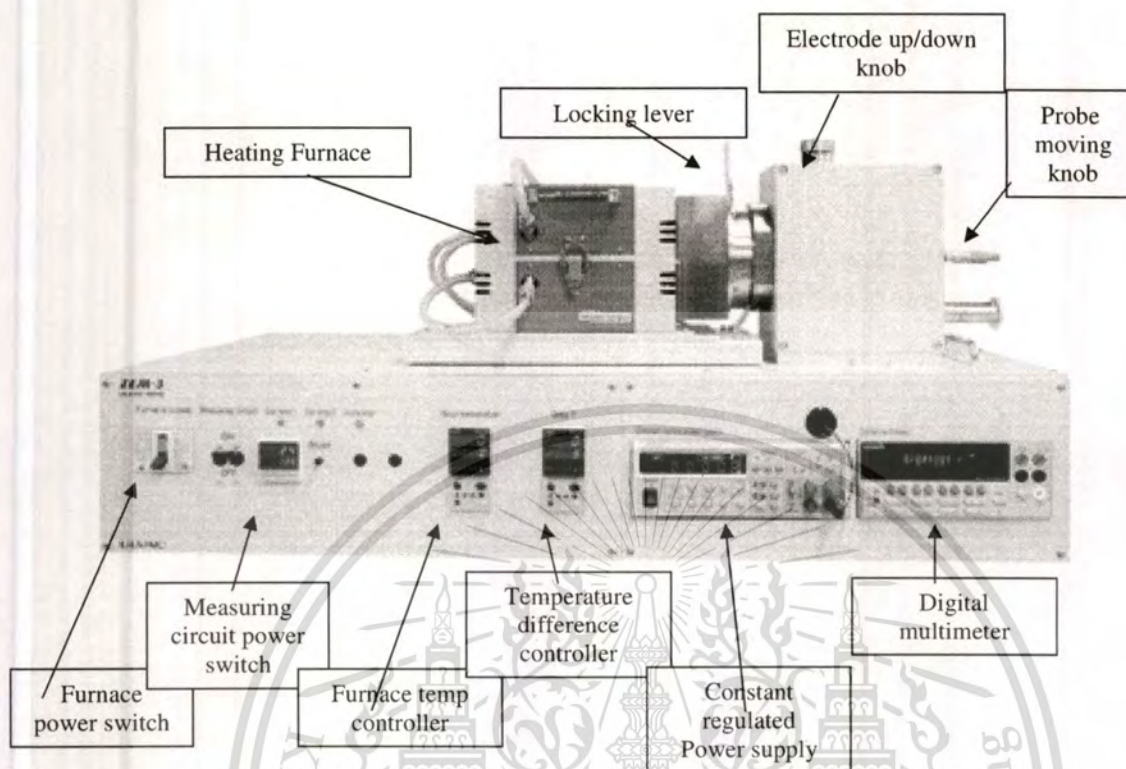


Figure 3.8 The configuration of ZEM-2 the Seebeck coefficient measuring system.

The shape of sample for measurement is in prism of 2-4 mm square and length 20 mm as shown **Figure 3.9 (b)**, and in cylinder of diameter 2 to 4 mm and length of 13 to 18 mm.

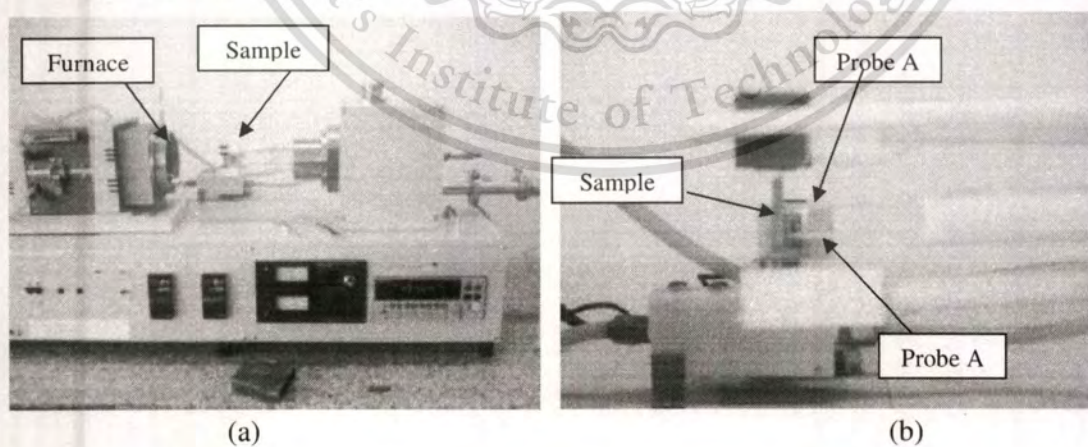


Figure 3.9 (a) System inside the furnace, (b) The sample operation.

3.3.2.1 SEEBECK COEFFICIENT

The Seebeck coefficient [42] is measured in the thermo-electromotive force as following in the relation:

$$\text{Thermo-electromotive force} = \frac{\Delta V}{\Delta T} \quad (3.2),$$

where ΔV is the electrical voltage.

ΔT is the temperature difference.

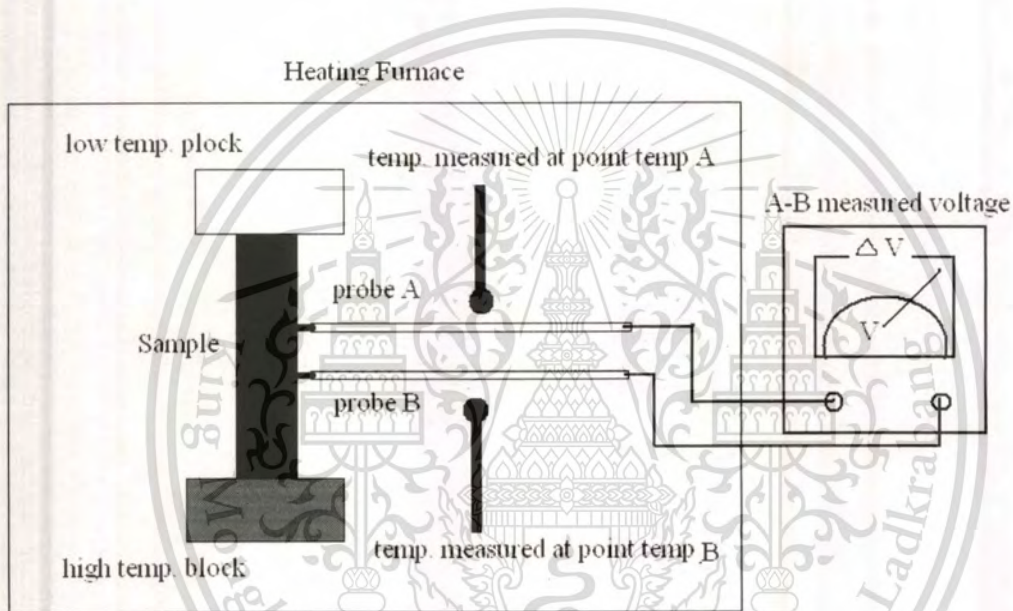


Figure 3.10 The diagram to measure Seebeck coefficient

In the **Figure 3.10**, the Seebeck coefficient is obtained by the relation:

$$\text{Thermo-electromotive force} = \frac{\Delta V}{\text{Temp.}B - \text{temp.}A} \quad (3.3).$$

The positive and negative sign of Seebeck coefficients are obtained from the plus and minus sign, respectively. The measurement of temperature is obtained in the relation:

$$\text{Measurement of temperature} = \frac{\text{Temp.}B + \text{temp.}A}{2} \quad (3.4).$$

This material is reserved for educational use only, not allowed for commercial use.

Forbidden to modify the content, and cite the document when use.

3.3.2.2 ELECTRICAL CONDUCTIVITY

This system measures electrical conductivity [42] in reciprocal of resistivity. The resistivity value is the specific resistance (r) as obtained from the relation:

$$r = \frac{R * L}{A} \quad (3.5),$$

where R is the resistance of sample,

L is distance between probes,

A is cross-sectional area of sample.

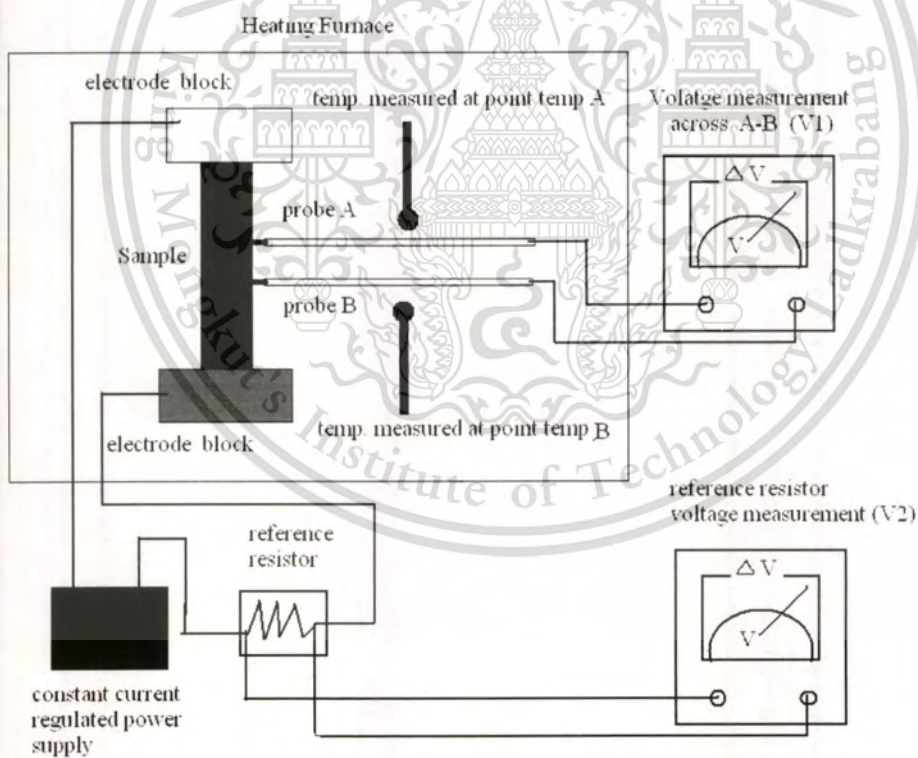


Figure 3.11 The diagram to measure electric resistivity.

The measurement temperature in **Figure 3.11** is obtained in the relation:

$$\text{Measurement of temperature} = \frac{\text{Temp.}B + \text{temp.}A}{2} \quad (3.6).$$

The sample resistance (R) in **Figure 3.11** is obtained in the equation:

$$R = \frac{V(1)}{V(2)_{ref}} \times R_{ref} \quad (3.7),$$

where $V(1)$ is the voltage measurement across probes,

$V(2)_{ref}$ is the voltage on reference resistor ,

R_{ref} is the reference resistor.

Also, the specific resistance (r) is obtained:

$$r = \frac{R * L_{probe}}{A_{sample}} \quad (3.8),$$

where r is the specific resistance,

L is distance between probes,

A is cross-sectional area of sample.

Finally, the electrical conductivity (σ) is obtained by equation:

$$\sigma = \frac{1}{r} \quad (3.9);$$

where σ is the electrical conductivity.

3.3.3 THERMAL CONDUCTIVITY

The Seebeck coefficient and thermal conductivity [43] are measured on the Laser Flash Method thermal constants measuring system in a model TC-7000 of the ULVAC-RIKO, Inc, Yokohama, Japan as shown in **Figure 3.12**. The measurement was performed in temperature range -150 to 1500 C within a system of nitrogen gas atmosphere.

This system measures the thermal conductivity of sample from the relation:

$$\kappa = aC_p d \quad (3.10),$$

where κ is the thermal conductivity(W/cm-k),

a is the thermal diffusivity (cm^2/sec),

C_p is the heat capacity of sample (J/g-K),

d is the sample density (g/cm^3).

This system measure thermal diffusivity, heat capacity indirectly, while the samples density is measure from experimental weight per volume of bulk sample.

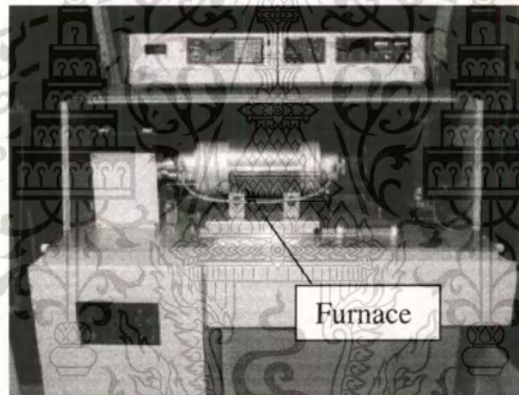


Figure 3.12 System of measuring thermal conductivity in a model TC-7000 of the ULVAC-RIKO.

The shape of sample for measurement is in solid disk of dimension 10 mm and thickness of 1 to 3 mm.

3.3.3.1 THERMAL DIFFUSIVITY MEASUREMENT

The laser flash method is used for measuring the thermal diffusivity (α)[43] of bulk samples as shown in **Figure 3.13**.

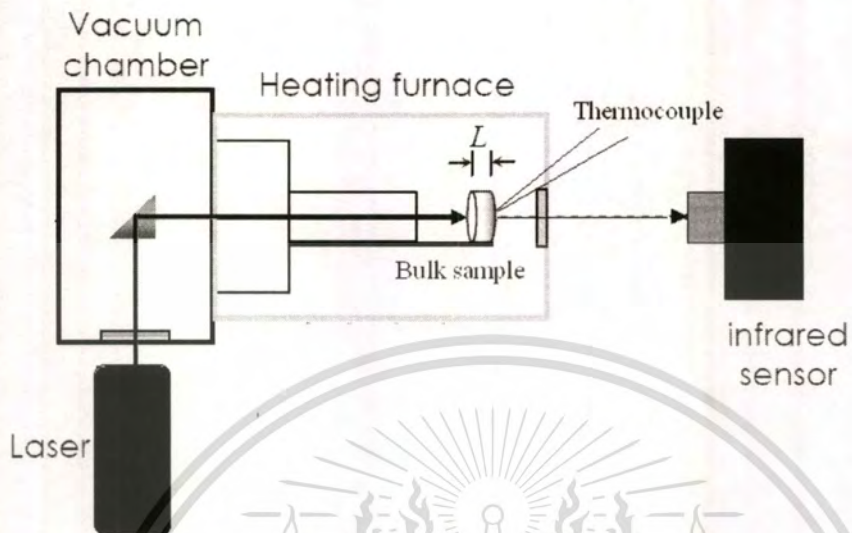


Figure 3.13 The diagram to measure thermal conductivity.

On measurement, the temperature rise of the sample back surface by laser irradiation is in transient phenomena. The time is a very short time of several 10^{-3} seconds to several 10 of seconds. This system memorizes transient phenomena by high speed signal memory. The measurement data is recoded in time and temperature with high accuracy, high resolution. Then, the data were plot between the time axis and temperature axis as shown in **Figure 3.14**.

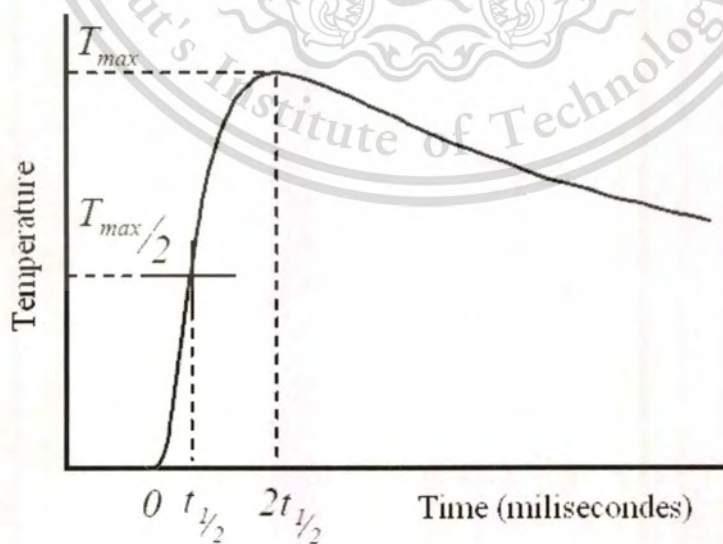


Figure 3.14 The curve of temperature vs. time measurement of by the laser flash technique.

The thermal diffusivity of bulk sample by the laser flash technique is given as following of the equation:

$$a = 1.37 \frac{L}{\pi^2 T_{1/2}} \quad (3.11),$$

where a is the thermal diffusivity (cm^2/sec),

L is the sample thickness,

$T_{1/2}$ is the time required for the temperature on the back side of the bulk sample to the half of the maximum temperature after the sample surface is irradiated with instantaneous heat source.

3.3.3.2 HEAT CAPACITY MEASUREMENT

The heat capacity (C_p) [43] is measured by the absolute measurement of specific heat method in laser flash technique. This method, a light receiving plate is bonded to bulk sample to heat capacity. The **Figure 3.15** shows the setup sample to the light receiving plate.

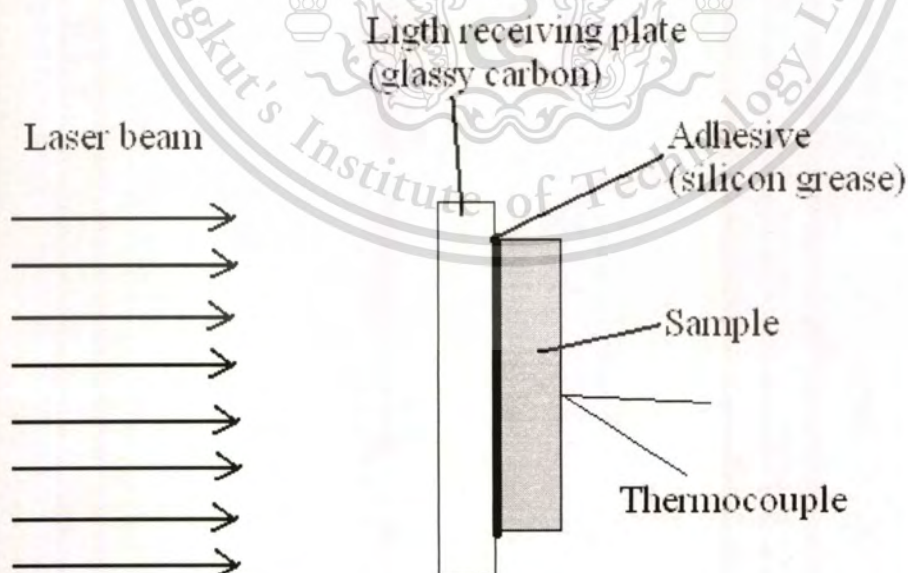


Figure 3.15 The diagram to measure heat capacity.

The heat capacity of bulk sample is obtained from the relation:

$$C_p = \frac{\left[\frac{Q}{Tm - (Mr \times Cr) - (Ma \times Ca)} \right]}{m} \quad (3.12),$$

where C_p is the heat capacity of bulk sample unknown,

Tm is the temperature risen on sample,

m is the weight of bulk sample,

Q is the heat absorption quantity of light receiving plate (glassy carbon),

Ma is the weight of adhesive (silicon grease),

Ca is the heat capacity of adhesive (silicon grease),

Mr is the weight of light receiving (glassy carbon),

Ca is the heat capacity of adhesive (glassy carbon).

3.3.3.3 SAMPLE DENSITY

The density (d) of bulk sample is calculated from the relation:

$$d = \frac{m}{V} \quad (3.13),$$

where m is the weight of bulk sample and V is the total volume of sample.

3.3.4 UV-VIS-NIR SCANNING SPECTROPHOTOMETER

3.3.4.1 ABSORPTION COEFFICIENT

The electromagnetic wave of well-known Maxwell equations can describe the propagation of light in medium. The solution the electric field strength [44] in the x-component of the polarized wave which propagates along the positive z-axis is commonly achieved by relation;

$$E_x = E_o \exp \left[i\omega \left(t - \frac{zn}{c} \right) \right] \quad (3.14),$$

where E_x is the electric field strength in the x-component

E_o is the maximum value of the electric field strength (amplitude),

$\omega = 2\pi f$ is the angular frequency,

n is refractive index, for the complex term, the complex index is $\hat{n} = n - ik$, where k is damping constant.

Also, the electric field strength in the x-component of the complex refractive index is

$$E_x = \left[E_o \exp\left(-\frac{\omega k}{c} z\right) \right] \left[\exp\left(i\omega\left(t - \frac{zn}{c}\right)\right) \right] \quad (3.15),$$

The first term of above equation is damped amplitude and second term is undamped wave. In the measurement, the electric field strength (E_x) is hard to measure; therefore, the intensity (I_e) is commonly used instead. The intensity can be measured by photodetector devices. The intensity is the square of the electric field strength. Also, the damping term in equation (3.16) is obtained

$$I_e = (E_x)^2 = I_o \exp\left(-\frac{2\omega k}{c} z\right) \quad (3.16),$$

Thus,

$$\frac{I_e}{I_o} = \exp\left(-\frac{2\omega k}{c} z\right) \quad (3.17),$$

The characteristic penetration depth W is the distance of light traveling to decrease in $1/e$ as equation:

$$W = \frac{c}{2\omega k} = \frac{c}{4\pi f k} = \frac{c}{4\pi k} \quad (3.18),$$

The attenuation or absorption coefficient (α) is defined by the inverse of the W as the relation:

$$\alpha = \frac{2\omega k}{c} = \frac{4\pi f k}{c} = \frac{4\pi k}{c} \quad (3.19),$$

Finally, the absorption coefficient is expressed as following:

$$\frac{I_e}{I_o} = \exp(-\alpha z) \quad (3.20),$$

The unit of absorption coefficient (α) is in cm^{-1} .

3.3.4.2 ABSORPTION MEASUREMENTS

The present work, the optical absorption was measured by a UV-VIS-NIR scanning spectrophotometer (Shimazu UV-3101PC) in the light of wavelength range from 200 to 2500nm as diagram shown in **Figure 3.16**. In general, the spectrophotometer measurement of the amount optical absorption in a material is analyzed the absorption as a function of wavelength. The optical absorption of each wavelength (λ) is measured in terms of optical absorbance (a_{ab}). From Beer's law of absorption [44], the absorbance can be obtained from the relation:

$$a_{ab}(\lambda) = \log \frac{I_e(\lambda)}{I_o(\lambda)} = \frac{\alpha t}{2.303} \quad (3.21),$$

where $a_{ab}(\lambda)$ is the absorbance of wavelength at λ ,

$I_o(\lambda)$ is intensity of the incident monochromatic light of wavelength at λ ,

$I_e(\lambda)$ is intensity of the light transmitted by the sample of wavelength at λ ,

λ is wavelength of the monochromatic light,

α is absorption coefficient,

t_h is thickness of the sample.

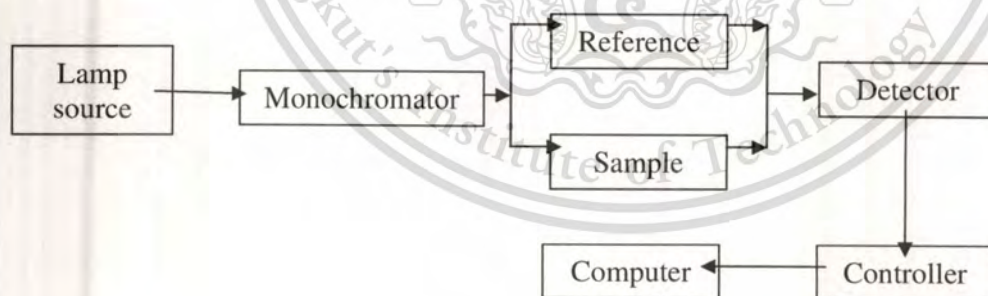


Figure 3.16 The diagram of UV-VIS-NIR scanning spectrophotometer.

In optical spectrophotometers, the measurement is obtained the optical density (OD) value as defined by $OD = \log(I_e/I_o)$.

3.3.5 THERMAL ANALYSIS

Thermal analysis technique [45] is used to investigate the properties of solids as a function of a temperature changing. This technique is useful for studying phase changes, decomposition, loss of water, and for making phase diagrams. In this work, the thermal analysis method uses in the thermogravimetric method (TG) and Difference thermal analysis (DTA). The Pyris Diamond TG/DTG (Perkin Elmer Instrument) was use in this work.

3.3.5.1 DIFFERENCE THERMAL ANALYSIS (DTA)

The DTA was used to analysis the phase changes [45]. In measurement, the sample is place in one chamber, and a reference solid, which will not change phase over the temperature range of the experiment, is in the other chamber. Both chambers are heated at a controlled uniform rate in a furnace. The difference in temperature between the two samples is recoded against time.

All reaction in the sample will be displaid as a peak of the plot in temperature difference. The exothermal reaction shows an increase in temperature, and the end thermal shows a decrease in temperature. Also, the peaks occur in opposite direction. This technique can depict the phase change, melting point and decomposition.

3.3.5.2 THERMOGRAVIMETRIC METHOD (TG)

This technique, the weight of a sample is investigated as a function of time, as the temperature is increased at a controlled uniform rate [45]. The water loss of crystallization and volatiles of oxygen is shown in the weight loss that is the decomposition. The oxidation and adsorption of gas is shown in the weight gain. This technique can depict the loss of adsorbed water and decomposition.

CHAPTER 4

EXPERIMENTAL RESULTS

In this chapter, the experimental results of the dissertation are reported. The results are separated in 7 sections consisting of:

- (1) Thermoelectric properties at high temperature of CuFeO_2 ,
- (2) Thermoelectric properties at high temperature of $\text{Cu}_{1-x}\text{Pt}_x\text{FeO}_2$,
- (3) Thermoelectric properties at high temperature of $\text{CuFe}_{1-x}\text{Al}_x\text{O}_2$,
- (4) Finite Element Analysis of $\text{CuFe}_{0.5}\text{Al}_{0.5}\text{O}_2$,
- (5) Thermoelectric properties at high temperature of $\text{CuFe}_{1-x}\text{Sn}_x\text{O}_2$,
- (6) Thermoelectric properties at high temperature of $\text{CuFe}_{1-x}\text{Pb}_x\text{O}_2$,
- (7) Thermoelectric prototype of p - $\text{CuPt}_{0.95}\text{Fe}_{0.05}\text{O}_2$ leg and n - $\text{CuFe}_{0.95}\text{Pb}_{0.05}\text{O}_2$ leg.

The detail of each section is described below.

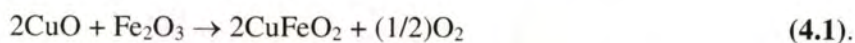
4.1 THERMOELECTRIC PROPERTIES AT HIGH TEMPERATURE OF CuFeO_2

4.1.1 INTRODUCTION

This section is concerned with the investigation results of thermoelectric properties of the CuFeO_2 sample due to its Seebeck coefficient at high temperature as increasing with increasing the temperature. The CuFeO_2 sample was synthesized. Thermoelectric and optical properties of the CuFeO_2 sample were measured. The results of thermoelectric properties were compared to the thermoelectric properties of Bi_2Te_3 and NaCoO_2 . In addition, the optimum thermoelectric value of the CuFeO_2 sample was discussed in relation of $E_G = 4k_B T$ as given the guideline of the development of high temperature thermoelectric materials [31].

4.1.2 EXPERIMENTAL PROCEDURE

The CuFeO_2 sample was prepared by conventional solid state reaction method as following a chemical formula:



The specimens were sintered in furnace at 1050 °C in air atmospheres for 15 - 25 h. The obtained samples are in black color as shown in **Figure 4.1**.



Figure 4.1 The pellets of the CuFeO₂ sinter sample.

4.1.3 RESULTS AND DISCUSSION

4.1.3.1 X-RAY DIFFRACTION

The X-ray diffraction (XRD) patterns of the CuFeO₂ sample are shown in **Figure 4.2**. The patterns exhibit peaks of pure phase of the hexagonal delafossite-type structure for space group: $R\bar{3}m$ (166) corresponding to the standard ICSD: 01-075-2146 file[46] and a trace impurity peak of the CuO phase relating to the standard ICSD: 01-089-5897 file[46]. The CuFeO₂ lattice parameters are 3.033 Å and 17.159 Å of a-axis and c-axis length, respectively, corresponding to the reported of literature [47]. The remaining of the CuO starting powder as in **Figure 4.2** implies that the lattice structure of the CuFeO₂ sample contains the Cu vacancy which is the natural non-stoichiometric of delafossite compound.

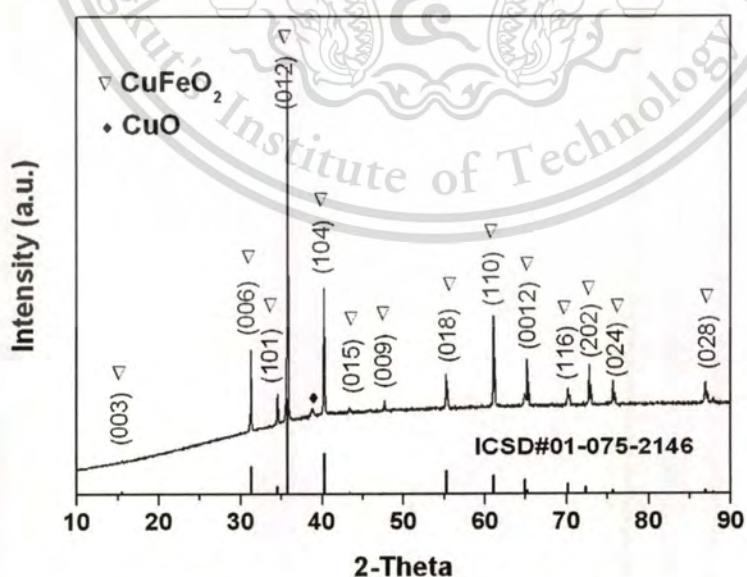


Figure 4.2 The XRD patterns of the CuFeO₂ sinter sample.

4.1.3.2 DENSITY

The bulk density (d) of sample is defined by the ratio of mass to volume of sample. The theoretical density (d_x) [64] is given by the equation:

$$d_x = \frac{3M}{N_A V} \quad (4.2),$$

where M is the molecular weight,

N_A is the Avogadro's number,

V is the volume of unit cell with the relation:

$$V = \frac{\sqrt{3}(a^2 c)}{2} \quad (4.3),$$

where a and c are the lattice constant.

The percentage ratio of bulk density to theoretical density (D_r) of samples is calculated by the relation:

$$D_r = \frac{d}{d_x} \times 100 \quad (4.4).$$

The bulk density of the CuFeO_2 sinter sample is 5.22 g/cm^3 and the theoretical density of the CuFeO_2 sample is 5.39 g/cm^3 . Also, the D_r of the samples is 96.84%. This result implies that the prepared sample has density closely to the theory density leading to reasonable in value of the measurement of thermal conductivity.

4.1.3.3 SCANNING ELECTRON MICROSCOPE

The SEM image of the CuFeO_2 sample is shown in **Figure 4.3**. Most of the microstructure in **Figure 4.3(a)** shows the crystal grain size in the range from 20 to 40 μm . The morphology of SEM image in **Figure 4.3 (b)** displays the crystal plane on the basal planes (0001) and the prism planes (10 $\bar{1}$ 0) of the hexagonal unit cell $R\bar{3}m$. The SEM image as displayed in **Figure 4.3 (c)** shows the surface morphology of the CuFeO_2 sample in the scaling of 6 μm .

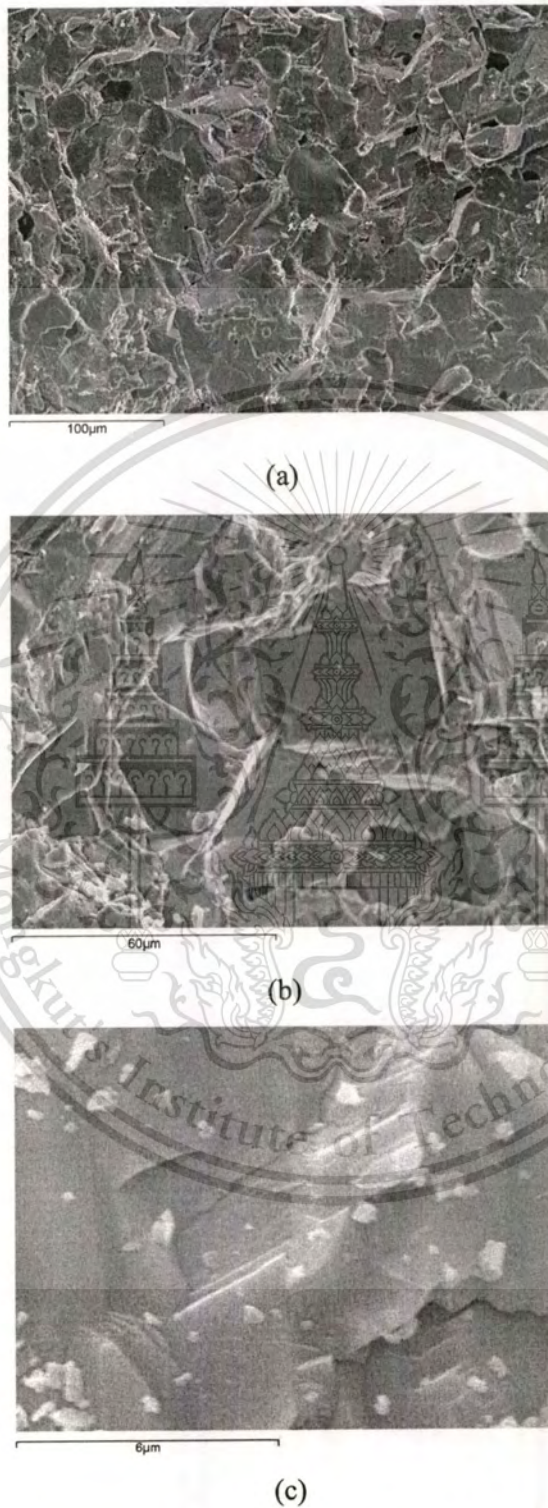


Figure 4.3 The microstructure and the morphology of the CuFeO_2 sinter sample.

This material is reserved for educational use only, not allowed for commercial use.

Forbidden to modify the content, and cite the document when use.

The quantitative chemical composition of the CuFeO_2 samples was determined by using an Energy-Dispersive X-ray spectroscopy (EDX). The EDX analysis was performed on an area of inserted image in **Figure 4.4**. The results of the EDX peaks show only Peaks of Cu, Fe and O for atomic in 28.99%, 28.57% and 42.44%, respectively, and for weight in 44.75%, 38.76% and 16.49%, respectively. For the results of percentage of weight, they show results closely to theoretical percentage of weight for the Cu, Fe and O in 41.97%, 36.89%, and 21.14%, respectively with the weight of chemical formula of the CuFeO_2 delafossite (151.45 g/mole). For the results of percentage of atomic, they show ratio for Cu:Fe:O approximately in 1:1:1.4, respectively, whereas, the ratio of Cu:Fe:O in the chemical formula (CuFeO_2) is 1:1:2. This result implies that the EDX method can analyze the atomic ration of the Cu and Fe metal in the sinter sample closely to the stoichiometric of the CuFeO_2 delafossite, while this method cannot correct the atomic ration of the O in the CuFeO_2 sample.

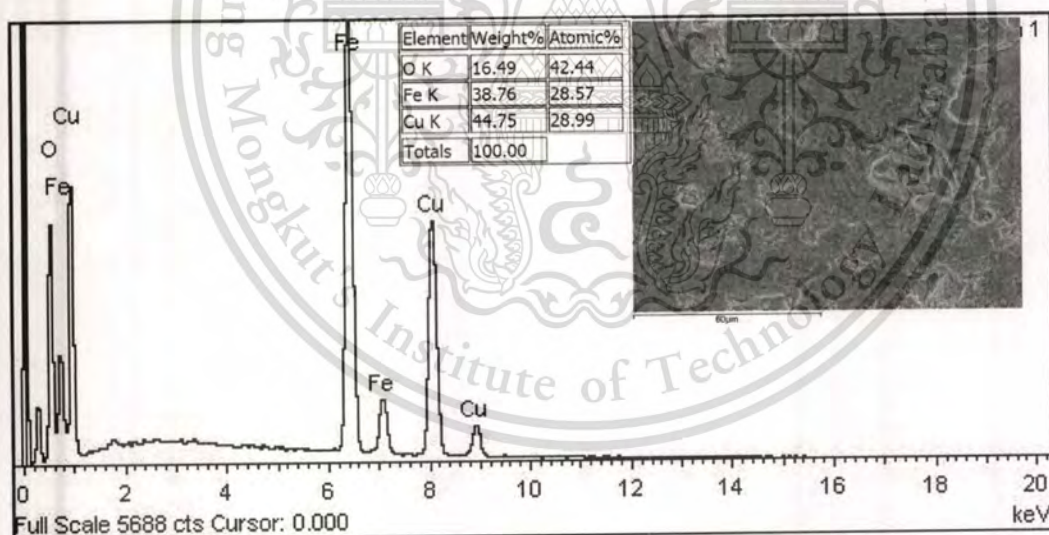


Figure 4.4 The Energy-Dispersive X-ray spectroscopy of the CuFeO_2 sinter sample.

4.1.3.4 THERMOGRAVIMETRIC AND DIFFERENTIAL THERMAL ANALYSIS

The decomposition of the CuFeO_2 sample is clearly verified by Thermogravimetric method (TG) in weighting loss and Differential Thermal Analysis (DTA) as shown in **Figure 4.5**. According to the entire range of measurement under the atmosphere, the first peak at 95 °C is shown the effect of humidity. The second peak at temperature 222 °C, the oxygen is inserted approximately 0.05% into the Cu layers [48–50]. The third weight loss at 283 °C is originated due to the oxygen excess.

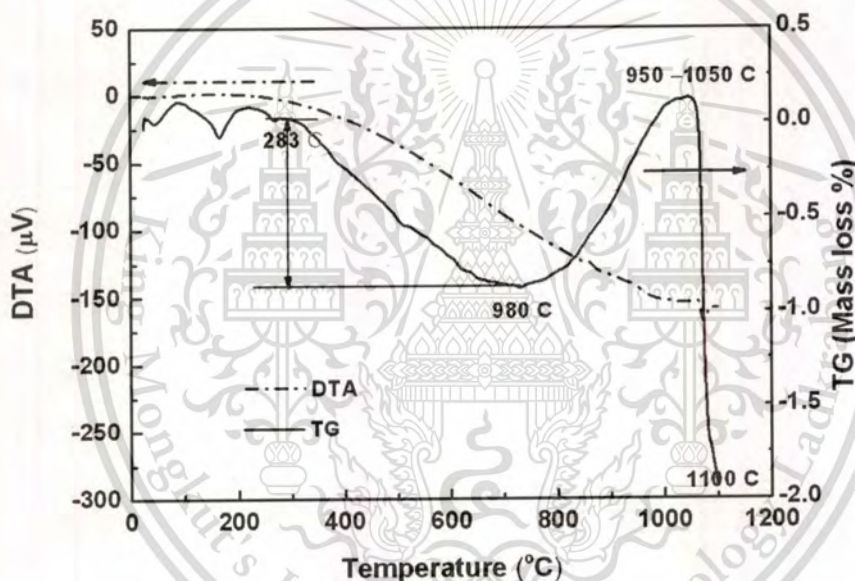


Figure 4.5 The TG-DTG curve of the CuFeO_2 sinter sample.

It is also interesting to point out that the end of the oxygen weight loss is in temperature at 707 °C. Its total weight loss is approximately 0.9% which is equivalent to the oxygen content of 0.14 atoms per unit formula as indicated δ of the chemical formula $\text{CuFeO}_{(2+\delta)}$ as $\text{CuFeO}_{(2+0.14)}$. The results of the excess oxygen atoms in the CuFeO_2 sample confirm that the nature of the delafossite compound allows interstitial oxygen in its structure. The inserting oxygen in the lattice layer leads to copper oxidation, which is oxidized during the synthesis process, as accurately formula $\text{Cu}^{+}_{1-2\delta}\text{Cu}^{2+}_{2\delta}\text{Fe}^{3+}\text{O}_{(2+\delta)}$. The results of TG and DTA data show

that the CuFeO_2 forms phase in temperature ranging from 950 to 1050 °C. The abrupt weight loss is in the temperature beyond 1100 °C (1365 K), indicating the melting point behavior of the CuFeO_2 delafossite.

4.1.3.5 SEEBECK COEFFICIENT

The temperature dependence of the Seebeck coefficient (S) of the CuFeO_2 sample with compared to value of the Bi_2Te_3 and Na_5CoO_2 is shown in **Figure 4.6**. The Seebeck coefficient of CuFeO_2 exhibits the value ranging from 261 to 300 $\mu\text{V/K}$ from temperature 300 to 960 K, respectively. The positive sign of the Seebeck value as p-type conducting is contribution by majority carrier of hole. Indeed, the CuFeO_2 delafossite is p-type conductive oxide material. The results of Seebeck coefficient show that the Seebeck value of the CuFeO_2 sample is higher than that value of the Bi_2Te_3 and Na_5CoO_2 in all temperature range.

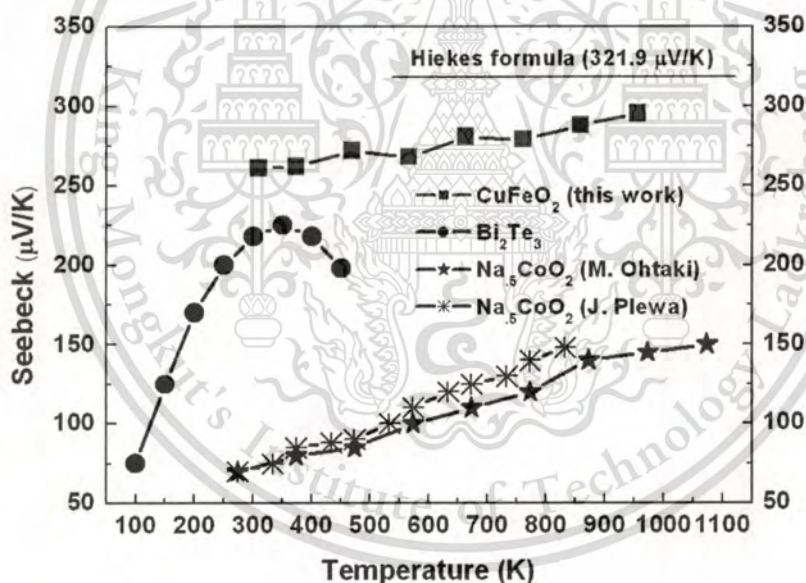


Figure 4.6 The temperature dependence of Seebeck coefficient of the CuFeO_2 sinter sample comparing with other compounds.

4.1.3.6 THE HEIKES FORMULA

The empirical formula of Seebeck coefficient has been developed to predict the maximum of value for material in high temperature to reduce in trial experiment. The limit of S

value at high temperature for localized carries of semiconductor materials has been proposed by Heikes formula[34, 35], which is the entropy per site as expressed by equation:

$$S = -\frac{k_B}{e} \ln \left[\frac{c}{(1-c)} \right] \quad (4.5),$$

where c is the carrier concentrations,

k_B/e is $86.17 \mu\text{V/K}$.

The prediction in the maximum of Seebeck coefficient of the CuFeO_2 sample in high temperature is computed by equation (4.5). By approximation, the c is calculated from the ration of $2*(0.14/12)$. The numeric of $0.14/12$ is obtained from the ration of the excess oxygen atom in a chemical formula of the CuFeO_2 structure with number of atom in a chemical of CuFeO_2 as 12 atoms. The numeric of 2 is obtained from the summation of excess oxygen atom in a chemical formula of CuFeO_2 and the Cu vacancy in Cu layer. Therefore, the Seebeck value of the Heikes formula is expressed by:

$$S = -(86.17 \mu\text{V/K}) \ln \left[\frac{\left(\frac{2*0.14}{12} \right)}{\left(1 - \left(\frac{2*0.14}{12} \right) \right)} \right] = 321.90 \mu\text{V/K}.$$

This result indicates that the maximum of Seebeck value of the CuFeO_2 sample is $321.90 \mu\text{V/K}$ corresponding to the experimental results as shown in **Figure 4.6**.

4.1.3.7 ELECTRICAL CONDUCTIVITY

The temperature dependence of electrical conductivity(σ) of the CuFeO_2 sample with comparing to value of the Bi_2Te_3 and $\text{Na}_{0.5}\text{CoO}_2$ is shown in **Figure 4.7**. The electrical conductivity of the CuFeO_2 sample increases from 3 to 13 S/cm with the temperature increasing from 300 to 960 K. At the high temperature 960K, the electrical conductivity of the CuFeO_2 sample has 13 S/cm. This result shows that the electrical conductivity of the CuFeO_2 sample at high temperature is higher than that value at low temperature. All results of electrical

conductivity show that the values of the CuFeO_2 sample are lower than that value of the Bi_2Te_3 and $\text{Na}_{0.5}\text{CoO}_2$ in all temperature ranges.

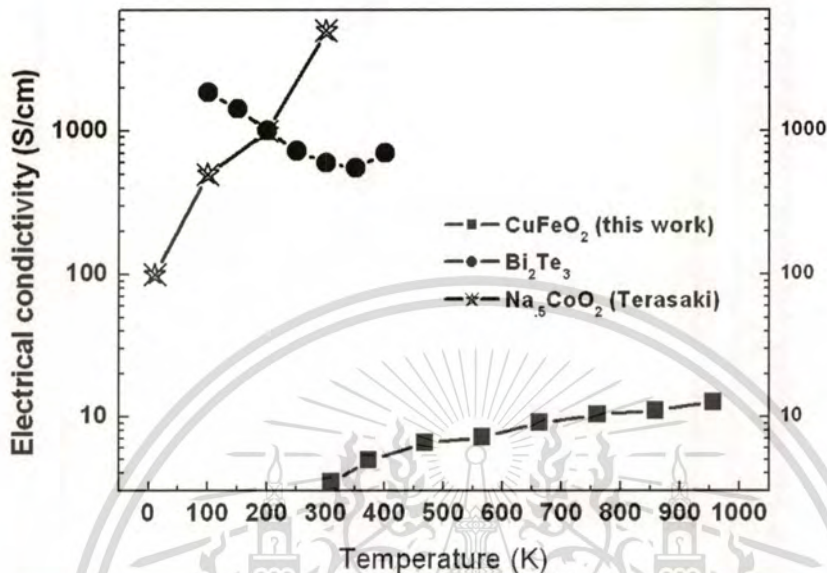


Figure 4.7 The temperature dependence of electrical conductivity coefficient of the CuFeO_2 sinter sample comparing with other compounds.

4.1.3.8 THERMAL CONDUCTIVITY

The temperature dependence of the thermal conductivity (κ) of the CuFeO_2 sample with compared to value of the Bi_2Te_3 and $\text{Na}_{0.5}\text{CoO}_2$ is shown in **Figure 4.8**. The thermal conductivity is measured by using a laser flash method with the relation[43]:

$$\kappa = dC_p a \quad (4.6),$$

where d is the bulk density of sample,

C_p is the heat capacity,

a is the thermal diffusivity.

The results show that thermal conductivity of the CuFeO_2 sample decreases in the range from 5.8 to 3.5 W/m-K with measuring temperatures from 300 to 960 K, respectively. In the experiment, the maximum of the κ value is 5.8 W/m-K at room temperature and minimum of the κ value is 3.5 W/m-K at temperature 960 K. These results exhibit that the thermal conductivity of the CuFeO_2 sample is decreased as the increasing temperature. Therefore, the high value of the

$ZT (= T\sigma S^2/\kappa)$ of the CuFeO_2 samples is dominant to occur at high temperature because the κ value is still contained the minimum value. All results of thermal conductivity shows that the values of the CuFeO_2 sample are higher than the values of the Bi_2Te_3 and Na_5CoO_2 in all temperature range.

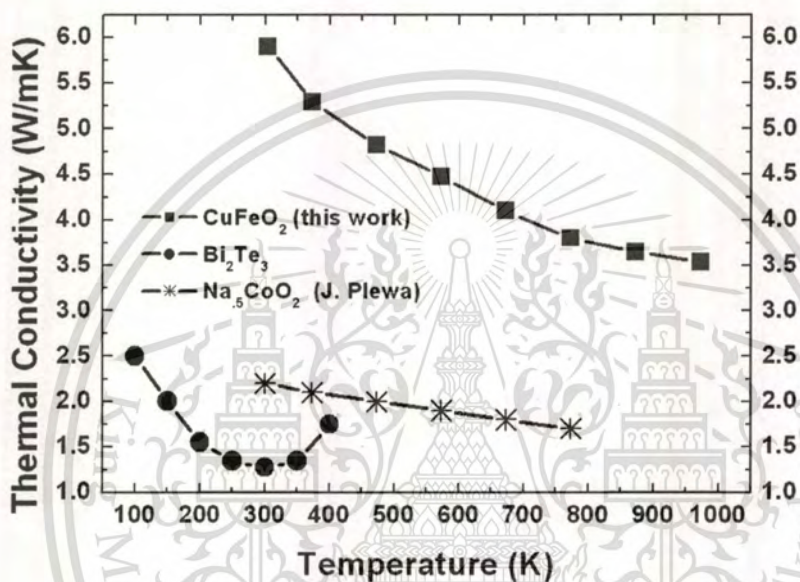


Figure 4.8 The temperature dependence of thermal conductivity of the CuFeO_2 sinter sample comparing with other compounds.

The total thermal conductivity (κ) consists of the two components [7, 33] of the lattice (phonon) component (κ_l) and electronic component (κ_e) as following relation:

$$\kappa = \kappa_l + \kappa_e \quad (4.7),$$

where κ is the total thermal conductivity,

κ_l is the thermal conductivity of phonon part,

κ_e is the thermal conductivity of electronic part.

From the Wiedmann-Franz law[7, 33], the κ_e is related by the equation:

$$\kappa_e = L_o T \sigma \quad (4.8),$$

where L_o is the Lorenz factor ($2.45 \times 10^{-8} \text{ W}\cdot\Omega/\text{K}^2$),

T is the absolute temperature,

σ is the electrical conductivity.

Consequently, the κ_e value of the CuFeO_2 sample at 960 K is $3.06 \times 10^{-2} \text{ W/m}\cdot\text{K}$ which is 1.545 % of the total κ value. This result indicates that the major effect of thermal conductivity of the CuFeO_2 sample is dominated by the phonon mechanism part.

4.1.3.9 DIMENSIONLESS OF FIGURE OF MERIT (ZT)

The temperature dependence of the ZT values of the CuFeO_2 sample with compared to the Bi_2Te_3 and Na_5CoO_2 are shown in **Figure 4.9**. The Power Factor (PF) value is calculated from the Seebeck coefficient and electrical conductivity. Also, the $ZT(=S^2\sigma T/\kappa)$ value is computed from the PF and temperature. The interesting results display that the ZT value of the CuFeO_2 sample are increased with increasing temperature. The ZT value is in range of 0.123×10^{-2} to 2.96×10^{-2} with temperature from 300 to 960 K, respectively. The maximum value of the ZT of the CuFeO_2 sample in the experiment is 2.96×10^{-2} at 960K. In conclusion, the CuFeO_2 delafossite oxide gives a high value of thermoelectric properties at high temperature. All results of ZT value show that the value of the CuFeO_2 sample is lower than that value of the Bi_2Te_3 and Na_5CoO_2 in all temperature range.

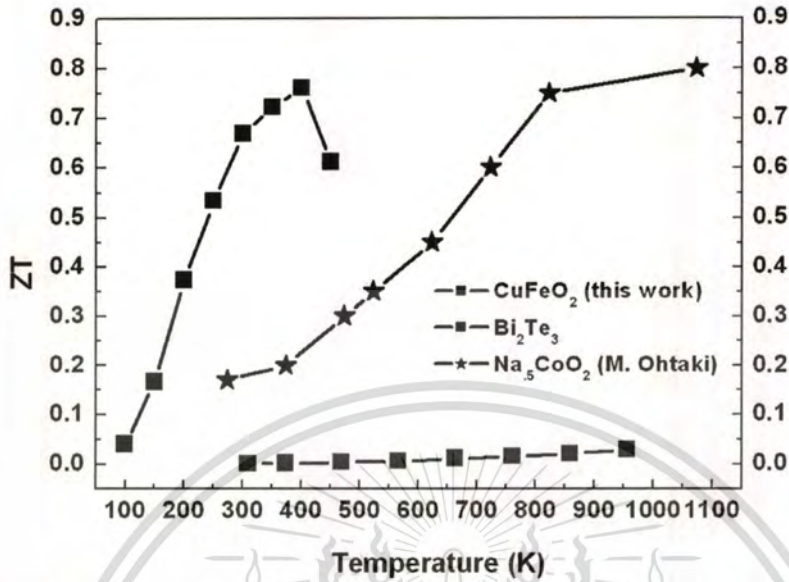


Figure 4.9 The temperature dependence of ZT of the CuFeO_2 sinter sample comparing with other compounds.

4.1.3.10 ACTIVATION ENERGY

4.1.3.10.1 ACTIVATION ENERGY OF PRODUCTION OF FREE CARRIERS (E_a)

For the applying of a p-type semiconductor, the equation of Seebeck coefficient (S) is given by the relation [35, 53]:

$$S = \frac{k_B}{e} \left(\frac{E_F - E_v}{k_B T} \right) = \frac{k_B}{e} \ln \left(\frac{N_v}{N_D} \right) \quad (4.9),$$

where k_B is the Boltzmann's constant,

e is the electronic charge constant,

E_v is the energy of the valance-band edge,

E_F is the Fermi energy level,

T is the absolute temperature,

N_v is the effective density of state,

N_D is the doping density (or the hole carriers density).

The results of Seebeck coefficient in **Figure 4.10** are slightly changed with increasing temperature relating with the Seebeck equation as a function of temperature. The activation energy for the production of free carriers (E_s) as $E_s = E_F - E_v$ is 27 meV as shown in **Figure 4.10**. The linearity decreasing of the E_s value with $1000/T$ implies that the hole carriers (N_D) is activated by thermal energy.

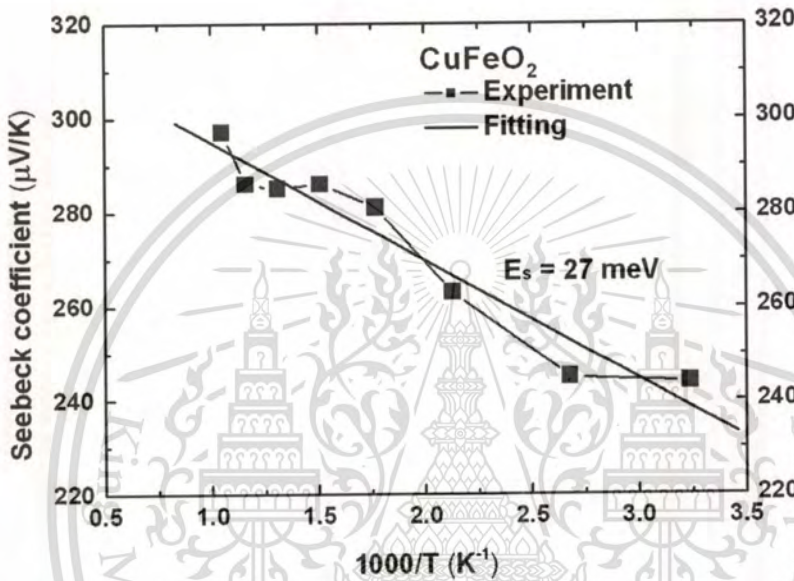


Figure 4.10 The Seebeck coefficient (S) vs. $1000/T$ curve.

4.1.3.10.2 ACTIVATION ENERGY OF CARRIER CONDUCTION (E_σ)

The Arrhenius plot of fitting of electrical conductivity with temperature is related by equation [35, 35]:

$$\sigma = A_o \exp\left(-\frac{E_\sigma}{k_B T}\right) \quad (4.10),$$

where k_B is the Boltzmann's constant,

E_σ is the activation energy of carrier conduction,

T is the absolute temperature,

A_o is constant.

The activation energy of carrier conduction (E_σ) is obtained from Arrhenius plot as $\log \sigma$ vs. $1000/T$. The E_σ value of the CuFeO_2 sample as in Arrhenius plot is shown in **Figure 4.10**. The slope shows that the E_σ value of the CuFeO_2 sample is 0.049 eV.

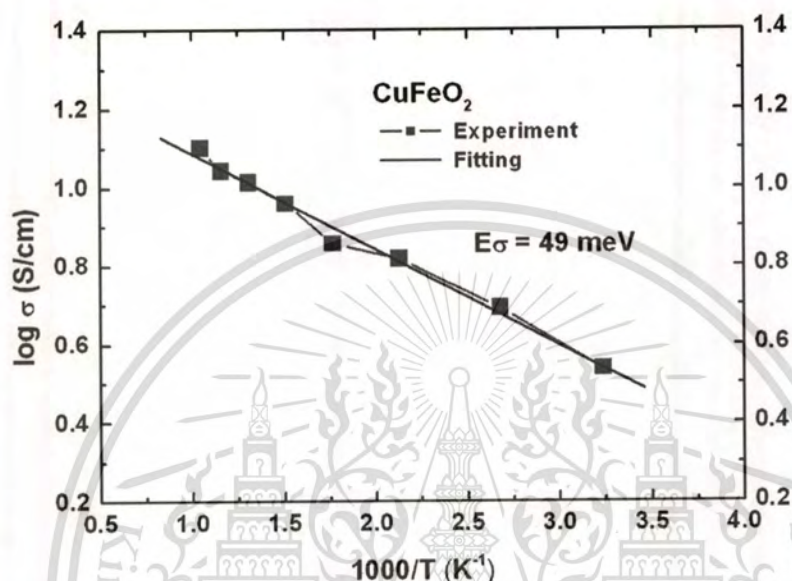


Figure 4.11 The curve of $\log \sigma$ vs. $1000/T$ of CuFeO_2 sintering sample.

4.1.3.10.3 ACTIVATION ENERGY OF CARRIER MOBILITY (E_μ)

The relation of electrical conductivity is given by the equation

$$\sigma = en\mu \quad (4.11),$$

where e is the carrier charge,

n is the carrier concentration,

μ is the mobility of carriers.

For the electronic transport in semiconductor, the charge carriers must be excited to free carriers, and then they move by hopping mechanism. The electrical conductivity for semiconductor is described [35] by the relation:

$$\sigma = eN_T \exp\left(-\frac{E_F - E_v}{k_B T}\right) \mu_o \exp\left(-\frac{E_\mu}{k_B T}\right) \quad (4.12),$$

where N_T is the effective density of states of charge carrier,

μ_o is the mobility constant.

The overall activation energy for semiconductor (E_σ) is a combination of two components as the relation[35]:

$$E_\sigma = E_u + E_s \quad (4.13),$$

where E_u is the activation energy for carrier mobility (hopping energy).

The E_u value is obtained by the mobility of carriers as following by the equation[51, 52]:

$$\mu = \mu_o \exp\left(-\frac{E_\mu}{k_B T}\right) \quad (4.14),$$

where μ is the mobility of carrier,

μ_o is the mobility constant.

From the value of the E_s (27 meV) and the value of the E_σ (49 meV), the value of the E_u of the CuFeO₂ sample is 22 meV which is less than the thermal energy at room temperature ($k_B T_{300K} \cong 25$ meV).

The small value of the E_u implies that the conductivity of the CuFeO₂ samples is major activating from the activation energy for carrier production and tiny activating from the mobility activation energy. These results confirm that the p-type (hole) conduction of the CuFeO₂ delafossite is good semiconductor because of the ionization of free carrier occurring in thermal activation energy nearly the room temperature. In addition, the carriers have high mobility due to requiring the activation energy of mobility less than the thermal energy at room temperature.

4.1.3.11 THE UMKLAPP RELATION

Considering in the lattice (phonon) thermal conductivity (κ), the Umklapp scattering contribution[31] in the phonon scattering process is expressed by the equation

$$\kappa_u = \delta[(T_m)^{3/2} M^{(-7/6)} \rho^{2/3}] T^{(-1)} \quad (4.15),$$

where κ_u is the Umklapp phonon thermal conductivity,

δ is the proportionality constant,

T_m is the melting temperature,

M is the average atomic mass,

ρ is the density,

T is the operation temperature.

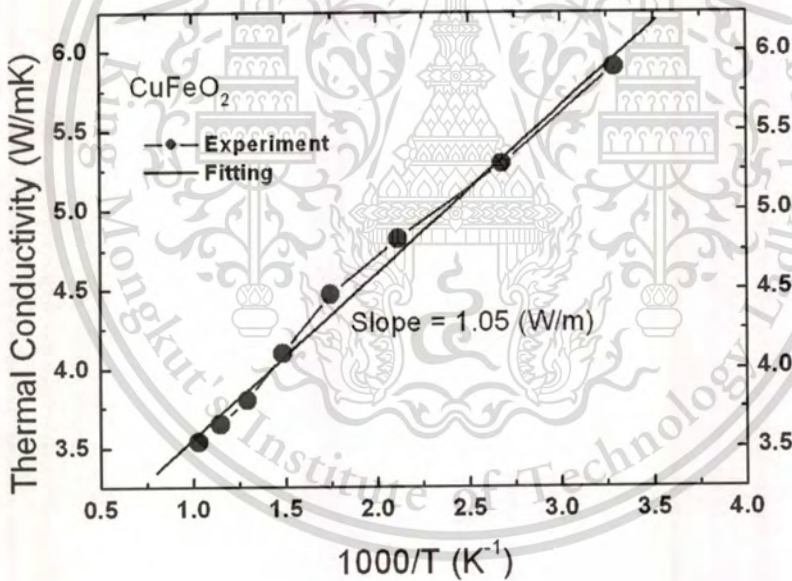


Figure 4.12 The thermal conductivity vs. $1000/T$ curve.

The Umklapp relation implies that the κ_u is proportion to $1/T$. **Figure 4.12** shows the relation of the thermal conductivity with function of inversion temperature. The curve shows that the thermal conductivity (κ) is linear with $T^{(-1)}$ corresponding with the Umklapp relation. These

results indicate that the major effect of thermal conductivity of the CuFeO_2 sample is controlled by the phonon mechanism as contribution by the Umklapp scattering.

The slope of the graph in **Figure 4.12** is 1.05 W/m which is the relation of the thermal conductivity (κ) vs. $1000/T$. In the Umklapp relation, the proportionality constant (δ) is related by the equation:

$$\delta = \left(\frac{\kappa}{\frac{1}{T}} \right) \left[(T_m)^{3/2} M^{(-7/6)} \rho^{2/3} \right]^{-1} \quad (4.16),$$

From the slope of graph, the δ value of the Umklapp process for the CuFeO_2 sample is $8.79 \times 10^{-4} \text{ W-m}^{(-3)} \text{g}^{1/2}/\text{K}^{3/2}$; where $T_m = 1356 \text{ K}$, $M = 454.14 \text{ g}$, and $\rho = 5.22 \text{ g/cm}^3$. Nolas et al. [54] have reported the δ value is $1.3 \times 10^{-3} \text{ W-m}^{(-3)} \text{g}^{1/2}/\text{K}^{3/2}$ for covalent materials, $1.5 \times 10^{-4} \text{ W-m}^{(-3)} \text{g}^{1/2}/\text{K}^{3/2}$ for ionic materials, $6 \times 10^{-4} \text{ W-m}^{(-3)} \text{g}^{1/2}/\text{K}^{3/2}$ for semiconductor. Also, the δ value of the CuFeO_2 sample shows the behavior of semiconductor. In addition, following the Umklapp relation, the minimization for thermal conductivity of the CuFeO_2 sample occurred in high temperature closely to melting point.

4.1.3.12 OPTICAL PROPERTIES

The absorption coefficient(α) [55] spectrum of the CuFeO_2 sample at room temperature is shown in **Figure 4.13**. The absorption coefficient is measured in ranging of energy from 0.5 to 6 eV. The results exhibit that the heavy steep absorbability is in the spectrum ranging from 4 to 6 eV (the UV light), and the week absorbability is in the spectrum ranging from 0.5 to 3.5 eV (the Near IR and the visible light).

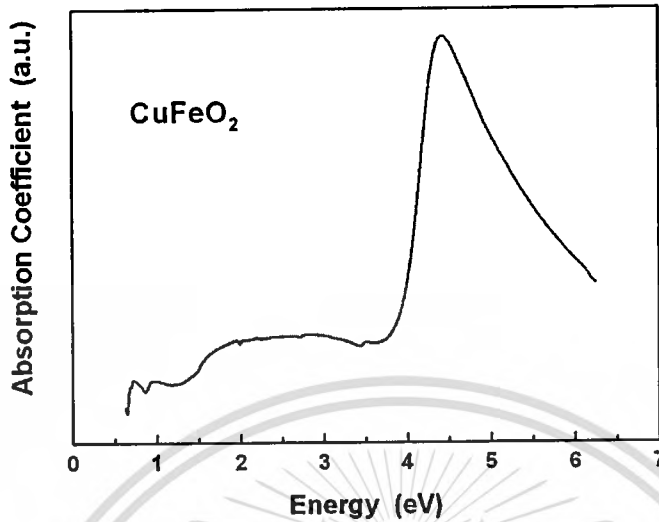


Figure 4.13 Absorbance spectrum of the CuFeO₂ sample at room temperature.

The energy gap is calculated from absorption coefficient by using the relation [56]:

$$(\alpha h\nu)^m = A(h\nu - E_g) \quad (4.17),$$

where α is the absorption coefficient,

$h\nu$ is the photon energy,

E_g is the optical band gap,

A is the constant which does not depend on $h\nu$,

m is $1/2$ and 2 for the indirect and the direct transition gap, respectively.

The region of energy spectrum of visible light is in the range from 1.5eV to 3.1eV. Also, the energy gap (E_g) of material for transparent visible light is must higher than 3.1 eV. The optical energy gap is obtained from a plot of $(\alpha h\nu)^m$ vs. $h\nu$ with taking the intercept on the energy axis[55, 56]. The indirect transition gap and the direct transition gap are indicated by $m = 1/2$ and $m = 2$, respectively.

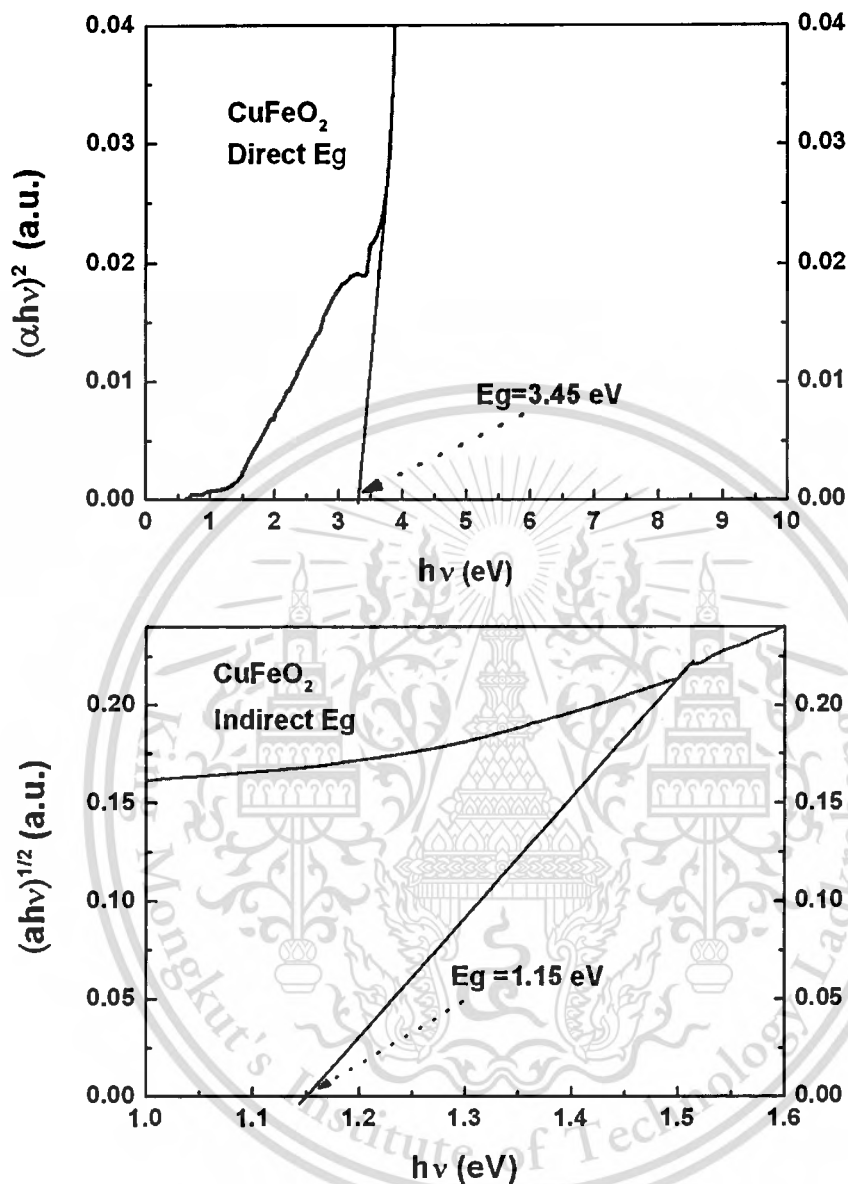


Figure 4.14 (a) Direct optical gap of the CuFeO₂ sample (b) Indirect optical gap of the CuFeO₂ sample.

The results show that the indirect and the direct energy gap at room temperature exhibit 1.15 eV and 3.45 eV as shown in Figure 4.14 (a) and (b), respectively. Evidently, the direct energy gap of the CuFeO₂ sample (3.45 eV) is larger than 3.1 eV. Consequently, the CuFeO₂ sample can transmit photons energy in region of visible light.

4.1.3.13 THE RELATION OF ENERGY GAP WITH TEMPERATURE

The experiment and approximation of the direct band gap (E_g) of the CuFeO_2 sample as a function of temperature is shown in **Figure 4.15**. The temperature dependence of the E_g value is calculated by the empirical formula[57]:

$$E_g(T) = E_g(0) - \left[\frac{aT^2}{(b+T)} \right] \quad (4.18),$$

where $E_g(T)$ is the band gap approximated at temperature T K,
 $E_g(0)$ is the band gap approximated at 0 K,
 a and b are parameters.

The values of a and b for delafossite are 0.00075 eV/K and 385 K, respectively, reported by Dittrich et al.[57]. The $E_g(0)$ value is obtained 3.45 eV by fitting with experimental value of E_g at room temperature. The result exhibits that the direct E_g decreases with increasing temperature. The fitting curve of the optical direct gap (E_g) shows that the E_g is obtained value under 3.1 eV with the temperature above 700 K.

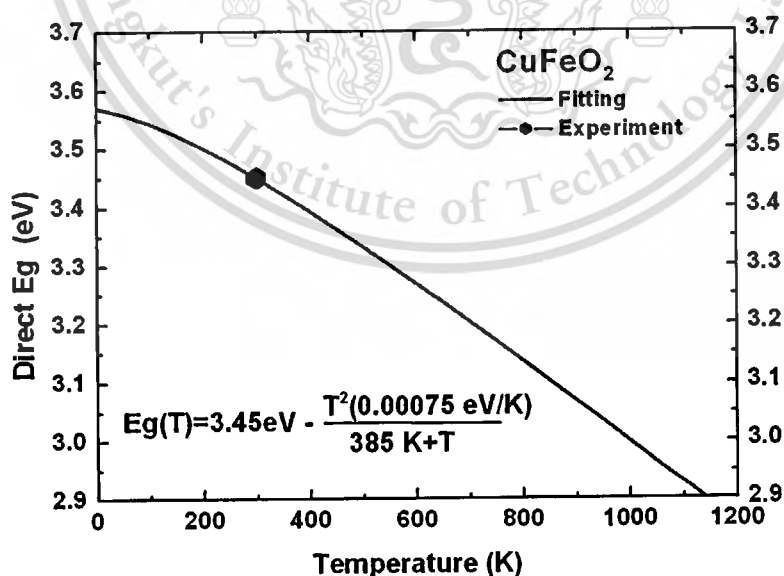


Figure 4.15. Temperature dependence of the direct band gap (E_g) of the CuFeO_2 sample.

4.1.3.14 ENERGY DIAGRAM

The band energy level diagram of the CuFeO_2 delafossite at room temperature is predicted from the obtained value of activation energy, Fermi energy level and optical energy gap, as shown in **Figure 4.16**. The band energy diagram shows the direct energy gap (E_g) of the CuFeO_2 samples is 3.45 eV. The Fermi's energy (E_F) level is above the valence band edge for 0.0275 eV, and the acceptor level (E_a) is above the valence band edge in 0.049 eV. In all energy measurement results, the energy level of the CuFeO_2 sample can be calculated as shown in **Figure 4.16**.

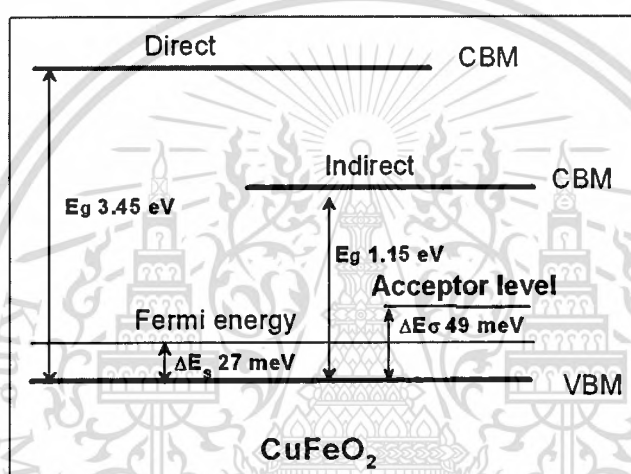


Figure 4.16 The energy level diagram of the CuFeO_2 delafossite (not exact to the scale).

4.1.3.15 RELATION OF MELTING POINT TO ENERGY GAP

For application at high temperature, Schwartz et. al. [31] have described the relation between energy gap and melting point of temperature for the good thermoelectric materials in the relation:

$$E_G = 4k_B T_h \quad (4.19),$$

where E_G is the optimal energy gap,

k_B is the Boltzmann's constant,

T_h is the operation temperature.

The optimal band gap plays important role for the best thermoelectric materials, so it can neglect the behavior in small and large band-gap. For example, the Bi_2Te_3 has the highest ZT (~ 1) at 400 K with $E_g = 0.13$ eV corresponding to the relation of $E_G = 4k_B T_h = 0.14$ eV at $T_h = 400\text{K}$. Another, the SiGe has the highest ZT (~ 1) at 1200 K with $E_g = 0.43$ eV corresponding to the relation of $E_G = 4k_B T_h = 0.413$ eV at $T_h = 1200\text{K}$. The small band-gap causes to thermally excite minority carriers to reduce the Seebeck coefficient, and causes to increase the thermal conductivity to decreased low thermoelectric performance.

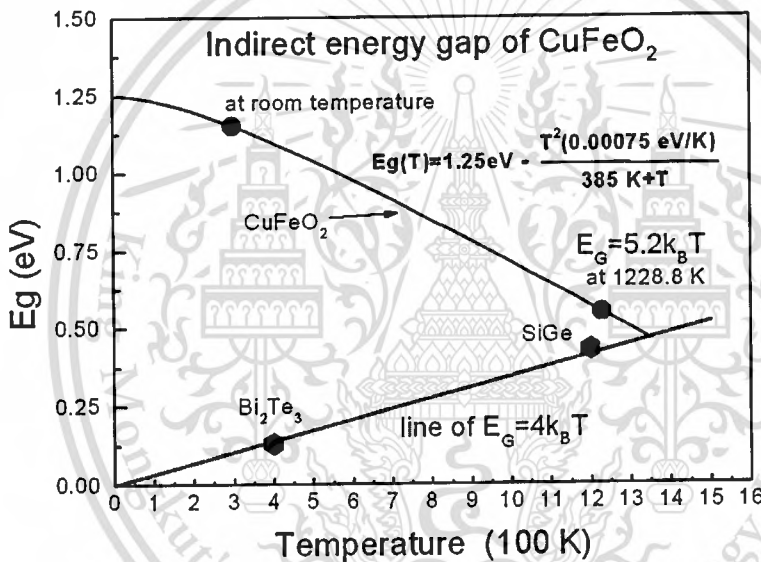


Figure 4.17 The relation curve of energy gap and temperature.

For high ZT value, Schwartz et. al. [31] has suggested that the range of T_h is used in the relation:

$$T_h = 0.9T_m \quad (4.20),$$

where T_h is the operation temperature.

T_m is the melting point of materials.

For the CuFeO_2 sample, the melting point (T_m) is 1365 K. Also, the T_h value of the the CuFeO_2 sample in the optimum indirect energy gap (E_G) is 1228.5 K. **Figure 4.17** shows the relation of the temperature dependence of indirect energy gap (E_g). The results shows that the E_G of the CuFeO_2 delafossite at $0.9T_m$ ($T_h = 1228.5$ K) is 0.55 eV. Also, the constant for the optimum E_G is $5.2k_B T$ at $T=T_h$ which stays above the constant line of $4k_B T$ as shown in **Figure 4.17**. This result implies that the optimum E_G constant of the CuFeO_2 delafossite is closely to $4k_B T_h$ at the high temperature. For the constant of $E_G = 4k_B T_h$ of the CuFeO_2 sample at $0.9T_m$, the E_g must has 0.42 eV. This result implies that the CuFeO_2 delafossite can improve to the high performance of the thermoelectric material by reducing the energy gap to constant of $4k_B T$. In conclusion, the optimum band-gap (E_G) for good thermoelectric materials of the CuFeO_2 delafossite occurs in the high temperature near the melting point.

4.1.4 SUMMARIES

The CuFeO_2 sample was synthesized by conventional solid state reaction method for investigation of the thermoelectric properties in high temperature with compared results to the well-known materials of the Bi_2Te_3 and the $\text{Na}_{0.5}\text{CoO}_2$ compounds.

The results show that the CuFeO_2 sample displays in p-type thermoelectric materials. The Seebeck coefficient displays in the range from 261 to 300 $\mu\text{V/K}$ with the temperature ranging from ambient to 960K. The maximum Seebeck value is 300 at 960 K corresponding to the Hiekes formula as 321.90 $\mu\text{V/K}$ which is maximum limit of Seebeck value in high temperature. The results of electrical conductivity increasing from 3 to 13 S/cm while, the results of thermal conductivity decrease from 5.8 to 3.5 W/m-K, with increasing temperature from ambient to 960K. The maximum value of the ZT are 2.96×10^{-2} at 960 K. In comparing results, the Seebeck value of the CuFeO_2 sample is higher than that value of the Bi_2Te_3 and $\text{Na}_{0.5}\text{CoO}_2$, whereas, the value of electrical conductivity is lower than that value of the Bi_2Te_3 and $\text{Na}_{0.5}\text{CoO}_2$. Clearly, the ZT value is lower than that value of the Bi_2Te_3 and $\text{Na}_{0.5}\text{CoO}_2$.

The activation energy of conductor, of production of free carriers, and of carrier mobility are 49, 27 and 22 meV, respectively. The optical band gap property at the room temperature is 1.15 eV for the indirect energy and is 3.45 eV for direct energy. The constant value of energy gap relating to operation temperature is $5.2k_B T$ at the temperature in 90% of melting point that is above the guide line direction of $E_G = 4k_B T_h$.

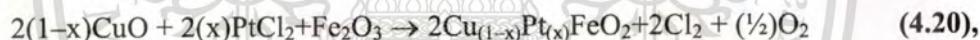
4.2 THERMOELECTRIC PROPERTIES AT HIGH TEMPERATURE OF $\text{Cu}_{1-x}\text{Pt}_x\text{FeO}_2$

4.2.1 INTRODUCTION

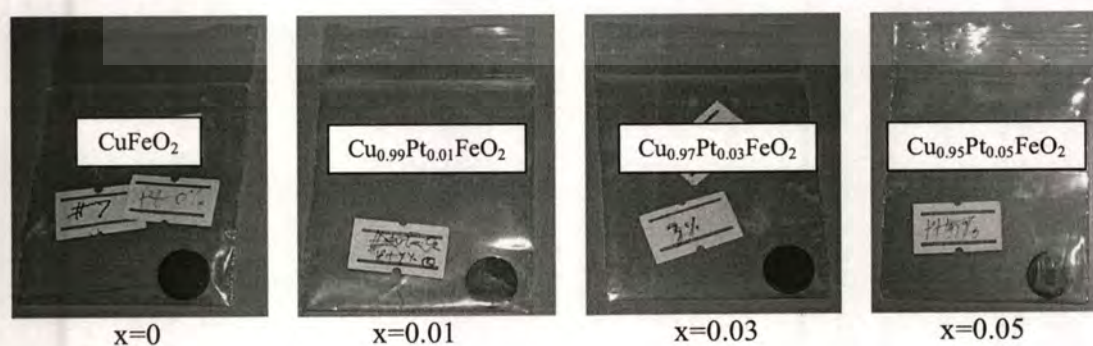
This section deals with the investigation of the thermoelectric properties of Pt-substituted into the CuFeO_2 delafossite. The Pt^{1+} cations are substituted into the Cu^{1+} sites of the CuFeO_2 compound. The Pt-substituted samples, which are mixed from the PtCl_2 compound, were synthesized in content of $x = 0.01, 0.03,$ and 0.05 as chemical formula of $\text{Cu}_{1-x}\text{Pt}_x\text{FeO}_2$, and their thermoelectric properties were compared to properties of the CuFeO_2 sample-based. In addition, the optical properties were measured at the room temperature. Finally, the optimum thermoelectric values of the $\text{Cu}_{1-x}\text{Pt}_x\text{FeO}_2$ samples were discussed in the relation of melting point to optical energy gap as constant of $E_G = 4k_B T$.

4.2.2 EXPERIMENTAL PROCEDURE

Bulk specimens of polycrystalline $\text{Cu}_{1-x}\text{Pt}_x\text{FeO}_2$ were synthesized by a conventional direct solid-state reaction according to the following equation:



where $x = 0, 0.01, 0.03,$ and 0.05 . The specimens were sintered in furnace at $1050\text{ }^\circ\text{C}$ in air atmospheres for 15 - 25 h. The sinter samples of $\text{Cu}_{1-x}\text{Pt}_x\text{FeO}_2$ are in black color as shown in **Figure 4.18**.



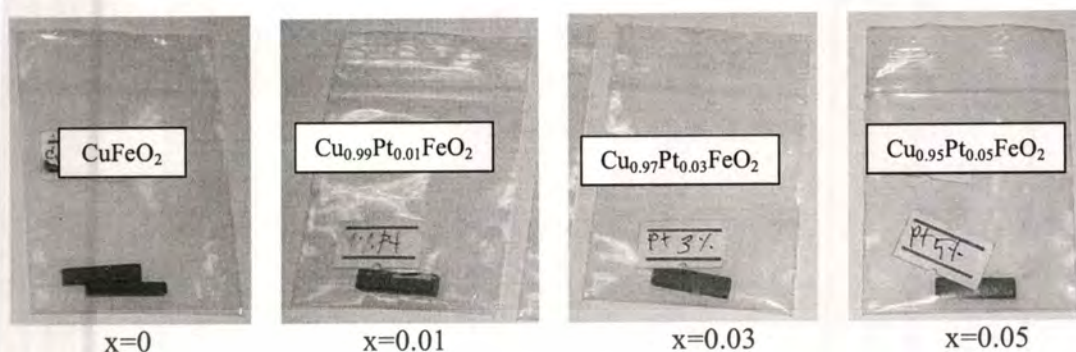


Figure 4.18 The pellet and bar of the $\text{Cu}_{1-x}\text{Pt}_x\text{FeO}_2$ samples.

4.2.3 RESULTS AND DISCUSSION

4.2.3.1 X-RAY DIFFRACTION

The XRD patterns of the CuFeO_2 sample-based and the $\text{Cu}_{1-x}\text{Pt}_x\text{FeO}_2$ sample in content of the $x = 0.01, 0.03$ and 0.05 are demonstrated in **Figure 4.19**. The XRD peaks of the CuFeO_2 sample-based exhibit crystal phase of delafossite-type structure for space group: $R\bar{3}m$ corresponding to the standard ICSD: 01-075-2146 file [46] and an impurity phase of the CuO related to the standard ICSD: 01-089-5897 file [46]. The others, the XRD patterns of the $\text{Cu}_{1-x}\text{Pt}_x\text{FeO}_2$ samples in content of $x = 0.01, 0.03$ and 0.05 display all peaks relating to the peak of the CuFeO_2 sample-based.

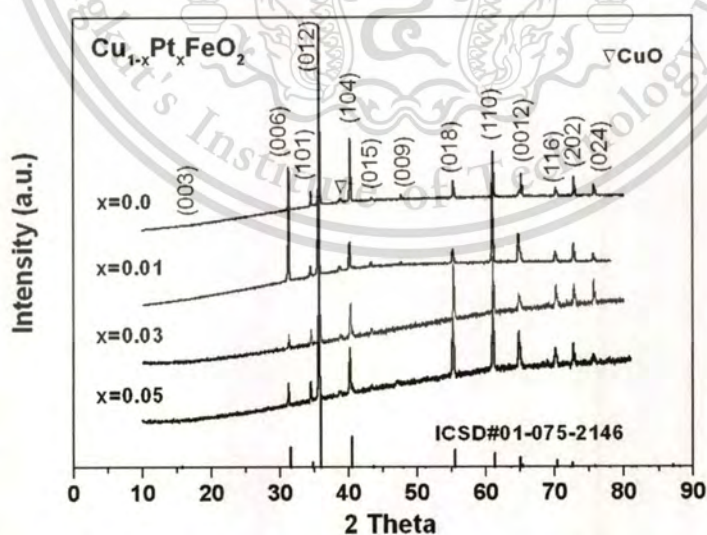


Figure 4.19 The XRD patterns of the CuFeO_2 and the $\text{Cu}_{1-x}\text{Pt}_x\text{FeO}_2$ samples with Pt content of the $x = 0.01, 0.03$ and 0.05 .

The lattice spacing parameter of the CuFeO_2 sample and the $\text{Cu}_{1-x}\text{Pt}_x\text{FeO}_2$ samples of the $x = 0.01, 0.03$ and 0.05 are shown in **Figure 4.20**. The lattice constant of the $\text{Cu}_{1-x}\text{Pt}_x\text{FeO}_2$ samples is depended on the Pt in content of the x . The lattice constant of the CuFeO_2 sample of the a -axis and the c -axis are 3.0334 \AA and 17.1598 \AA , respectively. In addition, the $\text{Cu}_{1-x}\text{Pt}_x\text{FeO}_2$ samples, the c -axis rapidly increase with increasing the Pt content of the x , while the a -axis length still remains unchanged with increasing the x content. The effect of the c -axis increases with Pt content of the x due to partial substitution of the large ion Pt^{1+} (0.60 \AA) [58] into the Cu^{1+} (0.46 \AA) [63] site.

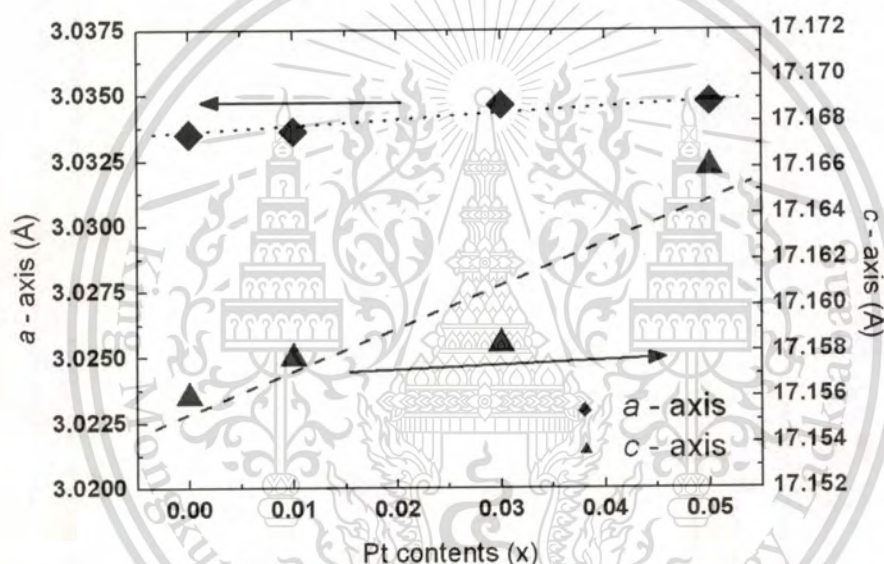


Figure 4.20 The lattice parameters as a function of the Pt concentration in x content of the $\text{Cu}_{1-x}\text{Pt}_x\text{FeO}_2$ ($x=0, 0.01, 0.03$ and 0.05) samples.

4.2.3.2 DENSITY

The bulk densities of the CuFeO_2 sample is 5.22 g/cm^3 , and the $\text{Cu}_{1-x}\text{Pt}_x\text{FeO}_2$ samples in content of the $x = 0.01, 0.03$ and 0.05 are $5.21, 5.20$ and 5.19 g/cm^3 , respectively. The theoretical density of the samples is obtained from equation 4.2. The percentage ratios of bulk density to theoretical density of the CuFeO_2 sample are 96.84% , and of the $\text{CuFe}_{1-x}\text{Sn}_x\text{O}_2$ samples are 95.94% , 94.20% and 91.97% for the content of the $x = 0.01, 0.03$ and 0.05 , respectively. These results implied that the prepared samples have density closely to the theory density.

4.2.3.3 SCANNING ELECTRON MICROSCOPE

The morphology of the microstructure of the CuFeO_2 sample and the $\text{Cu}_{1-x}\text{Pt}_x\text{FeO}_2$ samples in the content of the $x = 0.01, 0.03$ and 0.05 as shown in **Figure 4.21**. The microstructure of all samples shows the giant crystal grand size ($> 6 \mu\text{m}$) indicating the complete reaction in sintering process.

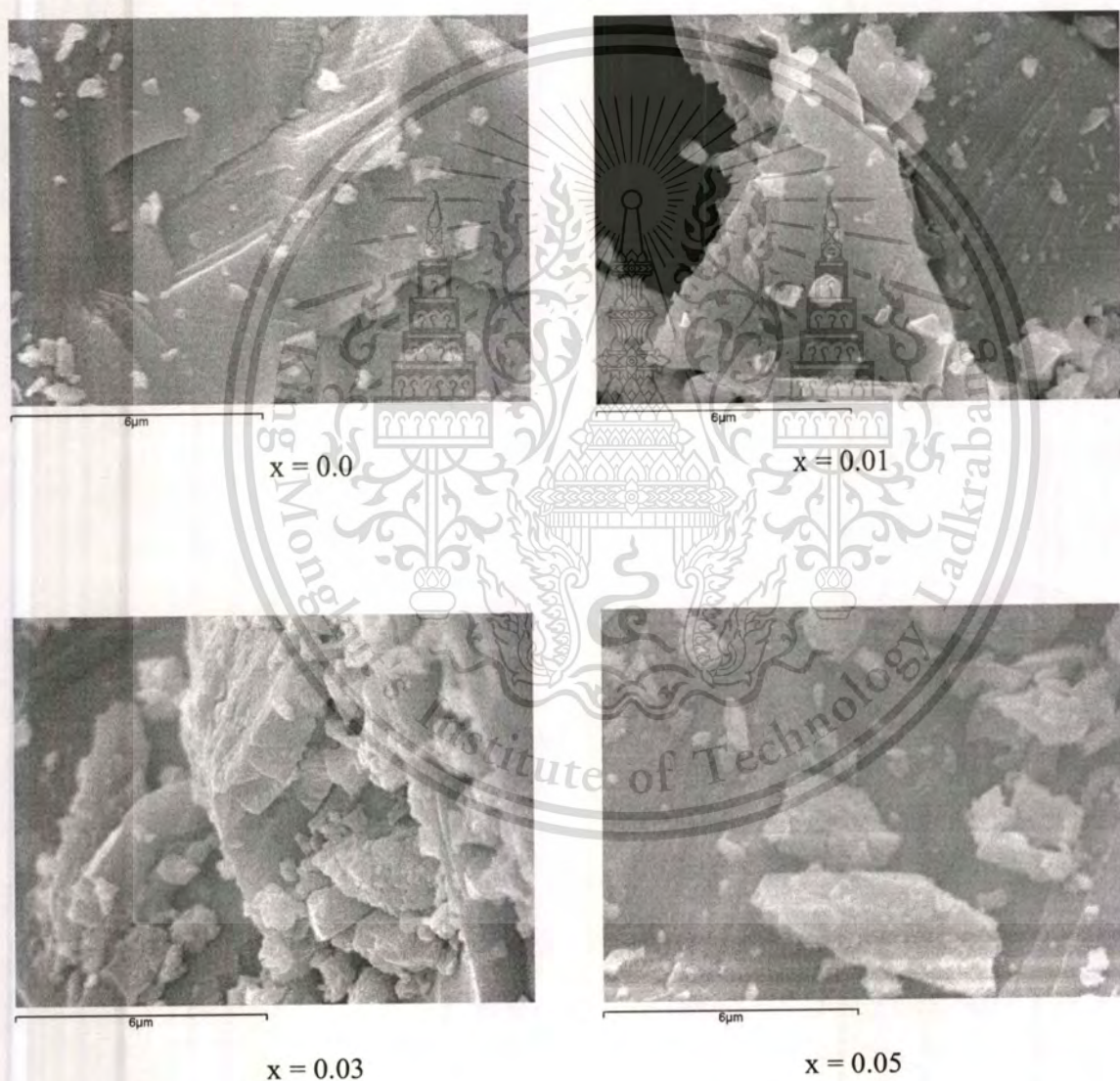


Figure 4.21 The microstructure on cutting surface of the $\text{Cu}_{1-x}\text{Pt}_x\text{FeO}_2$ samples.

4.2.3.4 SEEBECK COEFFICIENT

Figure 4.22 shows Seebeck coefficient (S) of the CuFeO_2 sample and the $\text{Cu}_{1-x}\text{Pt}_x\text{FeO}_2$ (x 0.01, 0.03 and 0.05) samples as a function of temperature in the range of temperature from 300 to 960 K. The results show that the Seebeck coefficients are positive sign over the measured temperature range for all samples, and remain positive upon substitution. These results indicate that the $\text{Cu}_{1-x}\text{Pt}_x\text{FeO}_2$ samples as the Pt^{1+} ions substituted into the Cu^{1+} sites with show p-type conductor of the thermoelectric materials. In addition, the Seebeck coefficient of the $\text{Cu}_{1-x}\text{Pt}_x\text{FeO}_2$ samples tends to increase with increasing temperature. However, the results of Seebeck coefficient minimal decrease as a result of increased the Pt content of the x . The Seebeck coefficients at room temperature are 261, 249, 242 and 240 $\mu\text{V/K}$ for the content of the $x = 0, 0.01, 0.03$ and 0.05 , respectively. The average value of the Seebeck coefficient of all samples increases from 250 to 290 $\mu\text{V/K}$ with increasing the temperature. The maximum value of the S value at 960 K is 290 $\mu\text{V/K}$. This operating point is suitable for using at high temperature for thermoelectric devices. The above results can be concluded that the Seebeck coefficient of the $\text{Cu}_{1-x}\text{Pt}_x\text{FeO}_2$ samples, which are the Pt^{1+} ions substituted into the Cu^{1+} sites, depends on temperature and minimal changes with the Pt substitution of the x content into the Cu site.

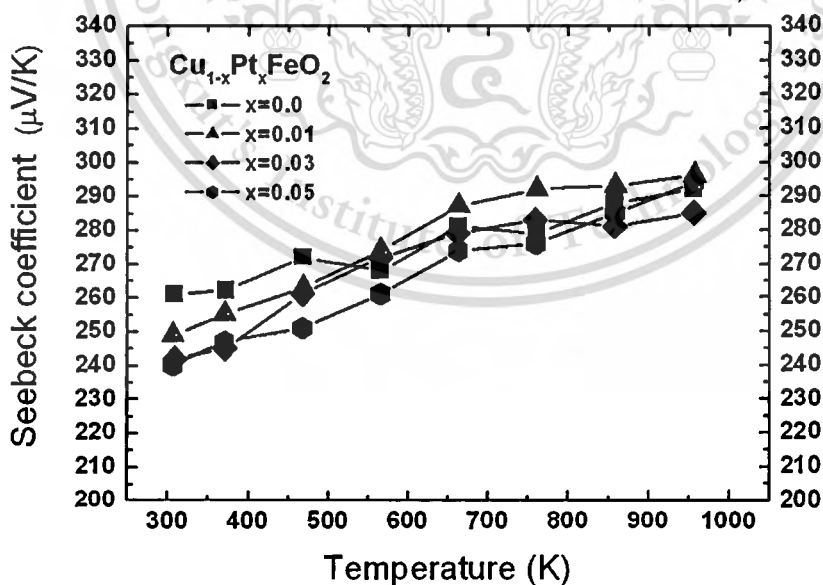


Figure 4.22 The Seebeck coefficient of the CuFeO_2 and the $\text{Cu}_{1-x}\text{Pt}_x\text{FeO}_2$ ($x = 0.01, 0.03$, and 0.05) samples vs. the temperature.

According to the results in **Figure 4.22**, the minimum Seebeck coefficient of the $\text{Cu}_{1-x}\text{Pt}_x\text{FeO}_2$ sample at room temperature is $240 \mu\text{V/K}$ in the content of the $x = 0.05$ which approximately reduce 8% from the CuFeO_2 sample-based as in $261 \mu\text{V/K}$. The height value of Seebeck coefficient reducing of the $\text{Cu}_{1-x}\text{Pt}_x\text{FeO}_2$ samples as in 8% is less than the reducing value of the $\text{CuFe}_{1-x}\text{Ni}_x\text{O}_2$ as in 26% [59] and the $\text{CuFe}_{1-x}\text{Zn}_x\text{O}_2$ as in 43% [60], at room temperature. These results imply that the Pt^{1+} substitution into the Cu^{+1} site of the CuFeO_2 delafossite is weakly influence in Seebeck value than the doped impurity of the trivalent into the Fe^{3+} site of CuFeO_2 compound.

4.2.3.5 THE HEIKES FORMULA

The Heikes formula[34, 35] as applying to localized carries, the Seebeck coefficient (S) in high temperature is expressed in relation:

$$S = -\frac{k_B}{q} \ln \left[\frac{c}{(1-c)} \right] \quad (4.21),$$

where c is the carrier concentrations.

The S value is obtained in $S = -86.17(\ln[c/(1-c)])$ by using the $c = 0.01, 0.03,$ and 0.05 for content of the $x = 0.01, 0.03,$ and $0.05,$ respectively. Also, the results of S value are obtained $395.96, 299.53,$ and $253.72 \mu\text{V/K}$ for the $x = 0.01, 0.03,$ and $0.05,$ respectively. For the CuFeO_2 , the S value is $321.90 \mu\text{V/K}$ that is displayed in the section 4.1.3.6. All results indicate that the limit of calculating the S value for the $\text{Cu}_{1-x}\text{Pt}_x\text{FeO}_2$ delafossite in high temperature is good agreement with the experimental results.

4.2.3.6 ELECTRICAL CONDUCTIVITY

The electrical conductivity (σ) of the CuFeO_2 sample and of the $\text{Cu}_{1-x}\text{Pt}_x\text{FeO}_2$ samples as a function in the range the temperature from 300 to 960 K is shown in **Figure 4.23**. The results show that the electrical conductivity of all samples is rapidly raised with increasing the temperature and the x content of the Pt substitution. The values of σ at room temperature, the CuFeO_2 sample-based is 3.5S/cm , and the $\text{Cu}_{1-x}\text{Pt}_x\text{FeO}_2$ samples for content of the $x = 0.01, 0.03$

and 0.05 are 3.5, 5.0, 8.0 and 11.0 S/cm, respectively. For the high temperature at 960 K, the σ value of the CuFeO_2 sample-based is up to 12.5 S/cm, and the $\text{Cu}_{1-x}\text{Pt}_x\text{FeO}_2$ samples are up to 16.5, 19 and 23 S/cm for the content of the $x = 0.01, 0.03$ and 0.05 respectively. These results point out that the electrical values the $\text{Cu}_{1-x}\text{Pt}_x\text{FeO}_2$ samples are larger than that value of the CuFeO_2 sample-based. For the $x = 0.05$ at room temperature, the σ value as in 11.0 S/cm is approximate four times larger than that of the CuFeO_2 sample-based as in 3.5 S/cm. The maximum of the σ value is obtained 23 S/cm for the $x = 0.05$ at temperature 960 K. This result points out that the Pt-substituted into the CuFeO_2 compound is suitable for using in the high temperature for thermoelectric devices.

In summary, the electrical conductivity of the $\text{Cu}_{1-x}\text{Pt}_x\text{FeO}_2$ samples highly increases as the Pt substitution of the x content is increased. Therefore, the electrical conductivity of the $\text{Cu}_{1-x}\text{Pt}_x\text{FeO}_2$ samples, which are the Pt^{1+} ions substituting into the Cu^{1+} sites, can be improved by the large substitution of Pt content into the CuFeO_2 compound. In addition, the electrical conductivity of the $\text{Cu}_{1-x}\text{Pt}_x\text{FeO}_2$ samples is increased as increasing of the temperature. Also, the $\text{Cu}_{1-x}\text{Pt}_x\text{FeO}_2$ samples are good conductor for using at high temperature.

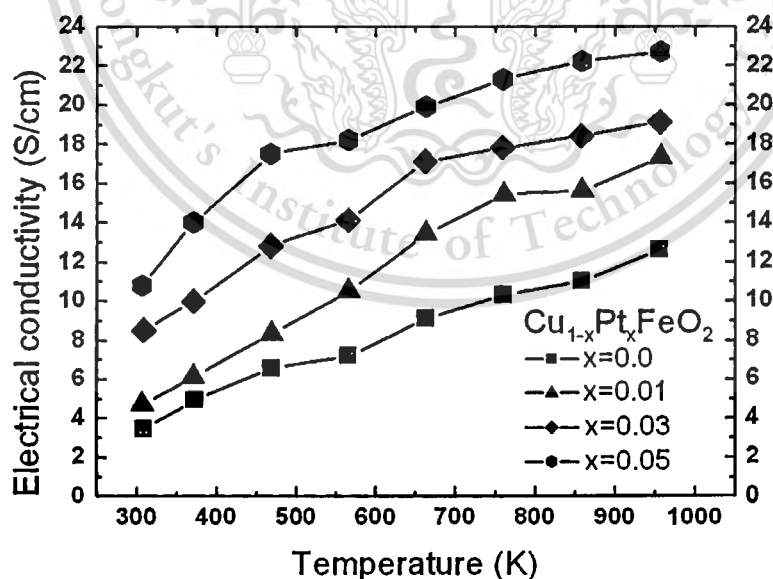


Figure 4.23 The electrical conductivity of the $\text{Cu}_{1-x}\text{Pt}_x\text{FeO}_2$ ($x=0, 0.01, 0.03,$ and 0.05) samples vs. the temperature.

According to the **Figure 4.23**, the maximum value of the conductivity at room temperature is 11 S/cm for the $x = 0.05$ as approximately 4 times higher than the CuFeO_2 sample-based as in 3 S/cm. The highest of conductivity as in 11 S/cm for the $\text{Cu}_{1-x}\text{Pt}_x\text{FeO}_2$ of the $x = 0.05$ samples at 300K is clearly higher than the high value from the most of delafossite compounds such as $\text{Cu}_{1-x}\text{Ag}_x\text{RhO}_2$ (5 S/cm) [61] and $\text{Cu}_{1-x}\text{Ag}_x\text{AlO}_2$ (2 S/cm) [62], $\text{CuFe}_{1-x}\text{Ni}_x\text{O}_2$ (8 S/cm) [59]. These results imply that the Pt^{1+} substitution into the Cu^{+1} site of the CuFeO_2 delafossite has higher sensitively effect in electrical conduction than the Ag substitution in the Cu side and the doped impurity of the trivalent (such as Ni^{3+} , Mn^{3+} , Co^{3+}) into the Fe^{3+} site.

The difference value of the electrical conductivity of the CuFeO_2 samples between before and after substitution the Pt substitution imply that the difference transport mechanisms in the CuFeO_2 sample-base and the $\text{Cu}_{1-x}\text{Pt}_x\text{FeO}_2$ ($x = 0.01, 0.03$ and 0.05) samples as effecting from the Pt substitution into the Cu-site. The p-type (hole) conductivity of the CuFeO_2 sample is dominated by the d-orbital of holes in the Cu^+ ($3d^{10}$) with charge compensation of the Cu^{2+} ($3d^9$). For the $\text{Cu}_{1-x}\text{Pt}_x\text{FeO}_2$ samples, the number of hole carriers is increased and easy ionized from the d-orbital of the $\text{Pt}^+(5d^9)$ cations. In conclusion, the increasing of electrical conductivity of the Pt substitution in CuFeO_2 delafossite is enhanced by increasing of hole carriers introduce into the the Cu-sites effected from the Pt substitution at near the edge of the valence band.

Figure 4.24 shows the results of the activation energy (E_σ) reduced with increasing the Pt substitution of the x content. These results exhibit that the E_σ value tends to fall to zero in heavily substitution for level content around $x = 0.15$, over which metallic conduction is occurred.

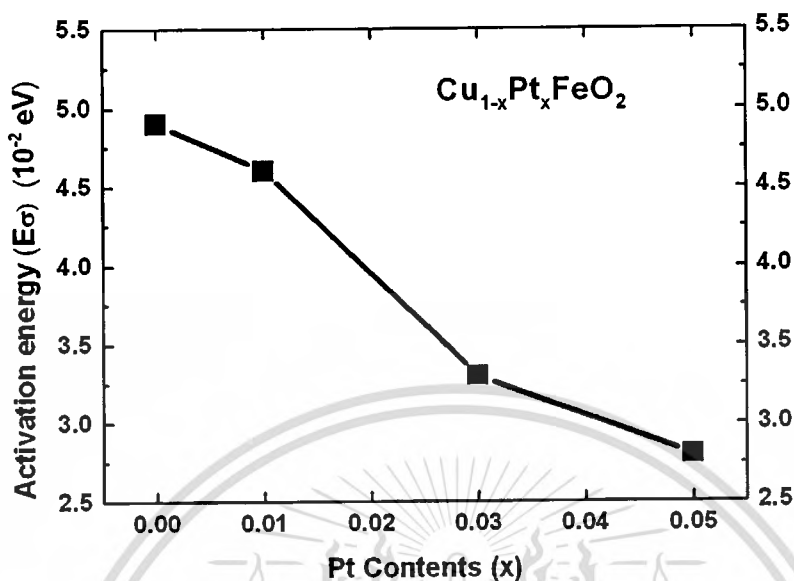


Figure 4.24 The activation energy (E_{σ}) as a function of the Pt substitution in x content.

Figure 4.25 shows the plot of the Mott's model[35] for the $\text{Cu}_{1-x}\text{Pt}_x\text{FeO}_2$ ($x = 0.01, 0.03$ and 0.05) samples with fitting temperature dependent on the equation:

$$\sigma = B \exp \left[- \left(\frac{T_0}{T} \right)^{1/4} \right] \quad (4.22),$$

where B and T_0 are constants.

The zero slope of the Mott equation implied the temperature independent of conduction which is metallic behavior. The plotted results of the $\log \sigma$ vs. $1/T^{1/4}$ in **Figure 4.8** display that the $x = 0.05$ is closely to zero slope. This confirmed that the $\text{Cu}_{1-x}\text{Pt}_x\text{FeO}_2$ sample of the content of the $x = 0.05$ is good semiconductor. In addition, the linear slope of the $\log \sigma$ vs. $1/T^{1/4}$ in **Figure 4.8** suggests that a variable-range-hopping mechanism is reasonable for all samples of the $\text{Cu}_{1-x}\text{Pt}_x\text{FeO}_2$ sample.

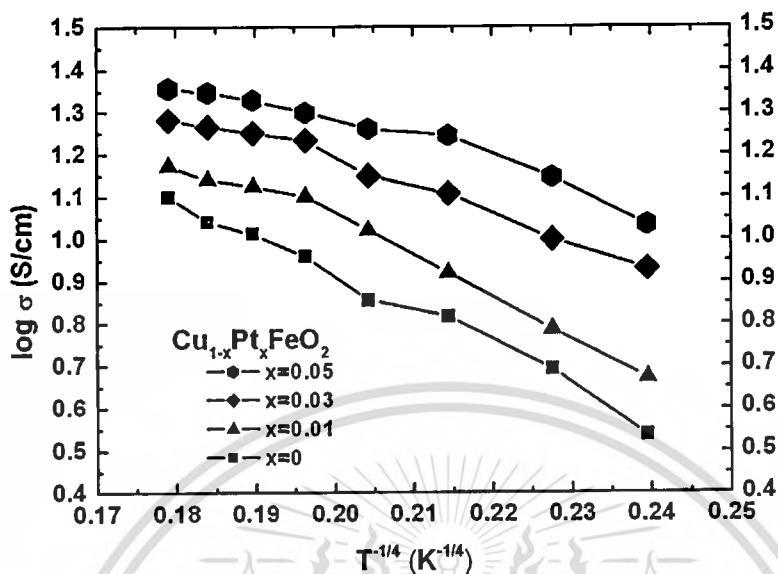


Figure 4.25 The $\log \sigma$ vs. $1/T^{1/4}$ curves.

4.2.3.7 POWER FACTOR

The power factor ($PF = \sigma S^2$) of the CuFeO_2 sample and the $\text{Cu}_{1-x}\text{Pt}_x\text{FeO}_2$ samples in content of the of the $x=0.01$, 0.03 and 0.05 calculated from the measured electrical conductivity and the Seebeck coefficient as a function of the temperature in the range of temperature from 300 to 960 K as shown in Figure 4.26. The power factor for all samples is increased with increasing temperature. The power factors at room temperature of the CuFeO_2 sample-based is estimated to be 0.2×10^{-4} W/mK^2 , and the $\text{Cu}_{1-x}\text{Pt}_x\text{FeO}_2$ samples are estimated to be 0.3×10^{-4} , 0.5×10^{-4} and 0.7×10^{-4} W/mK^2 in the content of the $x = 0.01$, 0.03 and 0.05 respectively. The high of power factors at 960 K of the CuFeO_2 sample-based is 1.1×10^{-4} W/mK^2 , and the $\text{Cu}_{1-x}\text{Pt}_x\text{FeO}_2$ samples are 1.5×10^{-4} , 1.7×10^{-4} and 2.0×10^{-4} W/mK^2 for the content of the $x = 0.01$, 0.03 and 0.05 , respectively. The maximum value of the power factor at room temperature is 0.7×10^{-4} W/mK^2 at the content of the $x = 0.05$.

The $\text{Cu}_{1-x}\text{Pt}_x\text{FeO}_2$ sample for the content of the Pt substitution of the $x = 0.05$ shows the high value of power factor by reaching 2.0×10^{-4} W/mK^2 at temperature 960 K. The PF value for the sample of the content of the $x = 0.05$ at 960 K displays 2 times and 3 times higher than that value of the CuFeO_2 sample-based at 960 k and at 300 K, respectively.

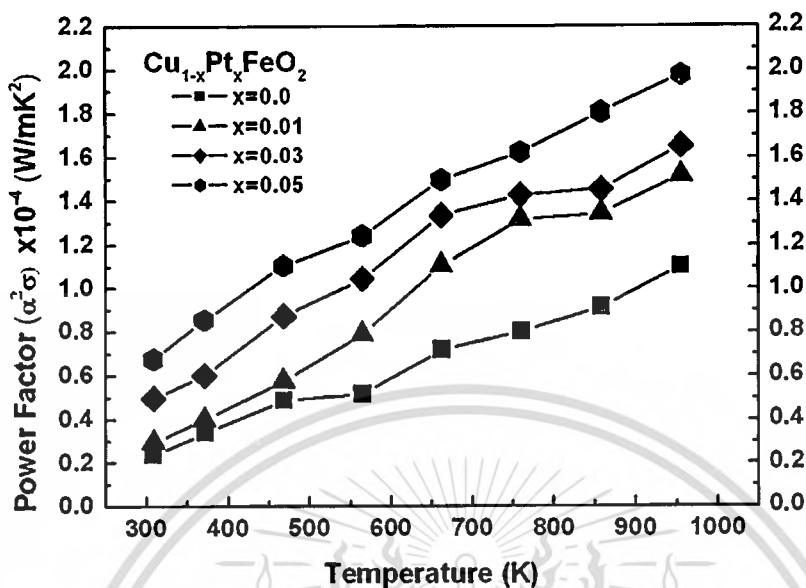


Figure 4.26 The power factor of the $\text{Cu}_{1-x}\text{Pt}_x\text{FeO}_2$ ($x = 0, 0.01, 0.03$ and 0.05) samples vs. the temperature.

Moreover, the high of the *PF* value of the $\text{Cu}_{1-x}\text{Pt}_x\text{FeO}_2$ sample in the content of the $x = 0.05$ at 960 K is higher than those reported for the CuFeO_2 as in $\text{PF} = 1.4 \times 10^{-4} \text{ W/mK}^2$ [60], $\text{CuFe}_{1-x}\text{Ni}_x\text{O}_2$ as in $\text{PF} = 1.8 \times 10^{-4} \text{ W/mK}^2$ [59], $\text{CuAl}_{1-x}\text{Fe}_x\text{O}_2$ as in $\text{PF} = 0.9 \times 10^{-4} \text{ W/mK}^2$ [63], respectively, at 960 K.

In summary, the Power Factor of the $\text{Cu}_{1-x}\text{Pt}_x\text{FeO}_2$ samples, which are the Pt^{1+} ions substituting into the Cu^{1+} sites into the CuFeO_2 compound, is enhanced by the increasing the content of the Pt substitution.

4.2.3.8 THERMAL CONDUCTIVITY

The temperature dependence of the thermal conductivity (κ) for the $\text{Cu}_{1-x}\text{Pt}_x\text{FeO}_2$ ($x = 0.01, 0.03$ and 0.05) samples as a function of temperature in the range of temperature from 300 to 960 K is shown in **Figure 4.27**. The thermal conductivity is measured by using a laser flash method with the relation $\kappa = dC_p a$, where d , C_p and a are the bulk density of sample, specific heat and thermal diffusivity respectively. The bulk density of the CuFeO_2 sample is 5.22 g/cm^3 , and the $\text{Cu}_{1-x}\text{Pt}_x\text{FeO}_2$ samples for the content of the $x = 0.01, 0.03$ and 0.05 are $5.21, 5.20$ and 5.19 , respectively. The ratios of bulk density to theoretically density of the CuFeO_2 sample are

96.84%, and of the $\text{Cu}_{1-x}\text{Pt}_x\text{FeO}_2$ samples are 95.94%, 94.20% and 91.97%, for the content of the $x = 0.01, 0.03$ and 0.05 , respectively.

The results of thermal conductivity of all samples are decreased as a result of increased the temperature as shown in **Figure 4.27**. The κ values of the $\text{Cu}_{1-x}\text{Pt}_x\text{FeO}_2$ samples lead to minimal increased with increasing the Pt substitution of the x content. The κ values of the CuFeO_2 sample-based are in the range from 5.8 to 3.5 W/mK with a region of temperature 300 to 960 K respectively. For the sample of the content of the $x = 0.05$, the κ values are slightly higher about 1.1 time than the CuFeO_2 sample-based. The minimum of the κ value of the CuFeO_2 sample-based is 3.5 W/mK at high temperature 960 K. The yield of thermal conductivity exhibits that the $\text{Cu}_{1-x}\text{Pt}_x\text{FeO}_2$ (0.01, 0.03 and 0.05) samples are decreased as the increasing temperature. Therefore, the high value of the Z and the ZT of the $\text{Cu}_{1-x}\text{Pt}_x\text{FeO}_2$ samples are dominant to occur at high temperature because the κ value is still contained the minimum value.

In summary, the thermal conductivity of the $\text{Cu}_{1-x}\text{Pt}_x\text{FeO}_2$ samples, which are the Pt^{1+} ions substituted into the Cu^{1+} sites, show the value closely to the CuFeO_2 sample-based. This result can be concluded that the Pt^{1+} substitution into the Cu^{1+} site of the CuFeO_2 delafossite is weakly effect to change the thermal conductivity

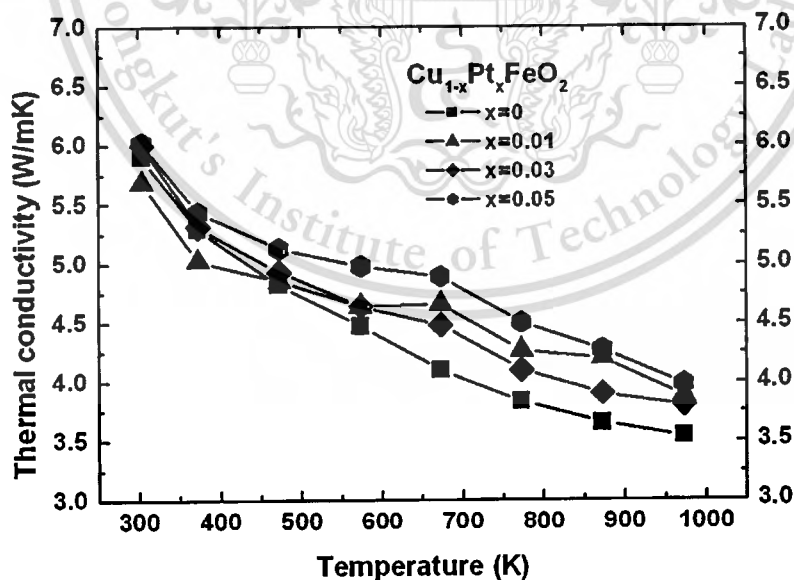


Figure 4.27 The thermal conductivity of the $\text{Cu}_{1-x}\text{Pt}_x\text{FeO}_2$ ($x = 0, 0.01, 0.03$ and 0.05) samples vs. the temperature.

The total thermal conductivity (κ) consists of the two components of the lattice (phonon) component (κ_l) and electronic (hole) component (κ_e). From the Wiedmann-Franz law [7, 33], the κ_e is related by $\kappa_e = L_o T \sigma$ where L_o is the Lorenz factor ($2.45 \times 10^{-8} \text{ W}\Omega/\text{K}^2$), T is the absolute temperature, σ is the electrical conductivity. From the highest σ value of the $\text{Cu}_{1-x}\text{Pt}_x\text{FeO}_2$ samples as 23 S/cm of the $x = 0.05$ at 960 K, the κ_e value is obtained $5.409 \times 10^{-2} \text{ W/mK}$ which is 1.545 % of the total κ value. This result indicates that the major effect of thermal conductivity for the CuFeO_2 sample is dominated by the phonon mechanism part.

4.2.3.9 DIMENSIONLESS OF FIGURE OF MERIT (ZT)

The temperature dependence of the ZT value of the CuFeO_2 sample and the $\text{Cu}_{1-x}\text{Pt}_x\text{FeO}_2$ samples for the content of the $x = 0.01, 0.03$ and 0.05 in the temperature range from 300 to 960 K are exhibited in Figure 4.28. The ZT values are also calculated from the Z value and the temperature value. The results show that the ZT values of all samples are rapidly raised with increasing the temperature. In addition, the ZT values of the $\text{Cu}_{1-x}\text{Pt}_x\text{FeO}_2$ samples are increased with increasing the Pt substitution of the x content. The maximum of ZT values at temperature 960 K of the CuFeO_2 sample is 0.03, and the $\text{Cu}_{1-x}\text{Pt}_x\text{FeO}_2$ samples are 0.038, 0.044 and 0.05 for the content of the Pt substitution of the $x = 0.01, 0.03$ and 0.05 , respectively. Obviously, the sample of the content of $x = 0.05$ exhibits the high value of ZT at temperature 960 K. Moreover, the sample of the content of the $x=0.05$ has value higher than 1.5 times than that value of the CuFeO_2 sample-based at high temperature. The sample of the content of the $x= 0.03$ and $x=0.01$ has value higher than 1.4 and 1.2 times than that value of the CuFeO_2 sample-based. These results point out that the Pt^{1+} ions substitution into the Cu^{1+} sites of the CuFeO_2 sample is affected to enhance the ZT values at high temperature.

In summary, the $\text{Cu}_{1-x}\text{Pt}_x\text{FeO}_2$ compounds, which are the Pt^{1+} ions substituted into the Cu^{1+} sites into the CuFeO_2 compound, can be improved the ZT value to good thermoelectric materials in high temperature.

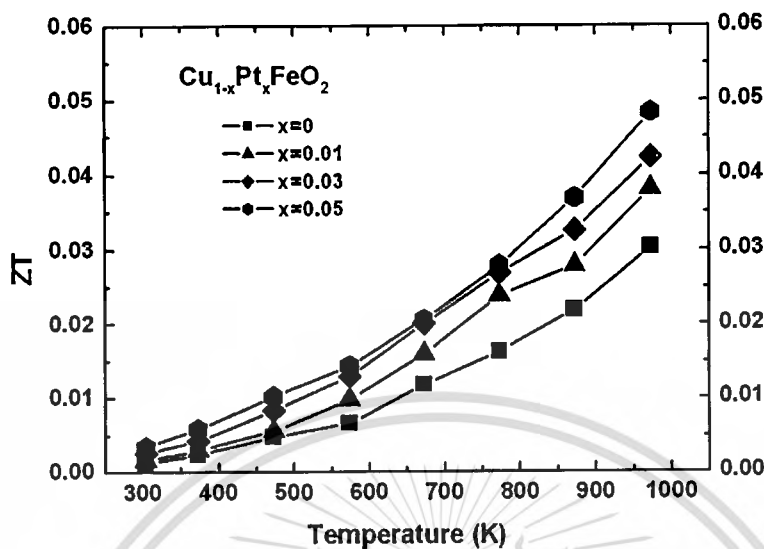


Figure 4.28 The ZT value of the $\text{Cu}_{1-x}\text{Pt}_x\text{FeO}_2$ ($x = 0.01, 0.03$ and 0.05) samples vs. the temperature.

The ZT value of the $\text{Cu}_{1-x}\text{Pt}_x\text{FeO}_2$ samples is higher than value of previous reported of the delafossite of the CuFeO_2 as in $ZT = 0.025$ [60], CuAlO_2 as in $ZT = 0.004$ [64], $\text{Cu}_{1-x}\text{Ag}_x\text{AlO}_2$ as in $ZT = 0.016$ [63], $\text{CuFe}_{1-x}\text{Ni}_x\text{O}_2$ as in $ZT = 0.045$ [62] at 960 K. At the important aim point is suitable for selected material in the application of high temperature of thermoelectric devices.

4.2.3.10 ACTIVATION ENERGY

4.2.3.10.1 ACTIVATION ENERGY OF PRODUCTION OF FREE CARRIERS (E_s)

In applying p-type semiconductor, the relation of the Seebeck coefficient is given [25, 53] by $S = (k_B/e)[(E_F - E_v)/k_B T]$, where k_B is the Boltzmann's constant, e is electronic charge constant, E_v is the energy of the valance-band edge, E_F is the Fermi energy level and T is the absolute temperature. The activation energy for the production of free carriers $E_s = (E_F - E_v)$ is obtained by plotting the S vs. $1000/T$ as shown in the **Figure 4.29**. An average of E_s value for all the $\text{Cu}_{1-x}\text{Pt}_x\text{FeO}_2$ samples is 27.5 meV. The result is slightly higher than value of the thermal energy at room temperature ($k_B T_{300K} \cong 25 \text{ meV}$). Thus, this value indicates that the $\text{Cu}_{1-x}\text{Pt}_x\text{FeO}_2$

samples is a good semiconductor material for thermoelectric because the acceptor charge carriers are ionized near the room temperature for conduction.

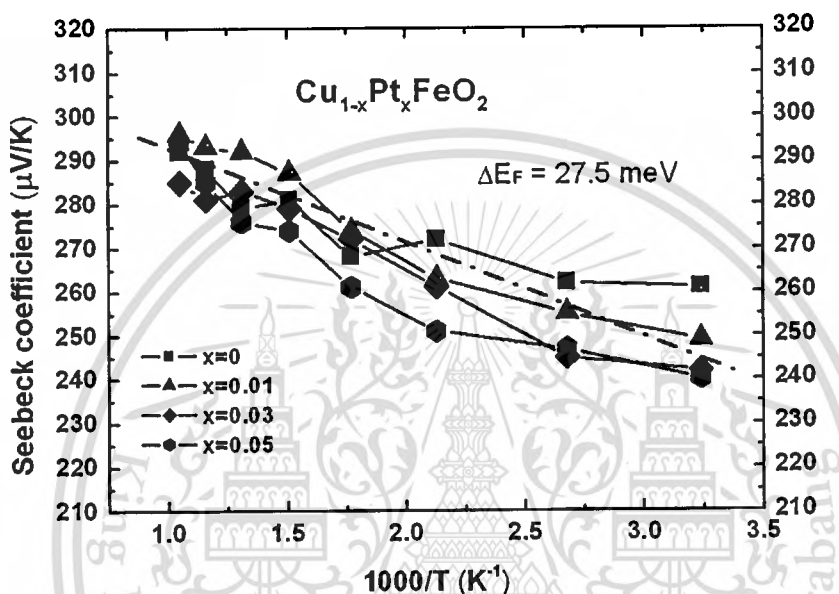


Figure 4.29 The Seebeck coefficient vs. $1000/T$ curve.

4.2.3.10.2 ACTIVATION ENERGY OF CARRIER CONDUCTION (E_a)

Figure 4.30 shows an Arrhenius plot of the $\text{Cu}_{1-x}\text{Pt}_x\text{FeO}_2$ samples plotted by the $\log \sigma$ vs. $1000/T$ with temperature. The Arrhenius plot corresponds to the temperature dependent of equation [35, 53] of $\sigma = A_o \exp(-E_a/k_B T)$. The activation energies (E_a) in the Arrhenius plot, $\log \sigma$ vs. $1000/T$ are 49, 46, 33 and 28 meV for samples of the content of the $x = 0.0, 0.01, 0.03$ and 0.05 , respectively. These results show the tendency of the activation energy (E_a) to decrease with increasing the x content which is the semiconducting of transition oxide behavior.

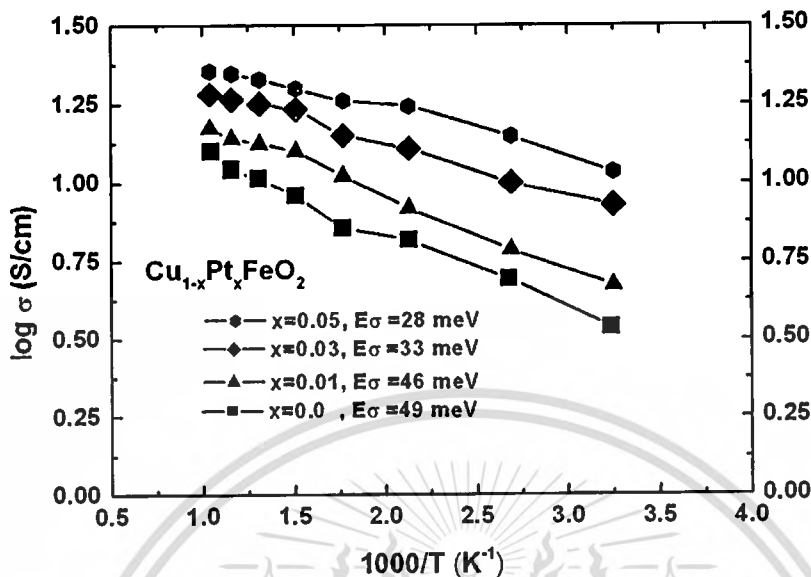


Figure 4.30 The $\log \sigma$ vs. $1000/T$ curve.

4.2.3.10.3 ACTIVATION ENERGY OF CARRIER MOBILITY (E_u)

The overall activation energy for conductor (E_σ) is a combination of two components as a relation [35, 53] of $E_\sigma = E_\mu + E_s$, where E_u is the activation energy for carrier mobility (hopping energy). The E_u is obtained by the mobility of carriers as following by a equation:

$$\mu = D \exp(-E_\mu/k_B T) \quad (4.23),$$

where μ is the mobility of carrier and D is constant.

From the average value of the E_s as in 27.5 meV and the value of the E_σ as in 49, 46, 33 and 28 meV for the content of the $x = 0.0, 0.01, 0.03$ and 0.05 respectively, of the $\text{Cu}_{1-x}\text{Pt}_x\text{FeO}_2$ samples, the value of the E_u is obtained 21.5, 18.5 5.5 and 0.5 meV for the $x = 0.0, 0.01, 0.03$ and 0.05 , respectively, which are less than the thermal energy at room temperature ($k_B T_{300\text{K}} \cong 25$ meV). The small value of the E_u implied that the temperature dependent for conductivity of the $\text{Cu}_{1-x}\text{Pt}_x\text{FeO}_2$ samples is major activating from the activation energy for carrier production and tiny activating from the mobility activation energy by a small polaron mechanism. Thus, these results confirmed that the p-type (hole) conduction of the $\text{Cu}_{1-x}\text{Pt}_x\text{FeO}_2$ delafossite is a good

semiconductor because of the ionization of free carrier occurring in thermal activation energy nearly the room temperature and the carriers moving with high mobility due to requiring the activation energy of mobility less than the thermal energy at room temperature.

4.2.3.11 UMKLAPP RELATION

For the lattice (phonon) thermal conductivity (κ_l), Umklapp scattering contribution in the phonon scattering process is expressed [31] by the relation:

$$\kappa_u = \delta[(T_m)^{3/2} M^{(-7/6)} \rho^{2/3}] T^{(-1)} \quad (4.24),$$

where κ_u is the Umklapp phonon thermal conductivity,

δ is a proportionality constant,

T_m is the melting temperature,

M is the average atomic mass,

ρ is the density,

T is operation temperature.

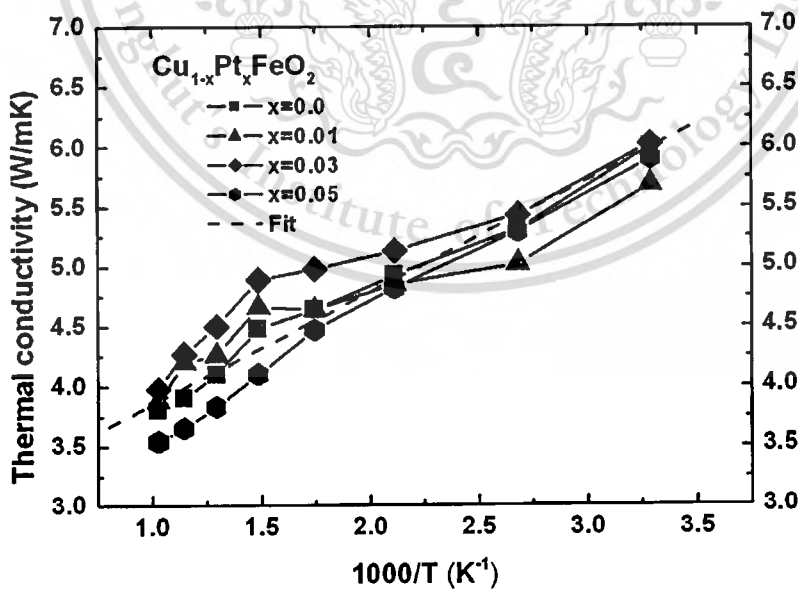


Figure 4.31 The thermal conductivity vs.1000/T curve.

The Umklapp relation implies that the κ_u value is proportion to inversion of temperature. From the **Figure 4.31**, the thermal conductivity of the $\text{Cu}_{1-x}\text{Pt}_x\text{FeO}_2$ samples can be plotted in function of inversion temperature as a relation of the κ vs. $1000/T$. The curve can show the thermal conductivity of the $\text{Cu}_{1-x}\text{Pt}_x\text{FeO}_2$ samples linearly with T^{-1} corresponding to the Umklapp relation. This result indicates that the major effect of thermal conductivity of the $\text{Cu}_{1-x}\text{Pt}_x\text{FeO}_2$ samples is controlled by phonon mechanism with contribution by the Umklapp scattering. From the Umklapp relation, the minimization of thermal conductivity for the $\text{Cu}_{1-x}\text{Pt}_x\text{FeO}_2$ samples is occurred by operating temperature in high value with nearly melting point (1365 K).

4.2.3.12 OPTICAL PROPERTIES

The measurement of absorption spectra of the $\text{Cu}_{1-x}\text{Pt}_x\text{FeO}_2$ ($x = 0.01, 0.03$ and 0.05) samples at room temperature are shown in **Figure 4.32**. The absorption coefficient (α) [55] is measured in wavelength ranging from 250 to 800 nm. The results of all samples exhibit that the heavy absorbability is in the spectrum ranging 250 to 300 nm which is region of the UV light, and the week absorbability is in the spectrum ranging 300 to 800 nm which is region of the Near IR and the visible light.

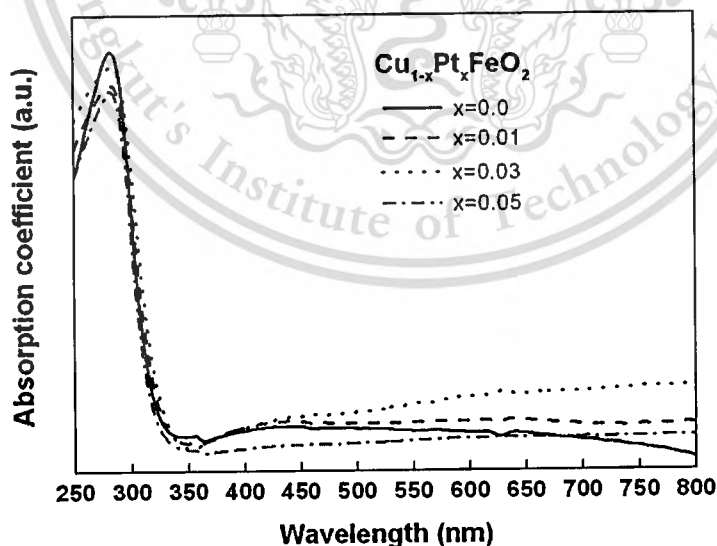


Figure 4.32 The absorption spectra of the $\text{Cu}_{1-x}\text{Pt}_x\text{FeO}_2$ ($x = 0.01, 0.03$ and 0.05) samples.

The results of absorption coefficient are used to calculate the optical energy gap according to the equation of [54] the $(\alpha h\nu)^m = A(h\nu - E_g)$, where α is the absorption coefficient, $h\nu$ is the incident photon energy, E_g is the optical band energy gap, A is the constant which does not depend on the $h\nu$. The optical energy gap is obtained from a plot of the $(\alpha h\nu)^m$ vs. $h\nu$ with taking the intercept on the energy axis[56]. The direct energy gap are indicated by $m=2$. **Figure 4.33** presents approximately 3.45 eV on the optical direct band gap of all samples at room temperature as corresponded to previous work of Benko and Koffyberg[47]. The indirect energy gap are indicated by $m=1/2$. **Figure 4.34** displays the indirect band gap $E_g = 1.15, 1.1, 1.05$ and 1.01 eV for $x = 0, 0.01, 0.03$ and 0.05 , respectively.

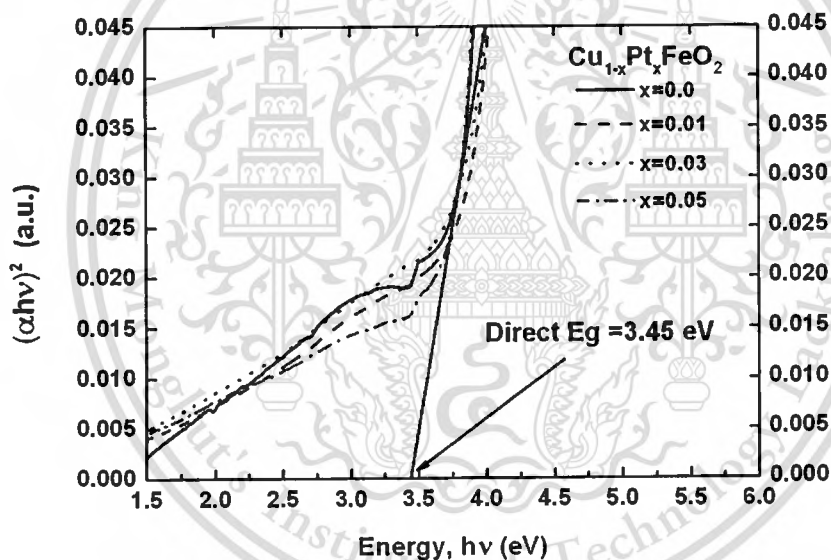


Figure 4.33 The direct optical gap of the $\text{Cu}_{1-x}\text{Pt}_x\text{FeO}_2$ ($x = 0.01, 0.03$ and 0.05) samples.

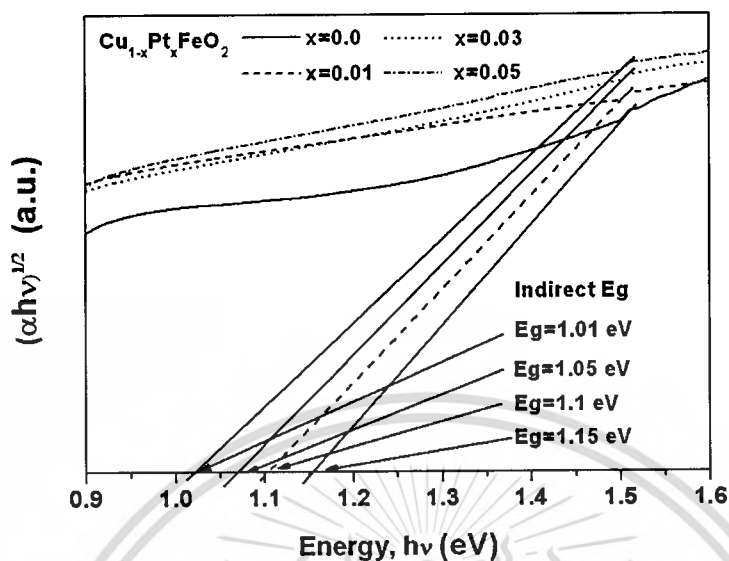


Figure 4.34 The indirect optical gap of the $\text{Cu}_{1-x}\text{Pt}_x\text{FeO}_2$ ($x = 0.01, 0.03$ and 0.05) samples.

4.2.3.13 THE RELATION OF ENERGY GAP TO TEMPERATURE

Figure 4.35 is given the approximate and experiment for the direct energy gap (E_g) of the $\text{Cu}_{1-x}\text{Pt}_x\text{FeO}_2$ samples as a function of temperature. The temperature dependence of direct band gap is calculated by an empirical formula[57] $E_g(T) = E_g(0) - [aT^2 / (b + T)]$, where $E_g(0)$ is the band gap approximated at 0 K, and a and b are the parameters. The values of a and b used for 0.00075 eV/K and 385K , respectively which estimated value from the CuAlO_2 delafossite reported by Dittrich et al.[57]. The value of the $E_g(0)$ is obtained 3.575 eV by fitting with experimental value of the direct band gap at room temperature. However, the fitting curve exhibits that the direct energy gap is decreased as a result of the increased temperature. Moreover, the fitting curve shows that the direct energy gap contains value under 3.1 eV with the range of temperature above 850K .

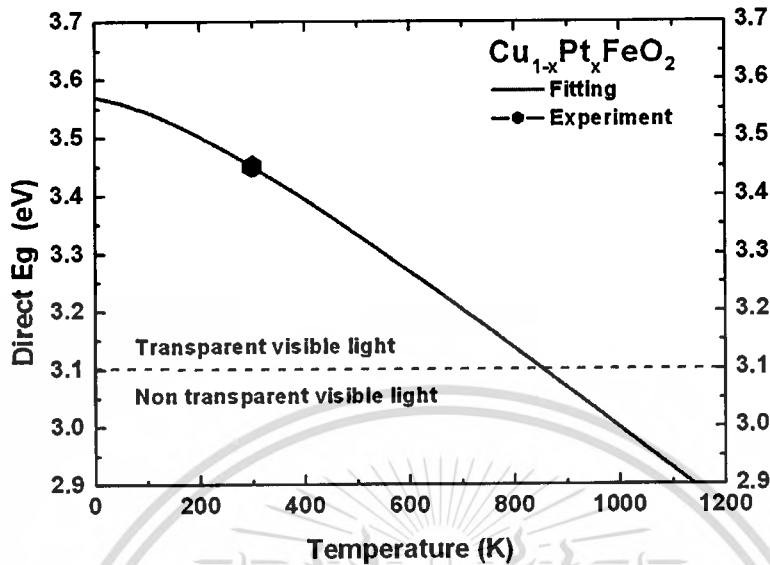


Figure 4.35 The temperature dependence of the direct band gap of the $\text{Cu}_{1-x}\text{Pt}_x\text{FeO}_2$ samples.

4.2.3.14 ENERGY DIAGRAM

The band energy level diagram of the $\text{Cu}_{1-x}\text{Pt}_x\text{FeO}_2$ delafossite at room temperature is predicted from the obtained value of activation energy, Fermi energy level and optical energy gap, as shown in **Figure 4.36**. The band energy diagram shows the direct energy gap (E_g) of the $\text{Cu}_{1-x}\text{Pt}_x\text{FeO}_2$ samples as in 3.45 eV. The Fermi's energy (E_F) level is above the valence band edge as in 0.0275 eV, and the acceptor level (E_a) is above the valence band edge in 0.049, 0.046, 0.033 and 0.028 eV for the content of the $x = 0, 0.1, 0.3,$ and 0.5 , respectively. The experiment value of the electron affinity (χ) of the CuFeO_2 is in 4.21 eV which obtained from previous work [65]. From all energy measurement results, the energy of work function (ϕ), which is in the range of Fermi level to vacuum level, of the $\text{Cu}_{1-x}\text{Pt}_x\text{FeO}_2$ samples can be calculated as shown in **Figure 4.36**.

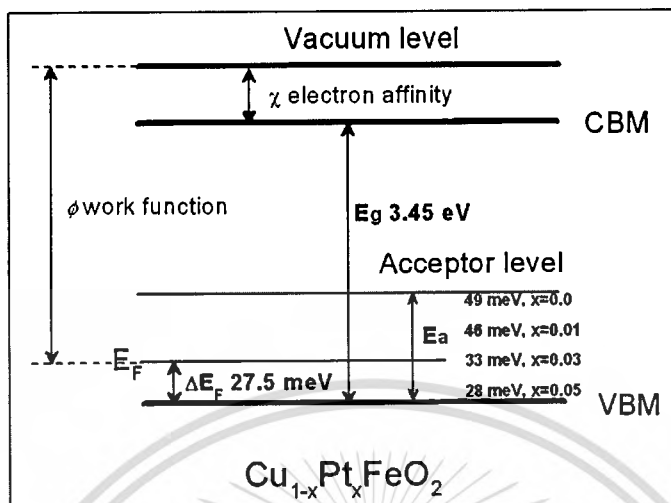


Figure 4.36 The energy level diagram of the $\text{Cu}_{1-x}\text{Pt}_x\text{FeO}_2$ delafossite (not exact to the scale).

4.2.3.15 RELATION OF MELTING POINT WITH ENERGY GAP

For application at high temperature, the relation between energy gap and melting point of temperature for optimal operating thermoelectric materials, Schwartz et. al. [31] have described in relation of $E_G = 4k_B T_h$. The optimal band gap plays important role for the best thermoelectric materials due to it can neglect the behavior in small and large band-gap. The small band-gap causes to thermally excite minority carriers to reduce the Seebeck coefficient, and causes to increase the thermal conductivity leading to low thermoelectric performance. In addition, the large band-gap causes to reduce the mobility of majority charge carriers to reduce the electrical conductivity leading to low ZT value. For high ZT value, Schwartz et. al. [31] has suggested that the range of T_h is used in $0.9T_m$; where T_m is the melting point of materials. For CuFeO_2 sample-based, the T_m value is 1365 K contributing to the T_h value containing at 1228.5 K for the optimum indirect energy gap (E_G). **Figure 4.37** shows the relation of the temperature dependence of indirect energy gap (E_g) of the $\text{Cu}_{1-x}\text{Pt}_x\text{FeO}_2$ samples. At $T_h = 1228.5$ K, the E_G of the CuFeO_2 sample-based is obtained 0.55 eV. For the $\text{Cu}_{1-x}\text{Pt}_x\text{FeO}_2$ samples with the content of the $x = 0, 0.01, 0.03$ and 0.05 , the indirect energy gap (E_g) decreases with the increasing the Pt content of the x , and the E_G value at $T_h = 1228.5$ K decreases with the increasing the Pt content of the x to the constant line of $E_G = 4k_B T_h$. This effect relates to the increasing of the ZT value in section

4.2.3.9. This result shows that the optimum the E_G constant value of the $\text{Cu}_{1-x}\text{Pt}_x\text{FeO}_2$ delafossite is closely to $4k_B T_h$ at the high temperature as affected from decreasing the indirect energy gap by the Pt-substituted into the Cu site. This result implies that the CuFeO_2 delafossite can improve to the high performance of the thermoelectric material by reducing the energy gap to constant of the $4k_B T$. In summary, the optimum band-gap (E_G) for good thermoelectric materials of the CuFeO_2 delafossite can be occurred at high temperature.

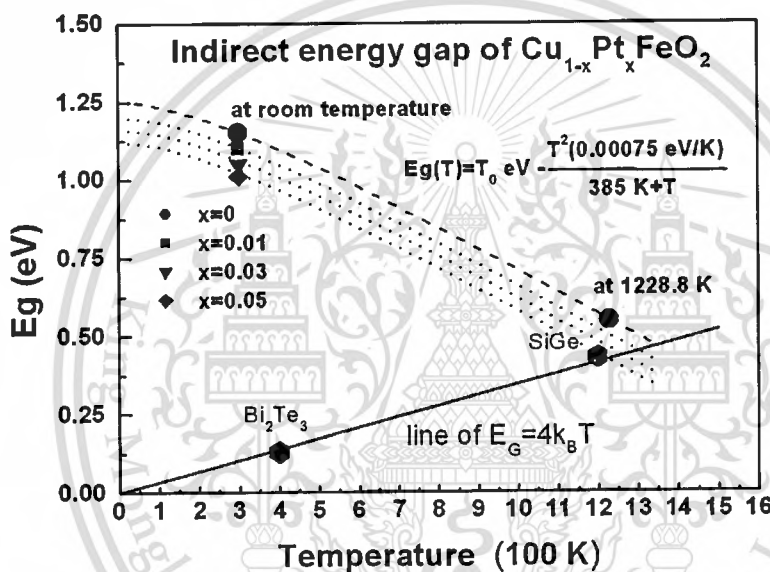


Figure 4.37 The relation curve of energy gap and temperature.

4.2.4 SUMMARIES

The thermoelectric properties (Seebeck coefficient, electrical conductivity and thermal conductivity) of the Pt substituted into the Cu site of the CuFeO_2 samples in content of the $x = 0.01, 0.03$ and 0.05 samples were measured in the high temperature ranging from 300 to 960 K. The results of the Seebeck coefficient of the $\text{Cu}_{1-x}\text{Pt}_x\text{FeO}_2$ ($x = 0.01, 0.03$ and 0.05) samples display the p-type semiconductor. The Seebeck value of the $\text{Cu}_{1-x}\text{Pt}_x\text{FeO}_2$ samples increases as temperature increasing, while mini changes as increasing the Pt substitution. The average Seebeck coefficient of all samples is $240 \mu\text{V/K}$ at room temperature and is $290 \mu\text{V/K}$ at 960 K. In

addition, electrical conductivity of the $\text{Cu}_{1-x}\text{Pt}_x\text{FeO}_2$ samples increases as increasing the Pt substitution and as increasing the temperature. The room temperature of the electrical conductivity increases from 3.5 to 11 S/cm with increased the Pt content of the x . The high electrical conductivity is 23 S/cm for the $x = 0.05$ at 960 K. The thermal conductivity of the $\text{Cu}_{1-x}\text{Pt}_x\text{FeO}_2$ samples decreases as increasing the temperature, while minimal changes with increasing the Pt substitution. Furthermore, the ZT value increases as increasing the Pt substitution and as increasing the temperature. Most interestingly, the highest ZT value of this research is 0.05 for content of the $x = 0.05$ at 960 K. The activation energy of carrier conduction, and of carrier mobility are decrease as increasing the Pt substitution, while the activation energy of production of free carriers is constant as increasing the Pt substitution. The indirect energy gap of the $\text{Cu}_{1-x}\text{Pt}_x\text{FeO}_2$ samples is decrease as increasing the Pt substitution, while the direct energy gap of the $\text{Cu}_{1-x}\text{Pt}_x\text{FeO}_2$ samples is constant with increasing the Pt substitution. Both, the direct and indirect energy gap are decrease with increasing of the temperature. At high temperature, the indirect energy gap reduces to the constant of $E_G=4k_B T$ with increasing the temperature. Indeed, this the research presents that the effect of the small Pt substitution into the CuFeO_2 delafossite can be enhanced the thermoelectric properties.

4.3 THERMOELECTRIC PROPERTIES AT HIGH TEMPERATURE OF $\text{CuFe}_{1-x}\text{Al}_x\text{O}_2$

4.3.1 INTRODUCTION

This section deals with the investigation of the thermoelectric properties of the $\text{CuFe}_{0.5}\text{Al}_{0.5}\text{O}_2$ delafossite. The $\text{CuFe}_{0.5}\text{Al}_{0.5}\text{O}_2$ and the CuAlO_2 samples were synthesized. The thermoelectric properties of the $\text{CuFe}_{0.5}\text{Al}_{0.5}\text{O}_2$ samples were compared to the properties of the CuFeO_2 sample as results of section 4.1 and the CuAlO_2 sample as in this experiment. In addition, the optical properties were measurement at room temperature. Finally, optimum thermoelectric values of the $\text{CuFe}_{1-x}\text{Al}_x\text{O}_2$ ($x=0, 0.05, \text{ and } 1$) were discussed in relation between the melting point and the optical energy gap as the constant of $E_G = 4k_B T$.

4.3.2 EXPERIMENTAL PROCEDURE

Polycrystalline samples of the CuFeO_2 , the $\text{CuFe}_{0.5}\text{Al}_{0.5}\text{O}_2$, and the CuAlO_2 were prepared by a conventional direct solid-state reaction as following equation:



where $x = 0, 0.5, \text{ and } 1$. The specimens were sintered in furnace at 1050°C in air atmospheres for 15 - 25 h. The results of the sinter samples of the CuFeO_2 , the $\text{CuFe}_{0.5}\text{Al}_{0.5}\text{O}_2$, and the CuAlO_2 are shown in **Figure 4.38**.

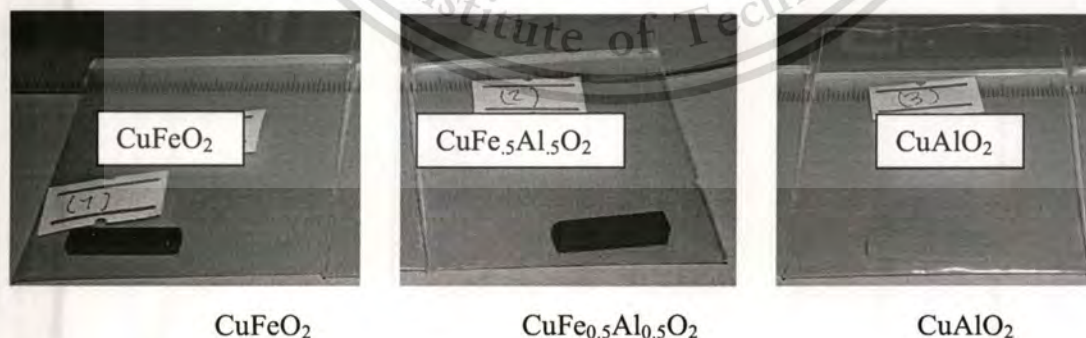


Figure 4.38 The pellet and bar samples of the CuFeO_2 , the $\text{CuFe}_{0.5}\text{Al}_{0.5}\text{O}_2$ and the CuAlO_2 samples.

4.3.3 RESULTS AND DISCUSSION

4.3.3.1 X-RAY DIFFRACTION

The XRD patterns of the sintered-samples of the $\text{CuFe}_{0.5}\text{Al}_{0.5}\text{O}_2$, the CuFeO_2 , and the CuAlO_2 are shown in **Figure 4.39**. The reference of the ICSD:01-075-2146 [66] for the CuFeO_2 delafossite and of the JCPDS:35-140 [46] for the CuAlO_2 delafossite are added to compare with the XRD-patterns of the sinter samples. The results show that the sintered samples of the CuFeO_2 and the CuAlO_2 are formed single phase of delafossite as hexagonal structure (space group: $R\bar{3}m$) with corresponding to its reference the card file of the ICSD:01-075-2146 and the JCPDS:35-140, respectively. For the phase of the $\text{CuFe}_{0.5}\text{Al}_{0.5}\text{O}_2$ sample, the XRD patterns display all peaks related in peak by peak of angle phase to the phase of the CuFeO_2 and the CuAlO_2 samples. It is found that the angle peaks of the $\text{CuFe}_{0.5}\text{Al}_{0.5}\text{O}_2$ sample stay middle of angle peak of the CuFeO_2 and the CuAlO_2 samples. In compared angle phase, the peaks of the CuFeO_2 sample are in the low angles (left side) of the phase of the $\text{CuFe}_{0.5}\text{Al}_{0.5}\text{O}_2$ sample, whereas the peaks of the CuAlO_2 sample are in high angles (right side) of the $\text{CuFe}_{0.5}\text{Al}_{0.5}\text{O}_2$ sample. These results confirm that the $\text{CuFe}_{0.5}\text{Al}_{0.5}\text{O}_2$ sample is formed single phase of the delafossite of space group $R\bar{3}m$.

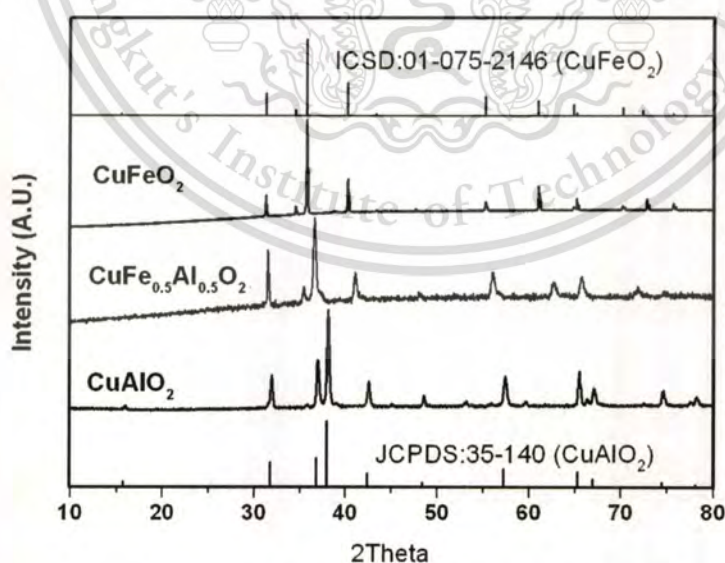


Figure 4.39 The XRD patterns of the sinter samples of the $\text{CuFe}_{0.5}\text{Al}_{0.5}\text{O}_2$, the CuFeO_2 , and the CuAlO_2 .

Figure 4.40 exhibits lattice constant of the $\text{CuFe}_{0.5}\text{Al}_{0.5}\text{O}_2$, the CuFeO_2 , and the CuAlO_2 samples. The results show that the lattice constants of the samples are changed with the content of B-site of sample. The lattice parameters are $a = 3.033 \text{ \AA}$, $c = 17.16 \text{ \AA}$ for the CuFeO_2 sample, and $a = 2.852 \text{ \AA}$, $c = 16.954 \text{ \AA}$ for the CuAlO_2 sample, as closely agree with previous reported [67-69]. The lattice parameters of the CuFeO_2 sample is higher than the value of the CuAlO_2 sample due to the ionic crystal radii of the Fe^{3+} (0.65 \AA) [66] larger than the value of the Al^{3+} (0.53 \AA) [66] where is in center of edge-shared octahedral by six oxygen atoms. For the lattice parameter of the $\text{CuFe}_{0.5}\text{Al}_{0.5}\text{O}_2$ sample, the a -axis and c -axis are 3.006 \AA and 17.166 \AA , respectively. These results show that the a -axis of the $\text{CuFe}_{0.5}\text{Al}_{0.5}\text{O}_2$ sample has the range between that value of the CuFeO_2 and the CuAlO_2 samples, while the c -axis has closely to that value of the CuFeO_2 sample. The results implied that the size of the ionic crystal radii of the B-site in center of octahedral affects on both length of a - and c -axis of the $\text{CuFe}_{1-x}\text{Al}_x\text{O}_2$ sample.

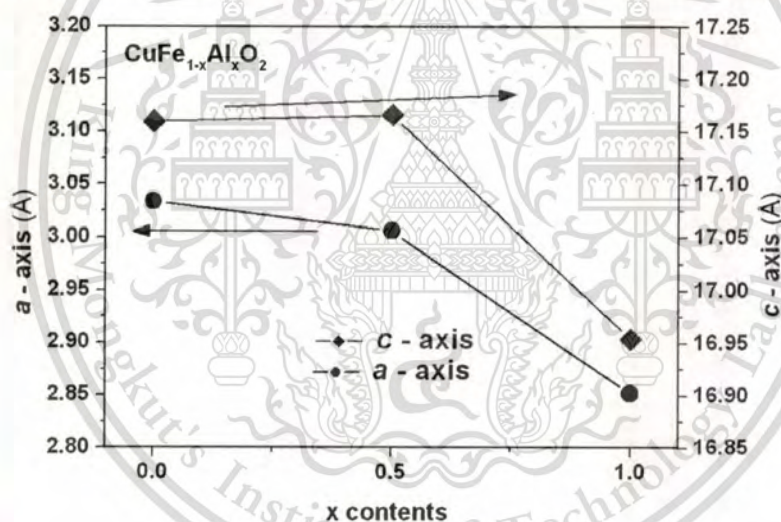


Figure 4.40 The lattice parameters of the sintered samples of the $\text{CuFe}_{0.5}\text{Al}_{0.5}\text{O}_2$, the CuFeO_2 , and the CuAlO_2 .

4.3.3.2 DENSITY

The bulk density of the $\text{CuFe}_{0.5}\text{Al}_{0.5}\text{O}_2$, the CuFeO_2 , and the CuAlO_2 samples are 5.77, 5.22, and 4.78 g/cm^3 , respectively. The ratios of bulk density to theoretical density for the $\text{CuFe}_{0.5}\text{Al}_{0.5}\text{O}_2$, the CuFeO_2 , and the CuAlO_2 samples are 97.26%, 94.74%, and 93.73%,

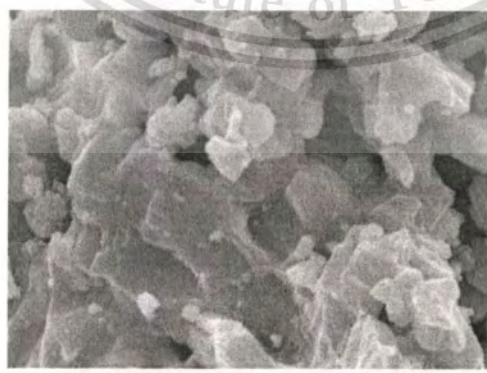
respectively. All results show that the density of sintered samples is closely to theoretical density.

4.3.3.3 SCANNING ELECTRON MICROSCOPE

The morphology in microstructure of the $\text{CuFe}_{0.5}\text{Al}_{0.5}\text{O}_2$, the CuFeO_2 , and the CuAlO_2 samples are observed by SEM as shown in **Figure 4.41**. The crystal grand size of the $\text{CuFe}_{0.5}\text{Al}_{0.5}\text{O}_2$, the CuFeO_2 , and the CuAlO_2 samples are in 1, 2, and $0.5\ \mu\text{m}$, respectively. The garn size of the $\text{CuFe}_{0.5}\text{Al}_{0.5}\text{O}_2$ sample is larger than the value of the CuAlO_2 sample, while is smaller than the value of the CuFeO_2 sample. The results show that the crystal grand size of sample is depended on the content of B-site ($\text{Fe}_{0.5}\text{Al}_{0.5}$, Fe and Al) in the structure of delafossite.



CuFeO_2



$\text{CuFe}_{0.5}\text{Al}_{0.5}\text{O}_2$

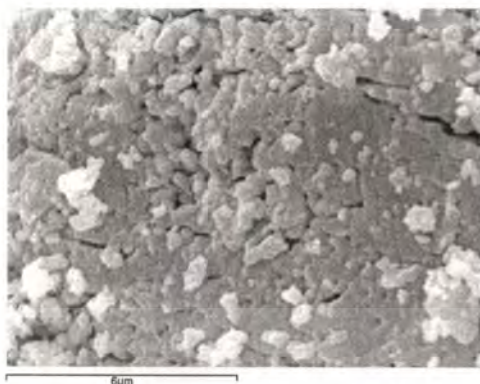
CuAlO₂

Figure 4.41 The microstructure and morphology of the CuFeO₂, the CuFe_{0.5}Al_{0.5}O₂ and the CuAlO₂ samples.

4.3.3.4 SEEBECK COEFFICIENT

Figure 4.42 shows the Seebeck coefficient (S) of the CuFe_{0.5}Al_{0.5}O₂, the CuFeO₂, and the CuAlO₂ samples as a function of temperature. The results show that the Seebeck coefficients are positive sign over the measured temperature range for all samples. These reveal that the all samples are p-type conductor due to the hole carriers. The CuAlO₂ sample displays Seebeck coefficient higher than that value of the CuFeO₂ and CuFe_{0.5}Al_{0.5}O₂ samples in all temperature range. The Seebeck coefficients at room temperature are 250 $\mu\text{V/K}$ for the CuFe_{0.5}Al_{0.5}O₂ sample, are 920 $\mu\text{V/K}$ for the CuFeO₂ sample, and are 260 $\mu\text{V/K}$ for the CuAlO₂ sample, respectively. The Seebeck of the CuAlO₂ sample slightly decreases from 920 to 450 $\mu\text{V/K}$ with the temperature increasing from 300 to 960 K. This result indicates that the CuAlO₂ sample shows the behavior of insulator-like as decreasing with temperature increasing. The Seebeck of the CuFe_{0.5}Al_{0.5}O₂ sample is closely to the value of the CuFeO₂ sample in all range temperature. The Seebeck coefficients of the CuFeO₂ and the CuFe_{0.5}Al_{0.5}O₂ samples increase from 260 to 290 $\mu\text{V/K}$ and 250 to 300 $\mu\text{V/K}$, respectively with increasing temperature. These results imply the behavior of semi-metallic like. In summary, the mixed half B-site of the CuFe_{0.5}Al_{0.5}O₂ sample shows Seebeck coefficient similar to the CuFeO₂ sample and displays the behavior of semi-metallic like.

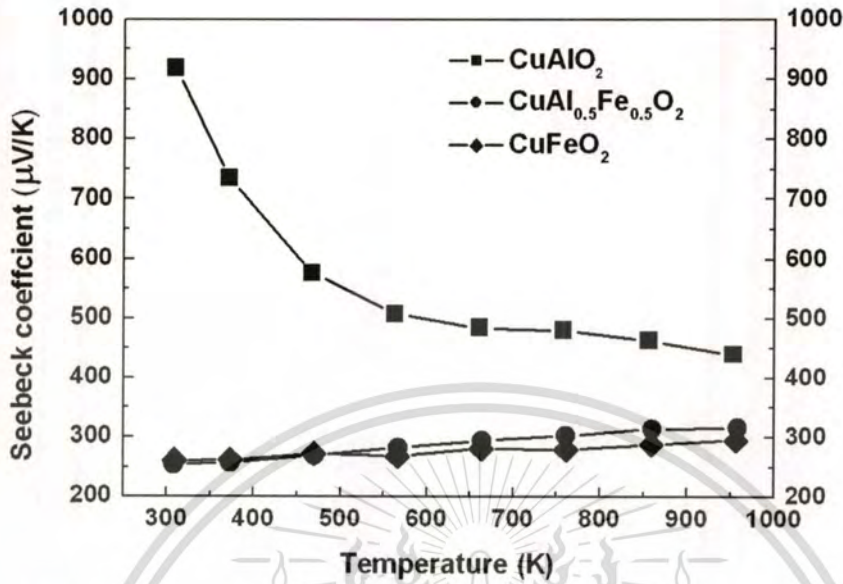


Figure 4.42 The Seebeck coefficient of the CuFeO_2 , the $\text{CuFe}_{0.5}\text{Al}_{0.5}\text{O}_2$, and the CuAlO_2 samples vs. the temperature.

4.3.3.5 EXTENSIONS HEIKES FORMULA

The Heikes formula as application of the Seebeck coefficient (S) of the CuFeO_2 and the CuAlO_2 samples at high temperature is expressed the relation:

$$S = -\frac{k_B}{q} \ln \left[\frac{c}{(1-c)} \right] \quad (4.25),$$

where c is the carrier concentrations.

The Heikes formula in application for the spin and orbital degeneracy and association with the carries concentration of the $\text{CuFe}_{0.5}\text{Al}_{0.5}\text{O}_2$ delafossite, the Seebeck coefficient at high temperature is expressed:

$$S_{T \rightarrow \infty} = -\frac{k_B}{q} \ln \left(\frac{g_3}{g_2} \right) - \frac{k_B}{q} \ln \left[\frac{c}{(1-c)} \right] \quad (4.26),$$

where g_2 is the spin and orbital degeneracy associated with the Fe^{2+} for the CuFeO_2 delafossite, g_3 is the spin and orbital degeneracy associated with the Fe^{3+} for the CuFeO_2 delafossite, c is the concentration of the g_2 state.

The mixed B-trivalent of the Fe^{3+} and the Al^{3+} in the B site of the $\text{CuFe}_{0.5}\text{Al}_{0.5}\text{O}_2$ sample induces to mixed valency of the Fe^{3+} and the Fe^{2+} as in chemical formula $\text{Cu}^{+}[\text{Fe}^{3+}]_{0.25}[\text{Fe}^{2+}]_{0.25}[\text{Al}^{3+}]_{0.25}[\text{Al}^{2+}]_{0.25}\text{O}_2$. The general state of the Fe^{3+} and Fe^{2+} in the CuFeO_2 compounds occurs in the high spin state as shown in **Figure 4.43**. Also, the electronic configuration of the $\text{Fe}^{3+}(3d^5)$ ion is 3 in the t_{2g} state $[(t_{2g})^2]$, and is 2 in the e_g state $[(e_g)^2]$. The $\text{Fe}^{2+}(3d^6)$ ion is 3 in the t_{2g} state $[(t_{2g})^3]$ and 1 in the e_g state $[(e_g)^1]$.

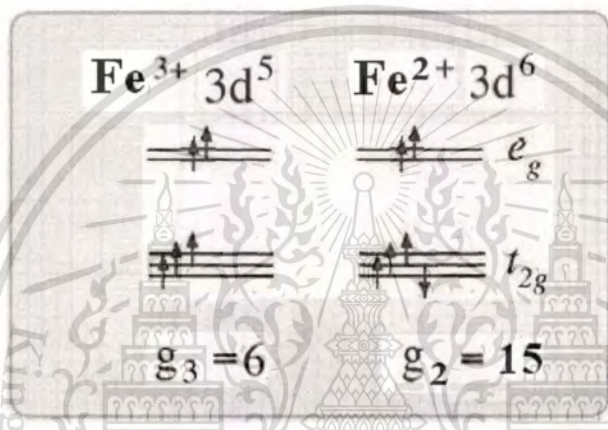


Figure 4.43 The degeneracy of high spin state of the CuFeO_2 delafossite.

Consequently, the g_3 state of the Fe^{3+} is 6 from the spin degeneracy of $S_d=6$ and orbital degeneracy of $L_d=1$. In addition, the g_2 state of the Fe^{2+} is 15 from the spin degeneracy of $S_d=5$ and orbital degeneracy of $L_d=3$. For the carrier concentration of concentration of the g_2 state, the c is 0.25. On the Al^{3+} , the Seebeck value at high temperature is applies by Heikes formula as applying by setting the $c = 0.25$ for the Al^{2+} concentration.

Therefore, the S value of the $\text{CuFe}_{0.5}\text{Al}_{0.5}\text{O}_2$ delafossite in high temperature is expressed:

$$S = -(86.17) \ln\left(\frac{6}{15}\right) - (86.17) \ln\left[\frac{0.25}{(1-0.25)}\right] - (86.17) \ln\left[\frac{0.25}{(1-0.25)}\right] = 268.29 \mu\text{V/K}$$

This result is limitation value of the S value for the $\text{CuFe}_{0.5}\text{Al}_{0.5}\text{O}_2$ sample in high temperature corresponding to the experimental result of the $\text{CuFe}_{0.5}\text{Al}_{0.5}\text{O}_2$ sample as in $300 \mu\text{V/K}$ at 960 K .

4.3.3.6 ELECTRICAL CONDUCTIVITY

Figure 4.44 shows the electrical conductivity (σ) of the CuFeO_2 , the $\text{CuFe}_{0.5}\text{Al}_{0.5}\text{O}_2$, and the CuAlO_2 samples as a function of temperature in the range from 300 to 960 K. The results show that the electrical conductivity of all samples at the high temperature is rapidly increased as a result of increasing temperature. The σ values increase in the ranging from 7 to 15 S/cm for the $\text{CuFe}_{0.5}\text{Al}_{0.5}\text{O}_2$ sample, from 5 to 13 S/cm for the CuFeO_2 sample, and from 2.5×10^{-4} to 2 S/cm for the CuAlO_2 sample, respectively. These results show that σ value of the $\text{CuFe}_{0.5}\text{Al}_{0.5}\text{O}_2$ sample is higher than that value of the CuFeO_2 and the CuAlO_2 samples in all temperature range. These imply that the electrical conductivity of the $\text{CuFe}_{0.5}\text{Al}_{0.5}\text{O}_2$ sample is enhanced from the mixed of haft trivalent of Fe^{3+} and Al^{3+} cation in the B-site.

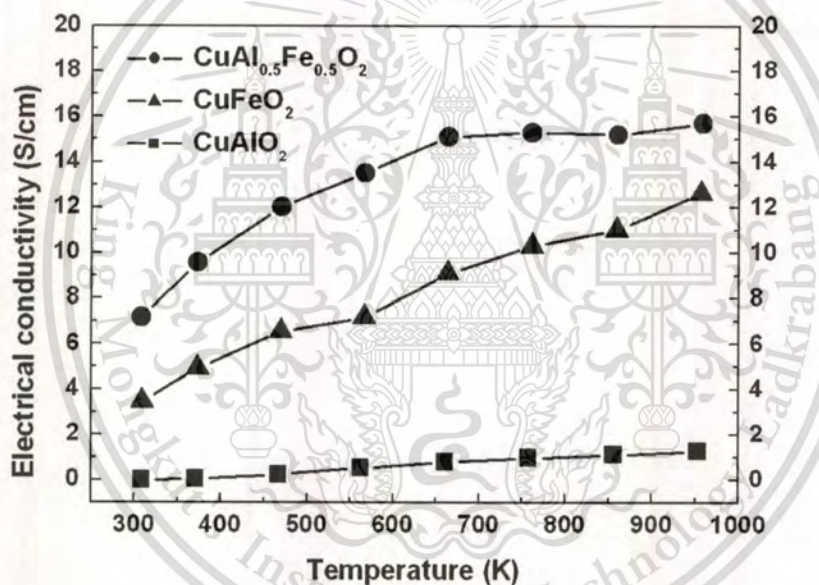


Figure 4.44 The electrical conductivity the $\text{CuFe}_{0.5}\text{Al}_{0.5}\text{O}_2$, the CuFeO_2 , and the CuAlO_2 samples vs. the temperature.

Figure 4.45 shows the plot of the Mott's model of the $\text{CuFe}_{0.5}\text{Al}_{0.5}\text{O}_2$, the CuFeO_2 , and the CuAlO_2 samples with plotting temperature dependence in the equation $\sigma = B \exp[-(T_0/T)^{1/4}]$. The zero slope of the Mott equation implies the temperature independence of conduction which exhibits metallic behavior. The plotted results of $\log \sigma$ vs. $1/T^{1/4}$ display that the $\text{CuFe}_{0.5}\text{Al}_{0.5}\text{O}_2$ sample which is closely to zero-slope. This confirms that the $\text{CuFe}_{0.5}\text{Al}_{0.5}\text{O}_2$ sample is a good semiconductor than that of the CuFeO_2 and the CuAlO_2 samples. In addition, the linear slope of

the $\log \sigma$ vs. $1/T^{1/4}$ suggests that a variable-range-hopping mechanism is reasonable for all $\text{CuFe}_{0.5}\text{Al}_{0.5}\text{O}_2$ sample in high temperature.

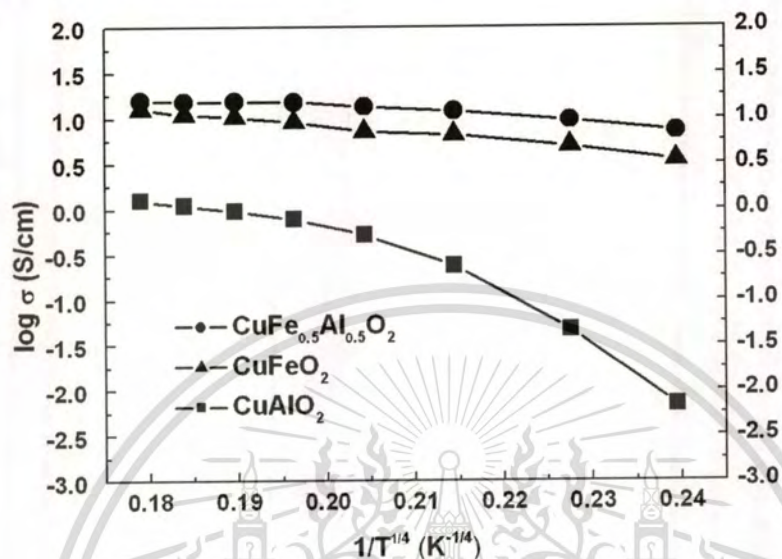


Figure 4.45 The $\log \sigma$ vs. $1/T^{1/4}$ curve.

4.3.3.7 THERMAL CONDUCTIVITY

The thermal conductivity of the CuFeO_2 , the CuAlO_2 , and the $\text{CuFe}_{0.5}\text{Al}_{0.5}\text{O}_2$ samples were measured by using a laser flash method by the relation of $\kappa = dC_p a$. The bulk density of the CuFeO_2 , the CuAlO_2 , and the $\text{CuFe}_{0.5}\text{Al}_{0.5}\text{O}_2$ samples are 5.22, 4.78, and 4.5 g/cm^3 , respectively. The ratios of bulk density to theoretical density of the CuFeO_2 , the CuAlO_2 , and the $\text{CuFe}_{0.5}\text{Al}_{0.5}\text{O}_2$ samples are 94.74%, 93.73%, and 88.76% respectively. All results show that the density of sintered samples is closely to theoretical density leading to reasonable in value of the measurement thermal conductivity.

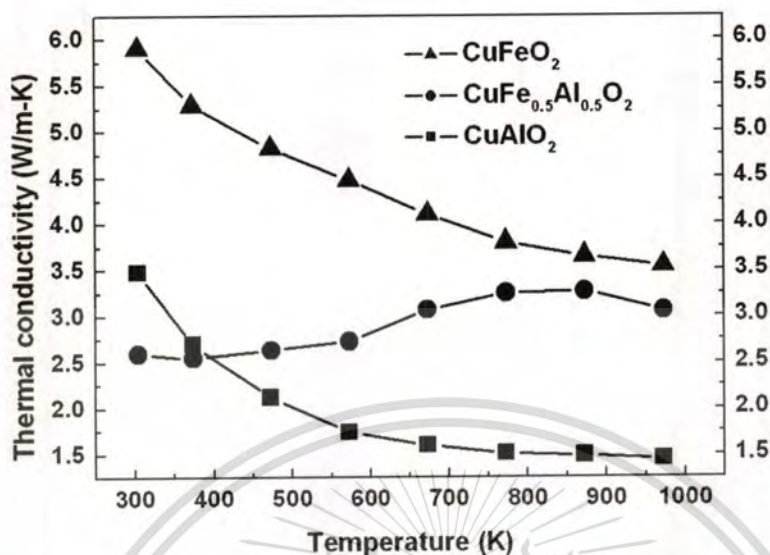


Figure 4.46 The thermal conductivity of the $\text{CuFe}_{0.5}\text{Al}_{0.5}\text{O}_2$, the CuFeO_2 and the CuAlO_2 samples vs. the temperature.

The thermal conductivity (κ) of the samples of the $\text{CuFe}_{0.5}\text{Al}_{0.5}\text{O}_2$, the CuFeO_2 and the CuAlO_2 samples vs. the temperature is shown in **Figure 4.46**. The results show that the value of the CuFeO_2 and the CuAlO_2 samples are decreased as a result of increased temperature, whereas the values of the $\text{CuFe}_{0.5}\text{Al}_{0.5}\text{O}_2$ sample minimal increase with increasing temperature. The κ values of the CuFeO_2 and the CuAlO_2 samples are reduced in the range from 5.8 to 3.5 W/m-K and from 3.5 to 1.5 W/m-K, respectively. The κ values of the $\text{CuFe}_{0.5}\text{Al}_{0.5}\text{O}_2$ sample minimal increase in the range from 2.5 to 3.3 W/m-K. The results show that the κ value of the $\text{CuFe}_{0.5}\text{Al}_{0.5}\text{O}_2$ sample contains middle value between the κ value of the CuFeO_2 and the CuAlO_2 samples.

Total thermal conductivity (κ) is combination from two parts of the lattice (phonon) part and the electronic part as in following the relation $\kappa = \kappa_l + \kappa_e$. The lattice conductivity (κ_l) is expressed by $\kappa_l = 1/3 C_v \nu l$ [70], where C_v is the specific heat, ν is the acoustic velocity, and l is the mean free path of phonons. From the Wiedmann-Franz law, the κ_e is related by $\kappa_e = L_o T \sigma$ [30], where L_o is the Lorenz factor ($2.45 \times 10^{-8} \text{ W}\Omega/\text{K}^2$), T is the absolute temperature, σ is the electrical conductivity. The κ_e values of the CuFeO_2 , the $\text{CuFe}_{0.5}\text{Al}_{0.5}\text{O}_2$ and the CuAlO_2 samples, at room temperature at 960 K, are 1.545 %, 0.820%, and 0.313%, respectively. These

results indicate that the major effect of thermal conductivity of all sample is dominated the by the thermal conductivity of phonon part which is controlled by phonon mechanism part.

4.3.3.8 POWER FACTOR AND DIMENSIONLESS OF FIGURE OF MERIT

Figure 4.47 shows the power factor ($PF = \sigma S^2$) of the $\text{CuFe}_{0.5}\text{Al}_{0.5}\text{O}_2$, the CuFeO_2 , and the CuAlO_2 samples calculated from the measured electrical conductivity and Seebeck coefficient as a function of temperature in the range of 300 to 960 K. The power factor for all samples is increased with increasing temperature. The $\text{CuFe}_{0.5}\text{Al}_{0.5}\text{O}_2$ sample displays Power Factor higher than that value of the CuFeO_2 and the CuAlO_2 samples for all temperature range. The PF value of the $\text{CuFe}_{0.5}\text{Al}_{0.5}\text{O}_2$ sample increases from 0.45×10^{-4} to $2.0 \times 10^{-4} \text{ W/m-K}^2$ as increasing temperature. Other samples, the CuFeO_2 and CuAlO_2 are increases from 0.2×10^{-4} to $1.5 \times 10^{-4} \text{ W/m-K}^2$ and from 0.01×10^{-4} to $2.0 \times 10^{-4} \text{ W/m-K}^2$ as increasing temperature. The maximum of the power factors in high temperature are 1.5×10^{-4} , 1.1×10^{-4} , and $2.0 \times 10^{-4} \text{ W/m-K}^2$ of the CuFeO_2 , the CuAlO_2 and the $\text{CuFe}_{0.5}\text{Al}_{0.5}\text{O}_2$ samples, respectively at 960 K. These results imply that the power factor of the $\text{CuFe}_{0.5}\text{Al}_{0.5}\text{O}_2$ sample has the value in 2 times and 4 times of the CuFeO_2 and the CuAlO_2 samples, respectively. Indeed, the result implies that the haft trivalent of the Fe and the Al of the $\text{CuFe}_{0.5}\text{Al}_{0.5}\text{O}_2$ sample is effect to enhance the value of power factor

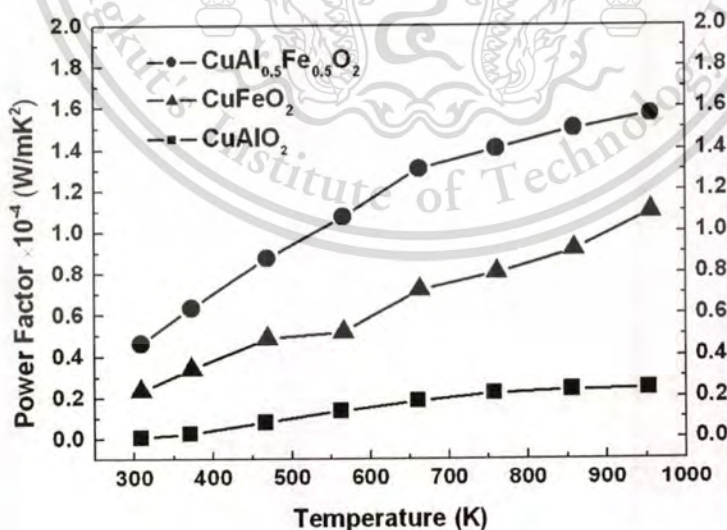


Figure 4.47 The power factor of the $\text{CuFe}_{0.5}\text{Al}_{0.5}\text{O}_2$, the CuFeO_2 and the CuAlO_2 samples vs. the temperature.

The temperature dependence of the ZT value for the CuFeO_2 , the CuAlO_2 and the $\text{CuFe}_{0.5}\text{Al}_{0.5}\text{O}_2$ samples in the temperature ranging from 300 to 960 K are exhibited in **Figure 4.48**. The ZT values are also calculated from the relation $ZT=PF(T)/\kappa$. The results show that the ZT values of all samples are rapidly raised with increasing temperature. The ZT values of the CuFeO_2 , the CuAlO_2 , and the $\text{CuFe}_{0.5}\text{Al}_{0.5}\text{O}_2$ samples at room temperature are 0.003, 0.001, and 0.006, respectively. The high ZT values of samples are 0.03, 0.015, and 0.04 for the CuFeO_2 , the CuAlO_2 , and the $\text{CuFe}_{0.5}\text{Al}_{0.5}\text{O}_2$ samples in temperature 960K. The results show that the ZT values of the $\text{CuFe}_{0.5}\text{Al}_{0.5}\text{O}_2$ sample are higher than that value of the CuFeO_2 and the CuAlO_2 samples in 2 times and 3 times, respectively. These results indicate that the half trivalent of the Fe and the Al of the $\text{CuFe}_{0.5}\text{Al}_{0.5}\text{O}_2$ sample is effect to enhance the ZT value for thermoelectric materials.

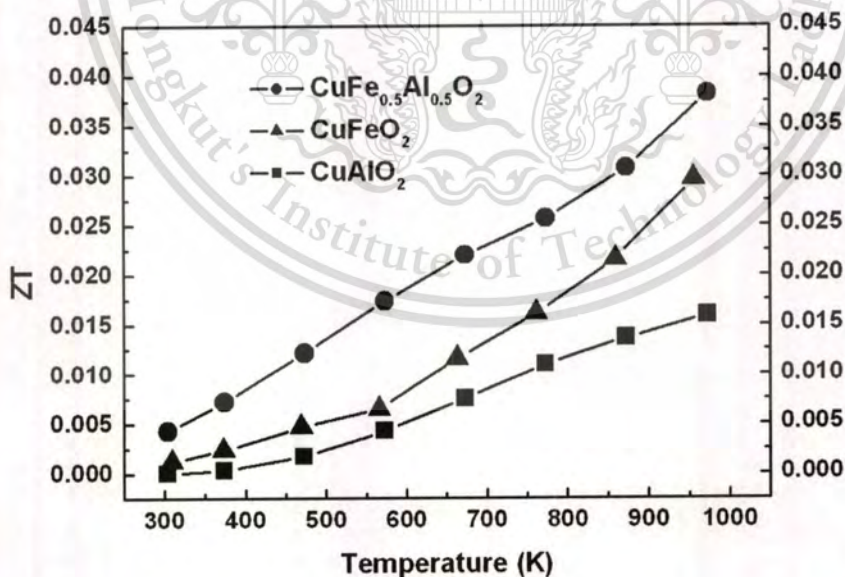


Figure 4.48 The dimensionless Figure of Merit (ZT) of the CuFeO_2 , the CuAlO_2 , and the $\text{CuFe}_{0.5}\text{Al}_{0.5}\text{O}_2$ samples vs. temperature.

4.3.3.9 ACTIVATION ENERGY

4.3.3.9.1 ACTIVATION ENERGY OF PRODUCTION OF FREE CARRIERS (E_s)

In applying the p -type of semiconductor, the relation of the Seebeck coefficient is given [35] by $S = (k_B/e)[(E_F - E_v)/k_B T]$. The activation energy for the production of free carriers $E_s = (E_F - E_v)$ is obtained by plotting the S vs. $1000/T$ as shown in the **Figure 4.49**. An average of E_s value for the $\text{CuFe}_{0.5}\text{Al}_{0.5}\text{O}_2$ sample is obtained 30 meV, for the CuFeO_2 sample is 27 meV, and for the CuAlO_2 sample is -83.4 meV and -282.9 meV in the $E_s(1)$ and the $E_s(2)$ region, respectively. The results of the $\text{CuFe}_{0.5}\text{Al}_{0.5}\text{O}_2$ and the CuFeO_2 samples are higher than the thermal energy at room temperature ($k_B T_{300\text{K}} \cong 25$ meV). Thus, this value indicates that the $\text{CuFe}_{0.5}\text{Al}_{0.5}\text{O}_2$ and the CuFeO_2 samples are a good semiconductor material for thermoelectric because the charge carriers are ionized near the room temperature for conduction. The minus sign of the CuAlO_2 sample represents that the activation energy for the production of free carriers requires from external system.

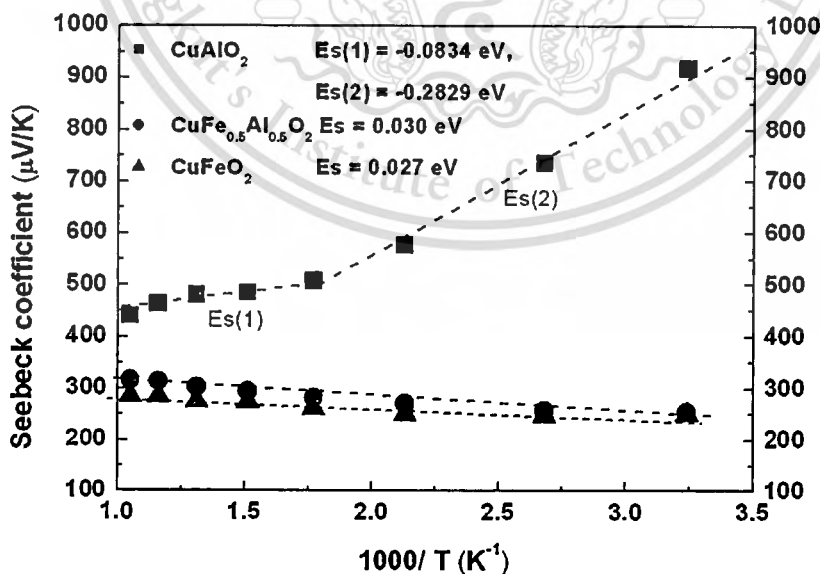


Figure 4.49 The Seebeck coefficient vs. $1000/T$ curve.

4.3.3.9.2 ACTIVATION ENERGY OF CARRIER CONDUCTION (E_σ)

The Arrhenius plot of the $\text{CuFe}_{0.5}\text{Al}_{0.5}\text{O}_2$, the CuFeO_2 , and the CuAlO_2 samples plotted by the $\log\sigma$ with invert temperature is shown in **Figure 4.50**. The Arrhenius relation corresponds to the equation of electrical conductivity by the following relation of $\sigma = \sigma_0 \exp(-E_\sigma / k_B T)$ [35] where k_B is the Boltzmann's constant, E_σ is the activation energy of conduction, T is the absolute temperature and σ_0 is the constant. The activation energy (E_σ) which is obtained by slopes of the $\log\sigma$ with invert of temperature corresponds to the activation energy of acceptor levels in a p-type semiconductor. **Figure 4.50** exhibits the slopes of the $\log\sigma$ vs. $1000/T$ of the $\text{CuFe}_{0.5}\text{Al}_{0.5}\text{O}_2$, the CuFeO_2 and the CuAlO_2 samples. The results show that the slopes are straight lines with negative slope in all samples indicating that the positive of activation energy (E_σ). The E_σ values of the CuFeO_2 and the $\text{CuFe}_{0.5}\text{Al}_{0.5}\text{O}_2$ samples are 0.049 and 0.203 eV respectively. The activation energy (E_σ) of the CuAlO_2 is found 2 regions of linear slopes with value of 0.124 eV for the $E_\sigma(1)$ region and 0.2554 eV for the $E_\sigma(2)$ region, respectively. The activation energies are presentation in shallow or deep acceptor levels in the band gap of the p-type semiconductor. All so, the E_σ values show that the activation energy of the $\text{CuFe}_{0.5}\text{Al}_{0.5}\text{O}_2$ sample is closely to the CuFeO_2 sample and is lower than that energy of the CuAlO_2 sample. The lower activation energy of the $\text{CuFe}_{0.5}\text{Al}_{0.5}\text{O}_2$ and the CuFeO_2 samples corresponds to the shallow acceptor level, while the higher activation energy of the CuAlO_2 sample corresponds to the deep acceptor level. In addition, the activation energy in the 2 regions of the CuAlO_2 sample, the E_σ values of the $E_\sigma(1)$ region lower than that of the $E_\sigma(2)$ region contributing to acceptor level of the $E_\sigma(1)$ region shallow than that of region of the $E_\sigma(2)$ region. All results of activation energy of conduction exhibit that all samples are thermally activation in all temperature range. The slope of the E_σ for the CuFeO_2 and the $\text{CuFe}_{0.5}\text{Al}_{0.5}\text{O}_2$ samples imply the behavior of metal-like, while the slope of the CuAlO_2 sample implied the behavior of semiconductor. In summary, the results imply that the haft trivalent of the Fe and the Al of the $\text{CuFe}_{0.5}\text{Al}_{0.5}\text{O}_2$ sample is affected to enhance the value of the activation energy of conduction.

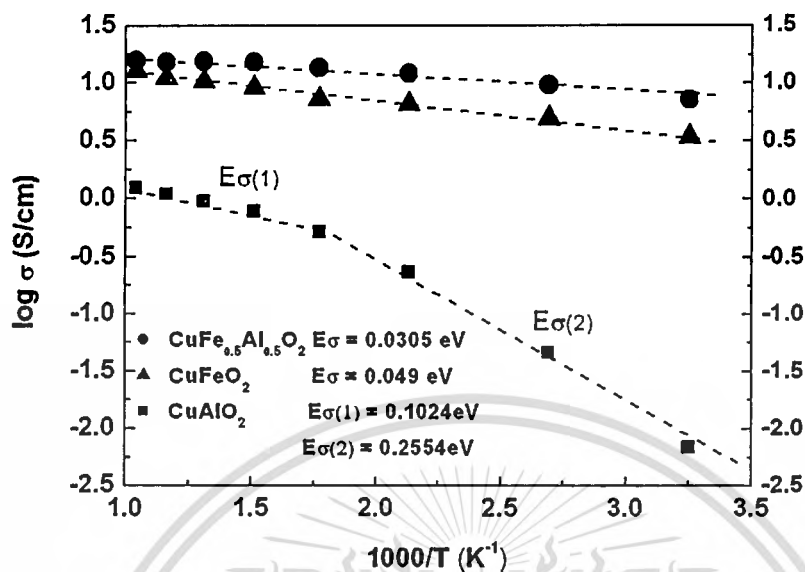


Figure 4.50 The $\log \sigma$ vs. $1000/T$ curve.

4.3.3.9.3 ACTIVATION ENERGY OF CARRIER MOBILITY (E_{μ})

Electrical conductivity of non-metals is activated by thermal energy which is energy to cross barriers for production carries and energy to motion of charge carries. The equation of the electrical conductivity is described by $\sigma = eN\mu$. Totally, the relation of electrical conductivity is expressed by $\sigma = \sigma_0 \exp(-E_s/k_B T) = e(N_0 \exp[-E_s/k_B T]) (\mu_0 \exp[-E_u/k_B T])$ [35, 53], The E_{σ} , E_s , and E_u represent the activation energy of conduction, of carries production, and of carries migration (hopping energy for polaron conduction), respectively. Consequently, the total activation energy for conductor is expressed by $E_{\sigma} = E_{\mu} + E_s$. The activation energies of the E_u for the CuFe_{0.5}Al_{0.5}O₂ and the CuFeO₂ samples are 0.5 and 22 meV respectively. The E_u value of the CuAlO₂ sample is 0.1858 eV and 0.5383 eV for the $E_u(1)$ and the $E_u(2)$ regions, respectively. The results of the E_u of the CuFeO₂ and the CuFe_{0.5}Al_{0.5}O₂ samples are less than the thermal energy at room temperature ($k_B T_{300K} \cong 25$ meV), while the value of the E_u in 2 regions of the CuAlO₂ sample higher than the thermal energy at room temperature. The E_u of the CuFe_{0.5}Al_{0.5}O₂ sample is lower than that energy of the CuFeO₂ and the CuAlO₂ samples. In summary, these imply that the haft trivalent of the Fe and the Al of the CuFe_{0.5}Al_{0.5}O₂ sample is affected to enhance in reducing of the value of the activation energy of carries migration.

4.3.3.10 OPTICAL PROPERTIES

The absorption coefficient(α) spectrum of the $\text{CuFe}_{0.5}\text{Al}_{0.5}\text{O}_2$, the CuFeO_2 and the CuAlO_2 samples at room temperature were measure as shown in **Figure 4.51**. The absorption coefficient is measured in ranging of energy from 1.5 to 6 eV. The results exhibit that the heavy absorbability of all samples is in the spectrum range from 4 to 6 eV (the UV light), and the week absorbability of all samples is in the spectrum range from 0.5 to 3.5 eV (the Near IR and the visible light).

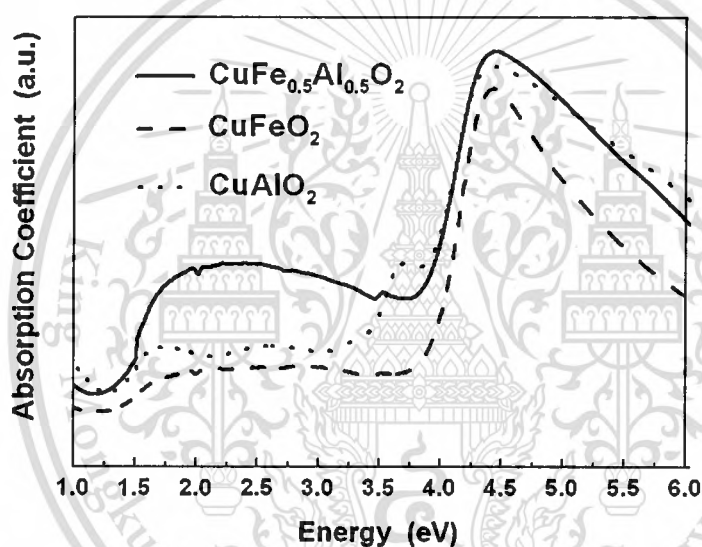


Figure 4.51 Absorbance spectrum of the CuFeO_2 , the CuAlO_2 , and the $\text{CuFe}_{0.5}\text{Al}_{0.5}\text{O}_2$ samples at room temperature.

The optical energy gap is obtained from a plot of $(\alpha h\nu)^m$ vs. $h\nu$ with taking the intercept on the energy axis. **Figure 4.52** shows the indirect and direct energy gap of the $\text{CuFe}_{0.5}\text{Al}_{0.5}\text{O}_2$, the CuFeO_2 and the CuAlO_2 samples, at room temperature. The results show that the indirect energy gaps of the $\text{CuFe}_{0.5}\text{Al}_{0.5}\text{O}_2$, the CuFeO_2 and the CuAlO_2 samples are 1.1, 1.15 and 2.2 eV as shown in **Figure 4.52 (a)** and the direct energy gaps exhibit 3.5, 3.45 and 3.2 eV as shown in **Figure 4.52 (b)**. These can see that the direct energy gap of all samples is larger than 3.1 eV. These results indicate that the haft trivalent of the Fe and the Al of the $\text{CuFe}_{0.5}\text{Al}_{0.5}\text{O}_2$ sample is

effect to reduce indirect energy gap, and it has direct energy gap higher than 3.1 eV contributing to transparent conducting oxide materials.

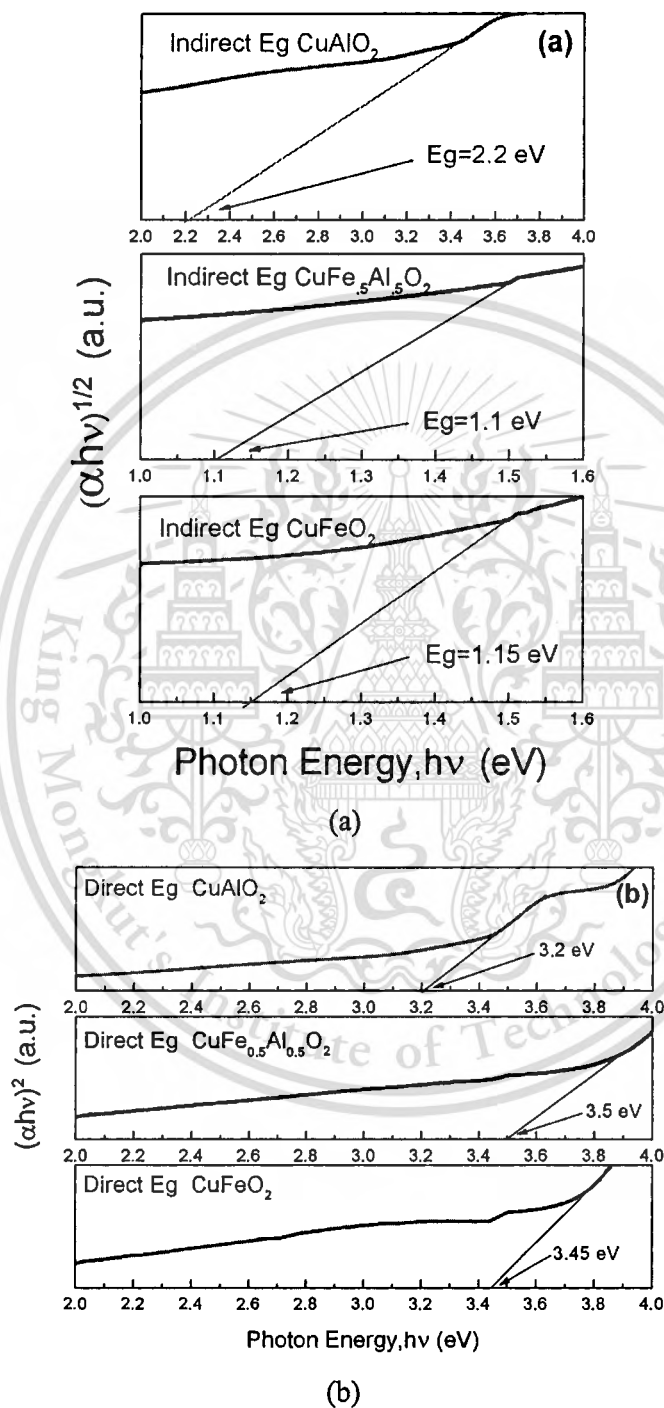


Figure 4.52 (a) Indirect and (b) Direct energy gap of the $\text{CuFe}_{0.5}\text{Al}_{0.5}\text{O}_2$, the CuFeO_2 and the CuAlO_2 samples.

4.3.3.11 RELATION OF ENERGY GAP WITH TEMPERATURE

The results of the direct band gap (E_g) of the $\text{CuFe}_{0.5}\text{Al}_{0.5}\text{O}_2$, the CuFeO_2 and the CuAlO_2 samples as a function of temperature are shown in **Figure 4.53**. The temperature dependence of the approximation of the E_g is calculated from the formula[57] of $E_g(T) = E_g(0) - [aT^2/(b+T)]$. The values of the a and the b for delafossite are given in 0.00075 eV/K and 385 K, respectively[57]. The $E_g(0)$ value is 3.6 eV for the $\text{CuFe}_{0.5}\text{Al}_{0.5}\text{O}_2$, 3.57 eV for the CuFeO_2 sample and 3.3 eV for the CuAlO_2 sample obtained from the fitting with the experiment E_g at room temperature. All results exhibit that the direct E_g decrease with increasing the temperature.

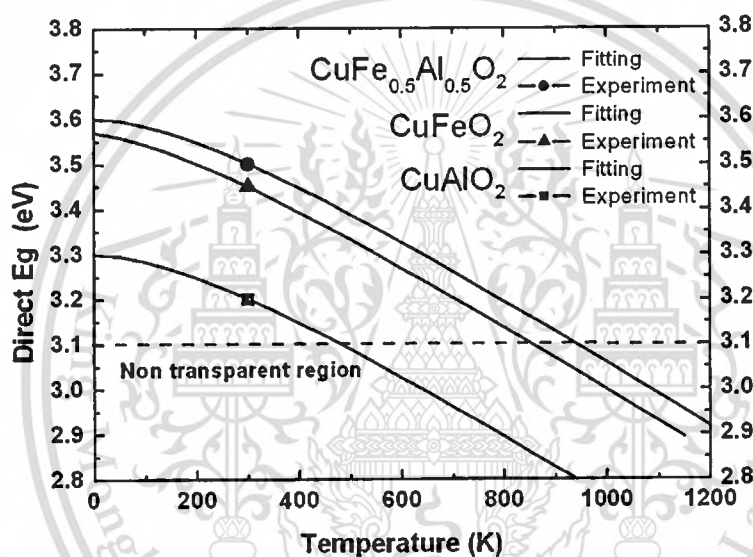
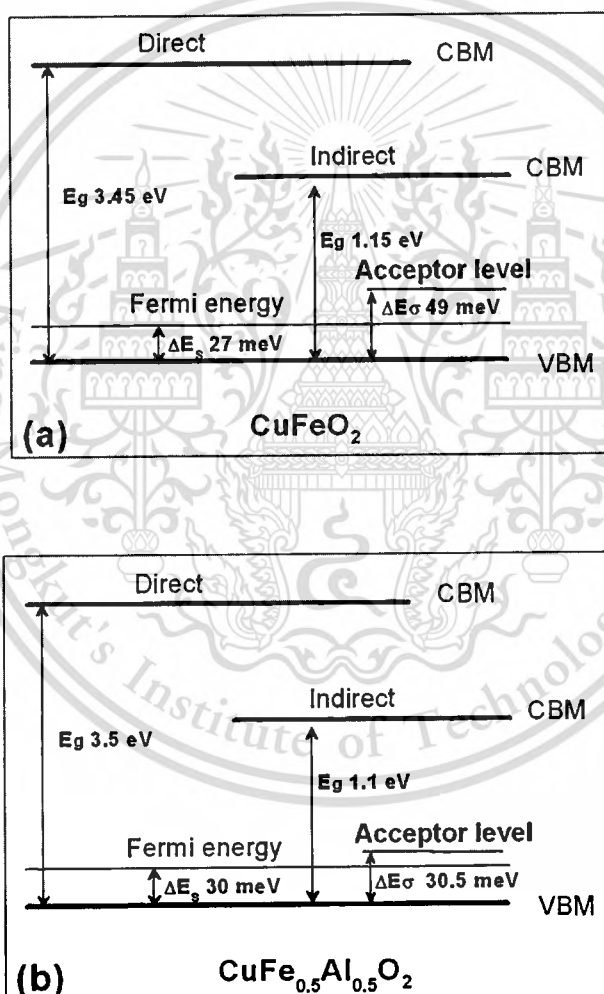


Figure 4.53 The temperature dependence of the direct band gap of the $\text{CuFe}_{0.5}\text{Al}_{0.5}\text{O}_2$, the CuFeO_2 and the CuAlO_2 delafossite.

4.3.3.12 ENERGY DIAGRAM

The band energy level diagram of the $\text{CuFe}_{0.5}\text{Al}_{0.5}\text{O}_2$, the CuFeO_2 and the CuAlO_2 samples at room temperature is predicted from the obtained value of activation energy, Fermi energy level and optical energy gap. The band energy diagram of the $\text{CuFe}_{0.5}\text{Al}_{0.5}\text{O}_2$, the CuFeO_2 and the CuAlO_2 samples are shown in **Figure 4.54** (a), (b) and (c), respectively. The band energy diagram shows that the direct and indirect energy gaps (E_g) of the samples are 3.5, 3.45 and 3.2 eV, and 1.1, 1.15, 2.2 eV for the $\text{CuFe}_{0.5}\text{Al}_{0.5}\text{O}_2$, the CuFeO_2 and the CuAlO_2 , respectively. The Fermi's energy (E_f) level and the acceptor level (E_σ) as above the valence band edge are 30, 27,

and 282.9 meV, and 30.5, 49, and 255.4 meV for the $\text{CuFe}_{0.5}\text{Al}_{0.5}\text{O}_2$, the CuFeO_2 and the CuAlO_2 , respectively. These results show that the half trivalent of the Fe and the Al of the $\text{CuFe}_{0.5}\text{Al}_{0.5}\text{O}_2$ sample is effect to reduce indirect energy gap and to reduce the acceptor level for contributing to enhance the electrical conductivity, hole concentration, and electrical mobility from the based delafossite of the CuFeO_2 and the CuAlO_2 . In conclusion, the $\text{CuFe}_{0.5}\text{Al}_{0.5}\text{O}_2$ sample can improve the properties for thermoelectric and optical materials.



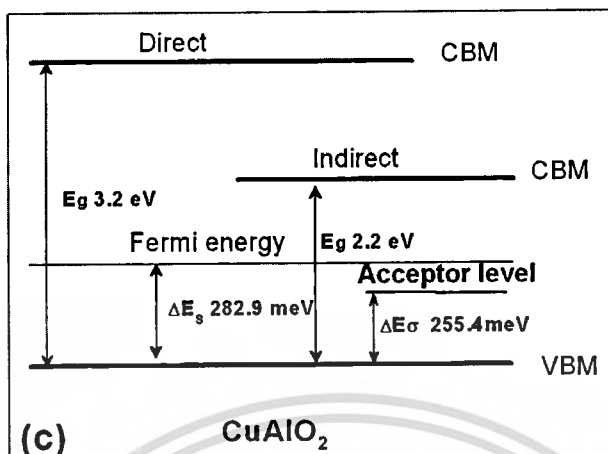


Figure 4.54 The energy level diagram of the (a) CuFeO_2 , (b) $\text{CuFe}_{0.5}\text{Al}_{0.5}\text{O}_2$, and (c) CuAlO_2 delafossite (not exact to the scale).

4.3.3.13 RELATION OF MELTING POINT TO ENERGY GAP

The relation between energy gap with melting point of temperature for optimal operating thermoelectric materials is described in relation of $E_G = 4k_B T_h$. For high ZT value, the range of T_h is used in $0.9T_m$; where T_m is the melting point of materials.

For the CuFeO_2 sample, the T_m value is 1365 K contributing to the T_h value containing at 1228.5 K for the optimum indirect energy gap (E_G). For the CuAlO_2 sample, the T_m value is 1359 K contributing to the T_h value containing at 1223.1 K for the optimum indirect energy gap (E_G). For the $\text{CuFe}_{0.5}\text{Al}_{0.5}\text{O}_2$ sample, the T_m value is averaged from the value of the CuFeO_2 and the CuAlO_2 samples obtained $T_m = 1363$ K. Also, the T_h value of the $\text{CuFe}_{0.5}\text{Al}_{0.5}\text{O}_2$ is 1226.7 K. Consequently, the calculation of optimum energy gap in the relation of $E_G = 4k_B T_h$ of the $\text{CuFe}_{0.5}\text{Al}_{0.5}\text{O}_2$, the CuFeO_2 and the CuAlO_2 samples must contain 0.442, 0.423, and 0.421 eV at $T_h = 1226.7$, 1228.5, and 1223.1 K, respectively.

Figure 4.55 shows the relation of the temperature dependence of the indirect energy gap (E_G) of the $\text{CuFe}_{0.5}\text{Al}_{0.5}\text{O}_2$, the CuFeO_2 and the CuAlO_2 samples. For the $\text{CuFe}_{0.5}\text{Al}_{0.5}\text{O}_2$ sample, the E_G is obtained 0.51 eV at $T_h = 1226.7$ K. For the CuFeO_2 sample, the E_G is obtained 0.55 eV at $T_h = 1228.5$ K. The results show that the experiments of the optimum E_G for the $\text{CuFe}_{0.5}\text{Al}_{0.5}\text{O}_2$ and the CuFeO_2 samples are above closely to the constant line of $4k_B T_h$ at the

high operation temperature of 0.9 time of melting temperature. The experiment of optimum E_G of the CuAlO_2 sample is far from the constant line of the $4k_B T_h$ at the high operation temperature. The experiment of the optimum E_G for the $\text{CuFe}_{0.5}\text{Al}_{0.5}\text{O}_2$ sample is closely to the constant line of the $4k_B T_h$ more than that value of the CuFeO_2 sample. Therefore, the ZT value of the $\text{CuFe}_{0.5}\text{Al}_{0.5}\text{O}_2$ sample is larger than that value of the CuFeO_2 and the CuAlO_2 samples which is correspondent to experimental of the ZT value in section 5.3.9. In summary, the optimum band-gap (E_G) for good thermoelectric materials of the $\text{CuFe}_{0.5}\text{Al}_{0.5}\text{O}_2$ and the CuFeO_2 occurs in high temperature. The improving thermoelectric properties of the $\text{CuFe}_{0.5}\text{Al}_{0.5}\text{O}_2$ and the CuFeO_2 delafossite can be improved by reducing the E_G value to the constant line of the $4k_B T_h$.

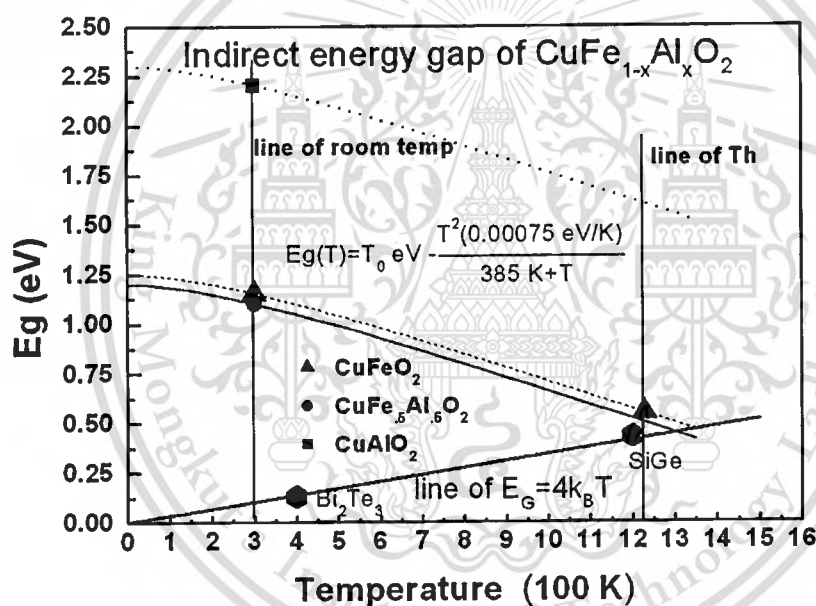
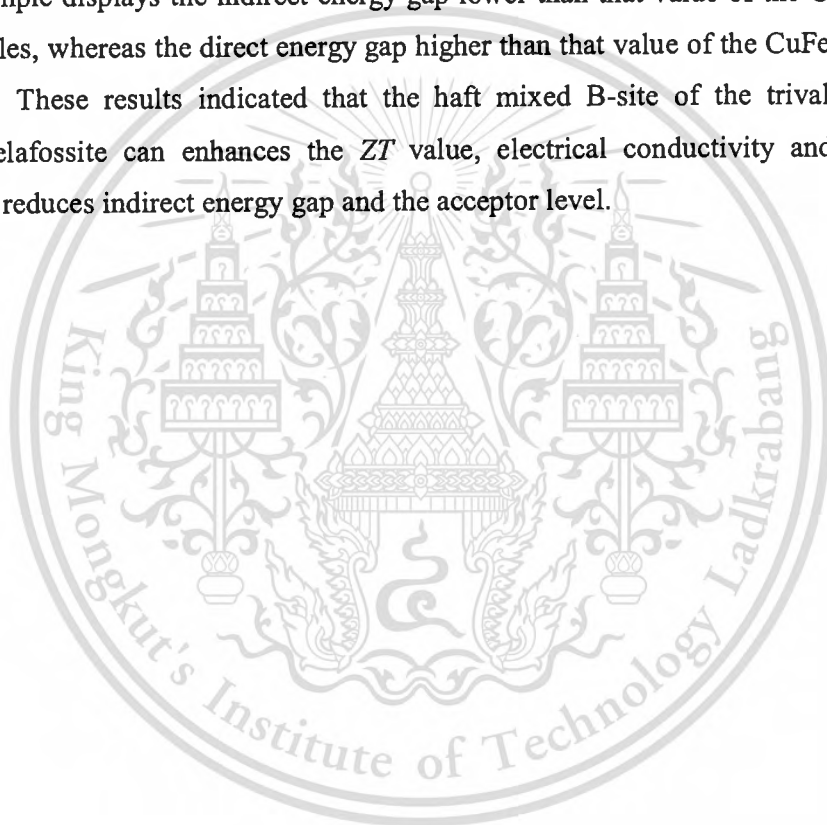


Figure 4.55 The relation curve of the energy gap and the temperature.

4.3.4 SUMMARIES

The objective of this section aims to study the thermoelectric properties of the haft-mixed in B-site of $\text{CuFe}_{0.5}\text{Al}_{0.5}\text{O}_2$ prepared to the properties of the CuFeO_2 and the CuAlO_2 sample-based. The properties of Seebeck coefficient, electrical conductivity and thermal conductivity were measured in the high temperature range from 300 to 960 K. The results display that the Seebeck coefficient of the $\text{CuFe}_{0.5}\text{Al}_{0.5}\text{O}_2$, the CuFeO_2 , and the CuAlO_2 samples display the p-type semiconductor in all temperature range. In addition, the Seebeck coefficient of the

$\text{CuFe}_{0.5}\text{Al}_{0.5}\text{O}_2$ and the CuFeO_2 samples are increased with increasing the temperature, while the CuAlO_2 sample is decreased with increasing temperature. The thermal conductivity of the CuFeO_2 and the CuAlO_2 samples are decreased with increasing temperature, whereas the value of the $\text{CuFe}_{0.5}\text{Al}_{0.5}\text{O}_2$ sample is minimal change with temperature. The maximum ZT values of the $\text{CuFe}_{0.5}\text{Al}_{0.5}\text{O}_2$, the CuFeO_2 and the CuAlO_2 samples are 0.04, 0.03, and 0.015 at temperature 960 K. These results suggest that the power factor and the ZT value of the $\text{CuFe}_{0.5}\text{Al}_{0.5}\text{O}_2$ sample higher than that value of the CuFeO_2 and the CuAlO_2 samples. For optical properties, the $\text{CuFe}_{0.5}\text{Al}_{0.5}\text{O}_2$ sample displays the indirect energy gap lower than that value of the CuFeO_2 and the CuAlO_2 samples, whereas the direct energy gap higher than that value of the CuFeO_2 and the CuAlO_2 samples. These results indicated that the half mixed B-site of the trivalent of the $\text{CuFe}_{0.5}\text{Al}_{0.5}\text{O}_2$ delafossite can enhances the ZT value, electrical conductivity and electrical mobility, and can reduces indirect energy gap and the acceptor level.



4.4 FINITE ELEMENT ANALYSIS OF $\text{CuFe}_{0.5}\text{Al}_{0.5}\text{O}_2$

4.4.1 INTRODUCTION

This section deals with the Finite Element technique to compute power generator on thermoelectric module of the $\text{CuFe}_{0.5}\text{Al}_{0.5}\text{O}_2$ sample. The single bar of the $\text{CuFe}_{0.5}\text{Al}_{0.5}\text{O}_2$ sample was analyzed the output electrical voltage. The computing results were confirmed by the experimental results. Furthermore, the thermoelectric module of the one n-leg and one p-leg was computed to predict the output electrical voltage. Finally, the output voltage of single bar of the $\text{CuFe}_{0.5}\text{Al}_{0.5}\text{O}_2$ sample and the thermoelectric module of the one n-leg and one p-leg were reported.

4.4.2 EXPERIMENTAL PROCEDURE

A bar of the $\text{CuFe}_{0.5}\text{Al}_{0.5}\text{O}_2$ sample in dimension $4.2 \times 2.5 \times 20 \text{ mm}^3$ as shown in **Figure 4.56** was measured thermoelectric power generator on applying temperature difference (ΔT) from 1 to 10 K. In measurement process, the top side of bar is attached to hot temperature (T_H) with varying temperature from 301 to 310 K, and the bottom side of bar is fixed at 300K (T_C).



Figure 4.56 The single bar of $\text{CuFe}_{0.5}\text{Al}_{0.5}\text{O}_2$ sample in dimension $4.2 \times 2.5 \times 20 \text{ mm}^3$.

The output electrical voltage of a $\text{CuFe}_{0.5}\text{Al}_{0.5}\text{O}_2$ bar was measured by testing kid as shown in **Figure 4.57** (a). The test kid used a resistor (R) for 50 W 50 A to generate the heat on the hot side of the bar with applying electrical current from the current generator. On measurement, the temperature difference (ΔT) was applied from 1 to 10 K by increment in 0.5 K on the bar as shown in **Figure 4.57** (b). The cold side of the bar was put on the heat sink for controlling heat to room temperature. The temperature values on the hot side and on the cold side of the bar were measured by the thermocouple. The output voltage on a bar was measured by the voltmeter.

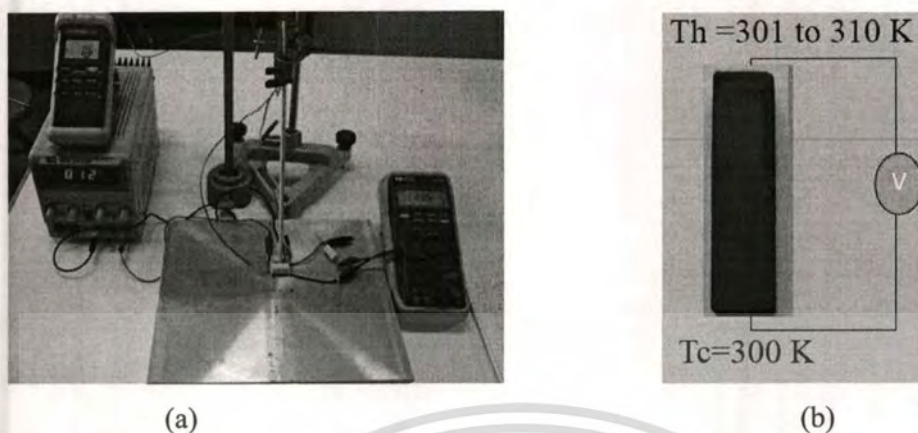


Figure 4.57 (a) The test kit for measurement the thermoelectric generator samples. (b) The temperature difference on the sample bar.

The results of electrical voltage on the thermoelectric generator of the $\text{CuFe}_{0.5}\text{Al}_{0.5}\text{O}_2$ bar with applying temperature difference from 2 to 10 K with incremental in 0.5 K are shown in **Figure 4.58**. The output voltages of the $\text{CuFe}_{0.5}\text{Al}_{0.5}\text{O}_2$ bar are in the range of 0.6 to 3 mV in the temperature difference from 2 to 10 K. The slope of graph is 0.34 mV/K, which is average value of the Seebeck coefficient for the $\text{CuFe}_{0.5}\text{Al}_{0.5}\text{O}_2$ sample.

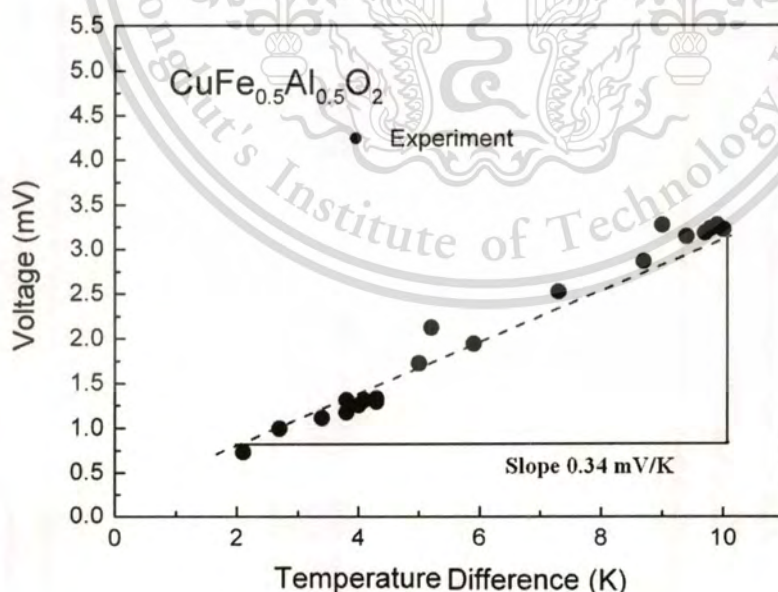
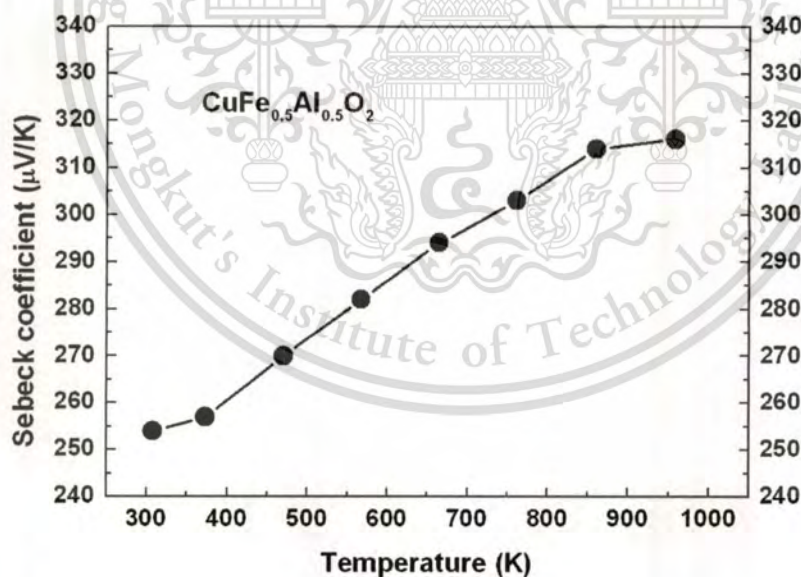


Figure 4.58 The output voltage of the $\text{CuFe}_{0.5}\text{Al}_{0.5}\text{O}_2$ bar after applying temperature difference.

4.4.3 THERMOELECTRIC PROPERTIES

The Seebeck coefficient and electrical resistivity were simultaneously measured on the $\text{CuFe}_{0.5}\text{Al}_{0.5}\text{O}_2$ sample bar by using an ULVAC-RIKO ZEM-2 thermoelectric property measurement system under a low-pressure Ar atmosphere. The thermal conductivity of the $\text{CuFe}_{0.5}\text{Al}_{0.5}\text{O}_2$ sample was determined from thermal diffusivity and specific heat on the relation of $\kappa = dC_p a$ by using the ULVAC SINKU RIKO Inc. model: TC-7000 laser-flash method. The results of thermoelectric properties (Seebeck coefficient, electric conductivity and electric conductivity) are shown in **Figure 4.59** as obtained from the section 4.3.

Figure 4.59 (a) exhibits the Seebeck coefficient of the $\text{CuFe}_{0.5}\text{Al}_{0.5}\text{O}_2$ sample ranging from 260 to 310 $\mu\text{V/K}$ with temperature range 300 to 960 K. **Figure 4.59** (b) presents the electrical conductivity of the $\text{CuFe}_{0.5}\text{Al}_{0.5}\text{O}_2$ sample displays value ranging from 7 to 16 S/cm in the temperature range 300 to 700 K. **Figure 4.59** (c) shows the thermal conductivity of the $\text{CuFe}_{0.5}\text{Al}_{0.5}\text{O}_2$ sample display value range from 3.2 to 4.2 W/cm-K with a region of temperature from 300 to 960 K.



(a)

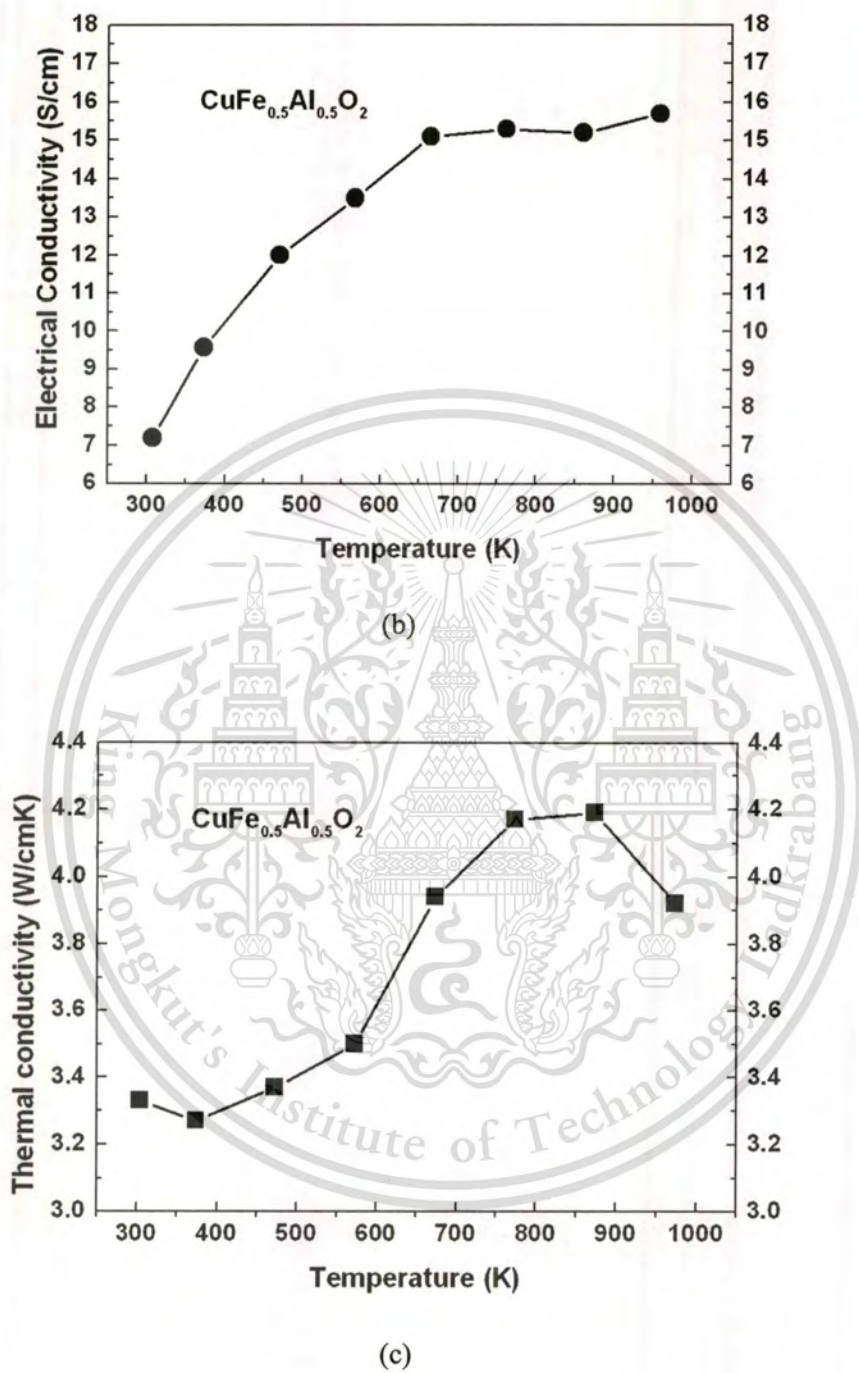


Figure 4.59 The properties of (a) Seebeck coefficient (b) electrical conductivity and (c) thermal conductivity of the $\text{CuFe}_{0.5}\text{Al}_{0.5}\text{O}_2$ samples.

4.4.4 FINITE ELEMENT ANALYSIS

4.4.4.1 GOVERNING EQUATION

The Finite Element technique was used to solve the two couple equations of the thermoelectric effect which are the heat transfer equation and the electric current density equation. The system equations of thermoelectric effect are governed by the couple equation of the heat transfer and the continuity of current density phenomena. The governing equations of the thermoelectric effect [29, 30] are shown below:

- 1) the equation of the heat transfer as in relation:

$$dC_p \frac{\partial T}{\partial t} + \nabla \cdot q = Q \quad (4.27),$$

- 2) the continuity of electric charge as in relation:

$$\nabla \cdot \varepsilon \frac{\partial \bar{E}}{\partial t} + \nabla \cdot \bar{J} = 0 \quad (4.28),$$

where T is the temperature,
 \bar{E} is the electric field,
 q is the heat flux,
 \bar{J} is the electrical current density,
 Q is the internal heat generator,
 t is the time,
 d is the simple bulk density,
 C_p the heat capacity,
 ε is the electric permittivity.

The heat flux (q) [29, 30] is generated from the coupling effects of the reversible Peltiel effect and the irreversible Fourier effect as showing below:

$$q = \Pi \bar{J} - \kappa \nabla T \quad (4.29),$$

where Π is the Peltiel coefficient ($=ST$).

The current density (J) [29, 30] is generated by the coupling of the reversible Seebeck effect and the irreversible joule effect as showing below:

$$\bar{J} = \sigma \bar{E} - \sigma S \nabla T \quad (4.30),$$

where E is the electric field.

The E is related in $-\nabla\phi$, where ϕ is the electric potential.

The constitutive equations of the q and J are inserted into the 2 main equations as obtained [28] following:

$$dCp \frac{\partial T}{\partial t} + \nabla \cdot (ST[\sigma \nabla \phi - \sigma S \nabla T]) - \nabla \cdot ([\kappa] \nabla T) = Q \quad (4.31),$$

$$\nabla \cdot (\epsilon \nabla \frac{\partial \phi}{\partial t}) + \nabla \cdot ([S\sigma] \nabla T) + \nabla \cdot ([\sigma] \nabla \phi) = 0 \quad (4.32).$$

4.4.4.2 FINITE ELEMENT EQUATION

For the Finite Element technique, the domain of the thermoelectric bar is divided into Finite Element mesh. The two main governing equations are transformed into the finite element equations by approximating of the unknown of temperature (T) and electrical potential (ϕ) into the interpolation functions. The values of nodal unknown are solved on an element[71-75]. The matrix equation of the unknown of temperature and electrical potential are shown below:

$$T = [N] \{T^e\} \quad (4.33),$$

$$\phi = [N] \{\phi^e\} \quad (4.34),$$

where T^e is the nodal unknown of the temperature on the element e ,

φ^e is the nodal unknown of the potential on the element e ,

N is the interpolation function,

e represents consider on element,

$[]$ represents the row matrix,

$\{\}$ represents the vector matrix.

The final Finite Element equations of the Galerkin weighting scheme [71-75] are derived as shown below:

$$\int \rho c [N][N] dv \left\{ \frac{\partial T^e}{\partial t} \right\} - \int [\nabla N][\kappa + \sigma S^2 T][\nabla N] dv \{T^e\} + \int [\nabla N][\sigma S T][\nabla N] dv \{\varphi^e\} = \{Q\} \\ + \int [\nabla N][S T]\{J\} dv + \int [N][E]\{J\} dv \quad (4.35),$$

$$\int \varepsilon [\nabla N][\nabla N] dv \left\{ \frac{\partial \varphi^e}{\partial t} \right\} + \int [\nabla N][\sigma S][\nabla N] dv \{T^e\} + \int [\nabla N][\sigma][\nabla N] dv \{\varphi^e\} = \{[N]\{j_s\}\} \quad (4.36).$$

The solution of the unknown of the temperature (T) and the voltage (φ) are obtained from the solving on the Finite Element equations (4.35) and (4.36).

The Finite Element technique was used to compute electric power on the model of thermoelectric bar. The model of thermoelectric for investigation in this work consists of 2 models as below:

- 1) The model of a $\text{CuFe}_{0.5}\text{Al}_{0.5}\text{O}_2$ sample bar.
- 2) The model of a thermoelectric module of n-type and p-type of $\text{CuFe}_{0.5}\text{Al}_{0.5}\text{O}_2$ bar.

4.4.4.3 THE MODEL OF A $\text{CuFe}_{0.5}\text{Al}_{0.5}\text{O}_2$ SAMPLE BAR.

4.4.4.3.1 THE GEOMETRY DOMAIN

A bar of the $\text{CuFe}_{0.5}\text{Al}_{0.5}\text{O}_2$ sample (**Figure 4.60**) in dimension $4.2 \times 2.5 \times 20 \text{ mm}^3$ was used to calculate on thermoelectric power by applying the temperature difference (ΔT) from 1 to 10 K. The domain of the $\text{CuFe}_{0.5}\text{Al}_{0.5}\text{O}_2$ bar was divided into the Finite Element mesh. The computing results of the thermoelectric properties on the bar of the $\text{CuFe}_{0.5}\text{Al}_{0.5}\text{O}_2$ sample were evaluated.

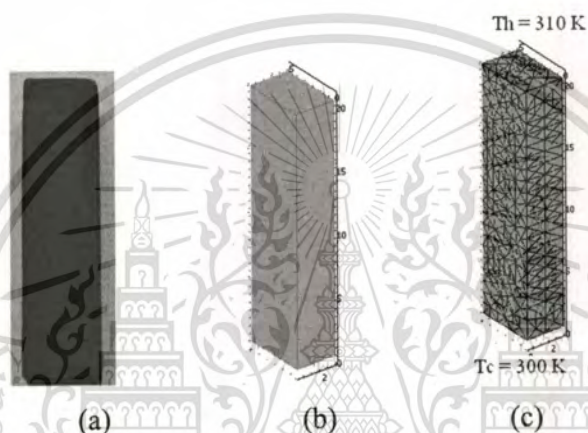


Figure 4.60 (a) The thermoelectric bar. (b) The Finite Element model. And (c) The Finite Element mesh.

4.4.4.3.2 THE BOUNDARY CONDITION

The boundary condition of the Finite element computing for applying on the $\text{CuFe}_{0.5}\text{Al}_{0.5}\text{O}_2$ sample as shown in **Figure 4.60** were set [71-75] as following.

- 1) The boundary conditions on the bar were specified by setting the cold temperature with (T_C) 300 K on the bottom of model.
- 2) The hot temperature (T_H) on the top side of the model was applied by varying the temperature from 301 to 400 K.
- 3) The voltage on bottom side of the modules was fixed to a zero reference level.
- 4) The outside of surface domain was set the symmetry condition by $\hat{n} \cdot \vec{E} = 0$ (no electric field in normal direction to the surface of domain) and $\hat{n} \cdot \vec{q} = 0$ (no thermal flux flow in normal direction to the surface of domain).

4.4.4.3.3 THE MATERIAL PROPERTIES

The material property of Seebeck coefficient, electrical and thermal conductivity of the $\text{CuFe}_{0.5}\text{Al}_{0.5}\text{O}_2$ sample for the finite element computing was applied from measurement results of the $\text{CuFe}_{0.5}\text{Al}_{0.5}\text{O}_2$ sample as in **Figure 4.59** (a),(b), and (c), respectively.

4.4.4.3.4 THE FINITE ELEMENT RESULTS

The Finite Element computing results of the voltage and the temperature distribution on applying the temperature difference from 10 K is shown in **Figure 4.61** (b) and (c), respectively.

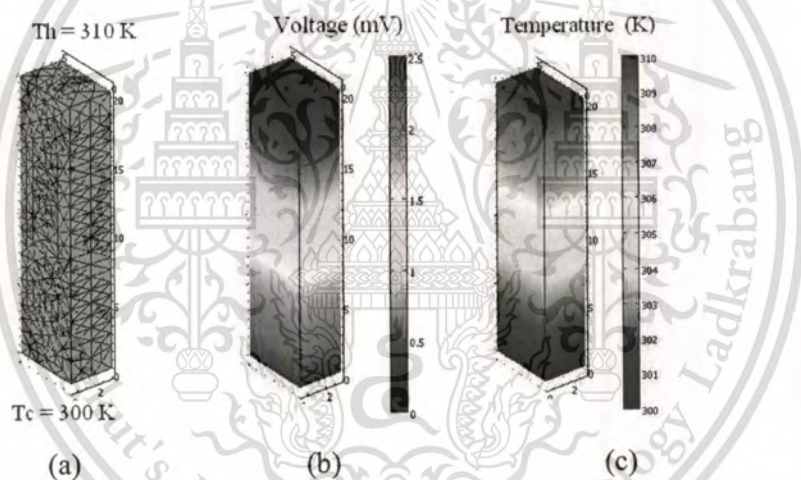


Figure 4.61 (a) The Finite Element model (b) Voltage and (c) Temperature distribution.

The computing results of the output voltage as a function of ΔT between 1 to 10 K are displayed in **Figure 4.62**. The output voltages of the $\text{CuFe}_{0.5}\text{Al}_{0.5}\text{O}_2$ bar are in the range of 0.3 to 2.5 mV in the temperature difference from 2 to 10 K. The results show that the Finite Element result is in close agreement with the experimental results.

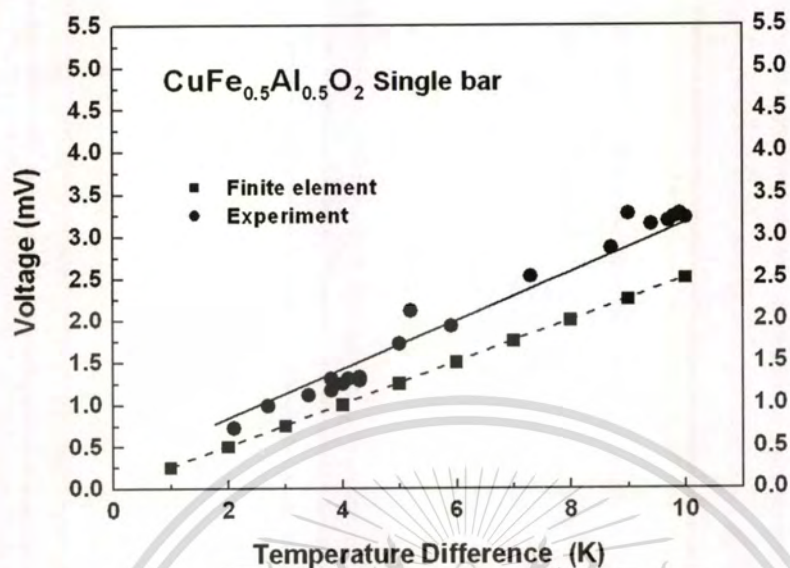


Figure 4.62 The output voltage of the CuFe_{0.5}Al_{0.5}O₂ bar on measurement, and the Finite Element computing.

4.4.4.4 THE MODEL OF A THERMOELECTRIC MODULE

The model a thermoelectric modules is shown in **Figure 4.63**. The thermoelectric module [4, 5] consists of an n-type bar and a p-type bar shape connected with 2 copper plates and has 2 alumina plates covering like a sandwich on top and bottom as shown in **Figure 4.63**.

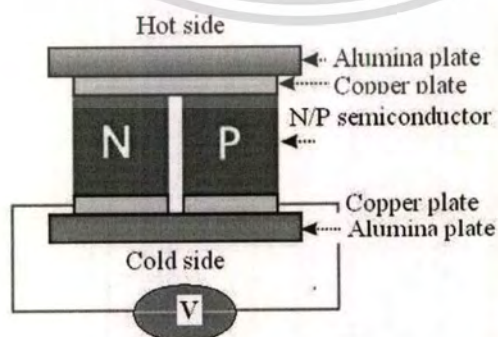


Figure 4.63 The model of thermoelectric module.

4.4.4.4.1 THE GEOMETRY AND FINITE ELEMENT DOMAIN

The Finite Element model for the module thermoelectric of the $\text{CuFe}_{0.5}\text{Al}_{0.5}\text{O}_2$ material is presented in **Figure 4.64** (a). The model consists of the n-type bar and the p-type bar shape connected with the copper plate and has the alumina covering like a sandwich. The domain of the bar and the module were divided in the Finite Element mesh as shown in **Figure 4.64** (b).

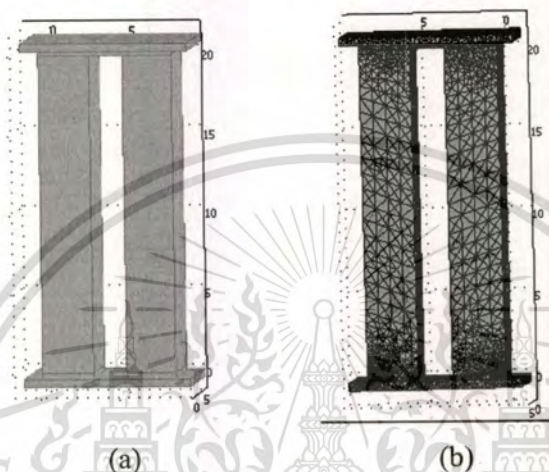


Figure 4.64 (a) The Finite Element model of the thermoelectric module and (b) The Finite Element mesh of the thermoelectric module.

4.4.4.4.2 THE BOUNDARY CONDITIONS

The output voltage was calculated by applying the $\Delta T (T_H - T_C)$ ranging from 1 to 100 K on of the thermoelectric module. The boundary condition [71-74] of the finite element computing for applying on the thermoelectric module as shown in **Figure 4.64** were set as following.

- 1) The boundary condition on the module was specified by setting the cold temperature with (T_C) 300 K on the bottom of model.
- 2) The hot temperature (T_H) on the top side of the model was applied by varying the temperature from 301 to 400 K.
- 3) The voltage on the bottom side of the modules was fixed to a zero reference level.
- 4) The outside of the surface domain was set to symmetry condition $\hat{n} \cdot \vec{E} = 0$ (no electric filed in normal direction to the surface of domain) and $\hat{n} \cdot \vec{q} = 0$ (no thermal flux flow in normal direction to the surface of domain).

4.4.4.4.3 THE MATERIAL PROPERTIES

The material property of the Seebeck coefficient, electrical and thermal conductivity of the p-leg of the thermoelectric module used the thermoelectric properties of the $\text{CuFe}_{0.5}\text{Al}_{0.5}\text{O}_2$ sample as shown in **Figure 4.59** (a), (b), and (c) respectively. For the n-type leg, the Seebeck coefficient was assumed to be the negative values of the Seebeck value of the p-type of the $\text{CuFe}_{0.5}\text{Al}_{0.5}\text{O}_2$ specimen. Other properties of the electrical and the thermal were set similar to the value of the p-leg of the $\text{CuFe}_{0.5}\text{Al}_{0.5}\text{O}_2$ sample.

The copper plate was specified the properties of Seebeck coefficient, electrical and thermal conductivity for $6.5 \mu\text{V/K}$, $5.9 \times 10^6 \text{ S/cm}$, and 3.5 W/cm-K , respectively. The properties of the alumina plate set the electrical and thermal conductivity for 10^{-16} S/cm and 0.4 W/cm-K , respectively.

4.4.4.4.4 THE FINITE ELEMENT RESULTS

The Finite Element results of the voltage and the temperature distribution on the applying ΔT of 100 K is shown in **Figure 4.65** (b) and (c), respectively.

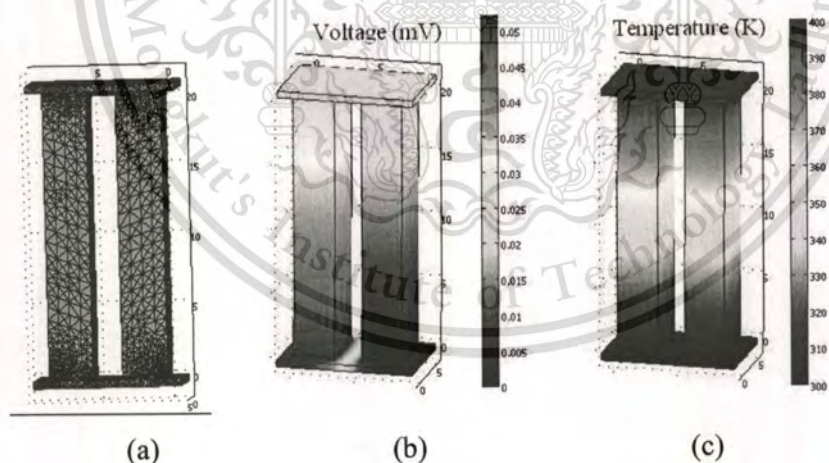


Figure 4.65 (a) The Finite Element mesh (b) Voltage and (c) Temperature distribution.

The computing results of the output voltage for the thermoelectric $\text{CuFe}_{0.5}\text{Al}_{0.5}\text{O}_2$ module on applied ΔT in the range of 1 to 100 K are shown in **Figure 4.66**. The output voltages of the $\text{CuFe}_{0.5}\text{Al}_{0.5}\text{O}_2$ bar are in the range from 5 to 5 mV in the temperature difference 2 to 10 K. The

results remarkably show that the output voltage of the thermoelectric module is two times as high as that of the single thermoelectric of the $\text{CuFe}_{0.5}\text{Al}_{0.5}\text{O}_2$ bar at similar temperature difference.

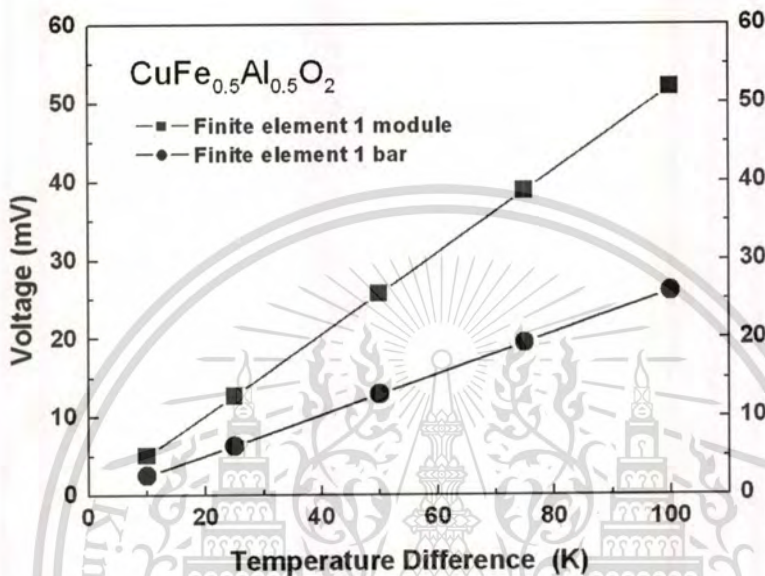


Figure 4.66 The output voltage of the single bar and the modules thermoelectric.

4.4.5 SUMMARIES

The thermoelectric bar and the module of the $\text{CuFe}_{0.5}\text{Al}_{0.5}\text{O}_2$ sample was computed by the Finite Element technique for investigation of the output voltage on applied temperature difference. The model of the thermoelectric bar and the module were divided into the finite element mesh and were solved on personal computer. The results show that the output voltage for the thermoelectric bar model is given ranging from 0.5 to 3 mV on applying temperature difference from 1 to 10K. The result is good agreement with the experimental results of the $\text{CuFe}_{0.5}\text{Al}_{0.5}\text{O}_2$ sample bar. In addition, the investigation is found that the finite element computing on the thermoelectric module gives in 2 times as high as the output voltage of the single $\text{CuFe}_{0.5}\text{Al}_{0.5}\text{O}_2$ bar at similar temperature difference.

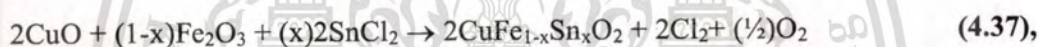
4.5 THERMOELECTRIC PROPERTIES AT HIGH TEMPERATURE OF $\text{CuFe}_{1-x}\text{Sn}_x\text{O}_2$

4.5.1 INTRODUCTION

This section deals with the investigation of the thermoelectric properties of Sn-substituted into the CuFeO_2 delafossite. The Sn^{2+} cations are substituted into the Fe^{3+} sites of the CuFeO_2 compound. The Sn-substituted samples, which are mixed from the SnCl_2 compound, were synthesized in content of $x = 0.01, 0.03, \text{ and } 0.05$ as chemical formula of $\text{CuFe}_{1-x}\text{Sn}_x\text{O}_2$, and their thermoelectric properties were compared to the properties of the CuFeO_2 sample-based.

4.5.2 EXPERIMENTAL PROCEDURE

Polycrystalline samples of the $\text{CuFe}_{1-x}\text{Sn}_x\text{O}_2$ were prepared by a conventional direct solid-state reaction as following equation:



where $x = 0, 0.01, 0.03 \text{ and } 0.05$. The specimens were sintered in furnace at $1050 \text{ }^\circ\text{C}$ in air atmospheres for 15 - 25 h. The obtained samples of $\text{CuFe}_{1-x}\text{Sn}_x\text{O}_2$ are in black color as shown in **Figure 4.67**.

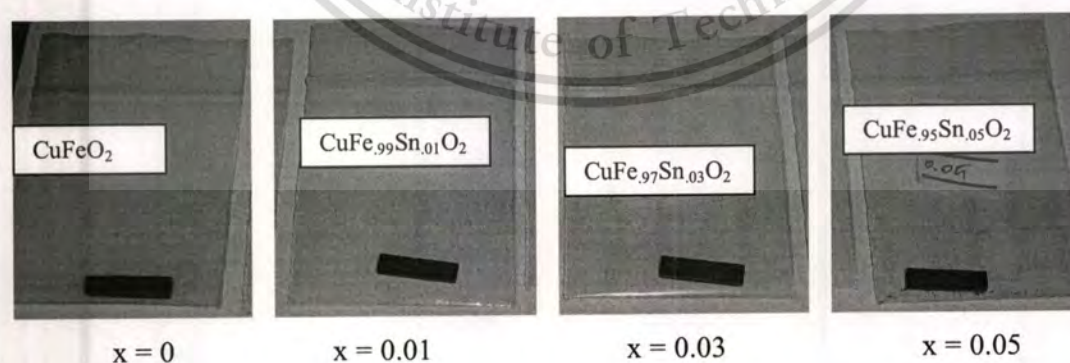


Figure 4.67 The specimen of the $\text{CuFe}_{1-x}\text{Sn}_x\text{O}_2$ samples.

4.5.3 RESULTS AND DISCUSSION

4.5.3.1 X-RAY DIFFRACTION

The XRD patterns of the CuFeO_2 sample-based and the $\text{CuFe}_{1-x}\text{Sn}_x\text{O}_2$ samples in content of the $x = 0.01, 0.03$ and 0.05 are demonstrated in **Figure 4.68**. The XRD peaks of the CuFeO_2 sample-based exhibit crystal phase of the delafossite-type structure for the space group: $R\bar{3}m$ corresponding to the standard ICSD: 01-075-2146 file. Others, the XRD patterns of the $\text{CuFe}_{1-x}\text{Sn}_x\text{O}_2$ samples in content of the $x = 0.01, 0.03$ and 0.05 display all peaks relating to the peak of the CuFeO_2 sample-based.

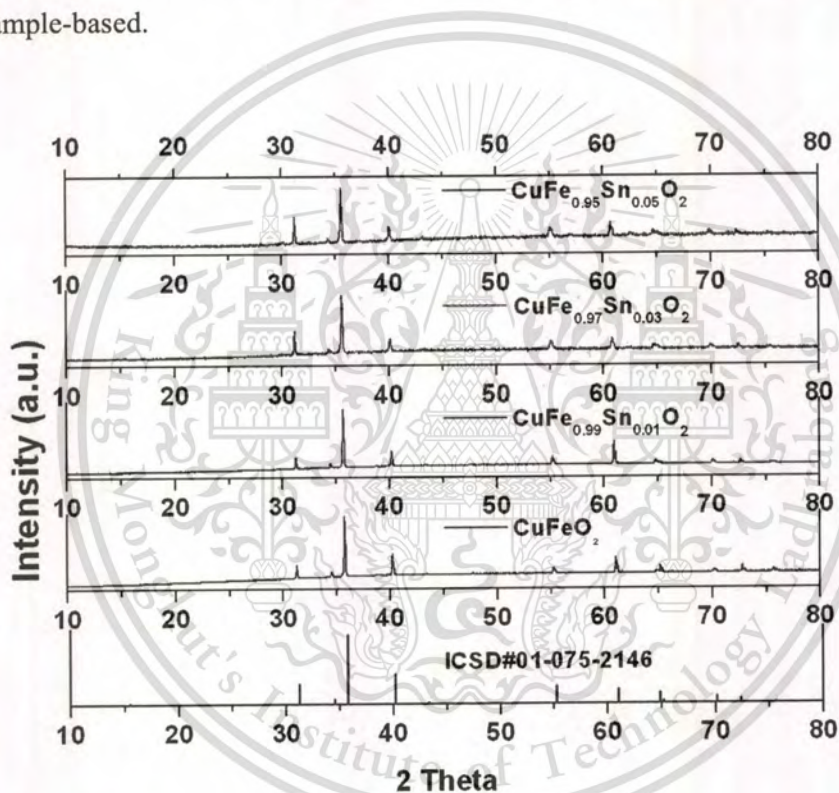


Figure 4.68 The XRD patterns of the CuFeO_2 and the $\text{CuFe}_{1-x}\text{Sn}_x\text{O}_2$ samples with the Sn content of the $x = 0.01, 0.03$ and 0.05 .

The lattice spacing parameter of the CuFeO_2 sample and the $\text{CuFe}_{1-x}\text{Sn}_x\text{O}_2$ samples of the $x = 0.01, 0.03$ and 0.05 are shown in **Figure 4.69**. The lattice constant of the $\text{CuFe}_{1-x}\text{Sn}_x\text{O}_2$ samples depends on the Sn in content of the x . The lattice distance of the CuFeO_2 sample-based of the a-axis and the c-axis 3.0334 \AA and 17.1598 \AA , respectively. The $\text{CuFe}_{1-x}\text{Sn}_x\text{O}_2$ samples, the a-axis and c-axis rapidly increase as increasing the Sn content of the x . The effect of the a-

axis and the c-axis increases with the Sn content of the x due to the partial substitution of the small ion of the Sn^{2+} (1.36 Å) ($\text{Sn}^{4+} = 0.83$ Å) [58, 70] into the Fe^{3+} (0.69 Å) [58, 70] site remaining the Fe^{2+} (0.692 Å) [58, 70] site .

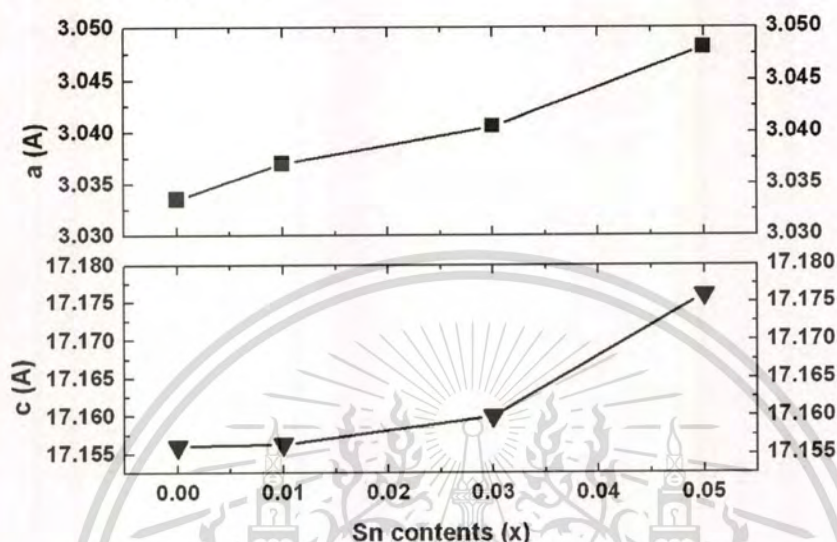


Figure 4.69 The lattice parameters as a function of the Sn concentration in the x content of the $\text{CuFe}_{1-x}\text{Sn}_x\text{O}_2$ ($x=0, 0.01, 0.03,$ and 0.05) samples.

4.5.3.2 DENSITY

The bulk density of the CuFeO_2 sample is 5.22 g/cm^3 , and of the $\text{CuFe}_{1-x}\text{Sn}_x\text{O}_2$ samples in content of the $x = 0.01, 0.03$ and 0.05 are $5.274, 5.173$ and 5.115 g/cm^3 , respectively. The percentage ratios of the bulk density to theoretical density of the CuFeO_2 sample is 96.84%, and of the $\text{CuFe}_{1-x}\text{Sn}_x\text{O}_2$ samples are 95.85%, 94.26% and 93.76% for the content of the $x = 0.01, 0.03$ and 0.05 , respectively.

4.5.3.3 SCANNING ELECTRON MICROSCOPE

The morphology of the microstructure of the CuFeO_2 sample and the $\text{CuFe}_{1-x}\text{Sn}_x\text{O}_2$ samples in the content of the $x = 0.01, 0.03$ and 0.05 as shown in **Figure 4.70**. The microstructure of all samples shows the crystal grand size growing with the increasing of the content of the Sn. The grand size for the content of the $x=0$ and $x=0.01$ is lower than $5 \mu\text{m}$. The grand size for the content of the $x=0.03$ is in $5\text{-}10 \mu\text{m}$, whereas the grand size for the content of the $x=0.05$ is in $10\text{-}40 \mu\text{m}$.

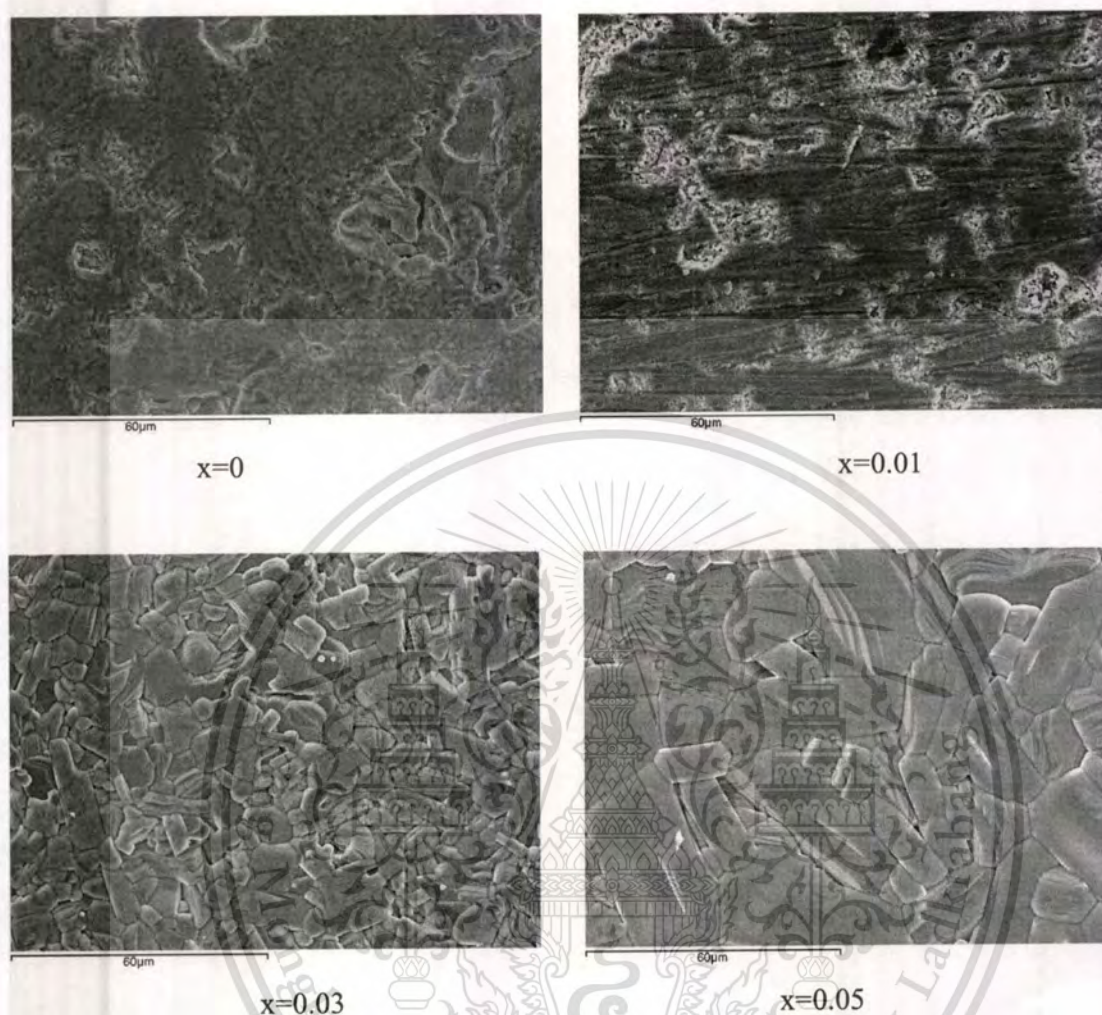


Figure 4.70 The microstructure on surface of the $\text{CuFe}_{1-x}\text{Sn}_x\text{O}_2$ sinter samples.

4.5.3.4 SEEBECK COEFFICIENT

The Seebeck coefficients of the CuFeO_2 sample and the $\text{CuFe}_{1-x}\text{Sn}_x\text{O}_2$ ($x=0.01, 0.03$ and 0.05) samples as a function of temperature in the range from 300 to 960 K are shown in **Figure 4.71**. The results show that the Seebeck coefficients are positive sign over the measured temperature range for all samples. These results indicate that the $\text{CuFe}_{1-x}\text{Sn}_x\text{O}_2$ samples as the Sn^{2+} ions substituted into the Fe^{3+} sites are shown p-type conductor. The all samples show the Seebeck coefficients minimal rising with increasing the temperature. The Seebeck values of the

$\text{CuFe}_{1-x}\text{Sn}_x\text{O}_2$ samples display values higher than that value of the CuFeO_2 sample-based. In addition, the Seebeck values of the $\text{CuFe}_{1-x}\text{Sn}_x\text{O}_2$ samples rapidly decrease as a result of increased the Sn content. The average values of the Seebeck coefficient of all samples increase from 250 to 290 $\mu\text{V}/\text{K}$ with increasing of temperature. The Seebeck values at room temperature are 261, 320, 300 and 270 $\mu\text{V}/\text{K}$ for the content of the $x = 0, 0.01, 0.03$ and 0.05 , respectively, and the Seebeck values at 960 K are 290 330, 300 and 320 $\mu\text{V}/\text{K}$ for the sample of the content of the $x = 0, 0.01, 0.03$ and 0.05 , respectively. The Seebeck values of the content of the $x=0.01$ are higher than that value in all temperature range. The value of the $x=0.01$ is in the range from 330 to 370 $\mu\text{V}/\text{K}$. This value is higher than approximate 1.3 times than that value of the CuFeO_2 sample-based. In summary, the Seebeck values of the $\text{CuFe}_{1-x}\text{Sn}_x\text{O}_2$ samples largely decrease depending on the Sn substitution of the x content. Therefore, the Seebeck values of the $\text{CuFe}_{1-x}\text{Sn}_x\text{O}_2$ samples, which are the Sn^{2+} ions substitution into the Fe^{3+} sites, can be improved by small substitution of the Sn content into the CuFeO_2 compound.

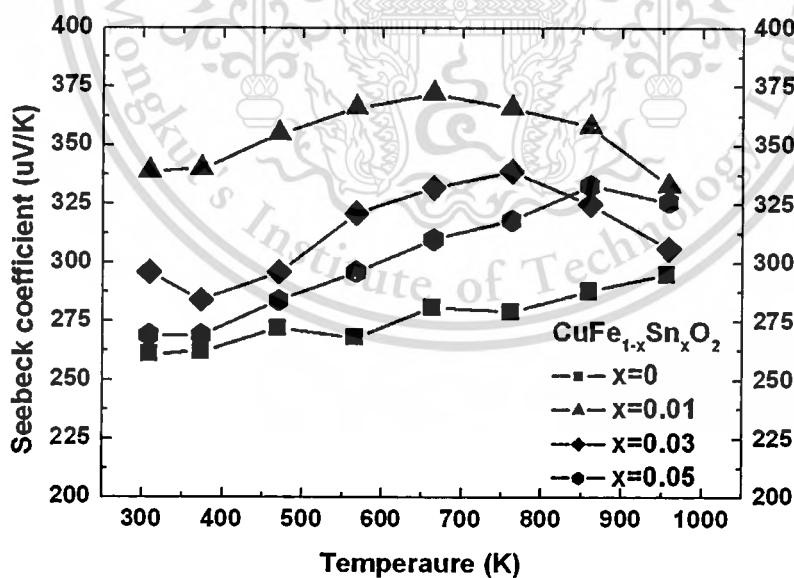


Figure 4.71 The Seebeck coefficient of the $\text{CuFe}_{1-x}\text{Sn}_x\text{O}_2$ ($x=0, 0.01, 0.03$, and 0.05) samples vs. the temperature.

4.5.3.5 EXTENSIONS HEIKES FORMULA

The Heikes formula as application of the spin and orbital degeneracy and association with the carries concentration of the $\text{CuFe}_{1-x}\text{Sn}_x\text{O}_2$ delafossite, the Seebeck coefficient at high temperature is expressed in the relation:

$$S_{T \rightarrow \infty} = -\frac{k_B}{q} \ln\left(\frac{g_3}{g_2}\right) - \frac{k_B}{q} \ln\left[\frac{c}{(1-c)}\right] \quad (4.38),$$

where g_2 is the spin and orbital degeneracy associated with the Fe^{2+} for the CuFeO_2 delafossite,

g_3 is the spin and orbital degeneracy associated with the Fe^{3+} for the CuFeO_2 delafossite,

c is the concentration of the g_4 state.

The Heikes formula (4.38) as application for the $\text{CuFe}_{1-x}\text{Sn}_x\text{O}_2$ delafossite, the transition octahedral oxide of FeO_6 layer produces the degeneracy of electronic state of the Fe^{2+} and Fe^{3+} ions during to crystal field effect to spitting 3d energy state into two state of the t_{2g} and the e_g . The mixed Fe-trivalent of the Fe^{3+} and the Sn^{2+} in the Fe site of the $\text{CuFe}_{1-x}\text{Sn}_x\text{O}_2$ compounds induces to mixed valiancy of the Fe^{3+} and the Fe^{2+} as chemical formula $\text{Cu}^+[\text{Fe}^{3+}]_{1-2x}[\text{Sn}^{4+}]_x[\text{Fe}^{2+}]_x\text{O}_2$. The general state of the Fe^{3+} and the Fe^{2+} in the CuFeO_2 compounds occurs in high spin state. Also, the electronic configuration of the $\text{Fe}^{3+}(3d^5)$ ion is 3 in the t_{2g} state $[(t_{2g})^2]$, and is 2 in the e_g state $[(e_g)^2]$. The $\text{Fe}^{2+}(3d^6)$ ion is 4 in the t_{2g} state $[(t_{2g})^4]$ and 2 in the e_g state $[(e_g)^2]$. The g_3 state of the Fe^{3+} is 6 and the g_2 state of the Fe^{2+} is 15.

The c which is the carrier concentration of concentration of the g_2 state is set to equal the $x = 0.01, 0.03$ and 0.05 .

Therefore, the S value of the $\text{CuFe}_{1-x}\text{Sn}_x\text{O}_2$ delafossite at high temperature is expressed in the relation:

$$S = -(86.17) \ln\left(\frac{6}{15}\right) - (86.17) \ln\left[\frac{x}{(1-x)}\right] \quad (4.39),$$

The S values for the content of the $x = 0.01, 0.03,$ and 0.05 are $474.91, 378.49,$ and $332.67 \mu\text{V/K}$. This result is the limitation of the S value for the $\text{CuFe}_{1-x}\text{Sn}_x\text{O}_2$ compound in high temperature corresponding to the experimental results at 960 K which is not more than the S

value. The equation (4.39) implies that the S value is decreased as increasing the content of x corresponding to the experimental results as in Figure 4.71.

In summary, from experimental results and the Heikes formula, the Seebeck value of the $\text{CuFe}_{1-x}\text{Sn}_x\text{O}_2$ samples, which are the Sn^{2+} ions substitution into the Fe^{3+} sites, can be improved by small substitution of the Sn content into the CuFeO_2 compound due to the mixed valency of the Fe^{3+} and the Fe^{2+} from small substitution of the Sn atom in the transition octahedral oxide of FeO_6 layer caused to crystal field effect splitting the 3d energy state into two state of the t_{2g} and the e_g .

4.5.3.6 ELECTRICAL CONDUCTIVITY

The electrical conductivity (σ) of the CuFeO_2 sample and the $\text{CuFe}_{1-x}\text{Sn}_x\text{O}_2$ samples as a function of the temperature in the range from 300 to 960 K are shown in Figure 4.72. The results show that the electrical conductivity of all samples rapidly increases with increasing the temperature. The electrical values of the $\text{CuFe}_{1-x}\text{Sn}_x\text{O}_2$ sample in content of the $x=0.01$ are lower than that value of the CuFeO_2 sample-based, while the electrical values of the $\text{CuFe}_{1-x}\text{Sn}_x\text{O}_2$ samples in content of the $x=0.03$ and 0.05 are higher than that value of the CuFeO_2 sample-based. The electrical values at room temperature of all samples are 3.5, 1, 2.5 and 8 S/cm, for the content of the $x=0, 0.01, 0.03$ and 0.05 , respectively, and the electrical values at 960 K, are 12.5, 5, 13 and 20 S/cm for $x=0.0, 0.01, 0.03$ and 0.05 respectively. For the sample of the content of the $x=0.05$ at room temperature, the electrical values as in 8.0 S/cm is approximate two times larger than that value of the CuFeO_2 sample as in 3.5 S/cm. The maximum of electrical values is obtained 20 S/cm as in the content of the $x=0.05$ at temperature 960 K. In summary, the electrical conductivity of the $\text{CuFe}_{1-x}\text{Sn}_x\text{O}_2$ samples largely increase depending on the Sn substitution of the x content. Therefore, the electrical conductivity of the $\text{CuFe}_{1-x}\text{Sn}_x\text{O}_2$ samples, which are the Sn^{2+} ions substitution into the Fe^{3+} sites, can be improved by the large substitution of the Sn content into the CuFeO_2 compound. In addition, the electrical conductivity of the $\text{CuFe}_{1-x}\text{Sn}_x\text{O}_2$ samples is increased as increasing of the temperature. Also, the $\text{CuFe}_{1-x}\text{Sn}_x\text{O}_2$ samples are good conductor for using at high temperature.

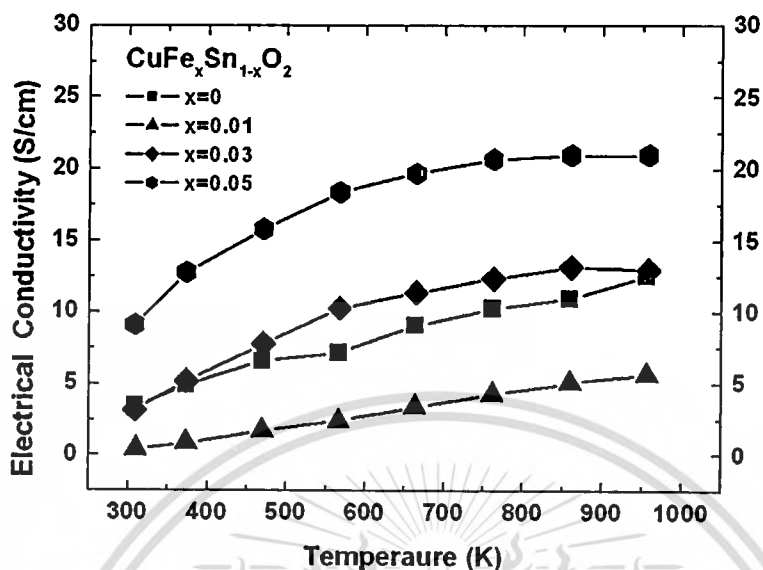


Figure 4.72 The electrical conductivity of the $\text{CuFe}_{1-x}\text{Sn}_x\text{O}_2$ ($x=0, 0.01, 0.03, \text{ and } 0.05$) samples vs. the temperature.

4.5.3.7 POWER FACTOR

The power factor ($PF = \sigma S^2$) of the CuFeO_2 sample and the $\text{CuFe}_{1-x}\text{Sn}_x\text{O}_2$ samples in content of the of the $x=0.01, 0.03$ and 0.05 calculated from the measured electrical conductivity and the Seebeck coefficient as a function of the temperature in the range from 300 to 960 K are shown **Figure 4.73**. The power factor for all samples is increased with increasing temperature. The PF values of the $\text{CuFe}_{1-x}\text{Sn}_x\text{O}_2$ sample in the content of the $x=0.01$ are lower than that value of the CuFeO_2 sample-based, while the PF values of the $\text{CuFe}_{1-x}\text{Sn}_x\text{O}_2$ samples in the content of the $x=0.03$ and 0.05 are higher than that value of the CuFeO_2 sample based. The PF values at room temperature are 0.2×10^{-4} , 0.01×10^{-4} , 0.25×10^{-4} and $0.6 \times 10^{-4} \text{ W/mK}^2$ for the content of the $x=0, 0.01, 0.03$ and 0.05 , respectively, and the PF values at 960 K are 1.1×10^{-4} , 10.6×10^{-4} , 1.25×10^{-4} and $2.25 \times 10^{-4} \text{ W/mK}^2$ for the content of the $x=0, 0.01, 0.03$ and 0.05 respectively. For the sample of the content of the $x=0.05$, the PF value at room temperature displays 2 times higher than that value of the CuFeO_2 sample-based, and the PF value at 960 K displays 4 times higher than that value of the CuFeO_2 sample-based. In summary, the Power Factor of the CuFe_{1-x} .

$x\text{Sn}_x\text{O}_2$ samples, which are the Sn^{2+} ions substitution into the Fe^{3+} sites into the CuFeO_2 compound, is enhanced by the increasing the content of the Sn substitution.

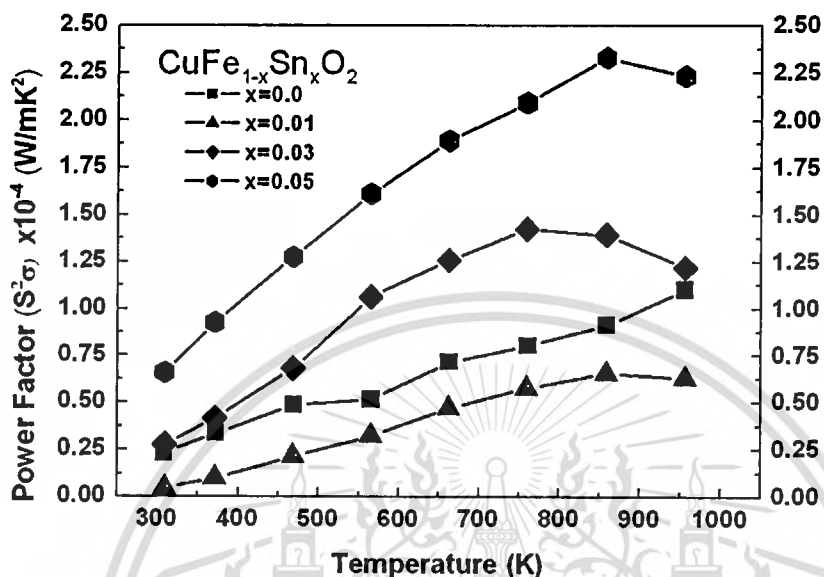


Figure 4.73 The power factor of the $\text{CuFe}_{1-x}\text{Sn}_x\text{O}_2$ ($x=0, 0.01, 0.03,$ and 0.05) samples vs. the temperature.

4.5.3.8 ACTIVATION ENERGY

4.5.3.8.1 ACTIVATION ENERGY OF PRODUCTION OF FREE CARRIERS (E_s)

The relation of the Seebeck coefficient is given by $S = (k_B/e)[(E_F - E_v)/k_B T]$. The activation energy for the production of free carriers $E_s = (E_F - E_v)$ is obtained by plotting the S vs. $1000/T$ as shown in Figure 4.74. The average of the E_s value of the CuFeO_2 sample is 27.5 meV and the $\text{CuFe}_{1-x}\text{Sn}_x\text{O}_2$ samples are 7.47, 18.04, and 29.55 meV for the content of the $x=0.01, 0.03,$ and 0.05 . The results of the content of the $x = 0.01$ and the $x=0.03$ are lower than the thermal energy at room temperature ($k_B T_{300K} \cong 25 \text{ meV}$), while result of the content of the $x=0.05$ is higher than the thermal energy at room temperature. Therefore, the $\text{CuFe}_{1-x}\text{Sn}_x\text{O}_2$ samples, which are the Sn^{2+} ions substitution into the Fe^{3+} sites into the CuFeO_2 compounds, can improve to good conductor by increasing the Sn content to ionize the charge carrier for conduction near the room temperature.

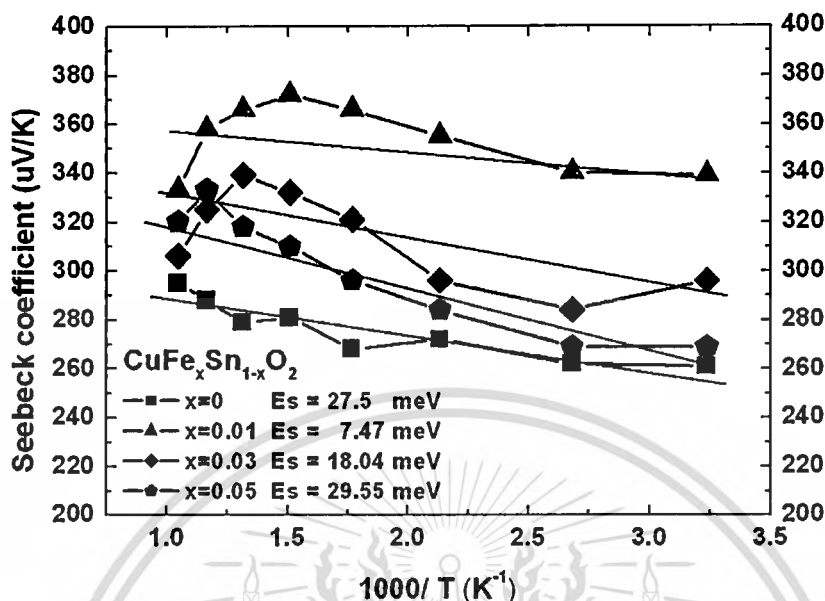


Figure 4.74 The Seebeck coefficient (S) vs. temperature and $1000/T$ curve.

4.5.3.8.2 ACTIVATION ENERGY OF CARRIER CONDUCTION (E_{σ})

An Arrhenius plot of the CuFeO_2 sample and the $\text{CuFe}_{1-x}\text{Sn}_x\text{O}_2$ samples plotted by $\log \sigma$ vs. $1000/T$ with temperature ranging from 300 to 960 K are shown in Figure 4.75. The Arrhenius plot corresponds to the temperature dependent of the equation $\sigma = A \exp(-E_{\sigma}/k_B T)$. The activation energies of carrier conduction (E_{σ}) in the Arrhenius plot, $\log \sigma$ vs. $1000/T$ is 49 meV for the CuFeO_2 sample, and are 104, 58 and 32 meV for the $\text{CuFe}_{1-x}\text{Sn}_x\text{O}_2$ samples in the content of the $x = 0.01$, 0.03 and 0.05, respectively. The activation energies of the carrier conduction for the content of the $x = 0.01$ are higher than that values of the CuFeO_2 sample-based, while values for the content of the $x = 0.03$, and $x = 0.05$ are lower than that values of the CuFeO_2 sample-based. These results show the activation energy for conduction of the $\text{CuFe}_{1-x}\text{Sn}_x\text{O}_2$ samples, which are the Sn^{2+} ions substitution into the Fe^{3+} sites into the CuFeO_2 compounds, are decreased by increasing the Sn content.

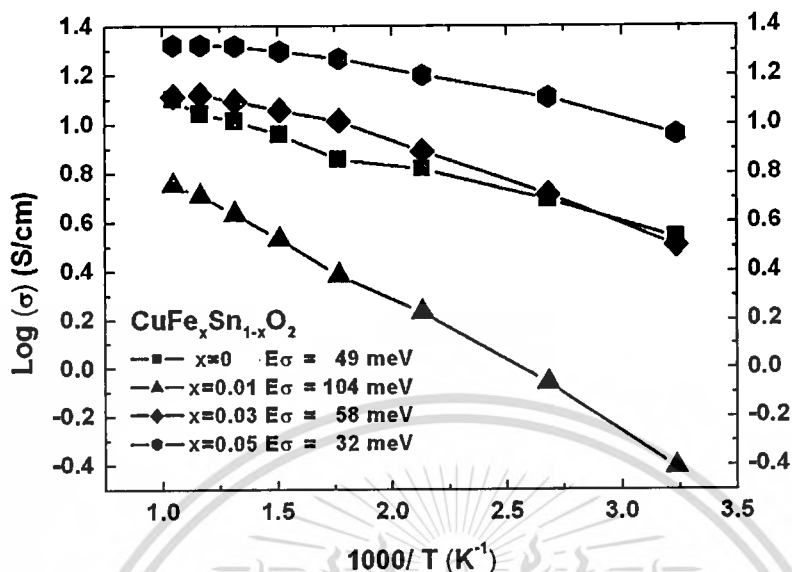


Figure 4.75 The $\log \sigma$ vs. $1000/T$ curve.

4.5.3.8.3 ACTIVATION ENERGY OF CARRIER MOBILITY (E_u)

The electrical conductivity for semiconductor is expressed [35] by $\sigma = eN_T \exp[-(E_F - E_v)/k_B T] \mu_o \exp(-E_u/kT)$. The overall activation energy for conductor (E_σ) is a combination of two components as a relation [35] of $E_\sigma = E_\mu + E_s$. The E_u is obtained by the mobility of carriers as following by a equation $\mu = D \exp(-E_\mu/k_B T)$.

From the activation energy for the production of free carriers (E_s) and activation energy for conductor (E_σ), the activation energy for carrier mobility is 49 meV for the CuFeO_2 sample and are 96.53, 39.96 and 2.45 meV for the $\text{CuFe}_{1-x}\text{Sn}_x\text{O}_2$ samples in the content of the $x = 0.01$, 0.03 and 0.05, respectively. The results show that the activation energy for carrier mobility of the $\text{CuFe}_{1-x}\text{Sn}_x\text{O}_2$ samples, which are the Sn^{2+} ions substituted into the Fe^{3+} sites, can decrease by increasing the Sn content. The value of the E_u implied that the temperature dependent for conductivity of the $\text{CuFe}_{1-x}\text{Sn}_x\text{O}_2$ samples is major activating from the activation energy for carrier production and tiny activating from the mobility activation energy from a small polaron mechanism.

4.5.3.9 THERMAL CONDUCTIVITY

The thermal conductivity of the $\text{CuFe}_{1-x}\text{Sn}_x\text{O}_2$ samples were measured by using a laser flash method by the relation of $\kappa = dC_p a$. The bulk density of the CuFeO_2 sample is 5.22 g/cm^3 , and the $\text{CuFe}_{1-x}\text{Sn}_x\text{O}_2$ samples are 5.27 , 5.17 and 5.11 g/cm^3 , for the content of the $x=0.01$, 0.03 , and 0.05 respectively. The percentage ratios of bulk density to theoretical density of the CuFeO_2 sample are 96.84% , and of the $\text{CuFe}_{1-x}\text{Sn}_x\text{O}_2$ samples are 95.85% , 94.26% and 93.76% , for the content of the $x=0.01$, 0.03 , and 0.05 respectively. All results show that the density of prepared samples is closely to theoretical density.

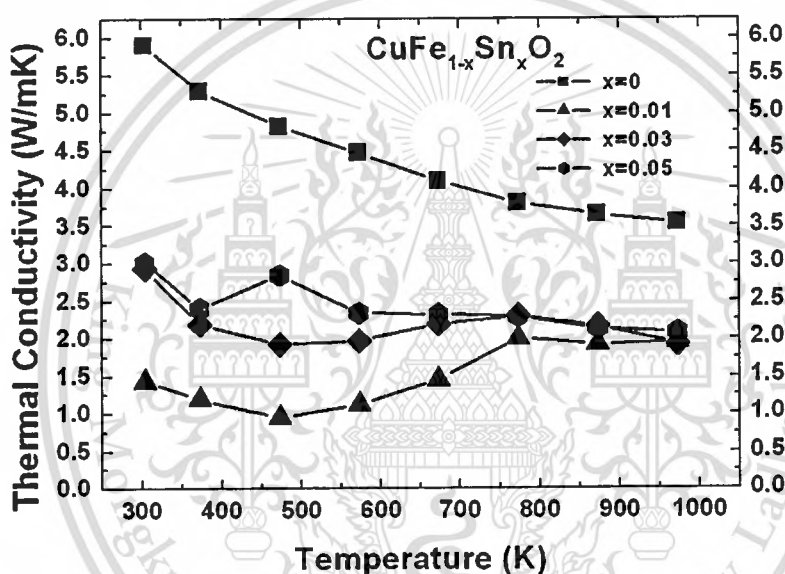


Figure 4.76 The thermal conductivity of the $\text{CuFe}_{1-x}\text{Sn}_x\text{O}_2$ ($x=0, 0.01, 0.03$, and 0.05) samples vs. the temperature.

The results of thermal conductivity (κ) of the CuFeO_2 sample and the $\text{CuFe}_{1-x}\text{Sn}_x\text{O}_2$ samples are shown in **Figure 4.76**. The results show that the thermal conductivity of the $\text{CuFe}_{1-x}\text{Sn}_x\text{O}_2$ ($x=0.01, 0.03$ and 0.05) samples is lower than that value of the CuFeO_2 sample-based in all temperature range. The κ values of the content of the $x=0.01$ show smaller value than that value in all temperature range. The low value of the $x=0.01$ is in the range from 1 to 2 W/m-K . The κ values of the content of the $x=0.03$ and $x=0.05$ display value middle between the CuFeO_2 sample-based and the sample of the content of $x=0.01$. In summary, the thermal conductivity of the $\text{CuFe}_{1-x}\text{Sn}_x\text{O}_2$ samples, which are the Sn^{2+} ions substitution into the Fe^{3+} sites, show the

smaller value than the CuFeO_2 sample-based. Therefore, the thermal conductivity of the $\text{CuFe}_{1-x}\text{Sn}_x\text{O}_2$ samples can be decreased by substitution of the Sn content.

In the lattice thermal conductivity, the phonon scattering process is expressed [31] by

$$\kappa_u = \frac{\delta}{T} \left[\frac{T_m^{3/2} \rho^{2/3}}{M^{7/6}} \right] \quad (4.39),$$

where κ_u is the Umklapp phonon thermal conductivity,

δ is the proportionality constant,

T_m is the melting temperature,

M is the atomic mass,

ρ is the density,

T is the operation temperature.

The equation (4.39) shows that the thermal conductivity is function of the invert of atomic mass. This implied that the thermal conductivity can decrease by selected the compound that has large of atomic mass. For atomic mass, the Fe atom is 55.84 g, and the Sn atom is 118.69 g. In obviously, the atomic mass of the Sn atom is higher than the Fe atom. Therefore, the thermal conductivity of the $\text{CuFe}_{1-x}\text{Sn}_x\text{O}_2$, which are the Sn^{2+} ions substitution into the Fe^{3+} sites, samples are lower than that value of the CuFeO_2 samples-based corresponding to experimental results. In summary, the lower the thermal conductivity of the CuFeO_2 compound is occurred by substitution the large atomic mass into the Fe^{3+} sites.

4.5.3.10 DIMENSIONLESS OF FIGURE OF MERIT (ZT)

The temperature dependence of the ZT value for the CuFeO_2 sample and for the $\text{CuFe}_{1-x}\text{Sn}_x\text{O}_2$ samples for the content of the $x=0.01, 0.03$ and 0.05 in the range from 300 to 960 K are shown in **Figure 4.77**. The results show that the ZT values of all samples are rapidly raised with increasing temperature and increasing the Sn content. The maximum ZT value is 0.1 occurring at 960K in the $\text{CuFe}_{1-x}\text{Sn}_x\text{O}_2$ sample of the content of the $x=0.05$. Moreover, the sample of the content of the $x=0.05$ is higher than 5 times than that value of the CuFeO_2 sample-based at high temperature. The sample of the content of the $x=0.03$ and $x=0.01$ is higher than 2 and 1.5 times

than that value of the CuFeO_2 sample-based. These results indicate that the Sn^{2+} ions substitution into the Fe^{3+} sites of the CuFeO_2 sample is affected to enhance the ZT values at high temperature. In summary, the $\text{CuFe}_{1-x}\text{Sn}_x\text{O}_2$ compounds, which are the Sn^{2+} ions substitution into the Fe^{3+} sites into the CuFeO_2 compound, can be improved the ZT value, which is thermoelectric properties, to good thermoelectric materials in high temperature.

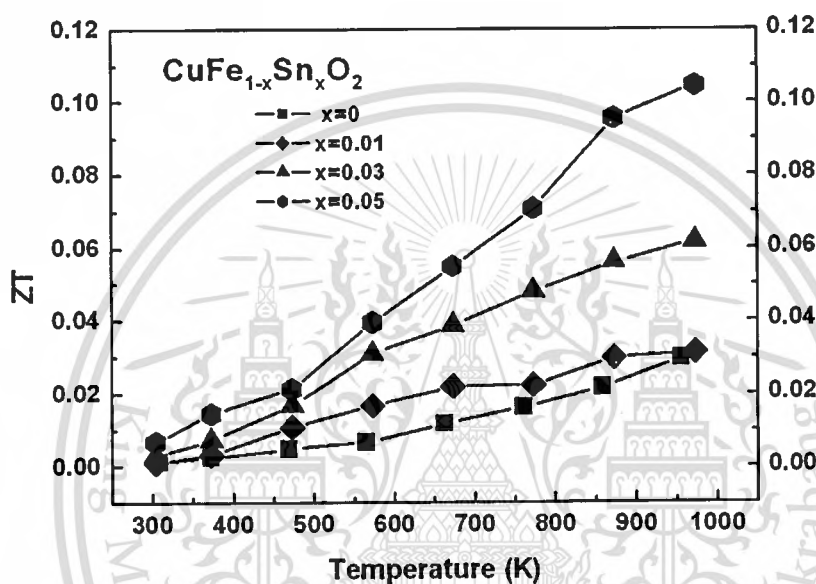


Figure 4.77 The ZT value of the $\text{CuFe}_{1-x}\text{Sn}_x\text{O}_2$ ($x=0, 0.01, 0.03,$ and 0.05) samples vs. temperature.

4.5.4 SUMMARIES

The objective of this section aims to investigate the thermoelectric properties of the substitution of the Sn with 2+ oxidation state into the Fe^{3+} site of the CuFeO_2 compound. The properties of Seebeck coefficient, electrical conductivity and thermal conductivity were measured in the high temperature ranging from 300 to 960 K. The results display that the Seebeck coefficient of the $\text{CuFe}_{1-x}\text{Sn}_x\text{O}_2$ samples display the p-type semiconductor in all temperature range. The Seebeck coefficient of the $\text{CuFe}_{1-x}\text{Sn}_x\text{O}_2$ samples is decreased with increasing the Sn contents. The high of Seebeck coefficient is occurred in small substitution of the Sn content as the content of the $x=0.01$. The electrical conductivity of the $\text{CuFe}_{1-x}\text{Sn}_x\text{O}_2$ samples is increased with increasing the Sn contents. Furthermore, the thermal conductivity of

the $\text{CuFe}_{1-x}\text{Sn}_{1-x}\text{O}_2$ samples is lower than that value of the CuFeO_2 sample-based due to the large atomic mass of the Sn-substituted atom. Obviously, the ZT values of the $\text{CuFe}_{1-x}\text{Sn}_{1-x}\text{O}_2$ samples increase with increasing the Sn content. The high ZT value of this experiment is 0.1 in the content of the $x=0.05$ at temperature 970K. Indeed, the Sn^{2+} ions substitution into the Fe^{3+} sites of the CuFeO_2 compound is affected to enhance thermoelectric properties in the CuFeO_2 delafossite.



4.6 THERMOELECTRIC PROPERTIES AT HIGH TEMPERATURE OF $\text{CuFe}_{1-x}\text{Pb}_x\text{O}_2$

4.6.1 INTRODUCTION

This section deals with the investigation of the thermoelectric properties of Pb-substituted into the CuFeO_2 delafossite. The Pb^{4+} cations are substituted into the Fe^{3+} sites of the CuFeO_2 compound. The Pb-substituted samples, which are mixed from the PbO_2 compound, were synthesized in content of $x = 0.01, 0.03, \text{ and } 0.05$ as the chemical formula of $\text{CuFe}_{1-x}\text{Pb}_x\text{O}_2$, and their thermoelectric properties were compared with the properties of the CuFeO_2 sample-based.

4.6.2 EXPERIMENTAL PROCEDURE

Polycrystalline samples of $\text{CuFe}_{1-x}\text{Pb}_x\text{O}_2$ were prepared by a conventional direct solid-state reaction as following equation:



where $x = 0.01, 0.03 \text{ and } 0.05$. The process was operated on the excess of lead technique because the PbO_2 compound decomposes at 290°C . In the excess of lead technique, the starting powder of the PbO_2 was used in 10 times of the x in the formula (4.40) in this experiment. The specimens were sintered in furnace at 1050°C in air atmospheres for 15 - 25 h. The obtained samples of the $\text{CuFe}_{1-x}\text{Pb}_x\text{O}_2$ are in black color as shown in **Figure 4.78**.

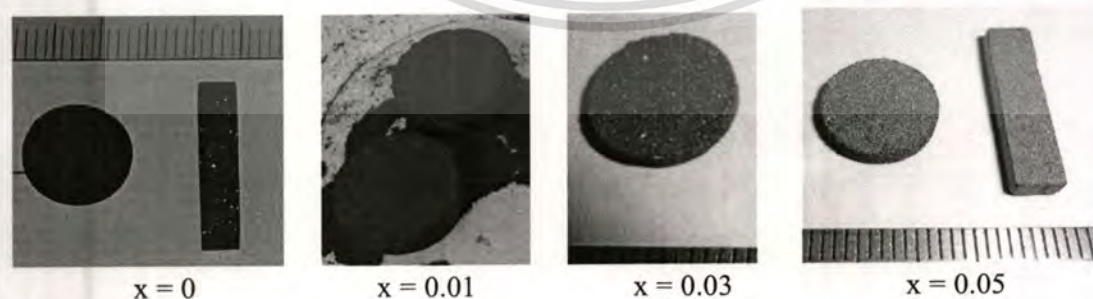


Fig. 4.78 The pellet and bar samples of the $\text{CuFe}_{1-x}\text{Pb}_x\text{O}_2$.

4.6.3 RESULTS AND DISCUSSION

4.6.3.1 X-RAY DIFFRACTION

The XRD patterns of the CuFeO_2 sample and the $\text{CuFe}_{1-x}\text{Pb}_x\text{O}_2$ samples for the content of the $x = 0.01, 0.03$ and 0.05 are demonstrated in **Figure.4.79**. The XRD peaks of the CuFeO_2 sample exhibit crystal phase of the delafossite-type structure for the space group: $R\bar{3}m$ corresponding to the standard ICSD: 01-075-2146 file. Others, the XRD patterns of the $\text{CuFe}_{1-x}\text{Pb}_x\text{O}_2$ samples in the content of the $x = 0.01, 0.03$ and 0.05 display all peaks relation to the peak of the CuFeO_2 sample. The trace impurity peak of the PbO phase relates with the standard JCPDS# 77-1971. The remaining of the PbO phase is resulted from the process of the excess lead technique. The sinter samples show that the $\text{CuFe}_{1-x}\text{Pb}_x\text{O}_2$ samples are formed phase of the delafossite compound with remaining of the impurity of the PbO .

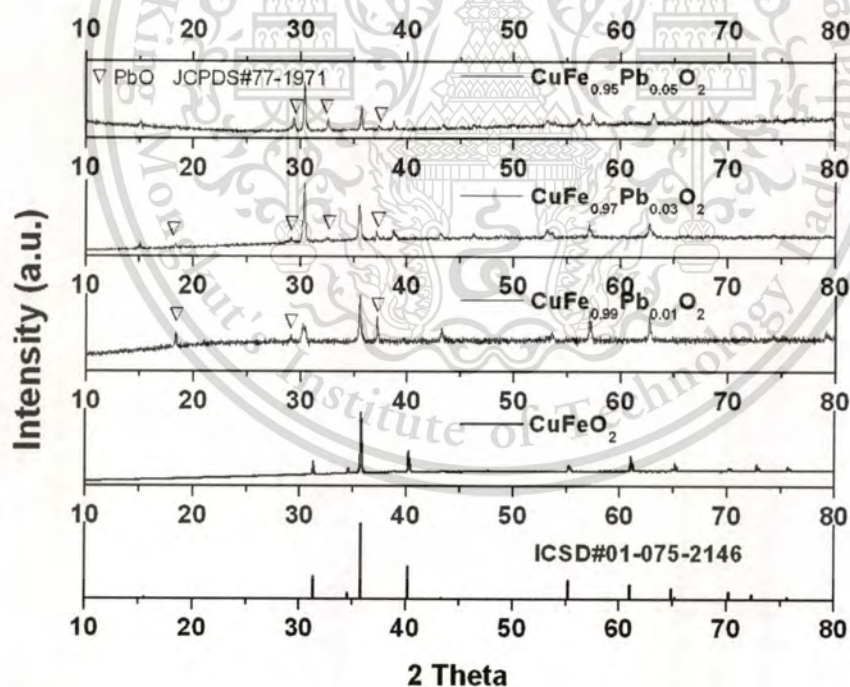


Figure 4.79 The XRD patterns of the CuFeO_2 and the $\text{CuFe}_{1-x}\text{Pb}_x\text{O}_2$ samples with Pb content of $x = 0.01, 0.03$ and 0.05 .

The lattice spacing parameter of the CuFeO_2 sample and the $\text{CuFe}_{1-x}\text{Pb}_x\text{O}_2$ samples of the content of the $x = 0.01, 0.03$ and 0.05 are shown in **Figure 4.80**. The lattice constants of the $\text{CuFe}_{1-x}\text{Pb}_x\text{O}_2$ samples are depended on the Pb in content of the x . The lattice distance of the CuFeO_2 sample for the a-axis and the c-axis are 3.0334 \AA and 17.1598 \AA , respectively. In addition, the a-axis and c-axis of the $\text{CuFe}_{1-x}\text{Pb}_x\text{O}_2$ samples are rapidly increased with increasing the Pb content of the x . The effect of the a-axis and c-axis increases with the Pb content due to the partial substitution of the large ions of the Pb^{4+} (0.915 \AA) [58, 70] into the Fe^{3+} (0.65 \AA) [58, 70] sites and remaining the Fe^{2+} (0.92 \AA) [58, 70] ions.

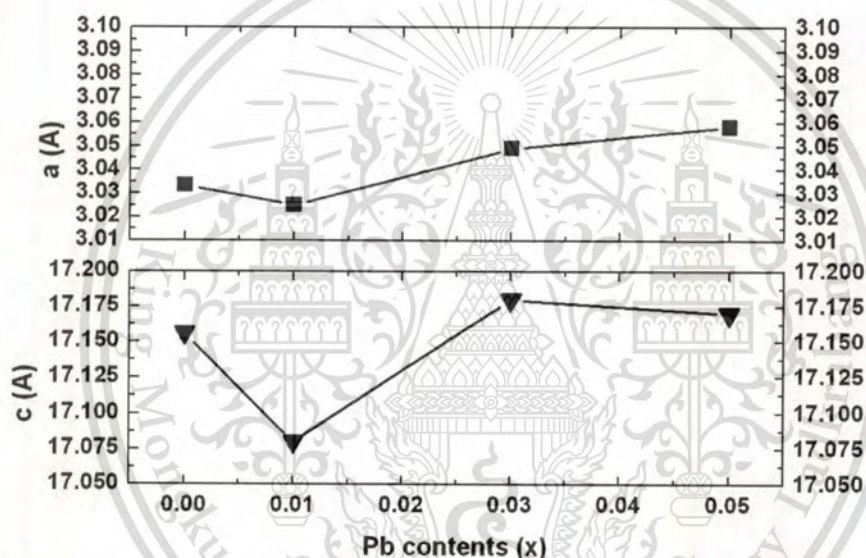


Figure 4.80 The lattice parameters as a function of the Pb concentration in the x content of the $\text{CuFe}_{1-x}\text{Pb}_x\text{O}_2$ ($x=0, 0.01, 0.03$, and 0.05) samples.

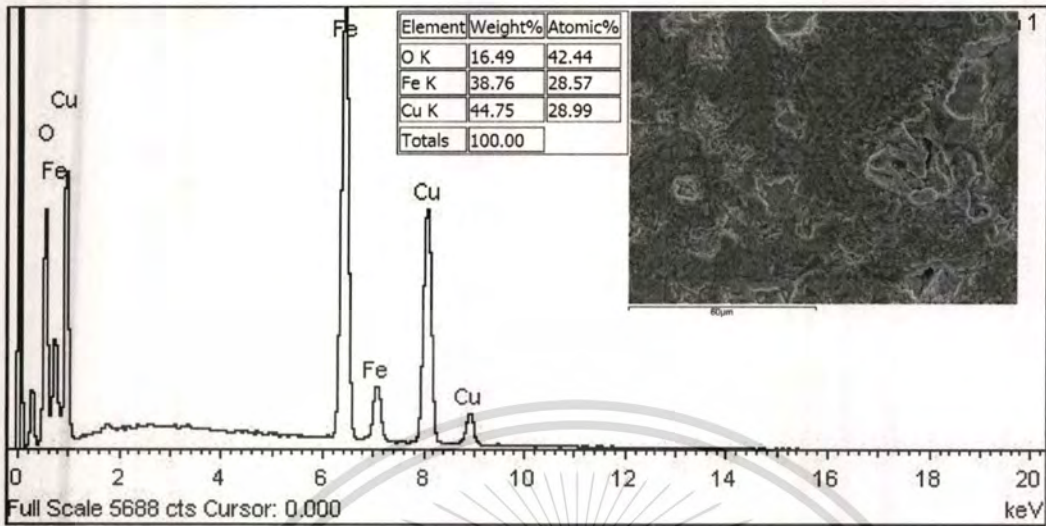
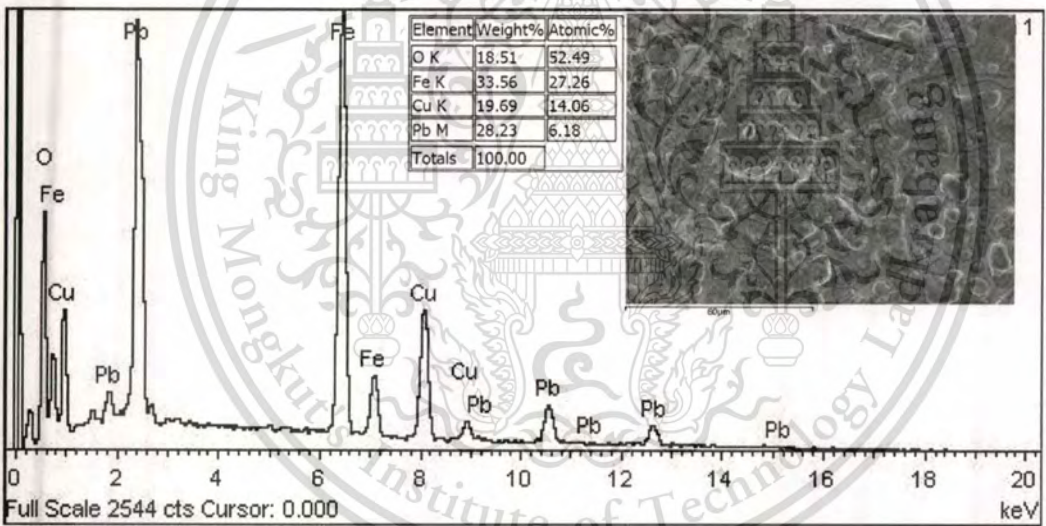
4.6.3.2 DENSITY

The bulk density of the CuFeO_2 sample is 5.22 g/cm^3 , and the $\text{CuFe}_{1-x}\text{Pb}_x\text{O}_2$ samples are $4.715, 5.441$ and 5.107 g/cm^3 for the content of the $x = 0.01, 0.03$ and 0.05 , respectively. The percentage ratios of the bulk density to theoretical density of the CuFeO_2 sample is 96.84% , and of the $\text{CuFe}_{1-x}\text{Pb}_x\text{O}_2$ samples are $84.65\%, 97.14\%$ and 94.22% for the content of the $x = 0.01, 0.03$ and 0.05 , respectively.

4.6.3.3 SCANNING ELECTRON MICROSCOPE

The SEM image and the chemical composition of the CuFeO_2 sample and the $\text{CuFe}_{1-x}\text{Pb}_x\text{O}_2$ ($x=0.03$ and 0.05) samples were simultaneously analysed by scanning electron microscope. The microstructure of the $\text{CuFe}_{1-x}\text{Pb}_x\text{O}_2$ samples of the content of the $x=0.03$ and 0.05 as inserted in **Figure 4.81** (b) and (c) shows the crystal grain size in the range from 10 to 40 μm which is higher than the crystal grain size of the CuFeO_2 sample with ranging from 6 to 10 μm as shown in **Figure 4.81** (a).

The chemical compositions of the CuFeO_2 sample and the $\text{CuFe}_{1-x}\text{Pb}_x\text{O}_2$ ($x=0.03$ and 0.05) samples was determined by using the Energy-Dispersive X-ray spectroscopy (EDX). The compositions result of the $\text{CuFe}_{1-x}\text{Pb}_x\text{O}_2$ samples are show in **Figure 4.81** (b) and (c) compared with the results of the CuFeO_2 sample as show in **Figure 4.81** (a). The peaks of percentage of the weight the $\text{CuFe}_{1-x}\text{Pb}_x\text{O}_2$ samples for the O, the Fe, the Cu and the Pb components are 18.51%, 33.56%, 19.69% and 28.23%, respectively for the $x=0.03$, and are 18.44%, 22.65%, 22.52% and 36.40%, respectively for the $x=0.05$. In addition, the results of the EDX as in **Figure 4.81** (a) can be analyzed the atomic ratio of the Cu and the Fe metal in the CuFeO_2 sample closely to ratio of theoretical stoichiometric of the CuFeO_2 compound. **Figure 4.81** (b) shows that the percentage of the atomic of the $\text{CuFe}_{1-x}\text{Pb}_x\text{O}_2$ samples of the $x = 0.03$ for the Cu, the Fe, the Pb, and the O components are 14.06%, 27.26%, 6.18%, and 52.49%, respectively, and the ratio of Cu:Fe:Pb:O is 1:1.93:0.43:3.73 as different from the ratio of the theoretical stoichiometric formula of the $\text{CuFe}_{0.97}\text{Pb}_{0.03}\text{O}_2$ with in 1:0.97:0.03:2. **Figure 4.81** (c) shows the percentage of the atomic of the $\text{CuFe}_{1-x}\text{Pb}_x\text{O}_2$ samples of the $x = 0.05$ for the Cu, the Fe, the Pb, and the O components are 16.97%, 19.42%, 8.41%, and 55.20%, respectively, and the ratio of Cu:Fe:Pb:O is 1:1.14:0.47:3.25 as different from the ratio of the theoretical stoichiometric formula of the $\text{CuFe}_{0.95}\text{Pb}_{0.05}\text{O}_2$ with in 1:0.95:0.05:2. These results show that the stoichiometric of the $\text{CuFe}_{1-x}\text{Pb}_x\text{O}_2$ samples far from the ration of theoretical stoichiometric the $\text{CuFe}_{1-x}\text{Pb}_x\text{O}_2$ compounds resulting from the remaining of impurity of the PbO as shown in XRD peak.

(a) CuFeO_2 (b) $\text{CuFe}_{1-x}\text{Pb}_x\text{O}_2$ for $x=0.03$

This material is reserved for educational use only, not allowed for commercial use.

Forbidden to modify the content, and cite the document when use.

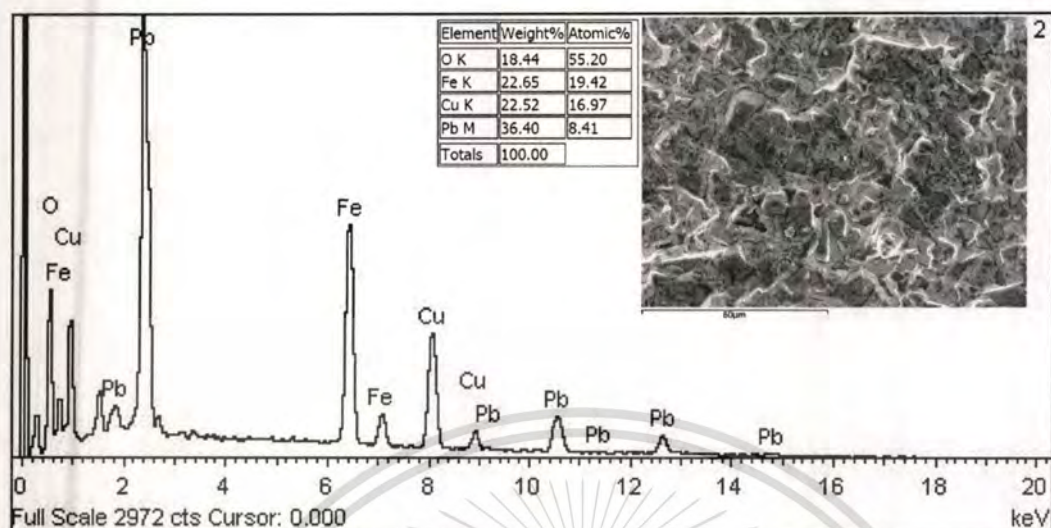
(c) $\text{CuFe}_{1-x}\text{Pb}_x\text{O}_2$ for $x=0.05$

Figure 4.81 The Energy-Dispersive X-ray spectroscopy of sinter sample (a) the CuFeO_2 , (b) $\text{CuFe}_{1-x}\text{Pb}_x\text{O}_2$ for $x=0.03$ and (c) $\text{CuFe}_{1-x}\text{Pb}_x\text{O}_2$ for $x=0.05$.

4.6.3.4. SEEBECK COEFFICIENT

Figure 4.82 shows the Seebeck coefficients of the CuFeO_2 sample and the $\text{CuFe}_{1-x}\text{Pb}_x\text{O}_2$ ($x=0.01, 0.03$ and 0.05) samples as a function of temperature in the range of 300 to 960 K. The results show that the Seebeck coefficients of the Pb substitution for the content of the $x=0.01, 0.03$ and 0.05 are negative sign over the measured temperature range for all samples. These results indicate that the $\text{CuFe}_{1-x}\text{Pb}_x\text{O}_2$ samples as the Pb^{4+} ions substituted into the Fe^{3+} sites show n-type conductor of the thermoelectric materials. Moreover, absolute value of the Seebeck coefficient of the $\text{CuFe}_{1-x}\text{Pb}_x\text{O}_2$ samples for the content of the $x=0.03$ and $x=0.05$ tends to increase with increasing temperature. The Seebeck coefficients at 300 K for the CuFeO_2 sample are $261 \mu\text{V/K}$, and for the $\text{CuFe}_{1-x}\text{Pb}_x\text{O}_2$ samples are $-65.29, -79.6,$ and $-88.31 \mu\text{V/K}$ for the content of the $x = 0.01, 0.03$ and 0.05 , respectively. In addition, all results show that the Seebeck coefficient of the $\text{CuFe}_{1-x}\text{Pb}_x\text{O}_2$ samples depends on increasing of the temperature. In summary, the n-type in CuFeO_2 delafossite can be occurred by substituting the Pb^{4+} ions into the Fe^{3+} sites.

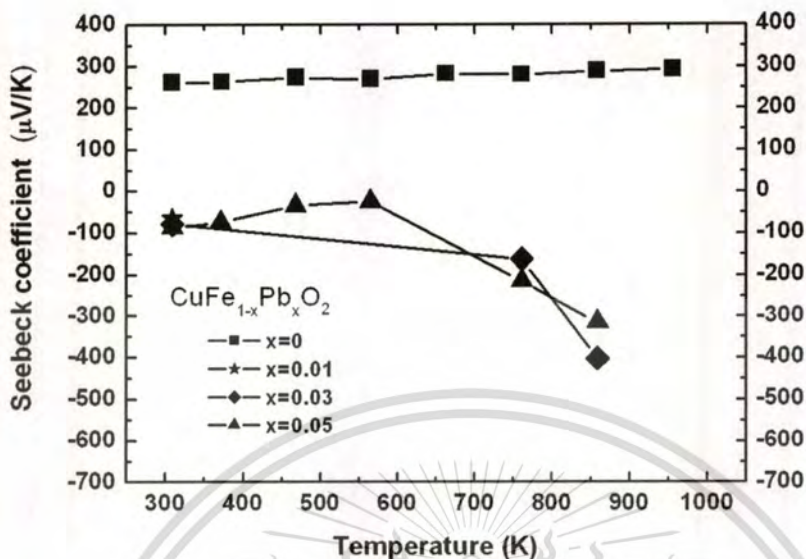


Figure 4.82 The Seebeck coefficient of the $\text{CuFe}_{1-x}\text{Pb}_x\text{O}_2$ ($x=0, 0.01, 0.03,$ and 0.05) samples vs. the temperature.

4.6.3.5 EXTENSIONS HEIKES FORMULA

The Heikes formula as application of the spin and orbital degeneracy associating to the carries concentration of the $\text{CuFe}_{1-x}\text{Pb}_x\text{O}_2$ samples, the Seebeck coefficient at high temperature is expressed in the relation:

$$S_{T \rightarrow \infty} = -\frac{k_B}{q} \ln\left(\frac{g_3}{g_2}\right) - \frac{k_B}{q} \ln\left[\frac{c}{(1-c)}\right] \quad (4.41),$$

where g_2 is the spin and orbital degeneracy associated with the Fe^{2+} for the CuFeO_2 delafossite, g_3 is the spin and orbital degeneracy associated with the Fe^{3+} for the CuFeO_2 delafossite, c is the concentration of the g_2 state.

The mixed B-trivalent of the Fe^{3+} and the Pb^{4+} in the B site of the $\text{CuFe}_{1-x}\text{Pb}_x\text{O}_2$ samples induces to mixed valency of the Fe^{3+} and the Fe^{2+} as in chemical formula $\text{Cu}^+[\text{Fe}^{3+}]_{1-2x}[\text{Fe}^{2+}]_x[\text{Pb}^{4+}]_x\text{O}_2$. The general state of the Fe^{3+} and the Fe^{2+} in the CuFeO_2 compounds occurs in high spin state. Also, the electronic configuration of the $\text{Fe}^{3+}(3d^5)$ ion is 3 in the t_{2g} state $[(t_{2g})^2]$, and is 2 in the e_g state $[(e_g)^2]$. The $\text{Fe}^{2+}(3d^6)$ ion is 4 in the t_{2g} state

$[(t_{2g})^4]$ and 2 in the e_g state $[(e_g)^2]$. The g_3 state of the Fe^{3+} is 6 and the g_2 state of the Fe^{2+} is 15.

The c which is the carrier concentration of concentration of the g_2 state is set to equal the $x = 0.01, 0.03$ and 0.05 .

Therefore, the S value of the $CuFe_{1-x}Pb_xO_2$ compound in the high temperature is expressed in equation:

$$S = -(86.17) \ln\left(\frac{6}{15}\right) - (86.17) \ln\left[\frac{x}{(1-x)}\right] \quad (4.42),$$

The S values for the $x = 0.01, 0.03,$ and 0.05 are $-474.91, -378.49,$ and $-332.67 \mu V/K,$ respectively. These results are limited of S values for the $CuFe_{1-x}Pb_xO_2$ compound in high temperature corresponding to the experimental results at $960 K$ which is not more than the S value.

4.6.3.6 ELECTRICAL CONDUCTIVITY

The electrical conductivity (σ) of the $CuFeO_2$ sample and the $CuFe_{1-x}Pb_xO_2$ samples as a function of the temperature in the range of 300 to $960 K$ are shown in **Figure 4.83**. The results show that the electrical conductivity of the $CuFe_{1-x}Pb_xO_2$ ($x=0.03$ and 0.05) samples are rapidly raised with increasing the temperature. The σ values at $300K$ for the $CuFeO_2$ sample are $3.4 S/cm,$ and for the $CuFe_{1-x}Pb_xO_2$ samples are $0.00251, 0.0002$ and $0.001 S/cm$ for content of the $x= 0.01, 0.03$ and 0.05 respectively. Moreover, the all results of the $CuFe_{1-x}Pb_xO_2$ ($x=0.01, 0.03$ and 0.05) show value smaller than that value of the $CuFeO_2$ sample-based in 2 to 3 order of magnitude. These results point out that the Pb^{4+} substitution into Fe^{3+} site into the $CuFeO_2$ compound is affected to decrease the electrical conductivity.

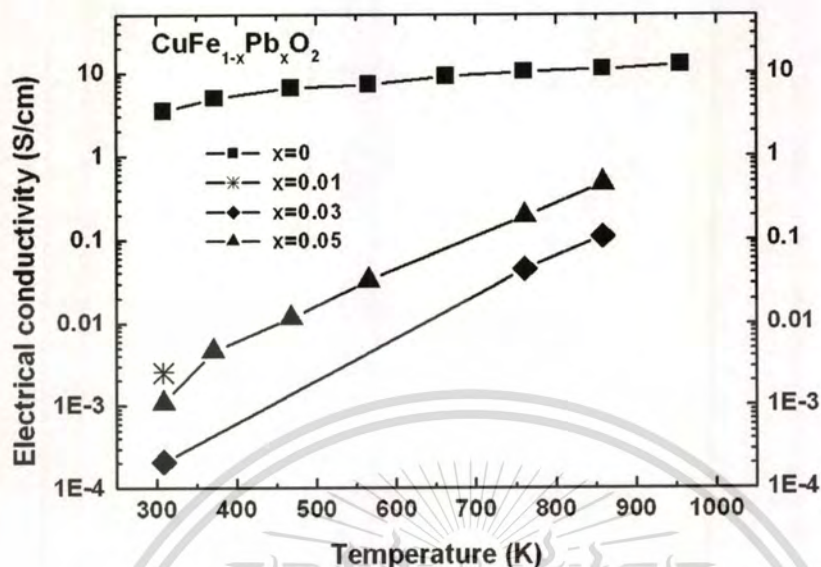


Figure 4.83 The electrical conductivity the $\text{CuFe}_{1-x}\text{Pb}_x\text{O}_2$ ($x=0, 0.01, 0.03, \text{ and } 0.05$) samples vs. the temperature.

4.6.3.7 THERMAL CONDUCTIVITY

The thermal conductivity of the CuFeO_2 sample and the $\text{CuFe}_{1-x}\text{Pb}_x\text{O}_2$ samples were measured by using a laser flash method in the relation of $\kappa = dC_p a$. The bulk density of the CuFeO_2 sample is 5.22 g/cm^3 , and the $\text{CuFe}_{1-x}\text{Pb}_x\text{O}_2$ samples are 5.441 and 5.107 g/cm^3 , for the content of the $x=0.03$, and 0.05 respectively. The percentage ratios of bulk density to theoretical density of the CuFeO_2 sample are 96.84% , and of the $\text{CuFe}_{1-x}\text{Pb}_x\text{O}_2$ samples are 97.14% and 94.22% for the content of the $x=0.01, 0.03, \text{ and } 0.05$, respectively. All results show that the density of sintered samples is closely to theoretical density.

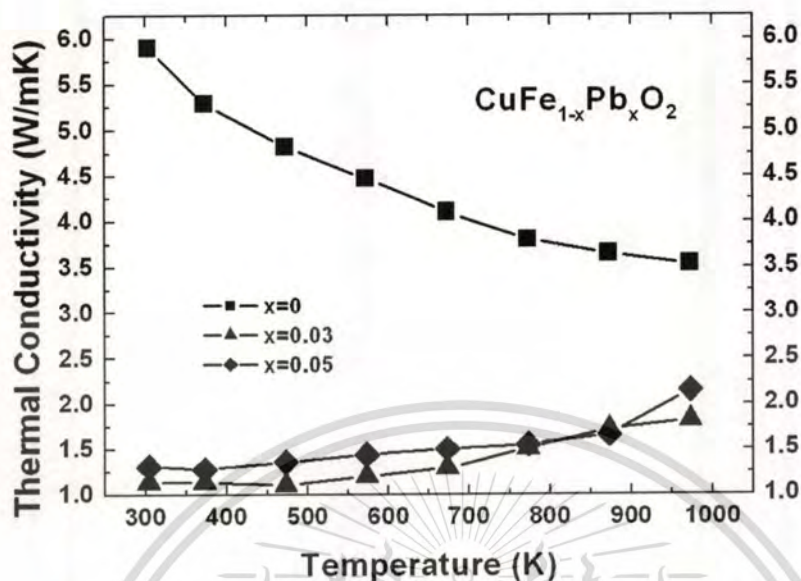


Figure 4.84 The thermal conductivity of the $\text{CuFe}_{1-x}\text{Pb}_x\text{O}_2$ ($x=0, 0.03,$ and 0.05) samples vs. the temperature.

The thermal conductivity (κ) of the CuFeO_2 sample and the $\text{CuFe}_{1-x}\text{Pb}_x\text{O}_2$ ($x=0.03,$ and $x=0.05$) samples are shown in **Figure 4.84**. The results show that the thermal conductivity of the $\text{CuFe}_{1-x}\text{Pb}_x\text{O}_2$ samples for the content of the $x=0.03$ and 0.05 are lower than that value of the CuFeO_2 sample-based in all temperature range. The κ values of the $\text{CuFe}_{1-x}\text{Pb}_x\text{O}_2$ ($x=0.03$ and 0.05) samples minimally increase with increasing the temperature as the average in ranging from 1.3 to 2.0 W/m-K. In addition, the κ values of the $\text{CuFe}_{1-x}\text{Pb}_x\text{O}_2$ samples are less than the values of the CuFeO_2 sample-based in 3 times. In summary, the thermal conductivity of the $\text{CuFe}_{1-x}\text{Pb}_x\text{O}_2$ samples, which are the Pb^{4+} ions substituting into the Fe^{3+} sites, show the smaller value than the CuFeO_2 sample-based. Therefore, the thermal conductivity of the CuFeO_2 compound can be decreased by substitution of the Pb content into the Fe sites.

The effect is contributed by the atomic mass of the Pb as in 207.19 g higher than the atomic mass of the Fe as in 55.84 g. Therefore, the thermal conductivity of the $\text{CuFe}_{1-x}\text{Pb}_x\text{O}_2$ sample is lower than that value of the CuFeO_2 sample-based. In summary, the lower of the thermal conductivity is occurred in large of the molecule mass of the compound. Indeed, the Pb substitution into the Fe site of the CuFeO_2 compound is affected to decrease the thermal conductivity.

4.6.3.8 DIMENSIONLESS OF FIGURE OF MERIT (ZT)

The temperature dependence of the ZT value of the CuFeO_2 sample and the $\text{Cu}_{1-x}\text{Pb}_x\text{FeO}_2$ ($x=0.03$ and 0.05) samples in the temperature range from 300 to 900 K are exhibited in **Figure 4.85**. The results show that the ZT values of all samples are rapidly raised with increasing the temperature. Obviously, the ZT values of the $\text{Cu}_{1-x}\text{Pb}_x\text{FeO}_2$ ($x=0.03$ and 0.05) samples are lower than that value of the CuFeO_2 samples-based in all temperature range. In summary, the Pb^{4+} ions substitution into the Fe^{3+} sites of the CuFeO_2 compound are affected to reduce the ZT value.

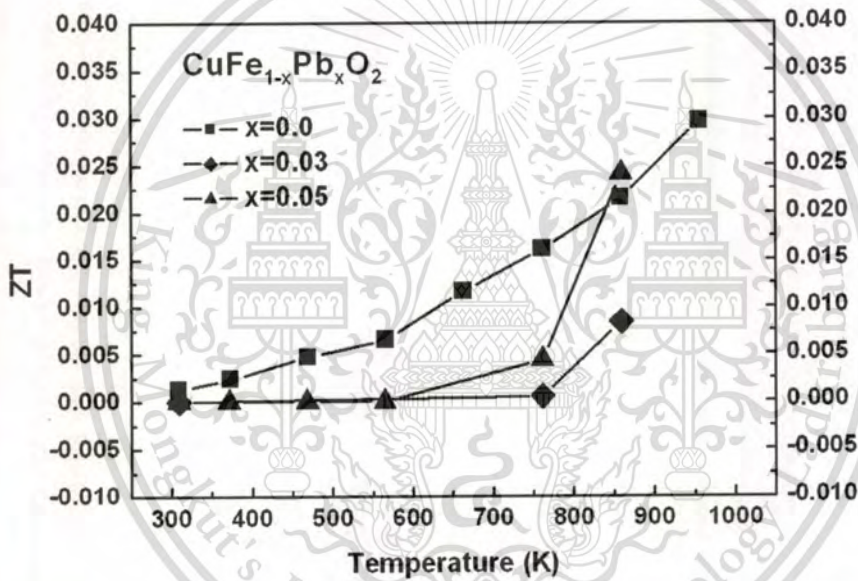


Figure 4.85 The ZT value of the $\text{CuFe}_{1-x}\text{Pb}_x\text{O}_2$ ($x=0, 0.03,$ and 0.05) samples vs. temperature.

4.6.4 SUMMARIES

The objective of this work aims to investigate the thermoelectric properties of the substitution of the Pb with 4^+ oxidation state into Fe^{3+} site of the CuFeO_2 compound. The Seebeck coefficient, electrical conductivity and thermal conductivity were measured in the high temperature from 300 to 900 K. The results display that the Seebeck coefficient of the $\text{CuFe}_{1-x}\text{Pb}_x\text{O}_2$ samples display the n-type semiconductor due to the Pb^{4+} ions substitution into the Fe^{3+}

sites. The absolute Seebeck coefficient of the $\text{CuFe}_{1-x}\text{Pb}_x\text{O}_2$ samples display higher than the value of the CuFeO_2 samples-based. The electrical conductivity of the $\text{CuFe}_{1-x}\text{Pb}_x\text{O}_2$ samples is lower than that value of the CuFeO_2 samples-based in 2 to 3 order of magnitude. Obviously, the thermal conductivity of the $\text{CuFe}_{1-x}\text{Pb}_x\text{O}_2$ samples is lower than the value of the CuFeO_2 sample-based resulting from the large atomic mass of the Pb-substituted atom. In addition, the ZT values of the $\text{CuFe}_{1-x}\text{Pb}_x\text{O}_2$ samples are lower than that value of the CuFeO_2 sample-based. Indeed, the Pb^{4+} ions substitution into the Fe^{3+} sites of the CuFeO_2 compound is affected to convert the type of thermoelectric from p-type to n-type.



4.7 PROTOTYPE OF THERMOELECTRIC MODULE

OF $p\text{-Cu}_{0.95}\text{Pt}_{0.05}\text{FeO}_2$ AND $n\text{-CuFe}_{0.95}\text{Pb}_{0.05}\text{O}_2$

4.7.1 INTRODUCTION

This chapter deals with the invention of prototype of thermoelectric module. The modules were invented with consisting of one couple of p-leg and n-leg, and two couples of p-leg and n-leg. The p-leg of the modules was invented from the $\text{Cu}_{0.95}\text{Pt}_{0.05}\text{FeO}_2$ sample, and the n-leg of modules was invented from the $\text{CuFe}_{0.95}\text{Pb}_{0.05}\text{O}_2$ sample. Furthermore, the modules of thermoelectric were measured the output voltage and electrical current in temperature difference. Finally, the results of output of voltage, electric current and electric power were repowered.

4.7.2 GEOMETRY OF MODULES

In general, the thermoelectric modules are assembled from several n-legs and p-legs of thermoelectric material. A module of the thermoelectric generator [4-5] consists of two legs of conductor type. One leg is an n-type conductor and another leg is p-type conductor of thermoelectric material. For thermoelectric module, the n-leg and the p-leg are connected by copper plate as shown in Figure 4.86. Copper wires were used to connect with the modules for flowing of electrical current. The top and the bottom of the module are attached by alumina plates for conducting of external heat and insulating of electric current. The top of module was set for passing the hot temperature, and the bottom module was set for passing the cold temperature. For thermoelectric generator, temperature gradient was operated between the top side and bottom site of the module.

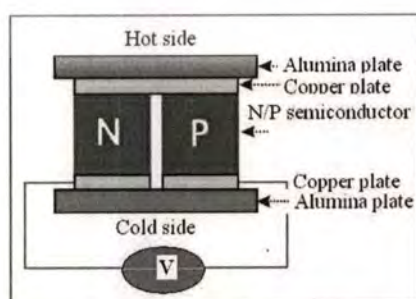


Figure 4.86 The model of thermoelectric module.

This work, the prototype of thermoelectric module was assembled by using the p-leg from the $\text{Cu}_{0.95}\text{Pt}_{0.05}\text{FeO}_2$ specimen with cutting in dimension $3.0 \times 5.0 \times 5 \text{ mm}^3$ and the n-leg from the $\text{CuFe}_{0.95}\text{Pb}_{0.05}\text{O}_2$ specimen with cutting in dimension $2.0 \times 5.0 \times 5 \text{ mm}^3$. The modules were invented in 1 couple and 2 couples of the n-p leg module. The 1 couple of the p-n leg module is consisted of one p-leg from the $\text{Cu}_{0.95}\text{Pt}_{0.05}\text{FeO}_2$ specimen and one n-leg from the $\text{CuFe}_{0.95}\text{Pb}_{0.05}\text{O}_2$ specimen as shown in **Figure 4.87**. Another, the 2 couples of the p-n leg module are consisted of two p-legs from the $\text{Cu}_{0.95}\text{Pt}_{0.05}\text{FeO}_2$ specimen and two n-legs from the $\text{CuFe}_{0.95}\text{Pb}_{0.05}\text{O}_2$ specimen as shown in **Figure 4.87**.



Figure 4.87 The prototypes of thermoelectric module.

4.7.3 THE ASSEMBLE PROCESS OF THERMOELECTRIC MODULES

The process to invent the thermoelectric modules consists of:

- 1) The specimens of the $\text{Cu}_{0.95}\text{Pt}_{0.05}\text{FeO}_2$ sample and of the $\text{CuFe}_{0.95}\text{Pb}_{0.05}\text{O}_2$ sample were cut in dimension $3.0 \times 5.0 \times 5 \text{ mm}^3$ and $2.0 \times 5.0 \times 5 \text{ mm}^3$, respectively, as shown in **Figure 4.88**.

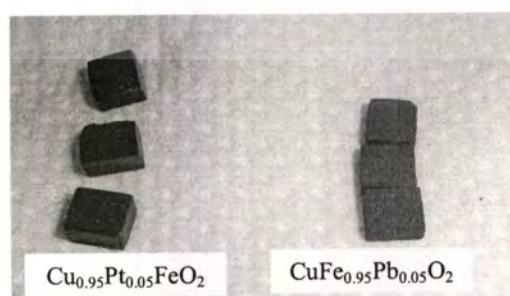


Figure 2.88 The specimens of the $\text{Cu}_{0.95}\text{Pt}_{0.05}\text{FeO}_2$ and the $\text{CuFe}_{0.95}\text{Pb}_{0.05}\text{O}_2$ samples.

2) The copper plates were contacted on the top surface of alumina plate between position of putting the n-leg and the p-leg for flowing of electric current. The alumina plate is used for insulator of the electric current and for the heat transfer as shown in **Figure 4.89**.

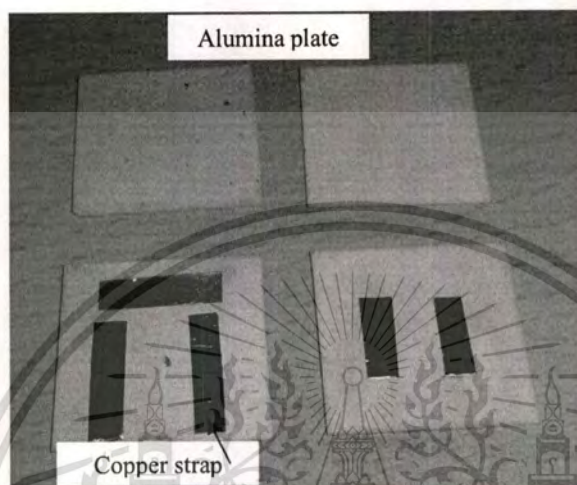


Figure 4.89 The copper straps contacted on the top surface of alumina plate.

3) Copper strap was used for connected the p-legs of the $\text{Cu}_{0.95}\text{Pt}_{0.05}\text{FeO}_2$ sample and the n-legs of the $\text{CuFe}_{0.95}\text{Pb}_{0.05}\text{O}_2$ sample. The silver paint, which is high electric conductor, was used to glue the specimen of n-leg and p-leg with copper plate. The module of the 1 couple of the p-n leg as one p-leg from the $\text{Cu}_{0.95}\text{Pt}_{0.05}\text{FeO}_2$ specimen and one n-leg from the $\text{CuFe}_{0.95}\text{Pb}_{0.05}\text{O}_2$ specimen is shown in **Figure 4.90 (a)**. The module of 2 couples of the n-p leg module as the 2 p-leg from the $\text{Cu}_{0.95}\text{Pt}_{0.05}\text{FeO}_2$ specimen and the 2 n-leg from the $\text{CuFe}_{0.95}\text{Pb}_{0.05}\text{O}_2$ specimen are shown in **Figure 4.90 (b)**.

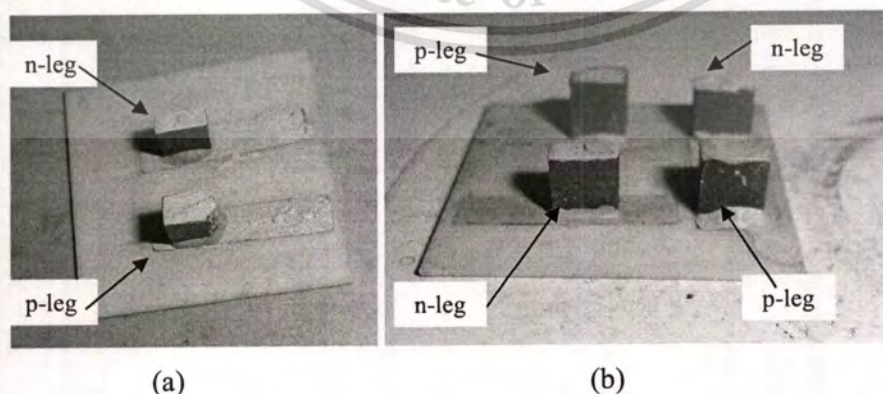


Figure 4.90 (a) The 1 couple of the n-p leg module and **(b)** the 2 couples of the n-p leg module.

4) The copper straps were attached on the top of n-leg specimen and the top of p-leg for connecting of flowing of the electric current circuit as shown in **Figure 4.91**.

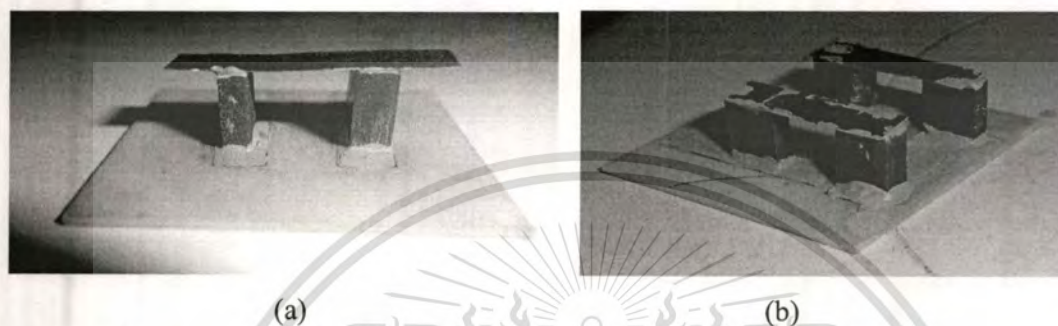
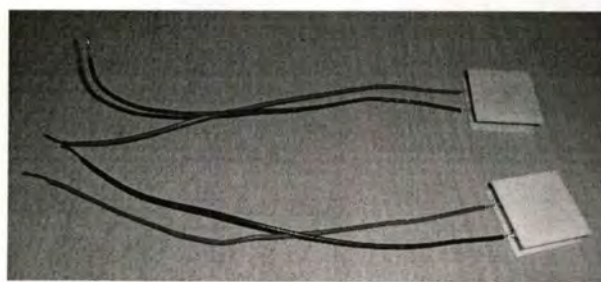


Figure 4.91 The copper strap on (a) The 1 couple of n-leg and p-leg and (b) the 2 couples of n-leg and p-leg.

5) Copper wires were connected to copper straps by one line connecting to p-pole, and another for n-pole for flowing of external current. Finally, the alumina plate was put on the top of module for transferring heat to the module. The complete of the thermoelectric module of the 1 and 2 p-leg of the $\text{Cu}_{0.95}\text{Pt}_{0.05}\text{FeO}_2$ and n-leg of the $\text{CuFe}_{0.95}\text{Pb}_{0.05}\text{O}_2$ is shown **Figure 4.92**.



Figure 4.92 (a) The connection of the copper wires, and (b) The topping of the alumina plate.



(a)



(b)



(c)

Figure 4.93 (a) The thermoelectric modules. (b) Thermoelectric module of 1 couple p-leg and n-leg and (c) The thermoelectric module of 2 couples p-legs and n-legs.

4.7.4 MEASUREMENTAL PROCEDURE

The output of electrical voltage and electrical current was investigated in applying temperature gradient on the thermoelectric modules of the 1 couple and the 2 couples of the p- $\text{Cu}_{0.95}\text{Pt}_{0.05}\text{FeO}_2$ specimen and the n- $\text{CuFe}_{0.95}\text{Pb}_{0.05}\text{O}_2$ specimen. The measurement, the modules was set as show in **Figure 4.93**. The thermoelectric modules were applied the temperature difference (ΔT) from 10 to 160 K. The top side of module was applied by the hot temperature, and the bottom of module side was applied by the cold temperature. The cold side of modules was put on top of the heat sink for control temperature to room temperature. The hot side of modules was put by the resistor (R) for generating heat as shown in **Figure 4.93**. The current source was supplied the electric current to the resistor (R) for generating the heat. The temperature value on the hot side and the cold side of modules were measured by the thermocouple with contacted to temperature indication value. The output of the electrical voltage and the electric current value were measured by the Keihley instrument multi-meter with setting the $R_{\text{load}} = r_{\text{internal}}$. The setup diagram of measurement thermoelectric module is shown in **Figure 4.94**.

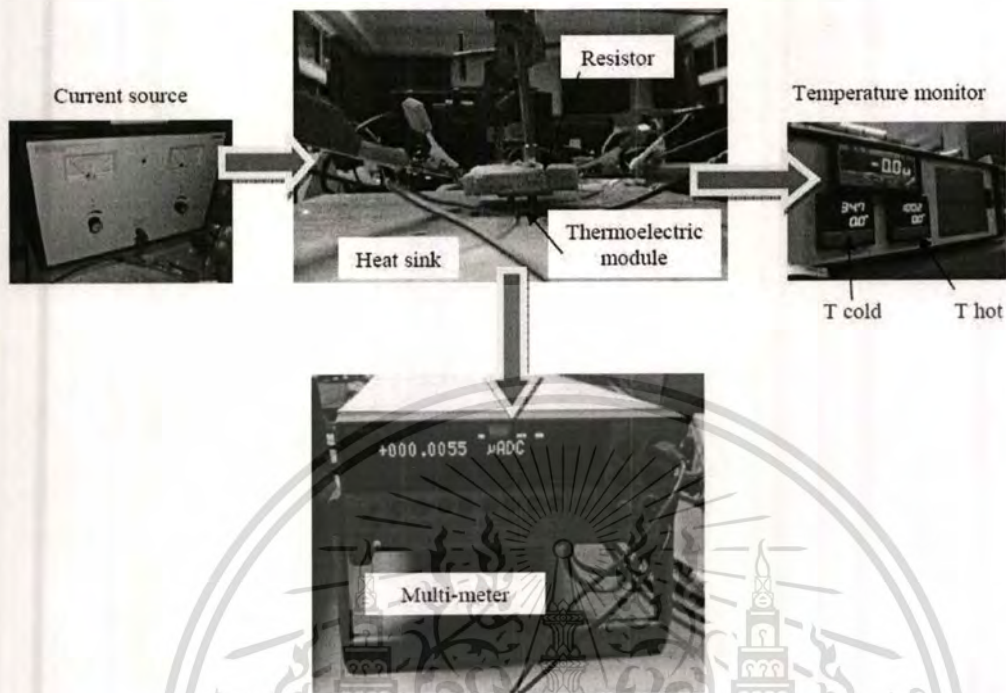


Figure 4.94 The setting measurement of output power of the thermoelectric module.

4.7.5 MEASUREMENT RESULTS

4.7.5.1 OUTPUT ELECTRICAL VOLTAGE AND CURRENT

The output voltage of the 1 couple and the 2 couples of the p-n leg module with applying the temperature difference in the range from 10 to 160 K are shown in **Figure 4.95**. The results of the thermoelectric of the 1 couple and the 2 couples of the p-n leg module show the results of output voltage increasing with the increasing of the temperature difference. The 1 couple of the p-n leg module show output voltage ranging from 5 to 40 mV, while the 2 couples of the p-n leg module displays output voltage ranging from 5 to 80 mV. These results show that the 2 couples of the p-n leg modules contain the output voltage higher than that value of the 1 couple of the p-n leg module in 2 times.

This material is reserved for educational use only, not allowed for commercial use.

Forbidden to modify the content, and cite the document when use.

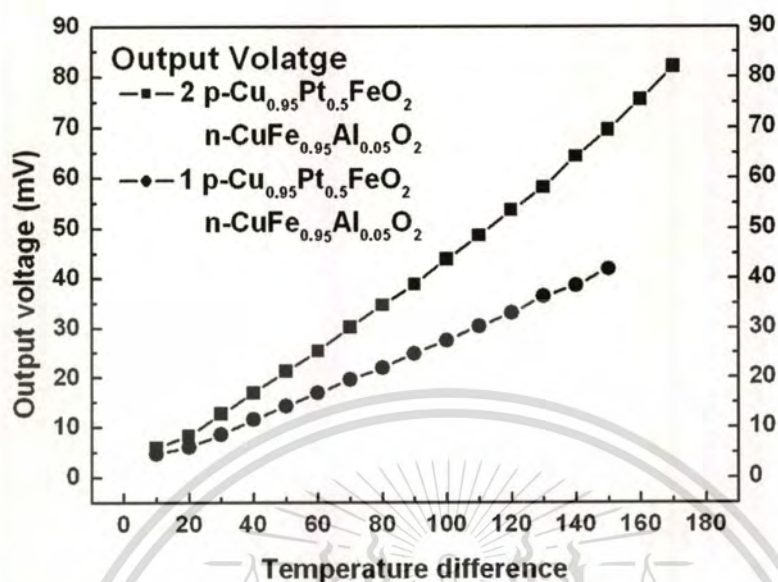


Figure 4.95 The output of electrical voltage of the thermoelectric modules with temperature difference.

The electric current voltage of the 1 couple and the 2 couples of the p-n leg module with applying temperature difference in the range from 10 to 160 K are shown in **Figure 4.96**. The 1 couple and 2 couples of the p-n leg module show output of the electric current increasing with increasing the temperature difference. The 1 couple of the p-n leg module shows output voltage ranging from 0.0036 to 0.0064 μA , while the 2 couples of the p-n leg module display output voltage ranging from 0.012 to 0.0341 μA . The results show that the 2 couples of the p-n leg module show the output voltage higher than that value of the 1 couple of the p-n leg module in 6 times.

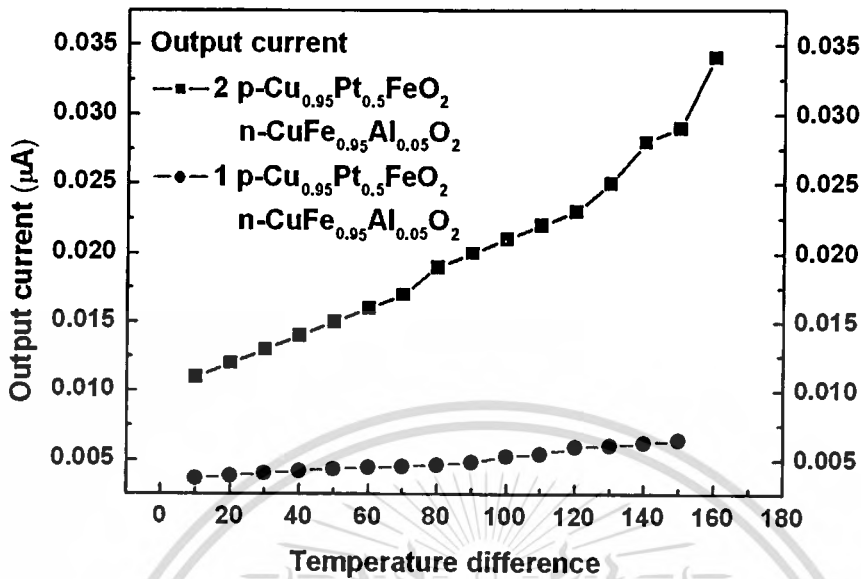


Figure 4.96 The output of electrical current of thermoelectric modules with temperature difference.

4.7.5.2 OUTPUT POWER

The output of electrical power of thermoelectric generator (P_{out}) is calculated from the output voltage and the electric current as in the relation [29, 30]:

$$P_{out} = V_{out} I_{out} \quad (4.43),$$

Where P_{out} is the output electrical power,

I_{out} is the output of electrical current by setting $R_{load} = R_{internal}$,

V_{out} is the output of electrical voltage.

Figure 4.97 shows the output of electrical power of the 1 couple and the 2 couples of the n-p leg module. The 1 couple of the n-p leg module shows output power ranging from 0.0171 to 0.26765 nW, while the 2 couples of the n-p leg module display output power ranging from 0.0649 to 2.57114 nW. The results show that the 2 couples of the n-p leg module contain the output power higher than that value of the 1 couple of the n-p leg in 10 times.

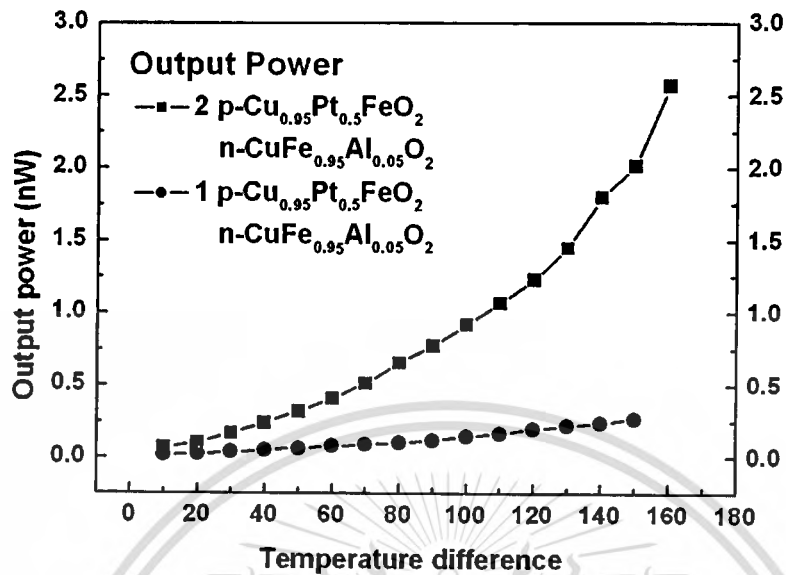


Figure 4.97 The Output power of the thermoelectric modules with temperature difference.

The output voltage and output power are plotted with the output current are shown in **Figure 4.98** and **Figure 4.99**, respectively. The results shows that the output voltage and the output power of the 1 couple and the 2 couples of the n-p leg module are increased with increasing the electrical current. The 2 couples of the n-p leg module contain the voltage value higher than that value of the 1 couple of the n-p leg module. In addition, the 2 couples of the n-p leg module contain the electrical power value higher than that value of the 1 couple of the n-p leg module. The high output of the electric power in this woke is 2.5 nWatt as in the output current 0.035 μA of the 2 couples of the n-p leg module. These results imply that the large number of the thermoelectric couple leg leading to high output of electric power.

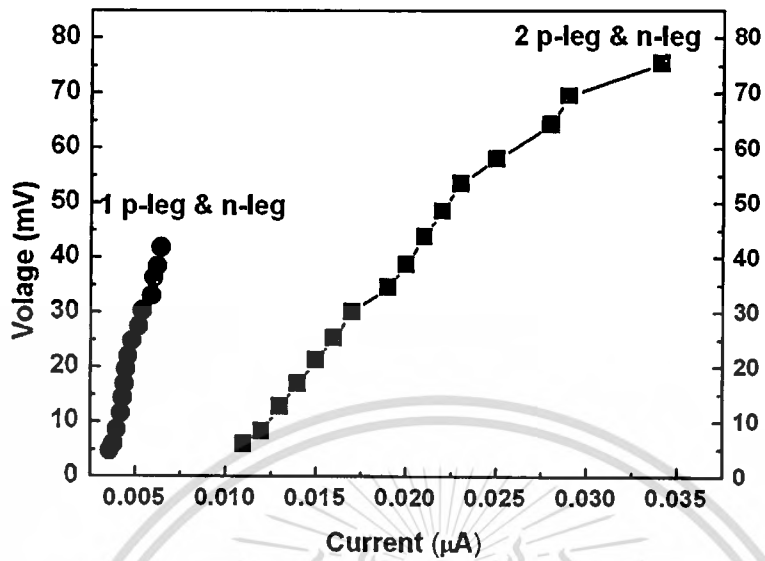


Figure 4.98 The output voltage of the thermoelectric modules with output current.

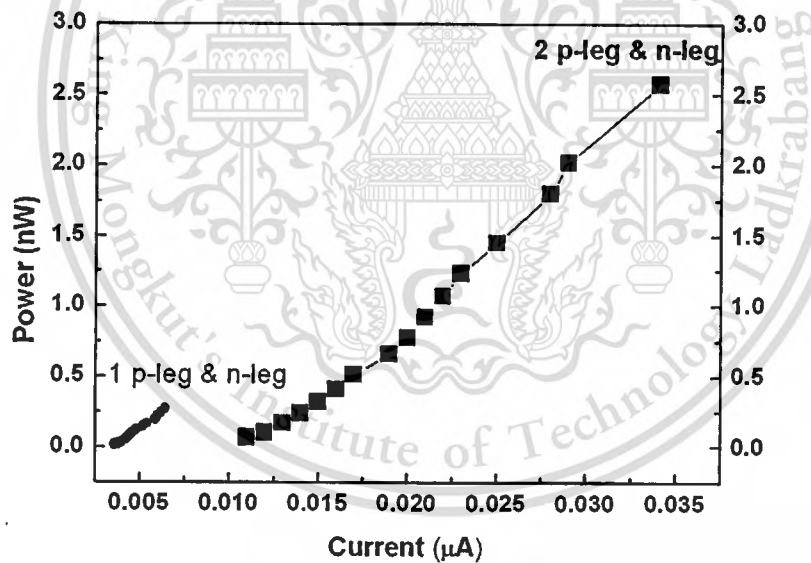


Figure 4.99 The output power of the thermoelectric modules with output current.

4.7.6 SUMMARIES

The prototype of thermoelectric modules was invented in model of 1 couple and 2 couples of the p-n leg module. The module components were used the p-leg from the $\text{Cu}_{0.95}\text{Pt}_{0.05}\text{FeO}_2$ specimen and the n-leg from the $\text{CuFe}_{0.95}\text{Pb}_{0.05}\text{O}_2$ specimen. The dimension of the p-leg is $3.0 \times 5.0 \times 5 \text{ mm}^3$ and the n-leg is $2.0 \times 5.0 \times 5 \text{ mm}^3$. The output power of the thermoelectric generator modules was measured by applied the temperature difference ranging from 10 to 160 K with increment in the stepping of 10 K. The results show that the output of electric voltage and electrical current of the 1 couple and the 2 couples of the p-n leg module are increase with increasing temperature. The 2 couples of the p-n leg module displays output voltage ranging from 0.012 to 0.0341 μA , which is higher that value of the 1 couple of the p-n leg module in 6 times. Furthermore, the 2 couples of the p-n leg module display output electrical power ranging from 0.0649 to 2.57114 nW, which is higher that value of the 1 couple of the p-n leg module in 10 times. These results confirm that the 2 couples of the p-n leg module show the output value higher than that value of 1 couple of the p-n leg module. The high value of the output of the electrical power on the 2 couples of the p-n leg module is 2.5 nW with the range of the output electric current in 0.035 μA , and with the temperature difference 160 K. In summary, the compound of the CuFeO_2 delafossite can be used for the thermoelectric generator device.

CHAPTER 5

RESULTS AND DISCUSSION

This thesis aims to investigate and improve the thermoelectric properties of the CuFeO_2 compound as the low-cost materials for invention of thermoelectric device with operation in high temperature. This section deals with the discussion of the experimental results. The detail of the discussion of each experimental result is reported below.

5.1 DISCUSSION OF EXPERIMENTAL RESULTS

This topic concerns with the comparison of the experimental results of the improvement of the CuFeO_2 compound by substituted the Pt, Al, Sn and Pb atom. In comparing results, the thermoelectric properties of the $\text{Cu}_{1-x}\text{Pt}_x\text{FeO}_2$, $\text{CuFe}_{0.5}\text{Al}_{0.5}\text{O}_2$, $\text{CuFe}_{1-x}\text{Sn}_x\text{O}_2$ and $\text{CuFe}_{1-x}\text{Pb}_x\text{O}_2$ samples were compared to results of the CuFeO_2 sample-based. Obviously, the best materials of thermoelectric occur in high ZT value as high Seebeck coefficient and electrical conductivity, and low thermal conductivity with operation in high temperature. Also, the detail of the comparison is reported by separating in each property as the Seebeck coefficient, electrical conductivity, thermal conductivity and the ZT value on all sample results as following:

➤ **The Seebeck coefficient:**

The comparison of the Seebeck coefficient of the CuFeO_2 , $\text{Cu}_{0.95}\text{Pt}_{0.05}\text{FeO}_2$, $\text{CuFe}_{0.5}\text{Al}_{0.5}\text{O}_2$, and $\text{CuFe}_{1-x}\text{Sn}_x\text{O}_2$ ($x=0.01, 0.03, \text{ and } 0.05$) samples is shown in **Figure 5.1**. The results show that the $\text{CuFe}_{0.99}\text{Sn}_{0.01}\text{O}_2$ sample as the Sn^{2+} ions substituted into the Fe^{3+} sites exhibits the highest value of the Seebeck coefficient of in this experiment. The high value of the $\text{CuFe}_{0.99}\text{Sn}_{0.01}\text{O}_2$ sample is $375 \mu\text{V/K}$, which is higher 1.3 times than that value of the CuFeO_2 sample-based.

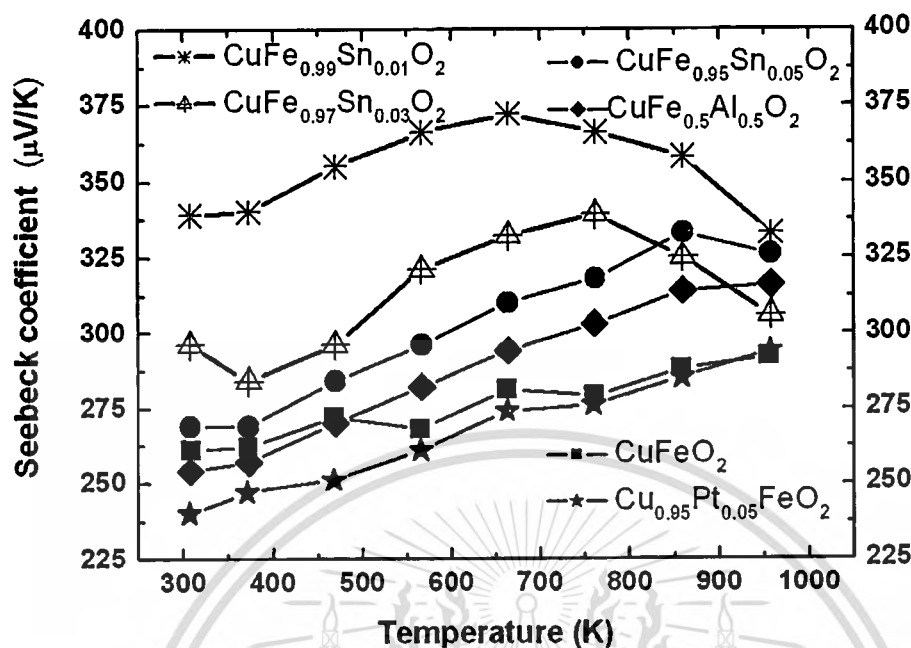


Figure 5.1 The Seebeck coefficient of the $\text{Cu}_{0.95}\text{Pt}_{0.05}\text{FeO}_2$, $\text{CuFe}_{0.5}\text{Al}_{0.5}\text{O}_2$, $\text{CuFe}_{1-x}\text{Sn}_x\text{O}_2$ ($x=0.01, 0.03, \text{ and } 0.05$) samples and the CuFeO_2 sample-based.

➤ **The electrical conductivity:**

The comparison of the electrical conductivity of the CuFeO_2 , $\text{Cu}_{0.95}\text{Pt}_{0.05}\text{FeO}_2$, $\text{CuFe}_{0.5}\text{Al}_{0.5}\text{O}_2$, and $\text{CuFe}_{0.95}\text{Sn}_{0.05}\text{O}_2$ samples is shown in Figure 5.2. The results show that the $\text{Cu}_{0.95}\text{Pt}_{0.05}\text{FeO}_2$ sample as the Pt^{1+} ions substituted into the Cu^{1+} sites exhibited the highest value of the electrical conductivity from all samples in this experiment. The high value of the $\text{Cu}_{0.95}\text{Pt}_{0.05}\text{FeO}_2$ sample is 23 S/cm at 960 K, which is higher 2 times than that value of the CuFeO_2 sample-based.

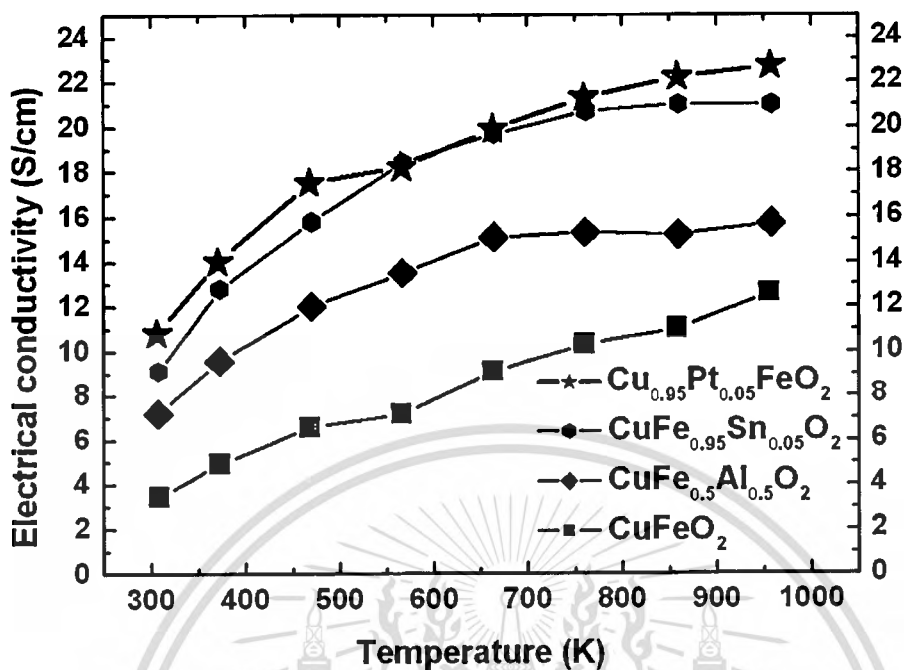


Figure 5.2 The electrical conductivity of the $\text{Cu}_{0.95}\text{Pt}_{0.05}\text{FeO}_2$, $\text{CuFe}_{0.5}\text{Al}_{0.5}\text{O}_2$, $\text{CuFe}_{0.95}\text{Sn}_{0.05}\text{O}_2$ samples and the CuFeO_2 sample-based.

➤ **The thermal conductivity:**

The comparison of the electrical conductivity of the CuFeO_2 , $\text{Cu}_{0.95}\text{Pt}_{0.05}\text{FeO}_2$, $\text{CuFe}_{0.5}\text{Al}_{0.5}\text{O}_2$, $\text{CuFe}_{1-x}\text{Sn}_x\text{O}_2$ ($x=0.01, 0.03, \text{ and } 0.05$) and $\text{CuFe}_{1-x}\text{Pb}_x\text{O}_2$ ($x=0.03 \text{ and } 0.05$) samples is shown in Figure 5.3. The results show that the low thermal conductivity occurs in the $\text{CuFe}_{0.99}\text{Sn}_{0.01}\text{O}_2$ sample as the Sn^{2+} ions substituted into the Fe^{3+} sites and the $\text{CuFe}_{0.97}\text{Pb}_{0.03}\text{O}_2$ and $\text{CuFe}_{0.95}\text{Pb}_{0.05}\text{O}_2$ as the Pb^{4+} ions substituted into the Fe^{3+} sites. These results are effect from the high atomic mass of the Sn and the Pb atom substituted into the Fe site. The thermal conductivity of the $\text{CuFe}_{0.99}\text{Sn}_{0.01}\text{O}_2$, $\text{CuFe}_{0.97}\text{Pb}_{0.03}\text{O}_2$, and $\text{CuFe}_{0.95}\text{Pb}_{0.05}\text{O}_2$ sample is approximately 1 W/mK which is lower 5 to 7 times than that value of the CuFeO_2 sample-based.

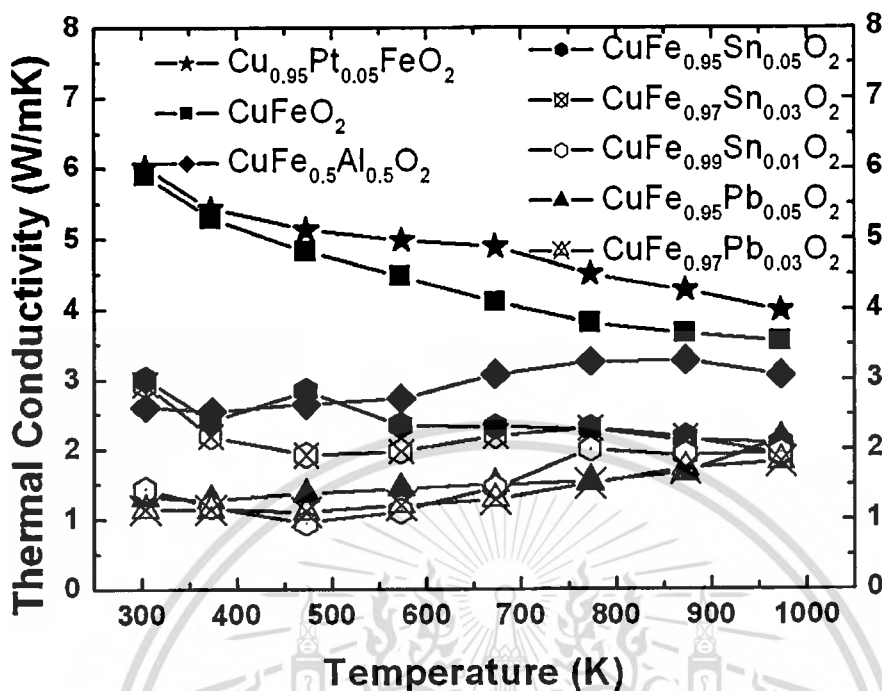


Figure 5.3 The thermal conductivity of the $\text{Cu}_{0.95}\text{Pt}_{0.05}\text{FeO}_2$, $\text{CuFe}_{0.5}\text{Al}_{0.5}\text{O}_2$, $\text{CuFe}_{1-x}\text{Sn}_x\text{O}_2$ ($x=0.01, 0.03, \text{ and } 0.05$), $\text{CuFe}_{1-x}\text{Pb}_x\text{O}_2$ ($x=0.03 \text{ and } 0.05$) samples and the CuFeO_2 sample-based.

➤ **The ZT value:**

The comparison of the ZT value of the CuFeO_2 , $\text{Cu}_{0.95}\text{Pt}_{0.05}\text{FeO}_2$, $\text{CuFe}_{0.5}\text{Al}_{0.5}\text{O}_2$, $\text{CuFe}_{0.95}\text{Sn}_{0.05}\text{O}_2$ and $\text{CuFe}_{0.95}\text{Pb}_{0.05}\text{O}_2$ samples is shown in **Figure 5.4**. The results show that the $\text{CuFe}_{0.95}\text{Sn}_{0.05}\text{O}_2$ sample exhibited the highest value of the ZT value from all samples in this experiment. The high value of the $\text{CuFe}_{0.95}\text{Sn}_{0.05}\text{O}_2$ sample is 0.1 at 960 K, which is higher 4 times than that value of the CuFeO_2 sample-based.

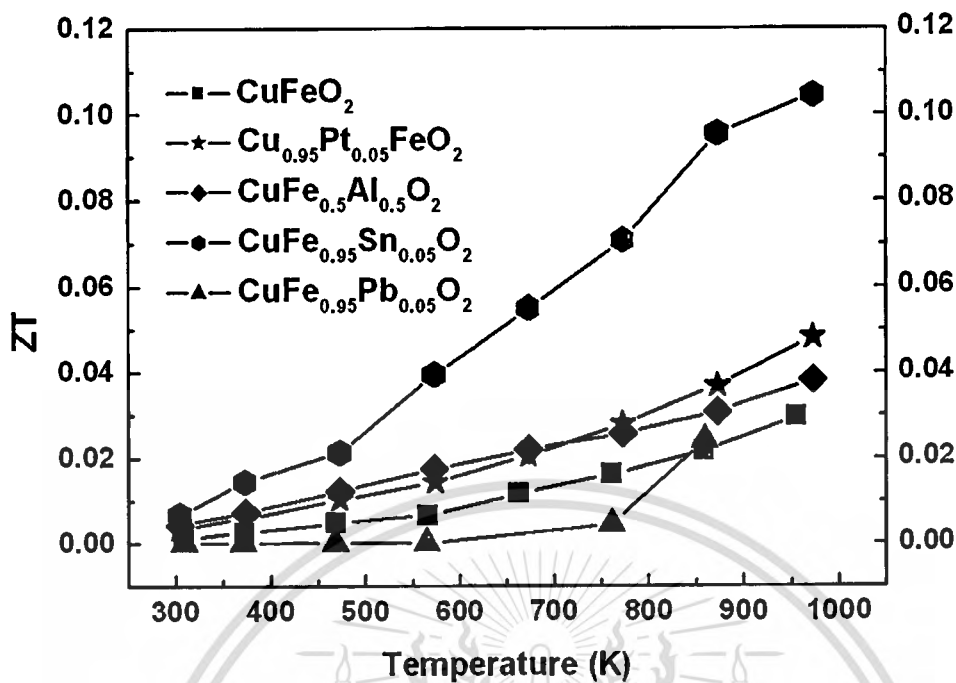


Figure 5.4 The ZT value of the $\text{Cu}_{0.95}\text{Pt}_{0.05}\text{FeO}_2$, $\text{CuFe}_{0.5}\text{Al}_{0.5}\text{O}_2$, $\text{CuFe}_{0.95}\text{Sn}_{0.05}\text{O}_2$, $\text{CuFe}_{0.95}\text{Pb}_{0.05}\text{O}_2$ and the CuFeO_2 sample-based.

5.2 SUMMARIES

The above results can be concluded that:

- 1) The high electrical conductivity of the CuFeO_2 compound can be improved by substituting of large number of the Pt^{1+} ion into the Cu site.
- 2) The high Seebeck coefficient of the CuFeO_2 compound can be improved by substituting the small amount Sn^{2+} ions into Fe site.
- 3) The low thermal conductivity of the CuFeO_2 compound can be improved by substituting the Sn or Pb atom as high atomic mass into Fe site.

In conclusion, the high ZT value in this experiment occurs in the $\text{CuFe}_{0.95}\text{Sn}_{0.05}\text{O}_2$ compound as value in 0.1.

CHAPTER 6

CONCLUSION AND SUGGESTION

This thesis aims to investigate the thermoelectric properties of the CuFeO_2 compound as the low-cost oxide materials, to improve the thermoelectric properties of the CuFeO_2 compounds for thermoelectric materials, to use the Finite Element technique for computing of the output thermoelectric generator performance, and to preliminary invent the prototype of thermoelectric device from our synthesized samples. The details of each purpose are separated as following:

1) For investigation the thermoelectric properties of the CuFeO_2 compound, the specimens were synthesized by the conventional solid state reaction method from the CuO and the Fe_2O_3 starting powder. The thermoelectric properties of the CuFeO_2 sample were analyzed and compared their properties to conventional thermoelectric materials of the Bi_2Te_3 and the NaCoO_2 .

2) For improvement the thermoelectric properties of the CuFeO_2 compound, the samples were synthesized with substituted the Pt, Al, Sn, and Pb atom by using the starting powder of PtCl_2 , Al_2O_3 , SnCl_2 and PbO_2 , respectively. The $\text{Cu}_{1-x}\text{Pt}_x\text{FeO}_2$ samples were using to investigate the effect of thermoelectric properties of the Pt^{1+} -substituted into the Cu^{1+} sites. The $\text{CuFe}_{0.5}\text{Al}_{0.5}\text{O}_2$ sample was using to investigate of the effect thermoelectric properties of the half-mixed trivalent with compared the properties to the CuFeO_2 and CuAlO_2 sample. The $\text{CuFe}_{1-x}\text{Sn}_x\text{O}_2$ samples were using to investigate the effect of thermoelectric properties of the Sn^{2+} -substituted into the Fe^{3+} sites. The $\text{CuFe}_{1-x}\text{Pb}_x\text{O}_2$ samples were using to investigate the effect of thermoelectric properties of the Pb^{4+} -substituted into the Fe^{3+} sites.

3) For the Finite Element computing, the results of output voltage of the thermoelectric generator of the $\text{CuFe}_{0.5}\text{Al}_{0.5}\text{O}_2$ model were compared to the results of the experiment from the $\text{CuFe}_{0.5}\text{Al}_{0.5}\text{O}_2$ sample.

4) For the thermoelectric prototype, the thermoelectric modules were invented from one p-leg from the $\text{Cu}_{0.95}\text{Pt}_{0.05}\text{FeO}_2$ sample and one n-leg from the $\text{CuFe}_{0.95}\text{Pb}_{0.05}\text{O}_2$ samples. The modules in thermoelectric generator were measured the output voltage, current, and power.

6.1 CONCLUSION

From the structure of the CuFeO_2 delafossite, its structure is alternative stacking by the layers of O-Cu-O dumbbell and FeO_2 edge-shared octahedral along with the c-axis. The Cu^+ cation is linearly connection with O^{2-} anion in c-axis. The $[\text{FeO}_2]^-$ octahedral-shaped are formed by charring of edge FeO_2 . The trivalent Fe^{3+} ions occupy in the middle of the octahedral block.

From the experimental results, the improvement of the CuFeO_2 delafossite to the high performance for the thermoelectric materials can be concluded that:

- 1) The electrical conductivity can be enhanced by partial substitution the monovalent of the Pt^{1+} ($5d^9$ ions) cations into the Cu^{1+} ($3d^{10}$ ions) site.
- 2) The Seebeck coefficient can be improved by small amount substitution the Sn^{2+} cations into the trivalent Fe^{3+} site.
- 3) The thermal conductivity can be decreased by substitution the Sn^{2+} or Pb^{4+} cations, which have large atomic weight, into trivalent the Fe^{3+} site
- 4) The production of n-type in the CuFeO_2 delafossite can be synthesized by substitution the Pb^{4+} into the trivalent Fe^{3+} site.

From the Finite Element computing and the output of electrical power of the prototype of thermoelectric module of p- $\text{Cu}_{0.95}\text{Pt}_{0.05}\text{FeO}_2$ leg and n- $\text{CuFe}_{0.95}\text{Pb}_{0.05}\text{O}_2$ leg, the experimental results can be concluded that:

- 5) The output of electric voltage, current, and power can be increased by increasing the number of leg in the module.

Indeed, the low-cost materials of the CuFeO_2 delafossite can be improved to high performance for thermoelectric device using in high temperature.

6.2 SUGGESTION AND FUTURE WORK

From the conclusions, the high electrical conductivity occurs on the Pt-substituted into Cu site, high Seebeck coefficient occurs on the case of the tiny Sn-substituted into Fe site Sn, and the low thermal conductivity occurs on the case of the Sn- or Pb- substituted into Fe site. From the above results, the high thermoelectric performance of CuFeO_2 delafossite may be occurred in $\text{Cu}_{1-x}\text{Pt}_x\text{Fe}_{1-y}\text{Sn}_y\text{O}_2$ and $\text{Cu}_{1-x}\text{Pt}_x\text{Fe}_{1-y}\text{Pb}_y\text{O}_2$ compounds. Also, these compounds will be synthesized and investigated in future work.

This material is reserved for educational use only, not allowed for commercial use.

Forbidden to modify the content, and cite the document when use.

REFERENCES

- [1] J. Li, W. Liu, L. Zhao and M. Zhou, *NPG Asia Mater.* **2** (2010) 152–158.
- [2] G. J. Snyder and E. S. Toberer, *Nature Materials* **7** (2008) 105–114.
- [3] A. Charoenphakdee, K. Kurosaki, A. Harnwunggmoung, H. Muta and S. Yamanaka, *J. Alloys Compd.* **496** (2010) 53–55.
- [4] G. J. Snyder, “Small thermoelectric generator”, The Electrochemical Society interface, 2008.
- [5] J. F. Li, W. S. Liu, L. D. Zhao and M. Zhou, High-performance nano structured thermoelectric materials, *NPG Asia Mater.* **2** (2010) 152–158.
- [6] X. Hou, Y. Zhou, L. Wang, W. Zhang and W. Zhang, L. Chen, *J. Alloys Compd.* **482**(2009) 544– 547.
- [7] D. Kenfaui, D. Chateigner, M. Gomina and J. G. Noudem, *J. Alloys Compd.* **490** (2010) 472–479.
- [8] W. Seifert, M. Ueltzen and E. Müller; Dimensional Modelling of Thermoelectric Cooling; *phys.stat.sol. (a)* **194** (2002) 277 – 290.
- [9] H. Ohta, K. Sugiura and K. Koumoto, *J. Inorg. Chem.* **47** (2008) 8429–8436.
- [10] T. Seetawan, V. Amornkitbamrung, T. Burinprakhon, S. Maensiri, P. Tongbai, K. Kurosaki, H. Muta, M. Uno and S. Yamanaka, *J. Alloys Compd.* **416** (2006) 291– 295.
- [11] S. Maensiri and W. Nuansing, *Mater. Chem. Phys.* **99** (2006) 104–108.
- [12] T. Kajitani, T. Nozaki and K. Hayashi, *Advances in Science and Technology*, **74**(2010) 66–71.
- [13] K. Hayashi, T. Nozaki and T. Kajitani, *Jpn. J. Appl. Phys.* **46** (2007) 5226–5229.
- [14] T. Nozaki, K. Hayashi and T. Kajitani, *J. Chem. Eng. Jpn.* **40** (2007) 1205–2007.
- [15] T. Nozaki, K. Hayashi and T. Kajitani, *J. Electron. Mater.* **39** (2010) 1798–1802.
- [16] S. Shibusaki, W. Kobayashi and I. Terasaki, *J. Phys. Rev. B*, **74** (2006) 235110.
- [17] F. Sauvage, D. Munoz-Rojas, K. R. Poeppelmeier and N. Casan-Pastor, *J. Solid State Chem.* **182** (2009) 374-380.

- [18] S. Goetzendorfer, R. Bywalez and P. Loebmann, *J. Sol-Gel Sci. Technol.* **52** (2009) 113-119.
- [19] N. W. Ashcroft and N. D. Mermin, "Solid State Physics", Saunders College Publishing, USA, 1976.
- [20] Y. Wang and et al., *Nature*, (2003) 423-425.
- [21] W. Koshibae, K. Tsutsui, and S. Maekawa, Thermopower in cobalt oxides, *PHYSICAL REVIEW B*, VOL. **62** (11) (2000) 6869- 6872.
- [22] J. Plewa et. al., proceeding of the 8th european workshop on thermoelectric material (ETS 2004), Krakow, polen, 2004.
- [23] M. Ohtaki, Y. Kubo and K. Eguchi, 17th international conference on thermoelectric, IEEE, 559, 1998.
- [24] Y. Ono, K. Satoh, T. Nozaki and T. Kajitani, *J. J. App. Phys.* **46** (2007) 1071.
- [25] J. Plewa et. al., proceeding of the 8th european workshop on thermoelectric material (ETS 2004), Krakow, polen, 2004.
- [26] M. Ohtaki, Y. Kubo and K. Eguchi, 17th international conference on thermoelectric, IEEE, 559, 1998.
- [27] Y. Ono, K. Satoh, T. Nozaki and T. Kajitani, *J. J. App. Phys.* **46** (2007) 1071.
- [28] D. Ebling, M. Jaegle, M. Bartel, A. Jacquot and H. Bottner, *J. electronic materials*, **38** (2009) 1456-1460.
- [29] Angrist S. W., "Direct energy conversion", 3rd Edi, Allyn and Bacon, Boston, (1976) 140-166.
- [30] D.M. Rowe (ed), "CRC Handbook of Thermoelectrics", CRC, Boca Raton, 1995.
- [31] N. Schwartz, W. Tantraporn and W. J. Van Der Grinten, *Advanced Energy Conversion*, **3**, (1963) 419-425.
- [32] I. G. Austin, *Proc. Phys. Soc.* **72**(1958) 545-552.
- [33] A. F. Ioffe, Infosearch limited, London, 1957.
- [34] D. W. Bruce, D. O. Hare and R. I. walon, "Functional oxides", John wiley and Sond Ltd, Publication 2010, United Kingdom.
- [35] P.A. Cox, "Transition metal oxides an introduction to their electrical structure and properties", Clarendon Press, Oxford, 1995.

- [36] M. A. Marquardt, N. A. Ashmore and D. P. Cann, *Thin Solid Films* **496** (2006) 146–56.
- [37] M. Beekman, J. Salvador, X. Shi, G.S. Nolas and J. Yang, *J. Alloys Compd.* **489**(2010) 336–338.
- [38] V. Eyert, R. Frésard and A. Maignan, *J. Chem. Mater.* **20** (2008) 2370–2373.
- [39] V. Eyert, R. Frésard and A. Maignan, *Phys. Rev. B* **78** (2008) 052402.
- [40] K. Park, K. Y. Ko, H.-C. Kwon and S. Nahm, *J. Alloy. Comp.* **437** (2007) 1-6.
- [41] L. E. Smart and E. A. Moor, “Solid State Chemistry An Introduction”, Boca Taton: CRC press, 2005.
- [42] Model ZEM-2, “Seebeck Coefficient Measuring System Instruction Manual”, ULVAC-Riko Inc, Yokohama, Japan.
- [43] Model TC-7000, “Laser Flash Method Thermal constants Measuring System Instruction Manual”, ULVAC-RIKO Inc, Yokohama, Japan.
- [44] R. E. Hummel, “Electronic Properties of Materials”, Narosa Publishing House, New Delhi Madras, 1994.
- [45] A. R. West, “Solid State Chemistry and Its Applications”, John Wiley, 1984.
- [46] ICSD Card File: 01-075-2146 and ICSD Card File:01-089-5897.
- [47] F. A. Benko and F. P. Koffyberg, *J. Phys. Chem. Solids.*, **48** (1987) 431-434.
- [48] B. Bellal, S.Saadi, N. Koriche, A.Bouguelia and M.Trari, *J. Phys. Chem. Solid.* **70** (2009) 1132.
- [49] R.J. Cava, R. J. Cava, H. W. Zandbergen, A. P. Ramirez, H. Takagi, C. T. Chen, J. J. Krajewski, W. F. Peck, Jr., J. V. Waszczak, G. Meigs, R. S. Roth and L. F. Schneemeyer, *J. Solid State Chem.* **104** (1993) 437.
- [50] K. Isawa ,Y. Yaegashi, M. Komatsu, M. Nagano, S. Sudo, M. Karppinen and H. Yamauchi, *J. Phys. Rev. B* **56** (1997) 3457.
- [51] M. Park, Y. Shin and *J. Korean Chemical Society* **53** (2009).
- [52] T. Kajiwara and K. Yoshiara, *J. J. App. Phys.* **44** (2005) 1237–1238.
- [53] D. Ko, J. J. Urban and C. B. Murray, *J. Nano Lett.*, **10**, (2010) 1842–1847.
- [54] G. S. Nolas, J. Sharp and H. J. Goldsmind, “Thermoelectric basic principles and new materials developments”, Germany, Spinger, 2011.

- [55] J. I. Pankove, "Optical processes in semiconductors", Dover Publication Inc, New York, 1971.
- [56] S. H. Lim, S. Desu and A. C. Rastogi, *J. Phys. Chem. Solid.*, **69** (2008) 2047–2056.
- [57] T. Dittrich, L. Dloczik, T. Guminskaya, M. Ch. Lux-Steiner, N. Grigorieva and I. Urban, *J. Appl. Phys. Lett.*, **85** (2004) 742-744.
- [58] C.T. Prewitt, R.D. Shannon and D.B. Rogers, *J. Inorg. Chem.* **10** (1971) 719–723.
- [59] K. Hayashi, T. Nozaki and T. Kajitani, *J. J. Appl Phys.* **46** (2007) 5226-5229.
- [60] T. Nozaki, K. Hayashi, and T. Kajitani, International conference on thermoelectrics (2008)167-170.
- [61] S. Shibusaki, W. Kobayashi and I. Terasaki, *J. Phys. Rev. B* **74** (2006) 235110.
- [62] S. Yanagiya, N. Nong, J. Xu and N. Pryds, *J. Materials*, **3** (2010) 318-328.
- [63] K. Park, K. Y. Ko, H.-C. Kwon and S. Nahm, *J. Alloy. Comp.* **437** (2007) 1-6.
- [64] S. Yanagiya, N. Nong, J. Xu and N. Pryds, *J. Materials*, **3** (2010) 318-328.
- [65] S. Omeiri, B. Bellal, A. Bouguelia, Y. Bessekhoud and M. Trari, *J. Solid State Elect.* **13** (2009) 1395-1401.
- [66] F.Sauvage, D.Munoz-Rojas, K. R. Poeppelmeier and N. Casan-Pastor, *J. Solid State Chem.* **182** (2009) 374-380.
- [67] T. Nozaki, K. Hayashi and T. Kajitani, *J. Chem. Eng. Jpn.* **40** (2007) 1205–2007.
- [68] T. Nozaki, K. Hayashi and T. Kajitani, *J. Electron. Mater.* **39** (2010) 1798–1802.
- [69] S. Shibusaki, W. Kobayashi and I. Terasaki, *J. Phys. Rev. B*, **74** (2006) 235110.
- [70] N. W. Ashcroft and N. D. Mermin, "Solid State Physics", Saunders College Publishing, USA, 1976.
- [71] E. E. Antonova and D. C.Looman, International conference on thermoelectric, (2005) 215-218.
- [72] J. Jin, "The finite element method in electromagnetic", 2nd Edition, Singapore, John Wiley & Sons, 2002.
- [73] P.G. Lau, and R. J. Buist, 16th International Conference on Thermoelectrics, (1997) 563-566.
- [74] V. Duyn D.C., *Solid-State Sensors and Actuators*, (1991) 432-435.

- [75] D. Ebling, M. Jaegle, M. Bartel, A. Jacquot and H. Bottner J. electronic materials, **38** (2009) 1456-1460.



This material is reserved for educational use only, not allowed for commercial use.

Forbidden to modify the content, and cite the document when use.

APPENDICES

A: PUBLICATION IN INTERNATIONAL JOURNALS

B: NATIONAL AND INTERNATIONAL PROCEEDING

**C: INVITATING EMAIL FROM THE INTERNATIONAL CENTRE OF
DIFFRACTION**

D: CRYSTALLOGRAPHIC REFERENCE



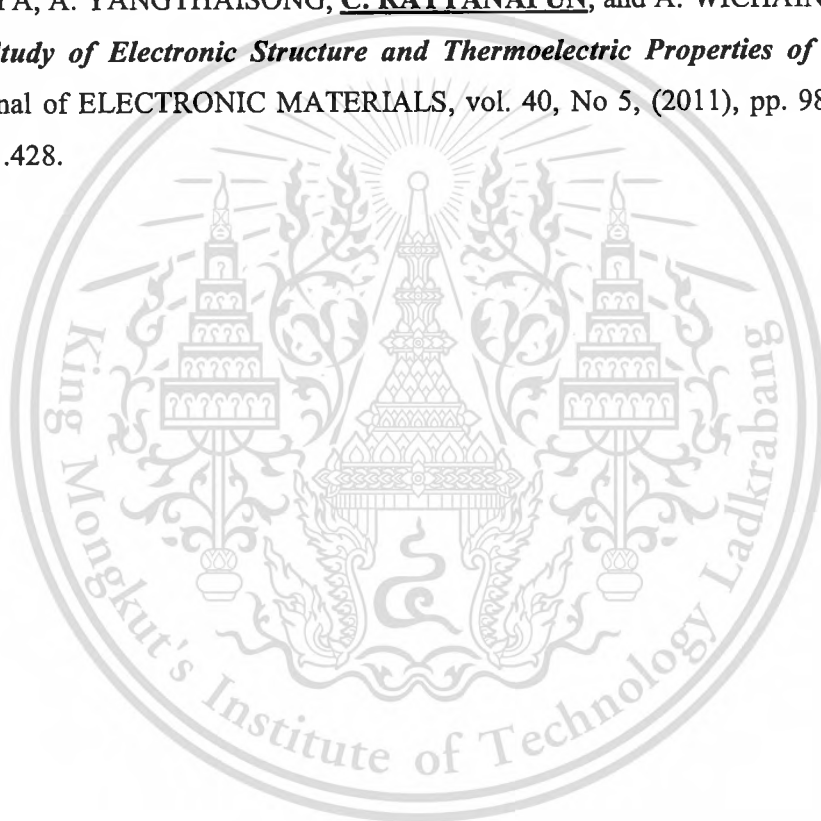
This material is reserved for educational use only, not allowed for commercial use.

Forbidden to modify the content, and cite the document when use.

A: PUBLICATION IN INTERNATIONAL JOURNALS

A.1: **Chesta Ruttanapun**, Aree Wichainchai, Wutthisak Prachamon, Anucha Yangthaisong, Anek Charoenphakdee and Tosawat Seetawan, "*Thermoelectric properties of $Cu_{1-x}Pt_xFeO_2$ ($0.0 \leq x \leq 0.05$) delafossite-type transition oxide*", Journal of Alloys and Compounds 509 (2011), pp. 4588-4594, impact factor: 2.135.

A.2: P. POOPANYA, A. YANGTHAISONG, **C. RATTANAPUN**, and A. WICHAINCHAI, "*Theoretical Study of Electronic Structure and Thermoelectric Properties of Doped $CuAlO_2$* ", Journal of ELECTRONIC MATERIALS, vol. 40, No 5, (2011), pp. 987-991, impact factor: 1.428.



A.1

Thermoelectric properties of $\text{Cu}_{1-x}\text{Pt}_x\text{FeO}_2$ ($0 \leq x \leq 0.05$) delafossite-type transition oxide,

Chesta Ruttanapun, Aree Wichainchai, Wutthisak Prachamon, Anucha Yangthaisong,

Anek Charoenphakdee and Tosawat Seetawan,

Journal of Alloys and Compounds,

509 (2011), pp. 4588-4594.





Contents lists available at ScienceDirect

Journal of Alloys and Compounds

journal homepage: www.elsevier.com/locate/jallcom

Thermoelectric properties of $\text{Cu}_{1-x}\text{Pt}_x\text{FeO}_2$ ($0.0 \leq x \leq 0.05$) delafossite-type transition oxide

Chesta Ruttanapun^{a,*}, Aree Wichainchai^a, Wutthisak Prachamon^b, Anucha Yangthaisong^b, Anek Charoenphakdee^c, Tosawat Seetawan^d

^a Department of Applied Physics, Faculty of Science, King Mongkut's Institute of Technology Ladkrabang, Chalokkrung Road, Ladkrabang, Bangkok 10520, Thailand

^b Department of Physics, Faculty of Science, Ubon Ratchathani University, Ubon Ratchathani 34190, Thailand

^c Thermoelectrics and Nano Technology Research Center, Faculty of Science and Technology, Rajamangala University of Technology Suvarnabhumi, 60 Moo 3, Asian Highway, Hunkra Phranakhon Si Ayutthaya 13000, Thailand

^d Thermoelectrics Research Center and Program of Physics, Faculty of Science and Technology, Sakon Nakhon Rajabhat University 680 Nittayo Rd., Sakon Nakhon 47000, Thailand

ARTICLE INFO

Article history:

Received 16 November 2010

Received in revised form 18 January 2011

Accepted 18 January 2011

Available online 25 January 2011

Keywords:

Copper iron oxide

$\text{Cu}_{1-x}\text{Pt}_x\text{FeO}_2$

Delafossite

Thermoelectric properties

Melting point

Activation energy

Dimensionless figure of merit

ABSTRACT

The samples of $\text{Cu}_{1-x}\text{Pt}_x\text{FeO}_2$ ($0 \leq x \leq 0.05$) delafossite were synthesized by solid state reaction method for studying thermoelectric properties. The properties of Seebeck coefficient, electrical conductivity and thermal conductivity were measured in the high temperature ranging from 300 to 960 K. The results of Seebeck coefficient, electrical conductivity and power factor were increased with increasing Pt substitution and temperature. The thermal conductivity was decreased from 5.8 to 3.5 W/mK with increasing the temperature from 300 to 960 K. An important results, the highest value of power factor and ZT is 2.0×10^{-4} W/mK² and 0.05, respectively, for $x=0.05$ at 960 K.

© 2011 Elsevier B.V. All rights reserved.

1. Introduction

Today, thermoelectric materials [1–3] have been displayed their potential as alternative sources of energy. The thermoelectric effect refers to a phenomenon whereby a gradient of temperature is converted directly into electrical current and vice versa. Furthermore, thermoelectric generators can be used to converting waste heat to produced by various sources to electrical power. The reverse effect can be practiced in thermoelectric coolers of refrigerators and other cooling systems. These conversion mechanisms have advantages of not having moving parts. The performance of the thermoelectric material is determined by the dimensionless figure of merit, $ZT = \sigma S^2 T / \kappa$, where T is the absolute temperature, S is the Seebeck coefficient, σ and κ are the electrical and thermal conductivity, respectively [3–5]. Ideally, the ZT value approaches its optimum value when σ and S are maximum, and κ is as small as possible. As the equation suggests, the efficiency increases at high temperature.

Conventional thermoelectric materials such as PbTe and Bi_2Te_3 show high values of ZT ; however, they easily decompose, oxidize or

melt at high temperatures in air [6]. In fact, heavy metals in Bi-Te and Pb-Te are costly and toxic [5]. This may result in a limited use in practical applications of thermoelectric power generation. Hence, the development of oxide materials with both high performance and environmentally stable at high temperature is crucial for practical applications. Recently, thermoelectric properties of oxide materials have been shown conversion efficiency close to that of conventional semimetallic materials. For example, thermoelectric voltage and direct current conductivity of transition-metal oxides such as NiO , NaCo_2O_4 and $\text{Ca}_3\text{Co}_4\text{O}_9$ have been reported to be large at high temperature conditions [5–8]. In addition, CuFeO_2 compound with delafossite structure has been reported to exhibit a large value of S (544 $\mu\text{V/K}$) and PF (0.44×10^4 W/mK²) [9].

Delafossite compounds are classified in a group of ternary oxides whose chemical formula is $\text{A}^+\text{B}^{3+}\text{O}_2$ [10,11]. Its structure is formed by alternative stacking layers of O–A–O dumbbell and BO_2 edge-shared octahedral along with the c -axis. The A^+ cation is linearly connection with O^{2-} anion in c -axis. The $[\text{BO}_2]^-$ octahedral-shaped are formed by charring of edge BO_2 . The trivalent B^{3+} ions occupy in the middle of the octahedral block. The delafossite crystal has a unit cell structure of hexagonal (space group: $R\bar{3}m$) and a primitive structure of rhombohedral. The A-site cations are composed of Cu, Ag, Pd, or Pt transition-metal ions maintained in a monovalent

* Corresponding author. Tel.: +66 2326 4339 53x285-6; fax: +66 2326 4413.

E-mail address: chesta.ruttanapun@gmail.com (C. Ruttanapun).

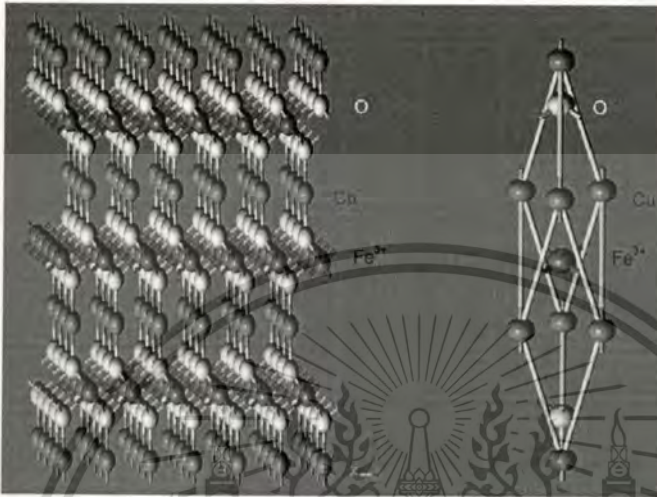


Fig. 1. The CuFeO_2 delafossite structure and its rhombohedral primitive cell structure.

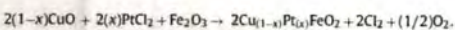
state. The properties of delafossite are strongly dependent on which types of A-site cations being used. Cu^+ and Ag^+ (d^{10} ions) cations are responsible for semiconducting behaviors, while Pt^4 and Pd^4 (d^9 ions) cations give rise to electrical conductivity. The B-site cations mostly consist of trivalent transition metals (Cr, Mn, Fe, Co, Ni, Rh), group III metal elements (Sc, Y, La), group 13 metal elements (Al, Ga, In, Tl), or rare earths (Pr, Nd, Sm, Eu). There are many compounds in a delafossite group such as CuFeO_2 , CuCoO_2 , PdCoO_2 and PtCoO_2 [10–12]. The delafossite structure and rhombohedral primitive cell structure of CuFeO_2 are shown in Fig. 1. The Cu-based and Ag-based delafossite such as CuFeO_2 or AgCoO_2 clearly display semiconducting behavior [11,13], while the Pd-based and Pt-based delafossite such as PdCoO_2 or PtCoO_2 are metallic conductors [11,12].

Moreover, many studies have reported that CuFeO_2 delafossite has a ZT value approximately 0.04 at 960 K [14]. Other studies report that the ZT value of CuFeO_2 was improved by doping trivalent and divalent metal such as Ni, Mg Co and Ti [14–16]. However, upon doping the ZT was increased by less than 0.05 at 960 K. Recently, many studies have report that the Ag cations can be doped into the Cu-based delafossite such as $\text{Cu}_{1-x}\text{Ag}_x\text{RhO}_2$ [17], $\text{Cu}_{1-x}\text{Ag}_x\text{CrO}_2$ [18], and $\text{Cu}_{1-x}\text{Ag}_x\text{AlO}_2$ [19], causing the ZT value to improve slightly. To the best of our knowledge; however, there has been no report concerning the improvement of the ZT value by substituting Pt cations into Cu-base delafossite.

This paper aims to improve the ZT of CuFeO_2 delafossite by Pt substitution using solid state reaction method. The effect of partial substitution of Pt into the CuFeO_2 on the thermoelectric properties has been investigated. Finally, the X-ray diffraction (XRD), the Seebeck coefficient, electrical and thermal conductivity, power factor and the ZT value are discussed. The thermoelectric properties of the $\text{Cu}_{1-x}\text{Pt}_x\text{FeO}_2$ delafossite by partial substitution of Pt into CuFeO_2 in content of x for $0.0 < x < 0.05$ using solid state reaction method are reported.

2. Experimental

Bulk specimens of polycrystalline $\text{Cu}_{1-x}\text{Pt}_x\text{FeO}_2$ with $0 \leq x \leq 0.05$ were synthesized by a conventional direct solid-state reaction [20,21] according to the following equation:



Stoichiometric amounts of high-purity powders CuO (Merk, 99.98%), Fe_2O_3 (Sigma-Aldrich, Inc., 99%), and PtCl_2 (Sigma-Aldrich, Inc., 98%) were sufficiently mixed and ground in an agate mortar to ensure homogeneity. A homogenous mixture was obtained and cool pressed into pellets of 12 mm diameter with 2–3 mm thickness. The resulting pellets were sintered by performing on the alumina boat in furnace at 1050 °C under air atmosphere for 15–25 h. After heat treatment, the samples were rapidly quenched to room temperature. The heated pellets were repeatedly subjected to grinding, pellet, and firing procedures for several times until the pure phase of samples was obtained.

The single phase of samples was characterized by the powder X-ray diffraction (XRD) of PHILIPS model: X' Pert MPD using Cu K α radiation with $2\theta = 10\text{--}80^\circ$ with 0.02 steps. The lattice parameter was determined by the Rietveld refinement program, X'Pert High Score Plus V2.0a. Microstructures of the samples were observed by scanning electron microscope (SEM) using the JEOL model: JSM-5410. The decomposition analysis of the samples was analyzed using thermogravimetric method (TG) by the Pyris Diamond TG/DTG (Perkin Elmer Instrument) under air atmosphere. The electrical conductivity and Seebeck coefficient were simultaneously measured on the 4.2 mm \times 2.5 mm \times 20 mm sample bar using the ULVAC-RIKO ZEM-2 thermoelectric property measurement system under a low-pressure Ar atmosphere. The thermal conductivity was determined from thermal diffusivity and specific heat on pellets of 12 mm diameter with thickness of 1.6 mm by using the ULVAC SINKU RIKO Inc. model: TC-7000 laser-flash method under N_2 atmosphere. The Hall coefficient measurements were performed on the sample bar of 1 cm \times 1 cm \times 0.25 cm by using the Ecopai Hall measurement system model: HMS-30000 with high magnetic field strength 1.0 T at room temperature.

3. Results and discussion

3.1. Material characterization

Fig. 2 demonstrates the XRD patterns for samples of CuFeO_2 and the $\text{Cu}_{1-x}\text{Pt}_x\text{FeO}_2$ for $x = 0.01, 0.03$ and 0.05 , respectively. The XRD peaks of the CuFeO_2 exhibit crystal phase of delafossite-type structure for space group: $R3m$ corresponding to the standard ICSD: 01-075-2146 file [22] and an impurity phase of CuO related to the standard ICSD: 01-089-5897 file [22]. The others, the XRD patterns of $x = 0.01, 0.03$ and 0.05 display all peaks with relation to the peak of CuFeO_2 .

The lattice spacing parameters of CuFeO_2 and $\text{Cu}_{1-x}\text{Pt}_x\text{FeO}_2$ for $x = 0.01, 0.03$ and 0.05 are shown in Fig. 3. The lattice constant of $\text{Cu}_{1-x}\text{Pt}_x\text{FeO}_2$ samples depends on the Pt in content of the x . The lattice distance of CuFeO_2 for the a -axis and the c -axis are obtained and confirmed with the finding of previous works as given 3.0334 Å and 17.1598 Å, respectively, which agrees with the standard file of

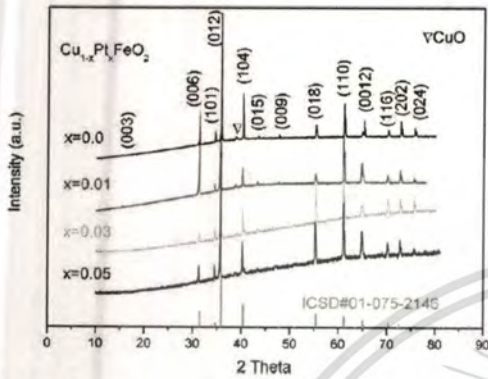


Fig. 2. The XRD patterns of the CuFeO_2 and the $\text{Cu}_{1-x}\text{Pt}_x\text{FeO}_2$ samples with Pt content of $x=0.01, 0.03$ and 0.05 .

ICSD: 01-075-2146 [22,23]. In addition, the $\text{Cu}_{1-x}\text{Pt}_x\text{FeO}_2$ samples, the c -axis rapidly increase with increasing Pt content of x , while the a -axis length still remains unchanged with increasing the x content. The effect of the c -axis increases with Pt content of x due to partial substitution of large ion Pt^{2+} (0.60 \AA) [24] into Cu^{2+} (0.46 \AA) site.

The morphology of the microstructure of $\text{Cu}_{1-x}\text{Pt}_x\text{FeO}_2$ for $x=0.0, 0.01, 0.03$ and 0.05 samples were observed by SEM as shown in Fig. 4. The microstructure of all samples shows the giant crystal grand size ($>6 \mu\text{m}$) indicating the complete reaction in sintering process.

The decomposition of CuFeO_2 sample is clearly verified by thermogravimetric method (TG) in weighting loss as shown in Fig. 5. According to the entire range of measurement under the atmosphere, the first peak (368 K) is shown the effect of humidity and the second peak (495 K), oxygen is inserted approximately 0.05% into Cu layers [25–27]. The third weight loss at 556 K is originated due to oxygen excess. It is also interesting to point out that the end of the oxygen weight loss is in temperature at 980 K . Its total weight loss is approximately 0.9% which is equivalent to the oxygen content of 0.14 atoms per unit formula as indicated δ of the chemical formula $\text{CuFeO}_{2+\delta}$. An abrupt weight loss is observed at the temperature beyond 1365 K , indicating the melting point of the CuFeO_2 sample.

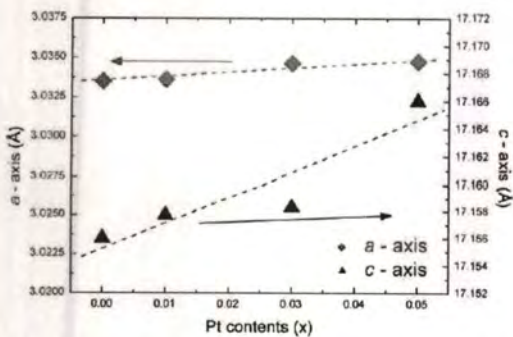


Fig. 3. The lattice parameters as a function of Pt concentration in x content of the $\text{Cu}_{1-x}\text{Pt}_x\text{FeO}_2$ ($0 \leq x \leq 0.05$) samples.

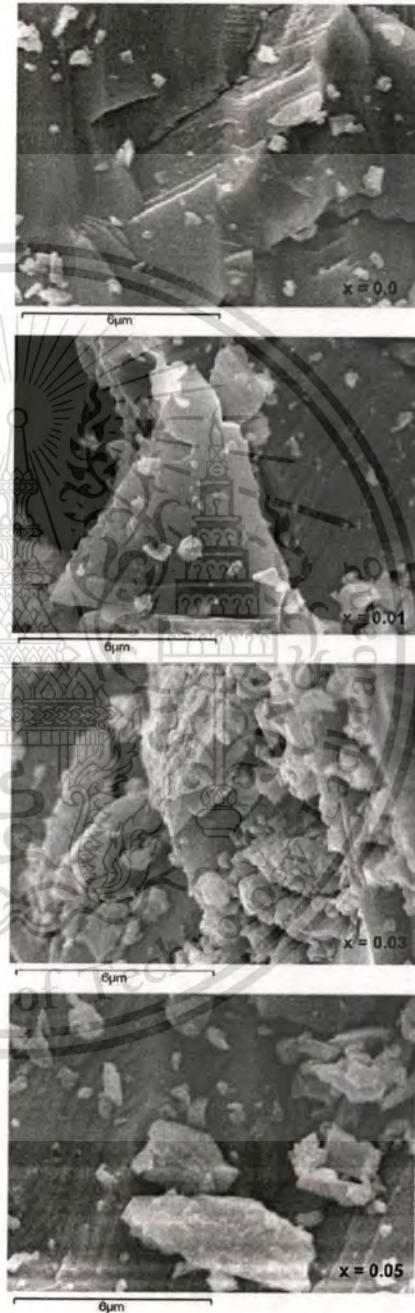


Fig. 4. The microstructure on cutting surface of the $\text{Cu}_{1-x}\text{Pt}_x\text{FeO}_2$ ($0 \leq x \leq 0.05$) samples.

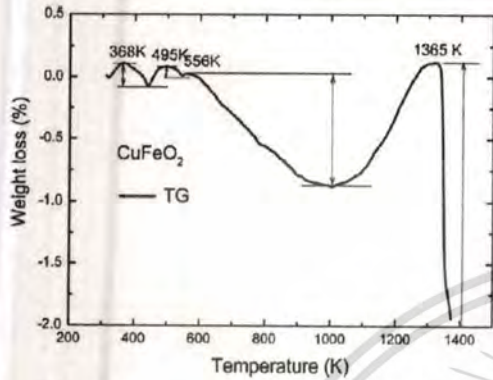


Fig. 5. The TG curve of the CuFeO_2 sample with temperature range from 300 to 1400 K.

3.2. Thermoelectric properties

Fig. 6(a) shows the Seebeck coefficient (S) of $\text{Cu}_{1-x}\text{Pt}_x\text{FeO}_2$ samples as a function of temperature in the range between 300 and 960 K. The results show that the Seebeck coefficients are positive sign over the measured temperature range for all samples, and they remain positive upon substitution. These results indicate that the

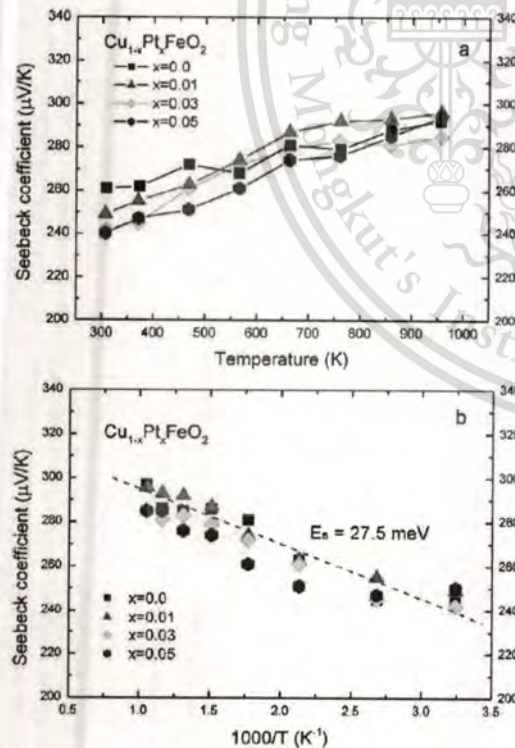


Fig. 6. (a) The Seebeck coefficient of the $\text{Cu}_{1-x}\text{Pt}_x\text{FeO}_2$ ($0 \leq x \leq 0.05$) samples vs. the temperature range from 300 to 960 K. (b) The curve of the Seebeck coefficient vs. $1000/T$.

$\text{Cu}_{1-x}\text{Pt}_x\text{FeO}_2$ samples with Pt substitution show p-type conductor of the thermoelectric materials. Moreover, the Seebeck coefficient of $\text{Cu}_{1-x}\text{Pt}_x\text{FeO}_2$ samples tends to increase with increasing temperature. However, the values of Seebeck coefficient decrease as a result of increased the Pt content of x . The Seebeck coefficient at 300 K is 261, 249, 242 and 240 $\mu\text{V/K}$ for content of $x=0, 0.01, 0.03$ and 0.05, respectively. The average value of the Seebeck coefficient of samples increases from 250 to 290 $\mu\text{V/K}$ when the temperature increases. The maximum value of S at a high temperature (at 960 K) is 290 $\mu\text{V/K}$. This operating point might be suitable for high temperature thermoelectric devices. In addition, the results show that the Seebeck coefficient of $\text{Cu}_{1-x}\text{Pt}_x\text{FeO}_2$ samples is dependent on temperature and it decreases as a result of substitution of x content.

According to Fig. 6(a), the lowest value at 300 K for the Seebeck coefficient of $\text{Cu}_{1-x}\text{Pt}_x\text{FeO}_2$ sample for $x=0.05$ is 240 $\mu\text{V/K}$ which approximately reduces 8% comparing with the CuFeO_2 sample (261 $\mu\text{V/K}$). The maximum value of the reduced Seebeck coefficient of $\text{Cu}_{1-x}\text{Pt}_x\text{FeO}_2$ samples (8%) is less than the reduced value of $\text{CuFe}_{1-x}\text{Ni}_x\text{O}_2$ (26%) [14] and $\text{CuFe}_{1-x}\text{Zn}_x\text{O}_2$ (43%) [28], at temperature 300 K. This result implies that Pt^{1+} substitution in Cu^{+} site of CuFeO_2 delafossite has fewer effects on the Seebeck value than the doped impurity of trivalent (such as Ni, Zn) in Fe^{3+} site of CuFeO_2 .

In applying p-type semiconductor, the relation of the Seebeck coefficient is given by $S = (k_B/e)[(E_F - E_V)/k_B T]$ [29], where k_B is the Boltzmann's constant, e is electronic charge constant, E_V is the energy of the valance-band edge, E_F is the Fermi energy level and T is the absolute temperature. The activation energy for the production of free carriers $E_S = (E_F - E_V)$ is obtained by plotting the S vs. $1000/T$ as shown in the Fig. 6(b). The average of E_S value for all $\text{Cu}_{1-x}\text{Pt}_x\text{FeO}_2$ ($0 \leq x \leq 0.05$) samples is 27.5 meV. The result is slightly higher than the thermal energy at room temperature ($k_B T_{300\text{K}} \approx 25$ meV). Consequently, this value indicates that $\text{Cu}_{1-x}\text{Pt}_x\text{FeO}_2$ ($0 \leq x \leq 0.05$) samples are good semiconductor materials which are shallow acceptor doping level for thermoelectric devices because the charge carriers are ionized near the room temperature for conduction mechanism.

The electrical conductivity (σ) of $\text{Cu}_{1-x}\text{Pt}_x\text{FeO}_2$ samples as a function of temperature in the range of 300–960 K is shown in Fig. 7(a). The electrical conductivity of all samples is rapidly raised along with the increasing temperature and the increasing x content of Pt substitution. The values of σ at 300 K for content of $x=0, 0.01, 0.03$ and 0.05 are 3.5, 5.0, 8.0 and 11.0 S/cm, respectively. For the sample of $x=0.05$ at room temperature, the σ (11.0 S/cm) value is approximate four times larger than that of the CuFeO_2 sample (3.5 S/cm). For a high temperature at 960 K, the values of σ are 12.5, 16.5, 19 and 23 S/cm for $x=0.0, 0.01, 0.03$ and 0.05 respectively. The maximum value of the σ is 23 S/cm for $x=0.05$ at a temperature of 960 K which points out that CuFeO_2 substitution by the Pt is suitable to use at high temperature for thermoelectric power devices. Fig. 7(b) shows the Arrhenius plot of $\text{Cu}_{1-x}\text{Pt}_x\text{FeO}_2$ ($0 \leq x \leq 0.05$) samples plotted by $\log \sigma$ vs. $1000/T$ in temperature ranging from 300 to 960 K. The Arrhenius plot corresponds to temperature dependence in equation $\sigma = A \exp(-E_\sigma/k_B T)$ [29], where k_B is the Boltzmann's constant, E_σ is the activation energy of conduction and A is a constant value. The activation energies (E_σ) in the Arrhenius plot, $\log \sigma$ vs. $1000/T$ are 49, 46, 33 and 28 meV for samples with x content = 0.0, 0.01, 0.03 and 0.05, respectively. These results show that the tendency of the activation energy (E_σ) decreases with increased the x content as the behavior of semi-conducting of transition oxide. Fig. 7(c) shows the results of the activation energy reduces with increased Pt substitution of x content. These results exhibit that the E_σ tends to fall to zero as the substitution of x content reduces to 0.15, when metallic conduction occurs. Fig. 7(d) shows the plot of Mott's model for $\text{Cu}_{1-x}\text{Pt}_x\text{FeO}_2$ ($0 \leq x \leq 0.05$) samples with plotting temperature dependence in equation $\sigma = B \exp[-(T_0/T)^{1/4}]$ [29] where B and T_0 are constant

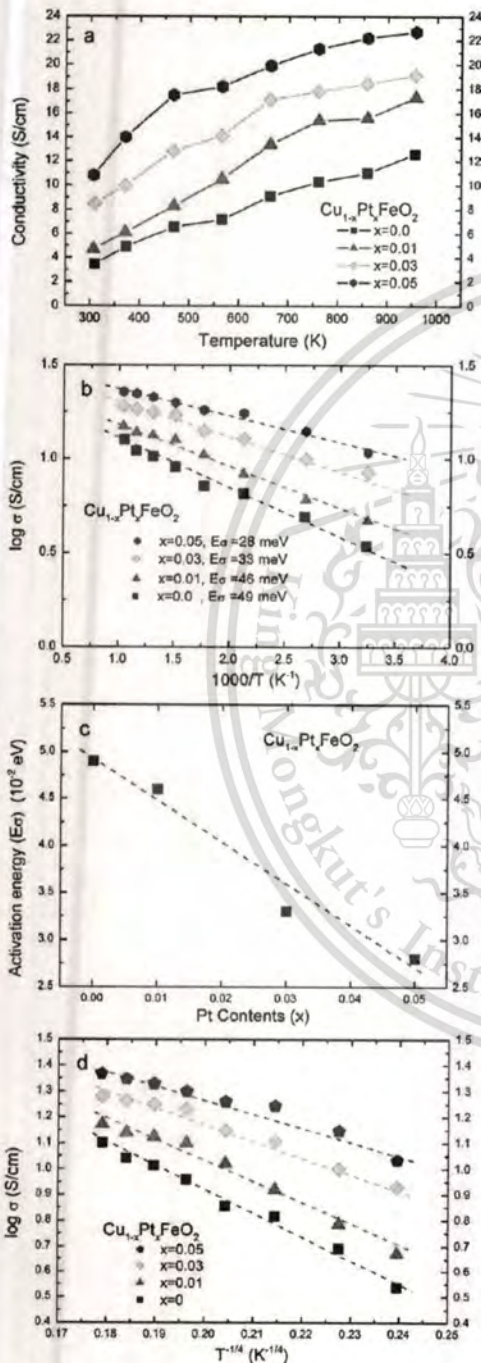


Fig. 7. (a) The electrical conductivity vs. the temperature range from 300 to 960 K. (b) The curve of $\log \sigma$ vs. $1000/T$ (c) The activation energy (E_{σ}) as a function of the Pt substitution in x content. (d) The curves of $\log \sigma$ vs. $1/T^{1/4}$.

value. The zero slope of the Mott equation implies the temperature independence of conduction which exhibits metallic behavior. The plotted results of $\log \sigma$ vs. $1/T^{1/4}$ in Fig. 7(d) display that $x=0.05$ which is close to zero slope. This confirms that $\text{Cu}_{1-x}\text{Pt}_x\text{FeO}_2$ sample for $x=0.05$ is a good semiconductor. In addition, the linear slope of $\log \sigma$ vs. $1/T^{1/4}$ in Fig. 7(d) suggests that a variable-range-hopping mechanism is reasonable for all samples of $\text{Cu}_{1-x}\text{Pt}_x\text{FeO}_2$ delafossite.

According to Fig. 7, the maximum conductivity value at 300 K is 11 S/cm for $x=0.05$ of $\text{Cu}_{1-x}\text{Pt}_x\text{FeO}_2$ sample, approximately 4 times higher than the CuFeO_2 sample (3 S/cm). It is interesting to point out that the highest conductivity (11 S/cm) of the $\text{Cu}_{1-x}\text{Pt}_x\text{FeO}_2$ ($x=0.05$) samples at 300 K is clearly higher than the highest value of most delafossite compounds such as $\text{Cu}_{1-x}\text{Ag}_x\text{RhO}_2$ (5 S/cm) [17], $\text{Cu}_{1-x}\text{Ag}_x\text{AlO}_2$ (2 S/cm) [19], and $\text{CuFe}_{1-x}\text{Ni}_x\text{O}_2$ (8 S/cm) [29]. These results imply that Pt^{1+} substitution in the Cu^{1+} site for CuFeO_2 delafossite has higher effects in electrical conduction than Ag substitution in the Cu^{1+} site and the doped impurity of trivalent (such as Ni, Mn, Co) into Fe^{3+} site. The difference value of the electrical conductivity and the activation energy of CuFeO_2 samples between before and after substituting Pt imply that the difference transport mechanisms in CuFeO_2 and $\text{Cu}_{1-x}\text{Pt}_x\text{FeO}_2$ samples is a result from the Pt substitution in the Cu-site. The p-type (hole) conductivity of the CuFeO_2 sample is dominated by d-orbital holes in Cu^+ ($3d_{9/4s_1}$) with electric charge compensation of Cu^{2+} ($3d_0$). For $\text{Cu}_{1-x}\text{Pt}_x\text{FeO}_2$ samples, the number of hole carriers increases due to ionized charge from the d-orbital of Pt^+ ($5d_{9/6s_1}$). In summary, the increase electrical conductivity by the Pt substitution in $\text{Cu}_{1-x}\text{Pt}_x\text{FeO}_2$ samples is enhanced because the increased hole carriers are introduced into the Cu-site.

From the equation of electrical conductivity, the relation is given by $\sigma = eN\mu$ where e is the carrier charge, N is the carrier concentration, and μ is the mobility for carriers. For the electronic transport in semiconductors, the charge carriers must be excited from bound charges to free charges, and then they are moved by mobility mechanism. Consequently, the electrical conductivity of the semiconductors is expressed by $\sigma = eN_T \exp[-(E_F - E_v)/k_B T] \mu_0 \exp[-E_u/k_B T]$ [29], where N_T is the effective density of states of charge carrier, and μ_0 is the mobility constant. Thus, the overall activation energy for conductor (E_{σ}) is a combination of two components as the relation $E_{\sigma} = E_{\mu} + E_s$ [29], where E_u is the activation energy for carrier mobility. The value of E_u is obtained from the equation $\mu = D \exp[-E_u/k_B T]$, where μ is the mobility of carrier and D is a constant value. From the average value of E_s (27.5 meV) and the value of E_{σ} (49, 46, 33 and 28 meV for $x=0.0, 0.01, 0.03$ and 0.05 , respectively), the values of E_u of $\text{Cu}_{1-x}\text{Pt}_x\text{FeO}_2$ samples are 21.5, 18.5, 5.5 and 0.5 meV for $x=0.0, 0.01, 0.03$ and 0.05 , respectively, which are less than the thermal energy at room temperature ($k_B T_{300\text{K}} \approx 25$ meV). The small value of E_u implies that the temperature dependence for conductivity of the $\text{Cu}_{1-x}\text{Pt}_x\text{FeO}_2$ samples is major effect from the activation energy for carrier production. Therefore, these results confirm that the p-type conduction of $\text{Cu}_{1-x}\text{Pt}_x\text{FeO}_2$ delafossite is a good semiconductor because of the ionized free carrier occurred by activation energy near the room temperature and the moving free carriers using the activation energy of mobility smaller than the thermal energy at room temperature.

For measurement of the Hall effect of $\text{Cu}_{1-x}\text{Pt}_x\text{FeO}_2$ ($0 \leq x \leq 0.05$) samples at room temperature, the results exhibit p-type carrier (hole) consistent with positive sign of Seebeck coefficient in Fig. 6. The hole carrier concentrations which are calculated from Hall constant (R_H) by the relation $R_H = 1/pe$ [29] are 1.56×10^{18} , 3.86×10^{18} , 8.08×10^{18} and $4.04 \times 10^{19} \text{ cm}^{-3}$ for $x=0.0, 0.01, 0.03$ and 0.05 , respectively as shown in Fig. 8. The concentrations of hole carriers are belong to high impurity doping of semiconductor which is difficult to find out. The results show that the hole densities increase

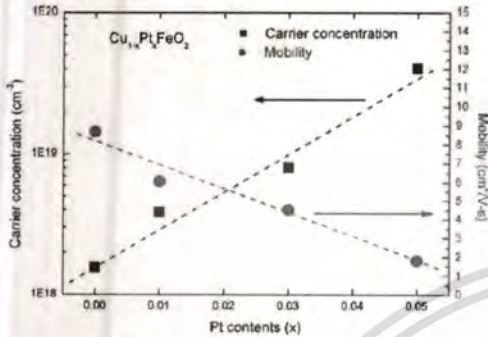


Fig. 8. The carrier concentration and mobility as a function of Pt content in x of $\text{Cu}_{1-x}\text{Pt}_x\text{FeO}_2$ ($0 \leq x \leq 0.05$) samples at room temperature.

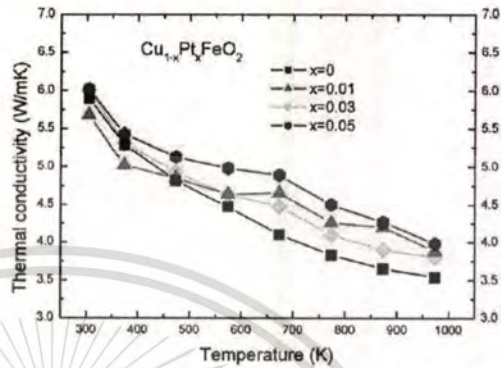


Fig. 10. The thermal conductivity of the $\text{Cu}_{1-x}\text{Pt}_x\text{FeO}_2$ ($0 \leq x \leq 0.05$) samples vs. the temperature range from 300 to 960 K.

with increased Pt substitution of x content. The Hall mobility (μ_H) of samples which is estimated from the relation $\sigma = pe\mu_H$ [29] are 8.6, 6.0, 4.5 and 1.8 cm^2/Vs for $x=0.0, 0.01, 0.03$, and 0.05, respectively as shown in Fig. 8. The value of Hall mobility in the region from 1.8 to 8.6 cm^2/Vs implies that $\text{Cu}_{1-x}\text{Pt}_x\text{FeO}_2$ samples not display the behavior of small polaron because the mobility of the polaron mechanism is lower than 0.1 cm^2/Vs [29].

Fig. 9 shows the power factor ($PF = \sigma S^2$) of $\text{Cu}_{1-x}\text{Pt}_x\text{FeO}_2$ ($0 \leq x \leq 0.05$) samples calculated from the measured electrical conductivity and Seebeck coefficient as function of temperature in the range of 300–960 K. The power factor of all samples is increased with increasing temperature. The power factors at 300 K for $x=0, 0.01, 0.03$ and 0.05 are estimated to be $0.2 \times 10^{-4}, 0.3 \times 10^{-4}, 0.5 \times 10^{-4}$ and 0.7×10^{-4} W/mK^2 , respectively. The highest power factors of $\text{Cu}_{1-x}\text{Pt}_x\text{FeO}_2$ samples at 960 K are $1.1 \times 10^{-4}, 1.5 \times 10^{-4}, 1.7 \times 10^{-4}$ and 2.0×10^{-4} W/mK^2 for $x=0, 0.01, 0.03$ and 0.05, respectively. The maximum power factor at room temperature is 0.7×10^{-4} W/mK^2 at $x=0.05$. The $\text{Cu}_{1-x}\text{Pt}_x\text{FeO}_2$ sample for $x=0.05$ shows highest value of power factor reaching 2.0×10^{-4} W/mK^2 at temperature 960 K. The PF value of $\text{Cu}_{1-x}\text{Pt}_x\text{FeO}_2$ sample for $x=0.05$ at 960 K displays 2 times and 3 times higher than the CuFeO_2 sample at 960 K and at 300 K, respectively. Moreover, the highest PF value of the sample for $x=0.05$ at 960 K is higher than those reported of CuFeO_2 ($PF = 1.4 \times 10^{-4}$ W/mK^2) [28], $\text{CuFe}_{1-x}\text{Ni}_x\text{O}_2$ ($PF = 1.8 \times 10^{-4}$ W/mK^2) [15], and $\text{CuAl}_{1-x}\text{Fe}_x\text{O}_2$ ($PF = 0.9 \times 10^{-4}$ W/mK^2) [30].

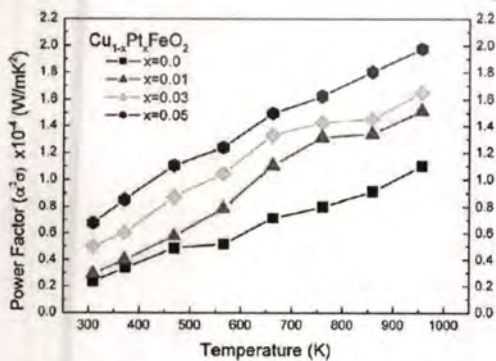


Fig. 9. The power factor of $\text{Cu}_{1-x}\text{Pt}_x\text{FeO}_2$ ($0 \leq x \leq 0.05$) samples vs. the temperature range of 300–960 K.

The temperature dependence of thermal conductivity on $\text{Cu}_{1-x}\text{Pt}_x\text{FeO}_2$ ($0 \leq x \leq 0.05$) samples as function of temperature in the range from 300 to 960 K is shown in Fig. 10. The samples were measured by using a laser flash method with the relation of $\kappa = dC_p a$ [31], where d , C_p and a are the density of sample, specific heat and thermal diffusivity, respectively. The bulk density of $\text{Cu}_{1-x}\text{Pt}_x\text{FeO}_2$ samples for $x=0, 0.01, 0.03$ and 0.05 are 5.22, 5.21, 5.20 and 5.19, respectively, as exhibited in Table 1. The ratios of bulk density to calculation density of $\text{Cu}_{1-x}\text{Pt}_x\text{FeO}_2$ samples have ranging from 91 to 96%. The results of thermal conductivity of $\text{Cu}_{1-x}\text{Pt}_x\text{FeO}_2$ samples decrease as a result of increasing temperature as shown in Fig. 10. The κ values of $\text{Cu}_{1-x}\text{Pt}_x\text{FeO}_2$ samples lead to minimal increase with increased Pt substitution x content. The κ values of CuFeO_2 sample are in the range from 5.8 to 3.5 W/mK with a region of temperature 300–960 K. For $\text{Cu}_{1-x}\text{Pt}_x\text{FeO}_2$ sample for $x=0.05$, the κ value is slightly higher about 1.1 time than that value of CuFeO_2 sample. The minimum of κ value (3.5 W/mK) is in CuFeO_2 sample at high temperature 960 K. The yield of thermal conductivity exhibits that $\text{Cu}_{1-x}\text{Pt}_x\text{FeO}_2$ samples decrease with increased temperature. Therefore, the high value of Z and ZT of $\text{Cu}_{1-x}\text{Pt}_x\text{FeO}_2$ samples is dominant to occur in high temperature because the κ value still contains minimum value in high temperature.

The total thermal conductivity (κ) consists of the two components: the lattice (phonon) component and electronic component as in following the reaction $\kappa = \kappa_l + \kappa_e$ [31], where the κ_l and κ_e are the thermal conductivity of phonon and the electronic contribution, respectively. From the Wiedemann–Franz law [31], the κ_e is related by $\kappa_e = L\sigma T$, where L_0 is the Lorenz factor (2.45×10^{-8} $\Omega\text{m}^2/\text{K}^2$), T is the absolute temperature, σ is the electrical conductivity. From the highest σ value (23 S/cm) of $\text{Cu}_{1-x}\text{Pt}_x\text{FeO}_2$ samples for $x=5$ at 960 K, the κ_e value is 5.409×10^{-2} W/mK which is 1.545% of the total κ value. This result indicates that the major effect of thermal conductivity of $\text{Cu}_{1-x}\text{Pt}_x\text{FeO}_2$ samples is dominated by the phonon mechanism part.

For the lattice thermal conductivity (κ_l), The Umklapp scattering contribution in the phonon scattering process is expressed by $\kappa_U = \delta[(T_m)^{3/2} M^{-7/6} \rho^{2/3}] T^{-1}$ [32], where κ_U is the Umklapp phonon thermal conductivity, δ is the proportionality constant,

Table 1
Bulk densities of the $\text{Cu}_{1-x}\text{Pt}_x\text{FeO}_2$ ($0 \leq x \leq 0.05$) samples and their ratios to the theoretical density.

| x | 0.0 | 0.01 | 0.03 | 0.05 |
|------------------------------------|-------|-------|-------|-------|
| Density (g/cm^3) | 5.22 | 5.21 | 5.20 | 5.19 |
| Ratio (%) | 96.84 | 95.94 | 94.20 | 91.97 |

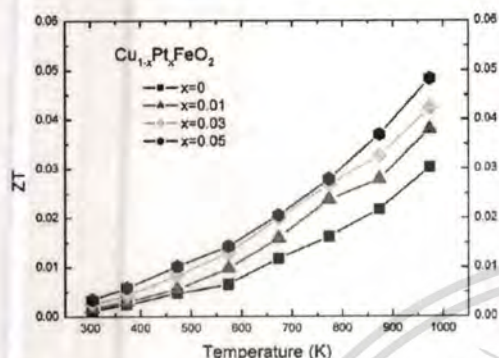


Fig. 11. The dimensionless figure of merit (ZT) of $\text{Cu}_{1-x}\text{Pt}_x\text{FeO}_2$ ($0 \leq x \leq 0.05$) samples vs. the temperature range from 300 to 960 K.

T_m is the melting temperature, M is the average atomic mass, ρ is the density, and T is the operation temperature. The Umklapp relation implies that the κ_{ph} value is proportion to inversion of temperature. From Fig. 10, the thermal conductivity of $\text{Cu}_{1-x}\text{Pt}_x\text{FeO}_2$ samples can plot in function of inversion temperature as the relation of κ vs. $1000/T$. The curve can show the thermal conductivity of $\text{Cu}_{1-x}\text{Pt}_x\text{FeO}_2$ samples linear with T^{-1} corresponding with the Umklapp relation. This result indicates that the major effect of thermal conductivity of $\text{Cu}_{1-x}\text{Pt}_x\text{FeO}_2$ samples is controlled by phonon mechanism with contribution by the Umklapp scattering. From the Umklapp relation, the minimum of thermal conductivity for $\text{Cu}_{1-x}\text{Pt}_x\text{FeO}_2$ samples is occurred by operating in high temperature near melting point (1365 K) temperature.

The temperature dependence of ZT for $\text{Cu}_{1-x}\text{Pt}_x\text{FeO}_2$ samples in temperature ranging from 300 to 960 K is exhibited in Fig. 11. The ZT values are also calculated from Z value and temperature. The results show that the ZT of $\text{Cu}_{1-x}\text{Pt}_x\text{FeO}_2$ samples rapidly is raised with increasing the temperature. In addition, the ZT values of $\text{Cu}_{1-x}\text{Pt}_x\text{FeO}_2$ samples are increased with increased Pt substitution of x content. The maximum ZT values of $\text{Cu}_{1-x}\text{Pt}_x\text{FeO}_2$ samples are 0.03, 0.038, 0.044 and 0.05 for $x = 0, 0.01, 0.03$ and 0.05 , respectively, at 960 K. Obviously, the $\text{Cu}_{1-x}\text{Pt}_x\text{FeO}_2$ sample of $x = 0.05$ exhibits the highest value of ZT (=0.05), at 960 K. This value is higher than those reported of CuFeO_2 ($ZT = 0.025$) [28], CuAlO_2 ($ZT = 0.004$) [19], $\text{Cu}_{1-x}\text{Ag}_x\text{AlO}_2$ ($ZT = 0.016$) [30], and $\text{CuFe}_{1-x}\text{Ni}_x\text{O}_2$ ($ZT = 0.045$) [14].

4. Conclusions

The objective of this study was to improve ZT value of CuFeO_2 delafossite by Pt substitution in content of $x = 0.0, 0.01, 0.03, 0.05$. The samples were prepared by the conventional solid state reaction method. The results of this study show that CuFeO_2 sample is decomposed at temperature over 1365 K. The properties of Seebeck coefficient, electrical conductivity and thermal conductivity were measured and discussed in the high temperature ranging from 300 to 960 K. The Seebeck coefficient of all $\text{Cu}_{1-x}\text{Pt}_x\text{FeO}_2$ samples not only display the p-type semiconductor, but also show the Seebeck coefficient at 300 K in 261, 149, 242 and 240 $\mu\text{V/K}$ for $x = 0, 0.01, 0.03$ and 0.05 , respectively. It is also to point out that the average Seebeck coefficient in high temperature (at 960 K) is in the order 290 $\mu\text{V/K}$. In addition, the room temperature of the electrical conductivity increases from 3.5 to 11 S/cm with increased Pt content of x . The highest electrical conductivity is 23 S/cm for $x = 0.05$ at

960 K. Furthermore, the highest power factor is $2.0 \times 10^{-4} \text{ W/mK}^2$ for $x = 0.05$ at 960 K. The thermal conductivity of CuFeO_2 sample decreases from 5.8 to 3.5 W/mK with increasing temperature. The minimum thermal conductivity is 3.5 W/mK of CuFeO_2 sample at 960 K. Most interestingly, the highest ZT is 0.05 for $x = 0.05$ at 960 K. These results suggest that the effect of small Pt substitution into CuFeO_2 improves the thermoelectric properties and enhances the good semiconductor behavior. In summary, the present work demonstrates that CuFeO_2 substituted by Pt has been given an enhanced performance on thermoelectric material. It will be interesting to see that $\text{Cu}_{1-x}\text{Pt}_x\text{FeO}_2$ delafossite material in the future can be invented the thermoelectric device for covering heat losses at high temperature.

Acknowledgments

The authors would like to thank the Department of Chemistry, Faculty of Science, Ubon Ratchathani University for providing TG-DTA facilities; the Department of Applied Physics, Faculty of Science, King Mongkut's Institute of Technology Ladkrabang (KMUTL) for providing PtCl_2 powder. The contribution of anonymous reviewers and language editors are also acknowledged for providing valuable feedback and suggestions to improve the article.

References

- [1] J. Li, W. Liu, L. Zhao, M. Zhou, *NPG Asia Mater.* 2 (2010) 152–158.
- [2] G.J. Snyder, E.S. Toberer, *Nat. Mater.* 7 (2008) 105–114.
- [3] A. Charoenphakdee, K. Kurosaki, A. Harnwungmong, H. Muta, S. Yamana, *J. Alloy Compd.* 496 (2010) 53–55.
- [4] X. Hou, Y. Zhou, L. Wang, W. Zhang, W. Zhang, L. Chen, *J. Alloy Compd.* 482 (2009) 544–547.
- [5] D. Kenfaui, D. Chateigner, M. Gomina, J.G. Noudem, *J. Alloy Compd.* 490 (2010) 472–479.
- [6] H. Ohta, K. Sugiura, K. Koumoto, *J. Inorg. Chem.* 47 (2008) 8429–8436.
- [7] T. Seetawan, V. Amornkitbamrung, T. Burinprakon, S. Maensiri, P. Tongbai, K. Kurosaki, H. Muta, M. Uno, S. Yamana, *J. Alloy Compd.* 416 (2006) 291–295.
- [8] S. Maensiri, W. Nuansing, *Mater. Chem. Phys.* 99 (2006) 104–108.
- [9] T. Kajitani, T. Nozaki, K. Hayashi, *Adv. Sci. Technol.* 74 (2010) 66–71.
- [10] M.A. Marquardt, N.A. Ashmore, D.P. Cann, *Thin Solid Films* 496 (2006) 146–156.
- [11] M. Beckman, J. Salvador, X. Shi, G.S. Nolas, J. Yang, *J. Alloy Compd.* 489 (2010) 336–338.
- [12] V. Eyert, R. Frésard, A. Maignan, *J. Chem. Mater.* 20 (2008) 2370–2373.
- [13] V. Eyert, R. Frésard, A. Maignan, *Phys. Rev. B* 78 (2008) 052402.
- [14] K. Hayashi, T. Nozaki, T. Kajitani, *Jpn. J. Appl. Phys.* 46 (2007) 5226–5229.
- [15] T. Nozaki, K. Hayashi, T. Kajitani, *J. Chem. Eng. Jpn.* 40 (2007) 1205–2007.
- [16] T. Nozaki, K. Hayashi, T. Kajitani, *J. Electron. Mater.* 39 (2010) 1798–1802.
- [17] S. Shibusaki, W. Kobayashi, I. Terasaki, *J. Phys. Rev. B* 74 (2006) 235110.
- [18] T. Okuda, T. Kishimoto, K. Uto, T. Hokazono, Y. Onose, Y. Tokura, R. Kajimoto, M. Matsuda, *J. Phys. Soc. Jpn.* 78 (2009) 13604.
- [19] S. Yanagiya, N. Nong, J. Xu, N. Pryds, *Materials* 3 (2010) 318–328.
- [20] A. Wichainchai, P. Dordor, J.P. Doumerc, E. Marquestaut, M. Pouchard, P. Hagenmuller, *J. Solid State Chem.* 74 (1988) 126.
- [21] P. Dordor, J.P. Chaminade, A. Wichainchai, E. Marquestaut, J.P. Doumerc, M. Pouchard, P. Hagenmuller, A. Ammar, *J. Solid State Chem.* 75 (1988) 105–112.
- [22] ICSD Card File: 01-075-2146, ICSD Card File: 01-089-5897.
- [23] T.R. Zhao, M. Hasegawa, T. Kondo, T. Yagi, H. Takei, *Mater. Res. Bull.* 32 (1997) 151–157.
- [24] C.T. Prewitt, R.D. Shannon, D.B. Rogers, *J. Inorg. Chem.* 10 (1971) 719–723.
- [25] B. Bellal, S. Saadi, N. Koriche, A. Bouguelia, M. Trari, *J. Phys. Chem. Solids* 70 (2009) 1132–1136.
- [26] R.J. Cava, R.J. Cava, H.W. Zandbergen, A.P. Ramirez, H. Takagi, C.T. Chen, J.J. Krajewski, W.F. Peck Jr., J.V. Waszczak, G. Meigs, R.S. Roth, L.F. Schneemeyer, *J. Solid State Chem.* 104 (1993) 437–452.
- [27] K. Isawa, Y. Yaegashi, M. Komatsu, M. Nagano, S. Sudo, M. Karppinen, H. Yamauchi, *J. Phys. Rev. B* 56 (1997) 3457–3466.
- [28] T. Nozaki, K. Hayashi, T. Kajitani, 26th International Conference on Thermoelectrics, ICT 2007, 2008, pp. 167–170.
- [29] P.A. Cox, *Transition Metal Oxides*, Clarendon Press, Oxford, 1995.
- [30] K. Park, K.Y. Ko, H.-C. Kwon, S. Nahm, *J. Alloy Compd.* 437 (2007) 1–6.
- [31] A.F. Ioffe, Infosearch limited, London, 1957.
- [32] N. Schwartz, W. Tantraporn, W.J. Van Der Grinten, *Advanced Energy Conversion*, Pergamon Press, 1963.

A.2**Theoretical Study of Electronic Structure and Thermoelectric Properties of Doped CuAlO_2 ,**

P. POOPANYA, A. YANGTHAISONG, C. RATTANAPUN, and A. WICHAINCHAI,

Journal of ELECTRONIC MATERIALS,

vol. 40, No 5, (2011), pp. 987-991.



Theoretical Study of Electronic Structure and Thermoelectric Properties of Doped CuAlO₂

P. POOPANYA,¹ A. YANGTHAISONG,^{1,3} C. RATTANAPUN,²
 and A. WICHAINCHAI²

1.—Computational Materials and Device Physics Group, Department of Physics, Ubon Ratchathani University, Ubon Ratchathani 34190, Thailand. 2.—Department of Applied Physics, Faculty of Science, King Mongkut's Institute of Technology Ladkrabang, Chalongkrung Road, Ladkrabang, Bangkok 10520, Thailand. 3.—e-mail: a.yangthaisong@gmail.com

The doping level dependence of thermoelectric properties of delafossite CuAlO₂ has been investigated in the constant scattering time (τ) approximation, starting from the first principles of electronic structure. In particular, the lattice parameters and the energy band structure were calculated using the total energy plane-wave pseudopotential method. It was found that the lattice parameters of CuAlO₂ are $a = 2.802$ Å and $c = 16.704$ Å, and the internal parameter is $u = 0.1097$. CuAlO₂ has an indirect band gap of 2.17 eV and a direct gap of 3.31 eV. The calculated energy band structures were then used to calculate the electrical transport coefficients of CuAlO₂. By considering the effects of doping level and temperature, it was found that the Seebeck coefficient $S(T)$ increases with increasing acceptor doping (A_d) level. The values of $S(T)$ in our experiments correspond to an A_d level at 0.262 eV, which is identified as the Fermi level of CuAlO₂. Based on our experimental Seebeck coefficient and the electrical conductivity, the constant relaxation time is estimated to be 1×10^{-16} s. The power factor is large for a low A_d level and increases with temperature. It is suggested that delafossite CuAlO₂ can be considered as a promising thermoelectric oxide material at high doping and high temperature.

Key words: Thermoelectric properties, delafossite CuAlO₂, first principles

INTRODUCTION

Thermoelectric properties of delafossite materials, CuMO₂ (M = Al, Ga, In, Sc, Y, La), have been extensively studied as good potential thermoelectric materials.^{1,2} The thermoelectric conversion performance of materials can be described by the dimensionless figure of merit ZT , which is defined as $ZT = S^2\sigma T/\kappa$, where S is the Seebeck coefficient, σ is the electrical conductivity, and κ is the thermal conductivity. To achieve high ZT , a high power factor ($S^2\sigma$) is required, for example, by changing the carrier concentration by doping, whilst keeping the thermal conductivity as low as possible. Since S , σ , and κ are all functions of carrier concentration

and are interrelated,³ optimization of the figure of merit can be considered as a challenging problem.

We focused on the delafossite CuAlO₂ due to its large power factor of 1.04×10^{-4} W/m K² and 2.0×10^{-5} W/m K² at 1073 K reported for single-crystal and polycrystalline forms,⁴ respectively. Besides, improvements of the thermoelectric properties of CuAlO₂ by internal doping have been widely investigated; for example, it was found that the highest power factor can reach 1.24×10^{-4} W/m K² at 1060 K⁵ by adding Ag and Zn to CuAlO₂. It was also reported that the addition of Fe in CuAl_{1-x}Fe_xO₂ results in an increase in electrical conductivity for $x = 0.1$, with the highest power factor of 1.1×10^{-4} W/m K² attained for CuAl_{0.9}Fe_{0.1}O₂ at 1140 K.⁶ In addition, the electrical conductivity of Mg-doped CuAlO₂ thin films at room temperature was found to be about three orders of magnitude

(Received May 30, 2010; accepted November 29, 2010;
 published online January 4, 2011)

larger than that of undoped CuAlO_2 films.⁷ From these experimental results, it is expected that CuAlO_2 can be considered as another promising material for thermoelectric devices. Apart from experimental investigation, calculations of electronic structures have also been used to investigate electronic conduction and optical property of CuAlO_2 and related compounds; for example, the energy band structure was calculated using the plane-wave ultrasoft pseudopotential based on first-principles calculations to study the charge neutrality level (CNL) in CuAlO_2 .⁸ The CNL energy can be used to describe the doping polarity achievable in CuAlO_2 and predict the system's response to doping. It was pointed out that the CNL increases in the gap from p -type to n -type materials. In addition, the effect of Cd impurity substitution on the electronic properties of CuAlO_2 was investigated using first-principles calculations.^{9–11} It was shown that CuAlO_2 could be made as both n -type and p -type material.

In the present work, the doping level dependence of thermoelectric properties of delafossite material CuAlO_2 has been investigated, starting from the first-principles electronic structure. The calculated band structures are then used in combination with the Boltzmann transport equation solver under the constant relaxation time (τ) approximation to calculate electrical transport quantities.

COMPUTATIONAL DETAILS

The space group of CuAlO_2 is $R\bar{3}m$ with hexagonal atom positions of Cu (0, 0, 0), Al (0, 0, 0.5), and O (0, 0, $\pm u$).¹² The electronic structures were calculated using the plane-wave pseudopotential method based on density functional theory (DFT), as implemented in the CASTEP code.¹³ The local-density approximation (LDA) was used for the exchange and correlation potential. The presence of tightly bound core electrons was represented by a nonlocal ultrasoft pseudopotential of Vanderbilt type. The states $\text{Cu-}3p^6 3d^{10} 4s^1$, $\text{Al-}3s^2 3p^1$, and $\text{O-}2s^2 2p^4$ were treated as valence states. A plane-wave cutoff energy of 380 eV and a $6 \times 6 \times 6$ grid of Monkhorst–Pack points were employed to ensure good convergence of the computed structures and energies. Geometry optimization was determined using the Broyden–Fletcher–Goldfarb–Shenno (BFGS) minimization technique, with thresholds of converged structure of energy change per atom $< 10^{-5}$ eV/atom, residual force < 0.03 eV/Å, stress < 0.05 GPa, and displacement of atoms during geometry optimization < 0.001 Å. The tolerance in the self-consistent field (SCF) calculation was 1.0×10^{-6} eV/atom. The doping level dependence of thermoelectric properties was then obtained in the rigid band approach and the constant τ approximation using the BoltzTraP program.¹⁴ The results are based on electronic eigenvalues calculated on a uniform $50 \times 50 \times 50$ grid of k -points (total k -points 11,050).

RESULTS AND DISCUSSION

The energy versus volume curve was obtained by using the third-order Birch–Murnaghan equation,¹⁵ as shown in Eq. 1, to find the optimized parameters.

$$P = \frac{3}{2}B \left[\left(\frac{V_0}{V} \right)^{7/3} - \left(\frac{V_0}{V} \right)^{5/3} \right] \times \left\{ 1 + \frac{3}{4}(4-B') \left[\left(\frac{V_0}{V} \right)^{2/3} - 1 \right] \right\}, \quad (1)$$

where V_0 is the equilibrium volume, B is the bulk modulus of the material, and $B' = dB/dP$. The lattice constants of the conventional cell CuAlO_2 , as shown in Fig. 1a, are $a = 2.802$ Å and $c = 16.704$ Å, and

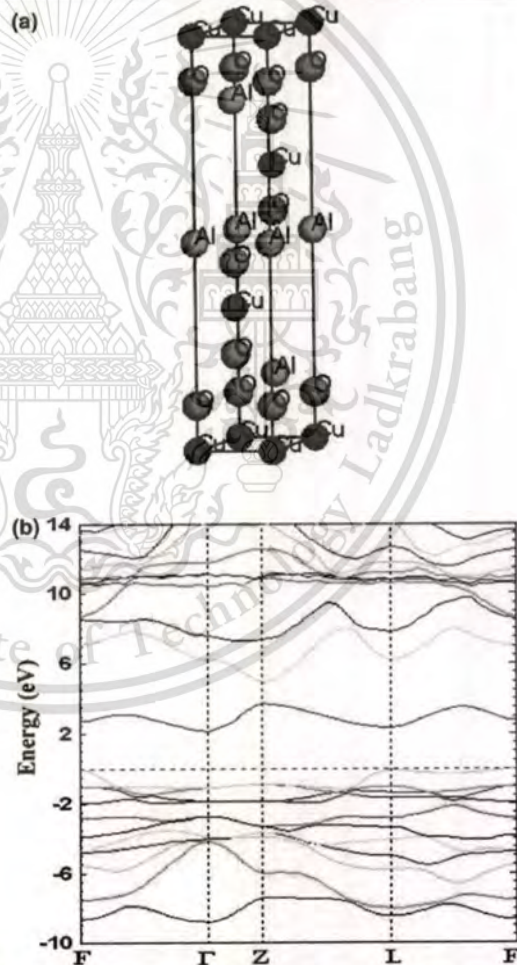


Fig. 1. (a) Structure of CuAlO_2 , belonging to the space group $R\bar{3}m$. (b) Calculated band structure of CuAlO_2 .

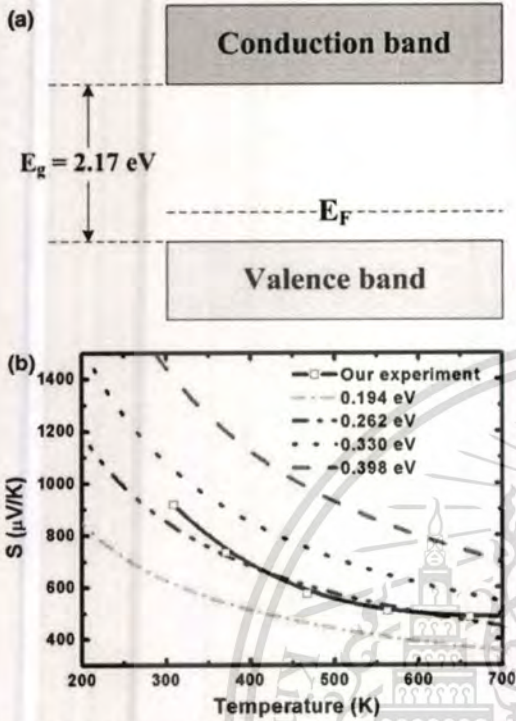


Fig. 3. (a) Band scheme for *p*-type CuAlO_2 from first-principles calculations. (b) Seebeck coefficient, $S(T)$, for various *p*-type doping levels, and experimental data.

with increasing temperature, because electrons can easily move into the acceptor level. However, this effect is less important at high temperature, since more electrons can be thermally excited to the acceptor level.

Figure 4b shows the temperature dependence of the power factor, from which it can be seen that the power factor increases with increasing temperature. Note that the power factor is large for a low A_d level. It is worthwhile to mention that the largest reported power factors of bulk thermoelectric materials are approximately $40 \mu\text{W}/\text{cm K}^2$ to $45 \mu\text{W}/\text{cm K}^2$,³¹ obtained for conventional thermoelectric materials such as Bi_2Te_3 and PbTe . Our calculated values are about two orders of magnitude lower than state-of-the-art values of conventional thermoelectric materials. Recently, it was demonstrated theoretically that the optimal Seebeck coefficient is in the range of $130 \mu\text{V}/\text{K}$ to $187 \mu\text{V}/\text{K}$ at a given temperature.³¹ Hence, CuAlO_2 may become a good thermoelectric material at high temperature, provided that the thermal conductivity is very low and its conductivity can be enhanced. Therefore, it will be instructive to investigate experimentally and theoretically the effect of heavy doping on conductivity while maintaining the high Seebeck coefficient in this material.

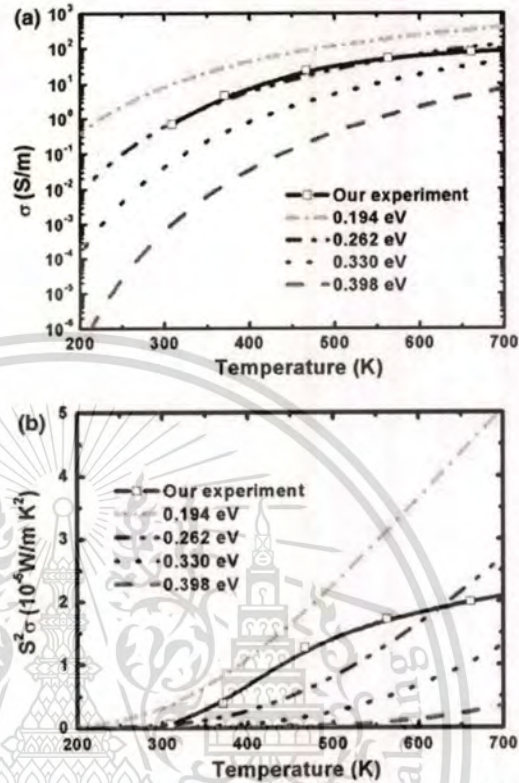


Fig. 4. (a) Electrical conductivity, $\sigma(T)$ and (b) power factor, $S^2\sigma(T)$ for various *p*-type doping levels with $\tau = 1 \times 10^{-16}$ s, and experimental data.

CONCLUSIONS

The lattice constants and electronic structures of delafossite CuAlO_2 were calculated by the first-principles method. The results for the lattice parameters show good agreement with other theoretical and experimental results. The energy band structure shows that CuAlO_2 is an indirect band gap material with a gap of 2.17 eV. Its direct energy gap value is 3.31 eV. The valence band is dominated by Cu-3d and O-2p states, whereas the conduction band is dominated by Al-3p , O-2p , and Cu-3p states. Based on the calculated electronic properties of CuAlO_2 , we calculated the thermoelectric parameters by employing the Boltzmann theory and rigid-band approach. Our investigation revealed that the power factor of CuAlO_2 increases with increasing doping level and temperature. It is expected that our calculations, combined with experimental data, may serve as a guide in designing high-efficiency thermoelectric devices based on delafossite CuAlO_2 and related compounds.

ACKNOWLEDGEMENTS

This work has partially been supported by the Human Resource Development in Science Project (Science Achievement Scholarship of Thailand, SAST), the National Nanotechnology Center (NANOTEC), National Science and Technology Development Agency (NSTDA), Ministry of Science and Technology, Thailand, through its Computational Nanoscience Consortium (CNC). A.Y. is very grateful to Dr. S.J. Clark of Durham University, UK for use of his codes.

REFERENCES

1. D.J. Singh, *Phys. Rev. B* 77, 205126 (2008).
2. A.N. Banerjee, R. Maity, P.K. Ghosh, and K.K. Chattopadhyay, *Thin Solid Films* 474, 261 (2005).
3. G.D. Mahan and J.O. Sofo, *Proc. Natl. Acad. Sci. USA* 93, 7436 (1996).
4. K. Koumoto, H. Koduka, and W.S. Seo, *J. Mater. Chem.* 11, 251 (2001).
5. S. Yanagiya, N.V. Nong, J. Xu, and N. Pryds, *Materials* 3, 318 (2010).
6. K. Park, K.Y. Ko, H.-C. Kwon, and S. Nahm, *J. Alloy Compd.* 437, 1 (2007).
7. G. Dong, M. Zhang, W. Lan, P. Dong, and H. Yan, *Vacuum* 82, 1321 (2008).
8. B. Falabretti and J. Robertson, *J. Appl. Phys.* 102, 123703 (2007).
9. M.V. Lalic, J. Mestnik-Filho, A.W. Carbonari, R.N. Saxena, and M.J. Moralles, *J. Phys. Condens. Matter* 14, 5517 (2002).
10. M.V. Lalic, J. Mestnik-Filho, A.W. Carbonari, and R.N. Saxena, *Solid State Commun.* 125, 175 (2003).
11. M.V. Lalic and J. Mestnik-Filho, *J. Phys. Condens. Matter* 18, 1619 (2006).
12. T. Ishiguro, A. Kitazawa, N. Mizutani, and M. Kato, *J. Solid State Chem.* 40, 170 (1981).
13. S.J. Clark, M.D. Segall, C.J. Pickard, P.J. Hasnip, M.J. Probert, K. Refson, and M.C. Payne, *Z. Kristallogr.* 567, 220 (2005).
14. G.K.H. Madsen and D.J. Singh, *Comput. Phys. Commun.* 175, 67 (2006).
15. F. Birch, *J. Geophys. Res.* 83, 1257 (1978).
16. I. Hamada and H. Katayama-Yoshida, *Phys. B* 376–377, 808 (2006).
17. L.J. Shi, Z.J. Fang, and J. Li, *J. Appl. Phys.* 104, 073527 (2008).
18. Q.J. Liu, Z.T. Liu, and L.P. Feng, *Phys. B* 405, 2028 (2010).
19. X. Nie, S.H. Wei, and S.B. Zhang, *Phys. Rev. Lett.* 88, 066405 (2002).
20. J. Robertson, K. Xiong, and S.J. Clark, *Thin Solid Films* 496, 1 (2006).
21. Th. Dittrich, L. Dloczik, T. Guminckaya, and MCh Lux-Steiner, *Appl. Phys. Lett.* 85, 724 (2004).
22. D.S. Kim, S.J. Park, E.K. Jeong, H.K. Lee, and S.Y. Choi, *Thin Solid Films* 515, 5103 (2007).
23. F. Aryasetiawany and O. Gunnarsson, *Rep. Prog. Phys.* 61, 237 (1998).
24. R. Dovesi, R. Orlando, C. Roetti, C. Pisani, and V.R. Saunders, *Phys. Stat. Sol. (b)* 217, 63 (2000).
25. V.I. Anisimov, J. Zaanen, and O.K. Andersen, *Phys. Rev. B* 44, 943 (1991).
26. B.M. Bylander and L. Kleinman, *Phys. Rev. B* 41, 7868 (1990).
27. P.P. Rushton, J.T. David, and S.J. Clark, *Phys. Rev. B* 65, 235203 (2002).
28. D.O. Scanlon, A. Walsh, B.J. Morgan, and G.W. Watson, *Phys. Rev. B* 79, 035101 (2009).
29. C.M. Bhandari and D.W. Rowe, *CRC Handbook of Thermoelectrics* (Boca Raton: CRC Press, 1995).
30. S. Lee and P. von Allmen, *Appl. Phys. Lett.* 88, 022107 (2006).
31. P. Pichanusakorn and P.R. Bandaru, *Appl. Phys. Lett.* 94, 223108 (2009).

B: NATIONAL AND INTERNATIONAL PROCEEDING

- B.1: **Chesta Ruttanapun**, Wutthisak Prachamon, and Aree Wichainchai, "*Synthesis and Thermoelectric Properties of p-type CuFeO_2 Delafossite-Type Oxide*" 6th Thailand Materials Science and Technology Conference, MSAT-6, Miracle Grand Hotel , Bangkok, Thailand, 26-27 September 2010, pp. 135-137. (Oral) (Proceeding book)
- B.2: **Chesta Ruttanapun**, Wutthisak Prachamon, and Aree Wichainchai, "*Synthesis and Thermoelectric, Electrical and Optical properties of p-type CuAlO_2 Delafossite*", 36th Congress on Science and Technology of Thailand, STT.36, Bangkok International Trade & Exhibition Center (BITEC) , Bangkok, Thailand, 26-28 October 2010. (Oral) (abstract book & Full only)
- B.3: **Chesta Ruttanapun**, Wutthisak Prachamon, and Aree Wichainchai, "*Synthesis, Thermoelectric Properties of $\text{CuFe}_{0.5}\text{Al}_{0.5}\text{O}_2$ Delafossite and Finite Element Computing for Power Generator on Its Module*", SPC2011: Siam Physics Congress, The 6th Annual Conference of the Thai Physics Society, Pattaya, Chonburi, Thailand, 23-26 March, 2011, pp. 196- 199. (Oral) (abstract book)
- B.4: **Chesta Ruttanapun** and Aree Wichainchai, "*Preparation and Comparison of Thermoelectric Properties of CuFeO_2 , CuAlO_2 and $\text{CuFe}_{0.5}\text{Al}_{0.5}\text{O}_2$ Delafossite Structure*", The 1st Southeast Asia Conference on Thermoelectrics, Krunsrri River Hotel, Ayutthaya, Thailand, 20-21 July 2011, pp. 34. (Oral) (abstract book)

B.1:**Synthesis and Thermoelectric Properties of p-type CuFeO_2 Delafossite-Type Oxide,**

Chesta Ruttanapun, Wutthisak Prachamon, and Aree Wichainchai,

6th Thailand Materials Science and Technology Conference, MSAT-6,

Miracle Grand Hotel, Bangkok, Thailand,

26-27 September 2010, pp. 135-137.



Synthesis and Thermoelectric Properties of p-type CuFeO_2 Delafossite-Type Oxide

Chesta Ruttanapun^{1*}, Wutthisak Prachamon² and Aree Wichainchai¹

¹Department of Applied Physics, Faculty of Science, King Mongkut's Institute of Technology Ladkrabang, Chalongkrung Road, Ladkrabang, Bangkok, 10520 Thailand

²Department of Physics, Faculty of Science, Ubonrajathaneer University, Ubon Ratchathani, 34190 Thailand

*Corresponding Author: Tel. +66-2-326-4339 ext 285, E-mail: Chesta.ruttanapun@gmail.com

Abstract

The CuFeO_2 sample was prepared by a solid state reaction method for investigating thermoelectric properties. The Seebeck coefficient, electrical and thermal conductivity were measured at high temperatures ranging from 300 to 960 K. Our study reveals that the Seebeck coefficients and electrical conductivity exhibited positive values (p-type semiconductor) of the range from 261 to 300 $\mu\text{V/K}$ and from 3 to 13 S/cm, respectively. The thermal conductivity decreased from 5.8 to 3.5 W/mK with increasing temperature. The values of power factor and dimensionless ZT ranged from 0.235×10^{-4} to 1.1×10^{-4} W/mK² and from 0.0012 to 0.03, respectively. The maximum value of ZT was 0.03 at temperature 960 K. Indeed, these results point out that the CuFeO_2 is candidate for high performance of thermoelectric material for operating in high temperature.

Keywords: CuFeO_2 , Delafossite, Thermoelectric, Seebeck coefficient, Dimensionless Figure of Merit (ZT)

1. Introduction

Recently, thermoelectric[1] materials have become to interesting for new source energy. The thermoelectric effect refers to phenomenon of the direct conversion of temperature gradients to electricity and vice versa. Furthermore, thermoelectric generators can be used to convert vest heat generated by various sources to electric

power. For indirect effect, thermoelectric coolers can be used to make refrigerators and other cooling systems. These conversion effects have advantages from non-moving part or non-chemical toxic. The performance of the thermoelectric material is evaluated by the dimensionless figure of merit, $ZT = \alpha^2 \sigma T / \kappa$, where T is the absolute temperature, α is the Seebeck coefficient, σ and κ are the electrical and thermal conductivity, respectively.

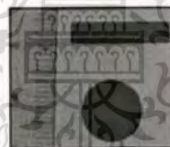


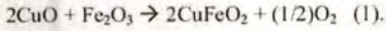
Fig. 1. The pellet and bar of CuFeO_2 samples.

Obviously, thermoelectric properties of oxide materials have been reported to have conversion efficiency close to that of conventional metallic materials. For examples, thermoelectric voltage and d.c conductivity of transition metal oxides [2] such as NiO, NaCo_2O_4 and CaCo_3O_6 have been reported to be large at high temperature conditions. However, the delafossite [3] compound which is transition metal oxide structure has been reported to exhibit a high ZT .

Therefore, in this work, the CuFeO_2 which is a kind of delafossite compound was prepared to investigate the thermoelectric properties at high temperature.

2. Experimental

The sample of CuFeO_2 was prepared by solid state reaction method by a chemical formula[3]:



The starting powders CuO and Fe_2O_3 were mixed, pressed into pellets, and several sintered at each time for 1050°C (15-20 hours) in air and finally, quenched at room temperature. The sample (Fig. 1.) was characterized by x-ray diffraction (XRD) using $\text{Cu K}\alpha$ radiation (PHILIPS model: X' Pert MPD) with scanning 2-Theta from 10° to 90° . Microstructure and morphology of the sample were analyzed by scanning electron microscope (SEM) model: JSM-5410 (JEOL). The Seebeck coefficient and the electrical conductivity were simultaneously measured using an ULVAC-RIKO ZEM-2. The thermal conductivity was determined from thermal diffusivity and specific heat measured using a ULVAC SINKU RIKO Inc. (Model: TC-7000H) laser-flash method.

3. Results & Discussion

3.1 XRD-pattern

The XRD pattern of CuFeO_2 is shown in Fig. 2. The pattern exhibited peaks of crystal phase of hexagonal CuFeO_2 delafossite structure (space group: $R\bar{3}m$ (166)) which are good agreement with the reference ICSD#01-075-2146[4]. The lattice parameter of CuFeO_2 was 3.033 \AA and 17.159 \AA for a -axis and c -axis length, respectively that they were corresponded with the reported of literature [4].

The SEM image of the CuFeO_2 sample is shown in the insert of Fig. 2. Most of the microstructure showed the crystal grain size in the range of 10 to $40 \mu\text{m}$.

3.2 Seebeck Coefficient

The temperature dependence of the Seebeck coefficient (α) is shown in Fig. 3. The results show that the Seebeck coefficient contained the value ranging from 261 to $300 \mu\text{V/K}$ from temperature 300 to 960 K , respectively.

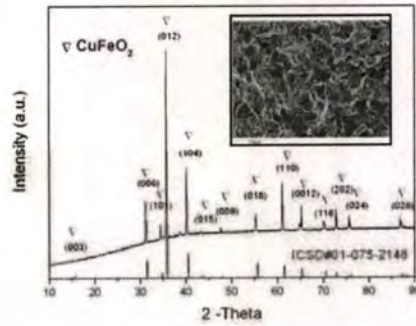


Fig. 2. The XRD patterns of CuFeO_2 sample and the insert shows SEM image.

The sign of Seebeck displayed positive that it is p-type semiconductor. Considering the Seebeck coefficients of well known thermoelectric materials such as Bi_2Te_3 ($218 \mu\text{V/K}$)[2] and NaCo_2O_4 ($100 \mu\text{V/K}$)[2] at room temperature, CuFeO_2 has high potential in thermoelectric applications.

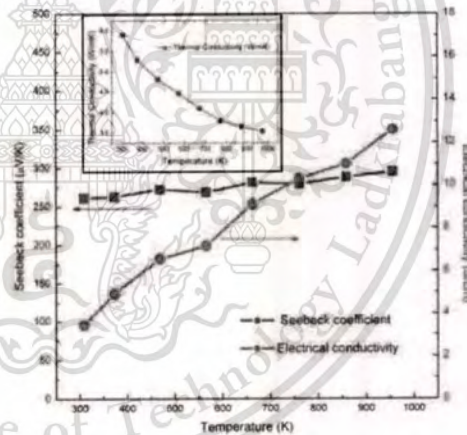


Fig. 3. The temperature dependent of Seebeck coefficient, electric and thermal conductivity of CuFeO_2 .

3.3 Electrical Conductivity

The temperature dependence of the electrical conductivity (σ) of CuFeO_2 sample is shown in Fig. 3.

The results show that the electrical conductivity displayed value increasing from 3 to 13 S/cm with increasing temperature from 300 to 960 K. The results exhibit that the electrical conductivity increased with the temperature increased. Note that the maximum of the electrical conductivity is 13 S/cm at temperature 960 K.

3.4 Thermal Conductivity

The temperature dependence of the thermal conductivity (κ) is shown in the insert of Fig. 3. The results showed that the values of thermal conductivity were decreased the range from 5.8 to 3.5 W/mK with measuring temperature from 300 to 960 K respectively. The maximum value of κ was 5.8 W/mK at room temperature and minimum value was 3.5 W/mK on the range temperature from 800 to 960 K. These results exhibited that the thermal conductivity of the CuFeO₂ sample were decreased depending on increasing temperature.

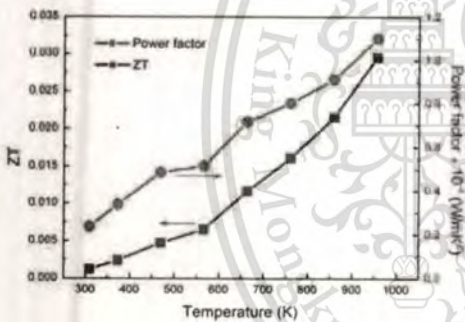


Fig. 4. The temperature dependence of dimensionless ZT and power factor of CuFeO₂ sample.

3.5 Power factor and Dimensionless ZT

Fig. 4 shows the temperature dependence of Power factor ($P = \alpha^2 \sigma$) and dimensionless $ZT (= T \alpha^2 \sigma / \kappa)$ of CuFeO₂ sample. The power factor was calculated from the measurement Seebeck coefficient and electrical conductivity, and the ZT was computed from the Figure of Merit ($Z = \alpha^2 \sigma / \kappa$) and temperature. Both, the power factor and ZT increased with increasing temperature. The power

factor value was in the range of 0.235×10^{-4} to 1.1×10^{-4} W/mK² and the ZT was range from 0.00123 to 0.03 with temperature 300 to 960 K, respectively. The maximum value of power factor and ZT were 1.1×10^{-4} W/mK² and 0.03 at temperature 960 K. This value exhibited that it was nearly the value of conventional NaCo₂O₄ compound ($ZT = 0.07$ at 580 K)[2].

4. Conclusion

The delafossite CuFeO₂ thermoelectric material was synthesized by a solid state reaction method. Our study show that the Seebeck coefficients of CuFeO₂ exhibited positive values (p-type semiconductor) from 261 to 300 μ V/K. The electrical and the thermal conductivity displayed value between from 3 to 13 S/cm and from 3.5 to 5.8 W/mK. In addition, the maximum value of the power factor and the ZT of CuFeO₂ samples are 1.1×10^{-4} W/mK² and 0.03, respectively at temperature 960 K. Furthermore, the CuFeO₂ sample displayed high performance thermoelectric properties at high temperature closely to 1000 K. This suggests CuFeO₂ has high potential for high temperature thermoelectric devices.

References

1. A. F. Ioffe, Infosearch limited, London, 1957.
2. D.M. Rowe (ed), *CRC Handbook of Thermoelectrics: Macro to Nano*, CRC, Boca Raton, 2005.
3. P. Dordor, J. P. Chaminade, A. Wichainchai, E. Marquestaut, J. P. Dourmerc, M. Pouchard, P. Hagenmuller, A. Ammar, "Crystal growth and electrical properties of CuFeO₂ single crystals", *J. Solid State Chem.*, 75 (1988) 105-112.
4. K. Park, et al., "Improvement in thermoelectric properties of CuAlO₂ by adding Fe₂O₃", *J. Alloy. Comp.*, 437 (2007) 1-6.

B.2

Synthesis and Thermoelectric, Electrical and Optical properties of p-type CuAlO_2 Delafossite,

Chesta Ruttanapun, Wutthisak Prachamon, and Aree Wichainchai,

36th Congress on Science and Technology of Thailand, STT.36,

Bangkok International Trade & Exhibition Center (BITEC), Bangkok, Thailand,

26-28 October 2010.



การสังเคราะห์และสมบัติทางเทอร์โมอิเล็กทริก ทางไฟฟ้าและเชิงแสงของ CuAlO_2 เเดลฟอสไซต์ชนิด-p

Synthesis and thermoelectric, electrical and optical properties of p-type CuAlO_2 Delafossite

เชษฐารัตน์พนันธุ์^{1*}, วุฒิสักดิ์ ประชามณ², อารีย์ วิเชียรฉาย¹

Chesta Ruttanapun^{1*}, Wutthisak Prachamon², Aree Wichainchai¹

¹ Department of Applied Physics, Faculty of Science, King Mongkut's Institute of Technology Ladkrabang, Chalongkrung Road, Ladkrabang, Bangkok, 10520 Thailand

² Department of Physics, Faculty of Science, Ubonrajathanee University, Ubon Ratchathani, 34190 Thailand

*e-mail: chesta.ruttanapun@gmail.com

บทคัดย่อ: ได้เตรียมตัวอย่างของสารประกอบ CuAlO_2 ด้วยวิธี ปฏิกิริยาของแข็งเพื่อตรวจสอบสมบัติทางเทอร์โมอิเล็กทริก ทางไฟฟ้าและเชิงแสง โดยค่าสัมประสิทธิ์ซีเบค สภาพการนำไฟฟ้า และสภาพการนำความร้อน ได้ถูกวัดที่อุณหภูมิจาก 300 ถึง 960 K ส่วนสมบัติเชิงแสงวัดค่าที่อุณหภูมิห้อง ผลจากการวัดได้ค่าสัมประสิทธิ์ ซีเบคมีค่าเป็นบวกแสดงว่า CuAlO_2 เป็นสารกึ่งตัวนำชนิด P ค่าสัมประสิทธิ์ซีเบคและค่าสภาพนำไฟฟ้ามีค่าจาก 960 ถึง 300 $\mu\text{V/K}$ และ 0.01 ถึง 2 S/cm ตามการเพิ่มของอุณหภูมิ และมีค่าพลังงานกระตุ้นการตัวนำ, การสร้างประจุอิสระ และสภาพคล่องตัวมีค่า 0.203, 0.233 และ 0.03 eV ตามลำดับ ค่าสภาพนำความร้อนลดลงจาก 3.5 ถึง 1.5 W/mk ตามการเพิ่มขึ้นของอุณหภูมิ ส่วนค่า power factor และ ZT มีค่าจาก 0.02×10^{-4} ถึง 0.25×10^{-4} W/mk² และจาก 0.001 ถึง 0.017 ตามลำดับ มีค่าสูงสุดของ ZT คือ 0.017 ที่ 960 K สำหรับค่า absorbance มีค่ามากที่สุดในช่วงพลังงาน 3.5 ถึง 6 eV ซึ่งเป็นช่วงของแสง UV และมีค่าต่ำสุดในช่วงพลังงาน 1.5 ถึง 3.5 eV ซึ่งเป็นช่วงของแสง Near IR และ visible light มีค่าของช่องว่างพลังงานเชิงแสงแบบไม่ตรงและแบบตรง คือ 2.2 และ 3.2 eV ตามลำดับ ดังนั้นสารประกอบ CuAlO_2 delafossite จึงมีศักยภาพสำหรับวัสดุทางเทอร์โมอิเล็กทริกที่อุณหภูมิสูงใกล้ 1000 K และมีประสิทธิภาพสำหรับวัสดุนำไฟฟ้าชนิด p ที่แสงช่วงตามองเห็นผ่านได้ที่อุณหภูมิต่ำกว่า 500K

Abstract: The CuAlO_2 sample was prepared by a solid state reaction method for investigating thermoelectric, electrical and optical properties. The properties of the Seebeck coefficient, the electrical and thermal conductivity were measured in temperature ranging from 300 to 960 K, but the optical property was measured at room temperature. The study reveals that the Seebeck coefficients exhibited positive value which is p-type conductor. The Seebeck coefficient and electrical conductivity displayed in the ranging from 960 to 300 $\mu\text{V/K}$ and from 0.01 to 2 S/cm, respectively, with increasing temperature. The activation energy for conductor, production of free carriers and mobility were obtained 0.203, 0.233 and 0.03 eV, respectively. The thermal conductivity decreased from 3.5 to 1.5 W/mK with increasing temperature. The power factor and ZT were the ranging from 0.02×10^{-4} to 0.25×10^{-4} W/mk² and from 0.001 to 0.017, respectively. The highest value of ZT was 0.017 at 960 K. The absorbance for the heavy absorb was in the ranging from 3.5 to 6 eV (the UV light) and the week absorb was in the ranging spectrum from 1.5 to 3.5 eV (the Near IR and the visible light). The optical energy for indirect gap and direct gap were obtained 2.2 and 3.4 eV, respectively. Indeed, the experimental results imply that the CuAlO_2 is possible to get higher thermoelectric material with operating at high temperature closely to 1000 K and high performance for p-type and transparent visible light material with working under 500K.

Introduction: Thermoelectric effect refers to the phenomenon of the direct conversion of temperature gradients to electric voltage and vice versa. Thus, thermoelectric generators can be used to convert heat generated by various sources such as automotive exhaust, solar radiation and industrial processes to electricity. On the other hand, thermoelectric coolers can be used to make refrigerators and other cooling systems. Recently, there has been a growing interest in thermoelectric due to the energy crisis.

The transparent conductor for the region of visible light which is in the range of 380 nm (3.26eV) to 780 nm (1.53eV) is interesting for industry transparent electrodes. Its application consists of electrical contacts in solar cell, flat panel display optoelectronic, smart windows, liquid crystal displays. The transparent of visible light occurs by the difference between a full valence and empty conduction band larger than the energy of photon and no electron in valence state can absorb. Thus, the energy gap of material for transparent of visible light is much higher than the minimum edge of energy for visible light spectrum (~3.1 eV).

The performance of thermoelectric materials is characterized by the dimensionless Figure of Merit, $ZT = \alpha^2 \sigma T / \kappa$, where T is the absolute temperature, α is the Seebeck coefficient, σ and κ are the electrical and thermal conductivity, respectively[1,]. Thus, a good thermoelectric material should have basically three important properties: high electrical conductivity, high thermoelectric power and low thermal conductivity. Hence, the development of oxide materials with both high performance and environmental stability at high temperature is one of the most crucial issues for practical applications. Recently, thermoelectric properties of oxide materials have been reported to have conversion efficiency close to that of conventional metallic materials. Besides, the delafossite[2] structure has been reported to exhibit a high figure of merit[6] and a large power factor ($\sigma\alpha^2$)[2]. In addition, Kawazoe et al. [3] have reported that the delafossite compound exhibits transparent visible light with p-type conductivity (> 1 S/cm) and optical gap higher than 3.1 eV at room temperature.

Therefore, in this work, the CuAlO_2 which is a kind of delafossite compound was prepared to investigate the thermoelectric and electrical properties at high temperature and optical properties for transparent visible light material at room temperature.

The CuAlO_2 is a ternary oxide of delafossite type [2,3,4] whose chemical formula is $\text{Cu}^+ \text{Al}^{3+} \text{O}_2$. Its structure can be described by alternative stacking layers of O-Cu-O dumbbell and AlO_2 edge-shared octahedral layer perpendicular along the c-axis as shown in Figure 1(a). The Cu^+ cation is linearly connecting with O^{2-} anion in c-axis. The $[\text{AlO}_2]$ octahedral-shaped are formed by charting of edge AlO_2 . The trivalent Al^{3+} ions occupy in the middle of the octahedral block.

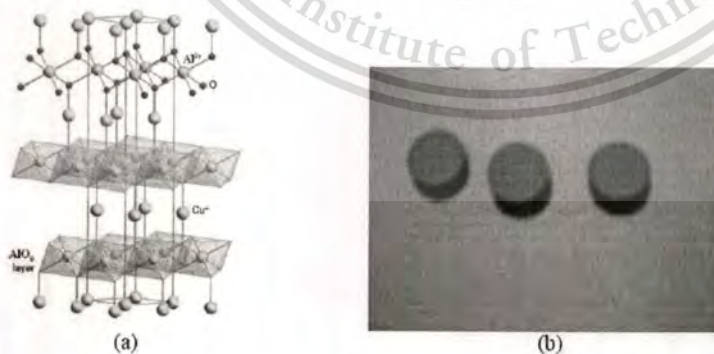
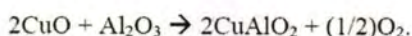


Figure 1. (a) The CuAlO_2 delafossite structure (b) The pellets of CuAlO_2 samples.

Methodology: The sample of CuAlO_2 was prepared by a conventional direct solid-state reaction according to the following equation [5]:



Stoichiometric amounts of high-purity powders CuO (Merk, 99.98%) and Al_2O_3 (Fluke; 99.99%) were sufficiently mixed and ground in an agate mortar to ensure homogeneity. Once a homogenous mixture was obtained and cool pressed into pellets of 12 mm diameter with 2-3 mm thickness. The resulting pellets were sintered by performed inside alumina boat in furnace at 1050 °C in air for 15 – 25 hours. After heat treatment the samples were rapidly quenched to room temperature. The heated pellets were repeated of grounding, pellet and firing procedures for several times until the pure phase of samples were obtained.

The sample (Fig. 1 (b)) was characterized by x-ray diffraction (XRD) using $\text{Cu K}\alpha$ radiation (PHILIPS model: X' Pert MPD) with scanning 2-Theta from 10° to 90°. Microstructure and morphology of the sample were analyzed by scanning electron microscope (SEM) model: JSM-5410 (JEOL). The Seebeck coefficient and the electrical conductivity were simultaneously measured using an ULVAC-RIKO ZEM-2. The thermal conductivity was determined from thermal diffusivity and specific heat measured using a ULVAC SINKU RIKO Inc. (Model: TC-7000H) laser-flash method. The absorbance was measured by a UV-VIS-NIR scanning spectrophotometer (Shimazu UV-3101PC) in the range of 200 to 2500nm.

Results, Discussion:

XRD-pattern: The XRD pattern of CuAlO_2 is shown in Figure 2. The pattern exhibited peaks of crystal phase of hexagonal CuAlO_2 delafossite structure (space group: $R\bar{3}m$ (166)) which is good agreement with the reference of JCPDS#35-1401[2,3,4]. The lattice parameter of CuAlO_2 was 2.852 Å and 16.954 Å for a-axis and c-axis length, respectively that they were corresponded with the reported of literature [4].

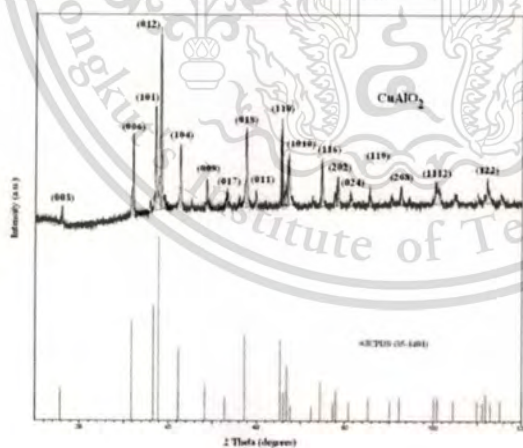


Figure 2. The XRD patterns of CuAlO_2 .

Figure 3 shows the SEM image of the CuAlO_2 sample. Most of the microstructure showed the crystal grain size in the range of 1 to 5 μm .

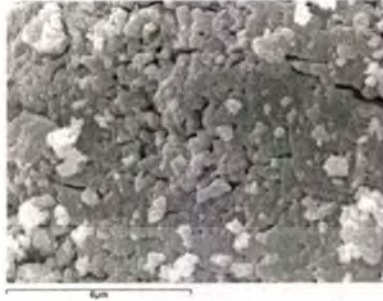


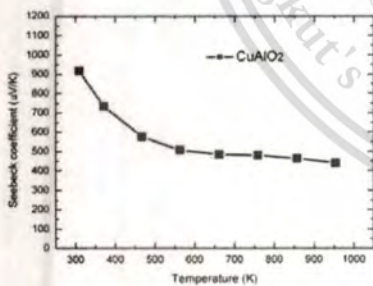
Figure 3. The microstructure and morphology of the CuAlO_2 sample.

Seebeck Coefficient: The temperature dependence of the Seebeck coefficient (α) is shown in Figure 4. The results showed that the Seebeck coefficient contained the value ranging from 300 to 900 $\mu\text{V/K}$ from temperature 960 to 300 K, respectively. The sign of the Seebeck displayed positive value which is p-type semiconductor. Considering the Seebeck coefficients of well known thermoelectric materials such as Bi_2Te_3 (218 $\mu\text{V/K}$)[2] and NaCo_2O_4 (100 $\mu\text{V/K}$)[2] at room temperature, CuAlO_2 has high potential in thermoelectric applications.

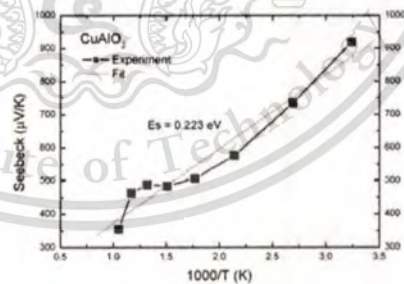
For the p-type semiconductor, the Seebeck coefficient (α) is given by the equation[6] of

$$\alpha = (k_B/e) [(E_v - E_F)/k_B T] = (k_B/e) \ln(N_v/N_D)$$

where k_B is the Boltzmann's constant, e is the electronic charge constant, E_v is the energy of the valance-band edge, E_F is the Fermi energy level, N_v is the effective density of state and N_D the doping density (or the hole carriers density). The results of the Seebeck in the Figure 4 (a) were decreased with increasing temperature as corresponding with the the Seebeck relation. The activation energy for the production of free carriers $E_s = (E_v - E_F)$ was obtained by plotted α vs $1000/T$ as shown in the Figure 4 (b). An average of the E_s value for the CuAlO_2 sample was 0.223 eV. The E_s value linear increasing with T implies that the doping density (N_D) is activated by thermal energy.



(a)



(b)

Figure 4. (a) The Seebeck coefficient of the CuAlO_2 sample vs. the temperature. (b) The curve of the Seebeck coefficient vs. $1000/T$ for the CuAlO_2 sample.

Electrical Conductivity: The temperature dependence of the electrical conductivity (σ) of the CuAlO_2 sample is shown in Figure 5 (a). The results displayed that the electrical conductivity displayed value increasing from 0.01 to 2 S/cm with increasing the temperature from 300 to 960 K. The results exhibited that the electrical conductivity increased with the temperature increased. Note that the maximum of the electrical conductivity was 13 S/cm at temperature 960 K.

Figure 5 (b) shows an Arrhenius plot for the CuAlO_2 sample with corresponding of fitting temperature dependent of equation[6]: $\sigma = \exp(-E_A/k_B T)$ where k_B is the Boltzmann's constant and E_A is the activation energy of conduction. The activation energy (E_A) in the Arrhenius plot, $\log \sigma$ vs. $1000/T$ was 0.203 eV.

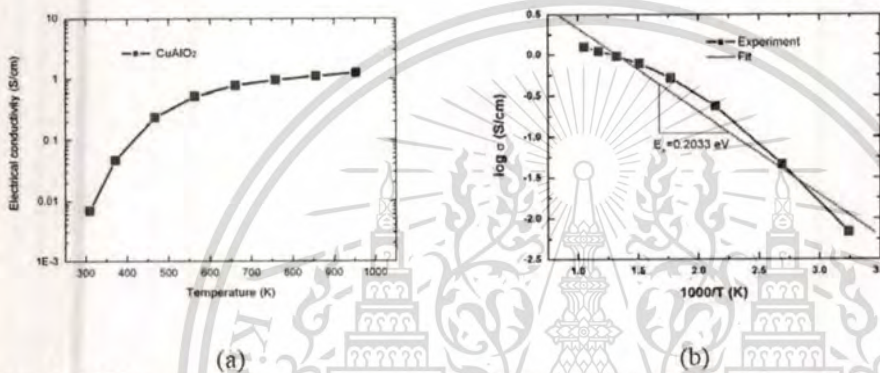


Figure 5. (a) The temperature dependence of the electrical conductivity of the CuAlO_2 sample. (b) The curve of the electrical conductivity vs. $1000/T$ for the CuAlO_2 sample.

The overall the activation energy for conductor (E_A) is a combination of two parts: $E_A = E_u - E_s$, where E_u is the activation energy for carrier hopping from site to site or the activation energy of mobility. The E_u is obtained from by the small polaron mechanism of carriers as following equation[6] of $\mu_h = \exp(-E_u/k_B T)$, where μ_h is the mobility of hole carrier. For the E_A (0.203eV) of the electrical conductivity and the E_s (0.233eV) of the Seebeck coefficient, the value of E_u was gained 0.03 eV which is greater than the thermal energy ($k_B T \sim 0.025$ eV) at room temperature. The difference in the activation energies of E_A and E_s implied that the CuAlO_2 was dominated by the small polaron hopping from site to site from thermal energy. Thus, this results can conclude that the p-type behavior of CuAlO_2 delafossite for hole mobility (μ_h) and the conduction of carriers are activated by thermal energy. Dordo et. al.[5] reported that the polaron conduction of the p-type delafossite compound are localized on the Cu sites for forming Cu^{2+} ions. From the Seebeck relation, the hole carriers density (N_D) was obtained $7.27 \times 10^{17} \text{ cm}^{-3}$ by the $\alpha = 900 \mu\text{V/K}$ at room temperature and magnitude of the density of the Cu atoms (N_v) = $2.5 \times 10^{22} \text{ cm}^{-3}$. The Hall mobility (μ_h) at room temperature, which estimated from the relation[6] $\mu_h = \sigma / e N_D$, was $8.58 \times 10^{-2} \text{ cm}^2/\text{V}\cdot\text{s}$. This result indicated that the conduction of the CuAlO_2 delafossite is the polaron mechanism ($< 1 \text{ cm}^2/\text{V}\cdot\text{s}$).

Thermal Conductivity: The temperature dependence of the thermal conductivity (κ) is shown in Figure 6. The results displayed that the values of the thermal conductivity were decreased in the range from 3.5 to 1.5 W/mK with measuring temperature from 300 to 960 K.

respectively. The maximum value of the κ value was 3.5 W/mK at room temperature and minimum value was 1.5 W/mK in the range of temperature from 700 to 960 K. These results exhibited that the thermal conductivity of the CuAlO_2 sample was decreased depending on increasing temperature.

The thermal conductivity (κ) consists of the two values of the phonon effect and electronic effect as in following reaction[2] $\kappa = \kappa_{ph} + \kappa_e$, where the κ_{ph} and κ_e is the thermal conductivity of phonon and electronic contribution, respectively. From the Wiedmann-Franz law[2], the electronic part is related by $\kappa_e = L_o T \sigma$ where L_o is the Lorenz number ($2.45 \times 10^{-8} \text{ W}\Omega/\text{K}^2$), T is absolute temperature, σ is electrical conductivity. The calculation of κ_e for CuAlO_2 sample at room temperature ($\sigma = 2.5 \times 10^{-4} \text{ S/cm}$) was obtained $1.8375 \times 10^{-7} \text{ W/mK}$ which was $5.25 \times 10^{-6}\%$ of the thermal conductivity (κ). This result indicated that the major effect of thermal conductivity for CuAlO_2 sample at room temperature is due to the phonon mechanism part.

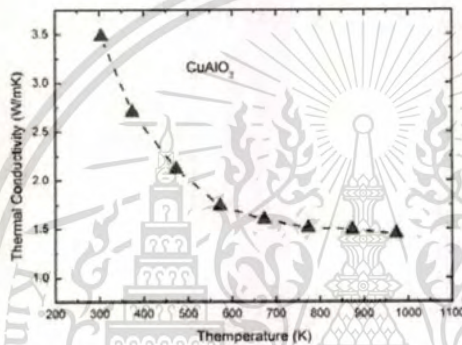


Figure 6. The temperature dependence of thermal conductivity of the CuAlO_2 sample.

Power factor and Dimensionless Figure of Merit: Figure 7 and 8 show the temperature dependence of Power factor ($PF = \alpha^2 \sigma$) and dimensionless Figure of Merit ($ZT = T \alpha^2 \sigma / \kappa$) of the CuAlO_2 sample. The power factor was calculated from the measurement Seebeck coefficient and the electrical conductivity, and the ZT was computed from the Figure of Merit ($Z = \alpha^2 \sigma / \kappa$) and the temperature. The power factor value was in the range of 0.02×10^{-4} to $0.25 \times 10^{-4} \text{ W/mk}^2$ (Figure 7) and the ZT value was in the range from 0.001 to 0.017 (Figure 8) with the temperature 300 to 960 K, respectively. Both, the power factor and the ZT increased with increasing temperature. The maximum value of the power factor and the ZT were $0.2 \times 10^{-4} \text{ W/mk}^2$ and 0.017, at temperature 960 K. This value exhibited that it was nearly the value of conventional NaCo_2O_4 compound ($ZT=0.07$ at 580 K)[2].

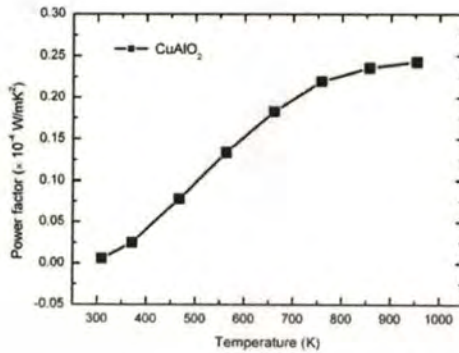


Figure 7. The temperature dependence of power factor of the CuAlO_2 sample.

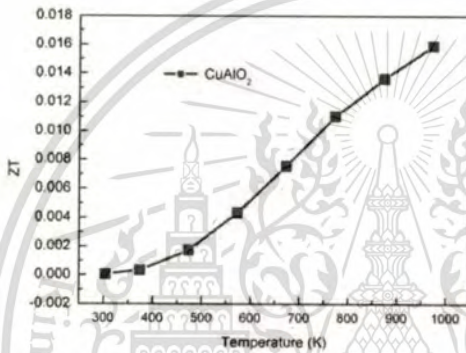


Figure 8. The temperature dependence of dimensionless ZT of the CuAlO_2 sample.

Optical Properties: Figure 9 and 10 show the experimental results of the optical property for UV-VIS-NIR spectrum of CuAlO_2 sample at room temperature. The optical absorption occurs by transition of electrons and holes between electronics states (bands, tail states, gap states). The absorbance (α) of the samples for ranging 1.5 to 5.0 eV is shown in Figure 10. The results exhibited that the heavy absorb band was in the ranging spectrum 3.5 to 6 eV which is the UV light and the weak absorb was in the ranging spectrum 1.5 to 3.5 eV which is the Near IR and the visible light. The highest absorbance value was 4.5eV. The results of absorbance were used to calculate the band energy gap according to the equation $(\alpha h\nu)^m = A(h\nu - E_g)$, where α is the absorption coefficient, $h\nu$ is photon energy, E_g is optical band gap, A is constant which does not depend on $h\nu$. The value of $m=1/2$ is a characteristic of the indirect allowed transition which dominates over the optical absorption and $m=2$ is a characteristic of the direct allowed transition. For photon energies $h\nu > E_g$, the material can absorb these photons. For $h\nu < E_g$ the photons cannot be absorbed anymore. The optical energy gap was obtained from a plot of $(\alpha h\nu)^m$ vs $h\nu$ and taking the intercept on the energy axis. The optical band gap for $m=1/2$ which is the indirect transition gap was plotted coefficient between $(\alpha h\nu)^{1/2}$ and photon energy ($h\nu$) of the sample and the optical energy gap for $m=2$ was plotted $(\alpha h\nu)^2$ vs $h\nu$ for taking the intercept on the energy axis. The results displayed that the indirect transition optical gap and the direct transition optical gap of CuAlO_2 sample exhibited 2.2 eV and 3.2 eV as shown in Figure 10. The results implied that this material can transmit visible light because of the direct E_g higher than 3.1 eV. Indeed, the CuAlO_2 delafossite is p-type conductor and transparent visible light material.

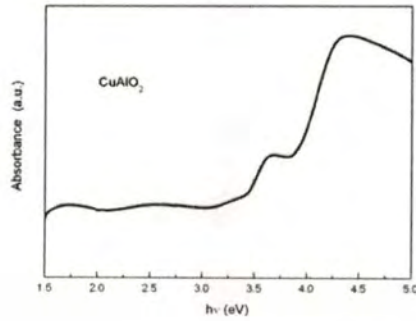


Figure 9. Absorbance spectra of CuAlO_2 .

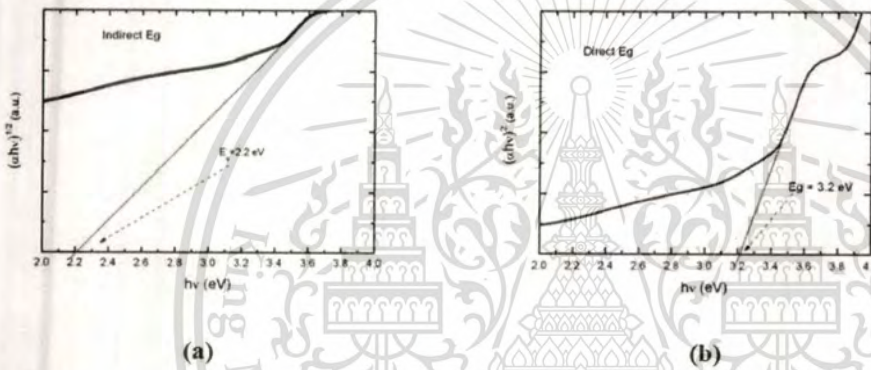


Figure 10. (a) Indirect optical band gap of CuAlO_2 . (b) Direct optical gap of CuAlO_2 .

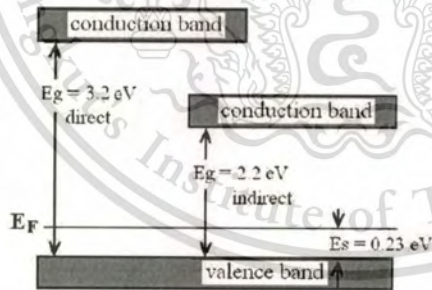


Figure 11. Energy band diagram of the CuAlO_2 delafossite.

The measured results of thermoelectric, electrical and optical properties of sample can predict the energy band diagram of the CuAlO_2 delafossite at room temperature as shown in Figure 11. The prediction of band diagram displayed that the direct and the indirect band gap (E_g) were 3.2 and 2.2 eV, respectively. The Fermi's energy (E_F) level was above the valence band edge 0.23 eV which is the activation energy for the production of free carriers $E_s = (E_v - E_F)$.

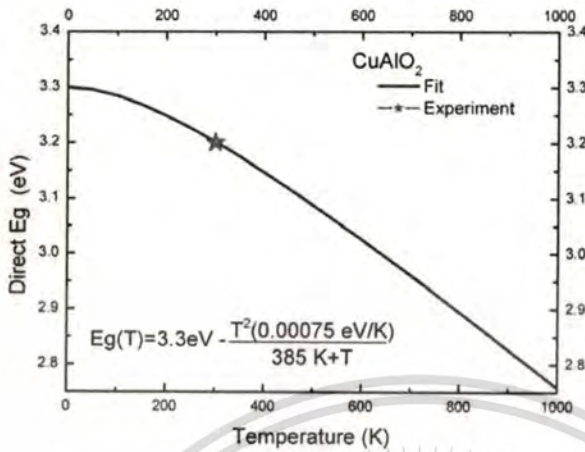


Figure 12. Temperature dependence of the direct band gap (E_g) of CuAlO_2 delafossite.

Figure 12 shows the approximated and experimental of the direct band gap (E_g) of CuAlO_2 as a function of temperature. The temperature dependence of E_g was calculated by an empirical formula: [7] $E_g(T) = E_g(0) - [aT^2/(b+T)]$, where $E_g(0)$ is the band gap approximated at 0 K, a and b are parameters. Dittrich et. al. [7] reported that the values of a and b parameters for delafossite were 0.00075 eV/K and 385 K, respectively. The value of $E_g(0)$ which used 3.3 eV was obtained by fitting with experimental E_g at room temperature. The results exhibited that the direct E_g decreased with increasing temperature. The calculated E_g obtained the value under 3.1 eV with the temperature above 500 K. This result implied that the CuAlO_2 delafossite can not transmit the visible light spectrum in temperature above 500 K. In conclusion, the CuAlO_2 delafossite can use for p-type conductor and transparent visible light material in the range of temperature under 500K.

Conclusion: The CuAlO_2 delafossite was synthesized by a solid state reaction method for investigation thermoelectric, electrical and optical properties. Our study revealed that the Seebeck coefficients of CuAlO_2 exhibited p-type semiconductor. The Seebeck coefficient and thermal conductivity were decreased, but electrical conductivity was increased dependent with increasing temperature ranging from 300 to 960 K. The results of Seebeck were ranging from 300 to 900 $\mu\text{V/K}$. The electrical conductivity displayed value in the ranging 0.01 to 2 S/cm. The activation energy for conductor, production of free carriers and mobility were obtained 0.203, 0.233 and 0.03 eV, respectively. The thermal conductivity was decreased from 3.5 to 1.5 W/mK with increasing temperature. Moreover, the highest value of the power factor and the ZT were $0.2 \times 10^{-4} \text{ W/mK}^2$ and 0.017, respectively at temperature 960 K. The absorbance exhibited values of the heavy absorbed band in the spectrum range of 3.5 to 6 eV (the UV light) and the weak absorbed was in the spectrum range of 1.5 to 3.5 eV (the Near IR and the visible light). The optical transition energy for indirect gap and direct gap were 2.2 and 3.2 eV, respectively. The value of direct energy gap ($E_g = 3.2 \text{ eV}$) indicated that the CuAlO_2 delafossite is transparent in visible light spectrum ($E_g > 3.1 \text{ eV}$). Indeed, the CuAlO_2 delafossite exhibits high performance for thermoelectric material at high temperature closely to 1000 K and high performance for p-type conducting and transparent visible light material for optical device with working under temperature under 500 K.

References:

1. A. F. Ioffe, *Infosearch limited, London, 1957.*
2. D.M. Rowe (ed), *CRC Handbook of Thermoelectrics:Macro to Nano*, CRC, Boca Raton, **2005.**
3. H. Kawazoe, M. Yasukawa, H. Hyodo, M. Kurita, H. Yanagi, H. Hosono, "*P-type electrical conduction in transparent thin films of CuAlO₂*", *J. Nature*, 389, **1997**, 939-942.
4. K. Park, et al., "*Improvement in thermoelectric properties of CuAlO₂ by adding Fe₂O₃*", *J. Alloy. Comp.*, 437, **2007**, 1-6.
5. P. Dordor, J. P. Chaminade, A. Wichainchai, E. Marquestaut, J. P. Doumerc, M. Pouchard, P. Hagenmuller, A. Ammar, "*Crystal growth and electrical properties of CuFeO₂ single crystals*", *J. Solid State Chem.*, 75 , **1988**, 105-112.
6. P.A. Cox, *Transition metal oxides "an introduction to their electrical structure and properties"*, Clarendon press, oxford, **1995.**
7. T. Dittrich, et al., "*Photovoltage characterization of CuAlO₂ crystallites*", *Appl. Phys. Lett.*, 85, **2004**, 742-744.

Keywords: CuAlO₂ delafossite, thermoelectric, Seebeck coefficient, dimensionless Figure of Merit (ZT), optical band gap, visible light transparent



B.3

Synthesis, Thermoelectric Properties of $\text{CuFe}_{0.5}\text{Al}_{0.5}\text{O}_2$ Delafossite and Finite Element Computing for Power Generator on Its Module,

Chesta Ruttanapun, Wutthisak Prachamon, and Aree Wichainchai,

SPC2011: Siam Physics Congress, The 6th Annual Conference of the Thai Physics Society,

Pattaya, Chonburi, Thailand,

23-26 March, 2011, pp. 196- 199.





Synthesis, Thermoelectric Properties of $\text{CuFe}_{0.5}\text{Al}_{0.5}\text{O}_2$ Delafossite and Finite Element Computing for Power Generator on Its Module

C. Ruttanapun^{1*}, W. Prachamon² and A. Wichainchai¹

¹Department of Applied Physics, Faculty of Science, King Mongkut's Institute of Technology Ladkrabang, Chalangkruing Road, Ladkrabang, Bangkok, 10520, Thailand

²Department of Physics, Faculty of Science, Ubonrajathane University, Ubon Ratchathani, 34190, Thailand

*Corresponding author. E-mail: chesta.ruttanapun@gmail.com

Abstract

The $\text{CuFe}_{0.5}\text{Al}_{0.5}\text{O}_2$ delafossite oxide has been synthesized by solid state reaction method for studying thermoelectric properties. The Finite Element analysis was used to compute the output voltage for thermoelectric generator in applying temperature difference on a bar model of $\text{CuFe}_{0.5}\text{Al}_{0.5}\text{O}_2$ and the calculated values were compared to the measurement results. The properties of Seebeck coefficient and electrical conductivity are range of 260 to 310 $\mu\text{V/K}$ and 7 to 16 S/cm in the temperature range of 300 to 960 K. The value of thermal conductivity, power factors and ZT are in the range of 3.2 to 4.2 W/cm-K , 0.4×10^{-4} to 1.5×10^{-4} W/m-K^2 and 0.004 to 0.04, respectively. The output voltage of the $\text{CuFe}_{0.5}\text{Al}_{0.5}\text{O}_2$ bar with dimension $4.2 \times 2.5 \times 20$ mm^3 obtained 0.5 to 3 mV on applying temperature difference from 1 to 10K. The Finite Element computing shows output voltage of a bar thermoelectric generator model closely to measurement results of the $\text{CuFe}_{0.5}\text{Al}_{0.5}\text{O}_2$ bar.

Keywords: $\text{CuFe}_{0.5}\text{Al}_{0.5}\text{O}_2$, Delafossite oxide, Dimensionless Figure of Merit (ZT), Finite element analysis, Seebeck coefficient, Thermoelectric

Introduction

Recently, there has been a growing interest in materials for thermoelectric. The thermoelectric[1] effect refers to phenomenon of the direct conversion of temperature gradients to electric voltage and vice versa. The power generation of thermoelectric can directly convert heat to electric voltage. The performance of thermoelectric materials is characterized by the values of Power Factor, $(S^2\sigma)$, and dimension less Figure of Merit, $ZT=TS^2\sigma/\kappa$ where S is the Seebeck coefficient, σ and κ are the electrical and thermal conductivity and T is temperature, respectively.

Delafossite compound of the ternary oxide in chemical formula $\text{A}^+\text{B}^{3+}\text{O}_2$ has been described to be an interesting thermoelectric material. The CuFeO_2 [2] and CuAlO_2 [3] delafossite-type have been reported that they have high performance of thermoelectric properties.

In addition, Ebling et al. [4] have used Finite Element technique to compute power generator on thermoelectric module. To the best of our knowledge; however, there has been no report concerning the preparation of $\text{CuFe}_{0.5}\text{Al}_{0.5}\text{O}_2$ delafossite, and analyzing by the Finite Element technique for computing power on it.

On this work aims to prepare $\text{CuFe}_{0.5}\text{Al}_{0.5}\text{O}_2$ a half mixed trivalent compound using the solid state reaction method. Its physical properties are

characterized in the x-ray diffraction (XRD), electrical resistivity, Seebeck coefficient, and thermal conductivity. The thermoelectric measurement is performed on a bar sample. The obtained thermoelectric properties of the sample are then used to evaluate the power of a thermoelectric module made from the bar by using Finite element method.

Materials and Methods

Non-stoichiometric $\text{CuFe}_{0.5}\text{Al}_{0.5}\text{O}_2$ was prepared by a conventional direct solid-state reaction as in the following equation:



Stoichiometric amounts of high-purity powders CuO (Merk, 99.98%), Fe_2O_3 (Sigma-Aldrich, Inc., 99%) and Al_2O_3 (Fluke; 99.99%) were sufficiently mixed and ground in an agate mortar to ensure homogeneity. Once a homogenous mixture was obtained, then, it was cold pressed into pellets. The resulting pellets were sintered by executing inside alumina boat in furnace at 1050 °C in air for 15 – 25 hours. After heat treatment the samples were rapidly quenched to room temperature. The heated pellets were subjected to grinding, pellet and firing procedures for several times until the pure of samples were obtained.

The single phase of $\text{CuFe}_{0.5}\text{Al}_{0.5}\text{O}_2$ samples was characterized by a powder x-ray diffraction (XRD) of



PHILIPS model: X¹ Pert MPD analysis using Cu K α radiation with $2\theta = 10^\circ$ to 80° . Microstructures of the samples were observed by scanning electron microscope (SEM) with a JEOL model: JSM-5410. The electrical conductivity and Seebeck coefficient were simultaneously measured by using an ULVAC-RIKO ZEM-2 measurement system under a low-pressure Ar atmosphere. The thermal conductivity was determined from thermal diffusivity and specific heat was measured by using a ULVAC SINKU RIKO Inc. (Model: TC-7000H) laser-flash method.

A bar of $\text{CuFe}_{0.5}\text{Al}_{0.5}\text{O}_2$ sample (Figure 1) in dimension $4.2 \times 2.5 \times 20 \text{ mm}^3$ was used to measure thermoelectric power by applied temperature difference (ΔT) from 1 to 10 K. In measurement process, the top side of this bar was attached to hot temperature (T_h) with varying temperature from 301 to 310 K, and the bottom side of bar was fixed at 300K (T_c). The main performance indicator which is the output voltage in a bar was measured by voltmeter.

Furthermore, the Finite element technique was used to compute power on model of a thermoelectric bar and a thermoelectric module with the consol commercial software. The bar model is represented a bar of $\text{CuFe}_{0.5}\text{Al}_{0.5}\text{O}_2$ sample. The thermoelectric module is represented in a device model which is connection of a single n-type $\text{CuFe}_{0.5}\text{Al}_{0.5}\text{O}_2$ bar and a single p-type $\text{CuFe}_{0.5}\text{Al}_{0.5}\text{O}_2$ bar by cooper plate, and stacking an alumina plate on top and bottom of the n-type and p-type bars. The Finite Element analysis was used to solve of two couple equations of the thermoelectric effect as following[4]:

$$\nabla(\alpha \sigma^2 T + \kappa \nabla T) + \nabla(\alpha \sigma T \nabla V) = -\sigma \nabla V^2 - \alpha \sigma \nabla V T \quad (2)$$

$$\nabla(\alpha \sigma \nabla T) + \nabla(\sigma T) = 0 \quad (3)$$

where T is temperature and V is voltage. The domain of the bar and the module were divided in Finite Element mesh. The computed results of thermoelectric properties on the bar of $\text{CuFe}_{0.5}\text{Al}_{0.5}\text{O}_2$ sample were evaluated. The boundary conditions on the bar and the module were specified by setting cold temperature with (T_c) 300 K on bottom of model. The hot temperature (T_h) on the top side of the model was applied by varying temperature from 301 to 400 K. The voltage on bottom side of the modules was fixed to a zero reference level.

Results and Discussion

The XRD pattern of the $\text{CuFe}_{0.5}\text{Al}_{0.5}\text{O}_2$ samples is exhibited in Figure 2. The ICSD:01-075-2146 of CuFeO_2 and JCPDS:35-140 of CuAlO_2 are added for the comparison. It is found that the $\text{CuFe}_{0.5}\text{Al}_{0.5}\text{O}_2$ sample is displayed a single phase with a hexagonal delafossite structure (space group: $R\bar{3}m$) with corresponding to the standard file of the ICSD#01-075-2146 and JCPDS#35-140. Furthermore, this result is clearly confirmed that the

$\text{CuFe}_{0.5}\text{Al}_{0.5}\text{O}_2$ sample forms single phase of the delafossite structure.



Figure 1 The single bar of $\text{CuFe}_{0.5}\text{Al}_{0.5}\text{O}_2$ sample

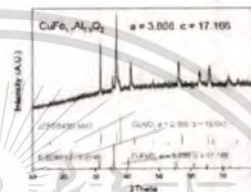


Figure 2 The XRD patterns of the $\text{CuFe}_{0.5}\text{Al}_{0.5}\text{O}_2$ sample.

Figure 3 shows the morphology of the $\text{CuFe}_{0.5}\text{Al}_{0.5}\text{O}_2$ sample by the SEM image. The majority of the primitive microstructure is shown the crystal grain size in the range of 1 to 10 μm



Figure 3 The microstructure and morphology of $\text{CuFe}_{0.5}\text{Al}_{0.5}\text{O}_2$ sample.

Figure 4 exhibits the Seebeck coefficient of the $\text{CuFe}_{0.5}\text{Al}_{0.5}\text{O}_2$ sample as a function of temperature in the range of 300 to 960 K. The result shows that the Seebeck coefficients are positive sign over the temperature range indicating p-type semiconductor. Moreover, the value of Seebeck is slightly increasing with increasing temperature. The value exhibits ranging from 260 to 310 $\mu\text{V/K}$ with temperature range 300 to 960 K.

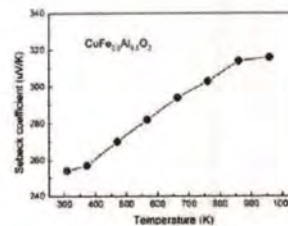


Figure 4 The temperature dependent of Seebeck coefficient of the $\text{CuFe}_{0.5}\text{Al}_{0.5}\text{O}_2$ sample.



Figure 5 presents the electrical conductivity of the $\text{CuFe}_{0.5}\text{Al}_{0.5}\text{O}_2$ sample as a function of temperature in the range of 300 to 960 K. The result is also shown the electrical conductivity exhibiting the value ranging from 7 to 16 S/cm with the same temperature range. Besides, the value rapidly increases in the temperature range 300 to 700 K, and reaches a plateau in the temperature range 700 to 960 K.

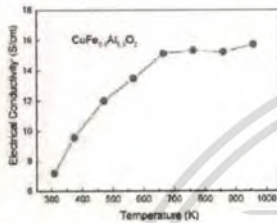


Figure 5 The temperature dependent of electrical conductivity of the $\text{CuFe}_{0.5}\text{Al}_{0.5}\text{O}_2$ sample.

Figure 6 shows the power factor ($PF = \sigma S^2$) of the $\text{CuFe}_{0.5}\text{Al}_{0.5}\text{O}_2$ sample calculated from the measured the electrical conductivity and the Seebeck coefficient as a function of the temperature in the range of 300 to 960 K. Subsequently, the power factor is rapidly increased with increasing the temperature. The power factors ranges between 0.4×10^{-4} to $1.5 \times 10^{-4} \text{ W/m}\cdot\text{K}^2$.

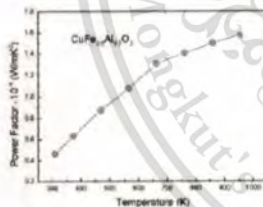


Figure 6 The temperature dependent of power factor of the $\text{CuFe}_{0.5}\text{Al}_{0.5}\text{O}_2$ sample.

The temperature dependence of the thermal conductivity on the $\text{CuFe}_{0.5}\text{Al}_{0.5}\text{O}_2$ sample as a function of in the temperature ranging from 300 to 960 K is shown in Figure 7. The thermal conductivity is in the range from 3.2 to 4.2 $\text{W/cm}\cdot\text{K}$ with a region of temperature 300 to 960 K. The thermal conductivity is slightly constant in 300 to 500 K, rapidly increase in 500 to 900 K and steeply decrease in temperature 900 to 960K.

The temperature dependence of the ZT of the $\text{CuFe}_{0.5}\text{Al}_{0.5}\text{O}_2$ sample in the temperature range from 300 to 960 K is exhibited in Figure 8. The ZT value is also calculated from the power factor, thermal conductivity and the temperature. The ZT is determined ranging from 0.004 to 0.04 with the temperature ranging from 300 to 960K. The results

show that the ZT steadily increase with increasing the temperature.

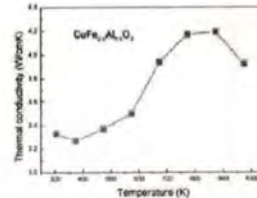


Figure 7 The thermal conductivity of the $\text{CuFe}_{0.5}\text{Al}_{0.5}\text{O}_2$ sample.

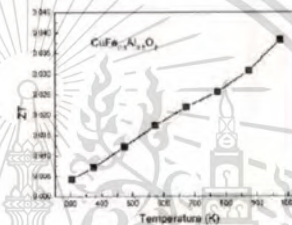


Figure 8 The ZT of the $\text{CuFe}_{0.5}\text{Al}_{0.5}\text{O}_2$ sample.

The results of electrical voltage for thermoelectric generator of the bar in Figure 1 under the applied temperature difference from 2 to 10 K are shown in Figure 9. The output voltages of 0.6 to 3 mV were obtained.

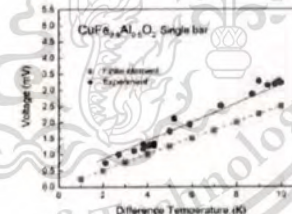


Figure 9 The output voltage of the bar on measurement and Finite Element computing.

However, the Finite Element model for thermoelectric generator of the single $\text{CuFe}_{0.5}\text{Al}_{0.5}\text{O}_2$ bar is shown in Figure 10(a). Then, the output of voltage is calculated on applying difference temperature ($\Delta T = T_h - T_c$) ranging from 1 to 10K. The computing used the properties of Seebeck, electrical and thermal conductivity from measurement results of $\text{CuFe}_{0.5}\text{Al}_{0.5}\text{O}_2$ sample as in Figure 3, 4 and 6, respectively. The Finite Element results of voltage and temperature distribution on applying difference temperature 10 K is shown in Figure 10(b) and (c), respectively. The computing results of output voltage as a function of ΔT between 1 to 10 K are displayed in Figure 9. The results show that the Finite Element



result is in close agreement with the experimental results.

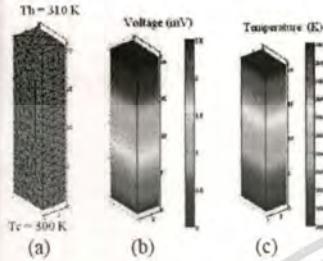


Figure 10 (a) The finite element model (b) voltage and (c) temperature distribution.

The finite element model for the module thermoelectric of $\text{CuFe}_{0.5}\text{Al}_{0.5}\text{O}_2$ materials is presented in Figure 11(a). The model consists of an n-type bar and a p-type bar shape connected with copper plate and has alumina covering like a sandwich. The output voltage is calculated by applying ΔT ($T_h - T_c$) ranging from 1 to 100 K. The simulation uses the measured thermoelectric data of the p-type sample for the p-type bar in the module. For the n-type bar, its Seebeck voltage was assumed to be the negative values of the Seebeck emf of the p-type specimen. The Seebeck coefficient, electrical and thermal conductivity for the copper plate used in the calculation are $6.5 \mu\text{V/K}$, $5.9 \times 10^6 \text{ S/cm}$, and 3.5 W/cm-K , respectively and the values of electrical and thermal conductivity for alumina are 10^{-16} S/cm and 0.4 W/cm-K , respectively. The Finite Element results of the voltage and temperature distribution on applying ΔT of 100 K is shown in Figure 11(b) and (c), respectively. The computing results of output voltage for module on ΔT in the range of 1 to 100 K are shown in Figure 12. The results remarkably show that the output voltage of the thermoelectric module is two times as high as that of the single thermoelectric bar.

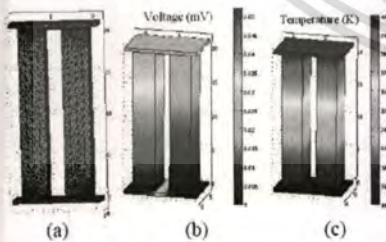


Figure 11 (a) The finite element model of module (b) voltage and (c) temperature distribution.

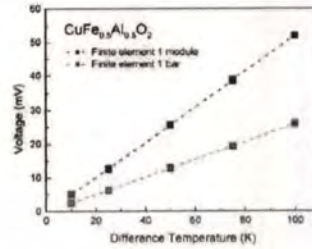


Figure 12 The output voltage of single bar and modules thermoelectric.

Conclusions

The delafossite $\text{CuFe}_{0.5}\text{Al}_{0.5}\text{O}_2$ thermoelectric material has been prepared by a solid state reaction method. Our study shows that the Seebeck coefficient exhibits positive values (p-type semiconductor) from 260 to 310 $\mu\text{V/K}$. The electrical and the thermal conductivity display value between from 7 to 16 S/cm and from 3.2 to 4.2 W/cm-K . The power factors and ZT are in the range from 0.4×10^{-4} to $1.5 \times 10^{-4} \text{ W/m-K}^2$ and 0.004 to 0.04, respectively. The output voltage for thermoelectric generator of the bar is given ranging 0.5 to 3 mV on applying difference temperature from 1 to 10K. The Finite Element computing of the $\text{CuFe}_{0.5}\text{Al}_{0.5}\text{O}_2$ bar shows output voltage which is in good agreement with the experimental results. In addition, it was found from the finite element simulation that the thermoelectric module gives the output voltage which is twice as high as the output voltage of the single bar. The further study is going to use multi-junction for forming an applicable thermoelectric device.

Acknowledgments

The authors would like to thank Thermoelectrics Research Center and Program of Physics, Faculty of Science and Technology, Sakon Nakhon Rajabhat University for measurement output voltage on a cell bar $\text{CuFe}_{0.5}\text{Al}_{0.5}\text{O}_2$ thermoelectric.

References

1. A. F. Ioffe, Infosearch limited, London, (1957).
2. C. Ruttanapun, A. Wichainchai, W. Prachanon, A. Yangrhaisong, A. Charoenphakdee, T. Seetawan, "Thermoelectric properties of $\text{Cu}_{1-x}\text{Pt}_x\text{FeO}_2$ ($0.0 \leq x \leq 0.05$) delafossite-type transition oxide", *J. Alloy. Comp.*, **509** (2011) 4588.
3. K. Park, K. Y. Ko, H.-C. Kwon, S. Nahm, "Improvement in thermoelectric properties of CuAlO_2 by adding Fe_2O_3 ", *J. Alloy. Comp.*, **437** (2007) 1.
4. D. Ebling, M. Jaegle, M. Bartel, A. Jacquot, H. Bottner, "Multiphysics simulation of thermoelectric systems for comparison with experimental device performance", *J. electronic materials*, **38** (2009) 1456.

B.4

Preparation and Comparison of Thermoelectric Properties of CuFeO_2 , CuAlO_2 and $\text{CuFe}_{0.5}\text{Al}_{0.5}\text{O}_2$ Delafossite Structure,

Chesta Ruttanapun and Aree Wichainchai,

The 1st Southeast Asia Conference on Thermoelectrics,

Krunsri River Hotel, Ayutthaya, Thailand,

20-21 July 2011, pp. 34.



Preparation and Comparison of Thermoelectric Properties of CuFeO₂, CuAlO₂ and CuFe_{0.5}Al_{0.5}O₂ Delafossite Structure

Chesta Ruttanapun* and Aree Wichainchai

Department of Physics, Faculty of Science, King Mongkut's Institute of Technology Ladkrabang, Chalalongkrong Road,
Ladkrabang, Bangkok, 10520, Thailand

E-Mail Address : chesta.ruttanapun@gmail.com

Abstract

Thermoelectric materials can convert thermal energy to electric energy or vice versa. The performance of TE materials is presented by the dimensionless figure of merit, $ZT = \sigma S^2 T / \kappa$, where T is the absolute temperature, S is the Seebeck coefficient, σ and κ are the electrical and thermal conductivity, respectively. This work aims to preparation CuFeO₂, CuAlO₂ and CuFe_{0.5}Al_{0.5}O₂ samples, which are a kind of delafossite-oxide structure compounds, by a solid state reaction. The crystallography of samples is determined by the powder x-ray diffraction and thermoelectric properties of all samples are investigated. The properties of Seebeck coefficients, the electrical and thermal conductivity are characterized in high temperature. The results of XRD patterns of sintered-samples CuFe_{0.5}Al_{0.5}O₂, CuFeO₂, and CuAlO₂ correspond to reference of ICSD:01-075-2146 for CuFeO₂ and JCPDS:35-140 for CuAlO₂ as shown in Fig.1. The comparison of thermoelectric properties of CuFeO₂, CuAlO₂ and CuFe_{0.5}Al_{0.5}O₂ samples will be reported.

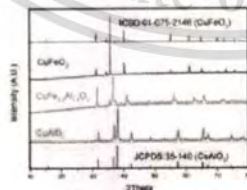


Fig. 1. The XRD patterns of the CuFeO₂, CuFe_{0.5}Al_{0.5}O₂, and CuAlO₂ samples.

Keywords: Thermoelectric; Seebeck Coefficient; Dimension lest ZT; Delafossite Compound

C: INVITATING EMAIL FROM THE INTERNATIONAL CENTRE OF DIFFRACTION

The letter of Request for Powder Diffraction Data on the new $\text{Cu}_{1-x}\text{Pt}_x\text{FeO}_2$ materials.



chesta.ruttanapun <chesta.ruttanapun@gmail.com>

Request for Powder Diffraction Data from your recently published paper.

3 messages

Editorial Editors <editor@icdd.com>
To: chesta.ruttanapun@gmail.com

Wed, May 18, 2011 at 1:36 AM

May 17, 2011

Chesta Ruttanapun

chesta.ruttanapun@gmail.com

Dear Dr. Ruttanapun:

The International Centre for Diffraction Data (ICDD) is a nonprofit scientific organization, founded by, and dedicated to scientists working in the field of X-ray analysis.

You recently published a paper: "Thermoelectric Properties Of $\text{Cu}_{1-x}\text{Pt}_x\text{FeO}_2(0.0 < x < 0.05)$ Delafossite-Type Transition Oxide", *J. Solid State Chem.*, 609, 4585 (2011), in which reference was made to X-ray diffraction data. However, the data were not published in the article.

These data would constitute a useful addition to the Powder Diffraction File and the ICDD would greatly appreciate your contribution for inclusion in the next edition.

The data needed are: the name and chemical formula of the material, accurate listing of the position of the interplanar spacings (2 θ , d , $\sin^2 \theta$, Q , etc.), the intensities of the interplanar spacings and radiation used. Also of interest would be the Miller indices, cell parameters, type of X-ray recording, method of measuring the intensities, preparation of material, and other relevant information. Submission of your raw powder diffraction data would also be greatly appreciated. Transfer of the ACSII data preferably as CIF (Crystallographic Information File) by e-mail to Lisa Lanno, Editorial Coordinator (LANNOL@ICDD.COM) would be appreciated. Alternatively your data can be transferred by going to the following link, <http://www.icdd.com/resources/submit/powderdata.doc>. When submitting data, please indicate Reference #28226. If you have any difficulty in providing the data in the requested format, just provide us with the missing information in the published paper (e.g powder data).

Further information regarding the Recognition Award Program can be found at this web site <http://www.icdd.com/resources/submit/inddata.htm>. If I can be of any assistance in this, please do not

hesitate to call or write.

-

Thank you for your cooperation and contribution in aiding our efforts to produce a more comprehensive and accurate File.

Very truly yours,

Jennifer Nilan

Editorial Assistant



Confidentiality Notice: This e-mail message, including any attachments, is for the sole use of the intended recipient(s) and may contain confidential and privileged information. Unless you are the intended recipient (or authorized to receive for the intended recipient), you may not view, copy or disclose to anyone the message or any information contained in the message. If you have received the message in error, please advise the sender at ICDD@wpi.edu and delete the message. Thank you.

This material is reserved for educational use only, not allowed for commercial use.

Forbidden to modify the content, and cite the document when use.

ICDD PDF Data Submission

Please fill out the following information when submitting data:

Name: Dr. Chesta Ruttanapun

Address: Department of Physics, Faculty of Science, King Mongkut's Institute of Technology Ladkrabang, Chalongkrung Road, Ladkrabang, Bangkok, 10520 Thailand

Phone: 66 (0) 2-326-4339-53 Ext. 285-6

Fax: 66 (0) 2 -326-4413

E-mail: chesta.ruttanapun@gmail.com

Data can be submitted electronically by e-mail in ASCII form (lanio@icdd.com) or on other computer readable medium. Or sent by postal mail or fax to:

Lisa Lanio

International Centre for Diffraction Data

12 Campus Blvd.

Newtown Square, PA USA

19073-3273

Phone: (610) 325-9814

Fax: (610) 325-9823

| CELL DATA | |
|--------------------------|------------------------|
| METHOD OF CELL DETN. | |
| CELL REFINEMENT METHOD | |
| a= 3.0481 | () Å |
| b= 3.0481 | () Å |
| c= 17.166 | () Å |
| α= 90 | ° (°) |
| β= 90 | ° (°) |
| γ= 120 | ° (°) |
| V= 138.199 | Å ³ Z=3 |
| D _m = 5.19 | () g cm ⁻³ |
| D _x = | () g cm ⁻³ |
| Formula Wt= | |
| CRYSTAL SYS. | |
| SPACE GROUP R -3 m (166) | NUMBER |
| CRYSTAL DATA INDEX No. | |
| FIGURE OF MERIT TYPE | VALUE |

REFERENCES

Ref1:(XRD run)

By:Wutthisak Prachamonb.

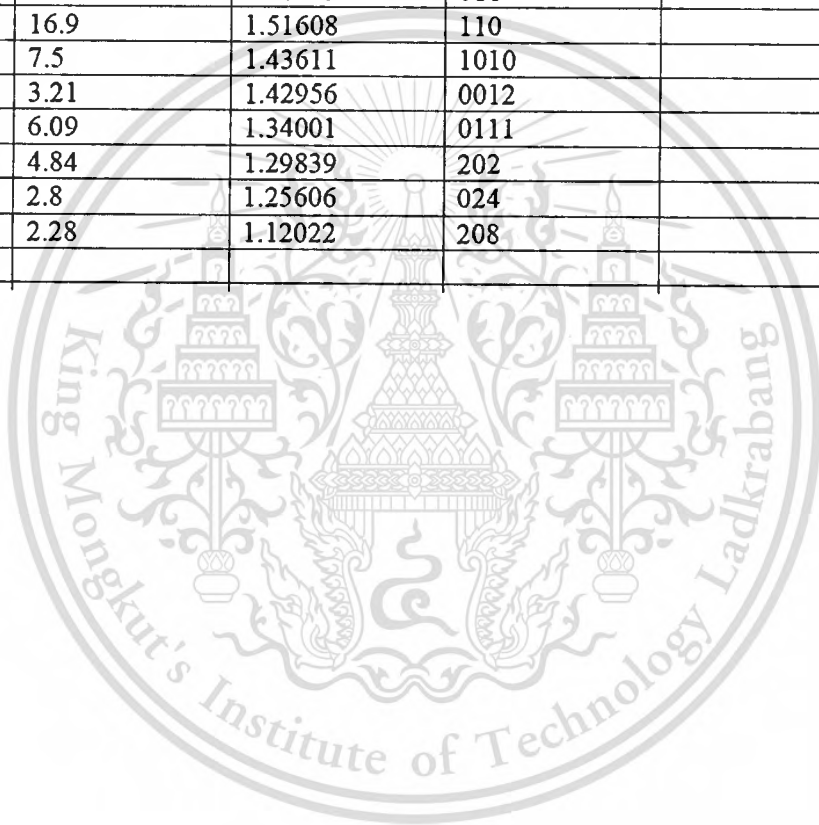
At:Department of Physics, Faculty of Science, Ubon Ratchathani University, Ubon Ratchathani 34190, Thailand

Ref2:(Article and Experiment)

By: Dr. Chesta Ruttanapun

Site: C. Ruttanapun, A. Wichainchai, W. Prachamon, A. Yangthaisong, A. Charoenphakdee, T. Seetawan, "Thermoelectric properties of Cu_{1-x}PtxFeO₂ (0.0≤x≤0.05) delafossite-type transition oxide",J. Alloy. Compd. 509 (2011) 4588-4594.

| ESSENTIAL | | DESIRED | | |
|-----------------------------|----------------------------|------------------|-------|-----------------------------|
| 2θ EXP* (DEGREES) | I/I_0 (1-1000) (%) | D_{EXP} (Å) | hkl | $2\theta^{**}$ (DEGREES) |
| 31.2889 | 22.66 | 2.85648 | 006 | |
| 34.5498 | 6.17 | 2.59398 | 101 | |
| 35.749 | 100 | 2.50966 | 012 | |
| 40.2595 | 16.2 | 2.23828 | 104 | |
| 43.1696 | 3.22 | 2.0939 | 015 | |
| 47.2044 | 1.9239 | 3.97 | 009 | |
| 55.2691 | 13.21 | 1.66073 | 018 | |
| 61.0726 | 16.9 | 1.51608 | 110 | |
| 64.875 | 7.5 | 1.43611 | 1010 | |
| 65.2089 | 3.21 | 1.42956 | 0012 | |
| 70.1779 | 6.09 | 1.34001 | 0111 | |
| 72.7791 | 4.84 | 1.29839 | 202 | |
| 75.6521 | 2.8 | 1.25606 | 024 | |
| 86.8857 | 2.28 | 1.12022 | 208 | |



D: CRYSTALLOGRAPHIC REFERENCE

D.1: CuFeO_2 ICSD#10-075-2146

D.2: CuO JCPDS#05-0661

D.3: Fe_2O_3 JCPDS#07-0322

D.4: CuAlO_2 JCPDS# 35-1401



This material is reserved for educational use only, not allowed for commercial use.

Forbidden to modify the content, and cite the document when use.

D.1

CuFeO₂: ICSD#10-075-2146

Date: 24/9/2009 Time: 14:40:42

File: 01-075-2146

User: Administrator

Name and formula

Reference code: 01-075-2146
 ICSD name: Copper Iron Oxide
 Empirical formula: CuFeO₂
 Chemical formula: CuFeO₂

Crystallographic parameters

Crystal system: Rhombohedral
 Space group: R-3m
 Space group number: 166

a (?): 3.0351
 b (?): 3.0351
 c (?): 17.1660
 Alpha (?): 90.0000
 Beta (?): 90.0000
 Gamma (?): 120.0000

Calculated density (g/cm³): 5.51
 Volume of cell (10⁶ pm³): 136.94
 Z: 3.00

RIR: 5.49

Subfiles and Quality

Subfiles: Inorganic
 Corrosion
 ICSD Pattern
 Quality: Calculated (C)

Comments

Additional pattern: See PDF 39-246 and 85-605.
 ICSD collection code: 031918

References

Primary reference: *Calculated from ICSD using POWD-12++*, (1997)
 Structure: Prewitt, C.T., Shannon, R.D., Rogers, D.B., *Inorg. Chem.*, **10**, 719, (1971)

Peak list

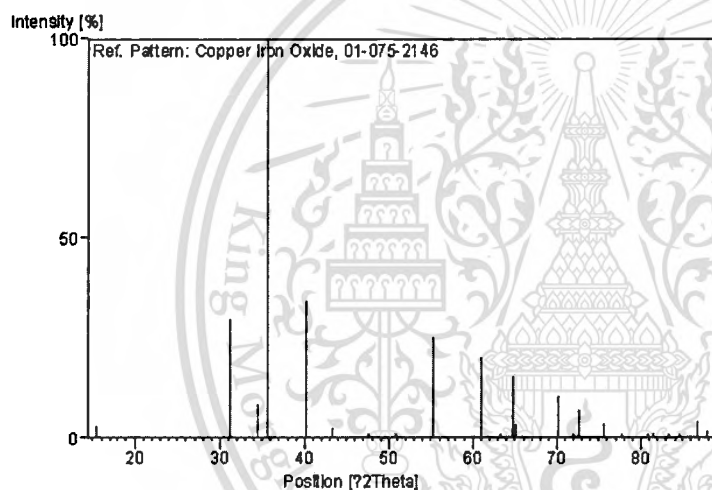
| No. | h | k | l | d [Å] | 2Theta [deg] | I [%] |
|-----|---|---|---|---------|--------------|-------|
| 1 | 0 | 0 | 3 | 5.72200 | 15.473 | 2.9 |
| 2 | 0 | 0 | 6 | 2.86100 | 31.238 | 29.6 |
| 3 | 1 | 0 | 1 | 2.59819 | 34.492 | 8.1 |
| 4 | 0 | 1 | 2 | 2.51326 | 35.696 | 100.0 |
| 5 | 1 | 0 | 4 | 2.24146 | 40.200 | 34.2 |
| 6 | 0 | 1 | 5 | 2.08704 | 43.319 | 2.4 |
| 7 | 0 | 0 | 9 | 1.90733 | 47.640 | 1.1 |

Date: 24/9/2009 Time: 14:40:42

File: 01-075-2146

User: Administrator

| | | | | | | |
|----|---|---|----|---------|--------|------|
| 8 | 1 | 0 | 7 | 1.79308 | 50.884 | 0.2 |
| 9 | 0 | 1 | 8 | 1.66221 | 55.216 | 25.1 |
| 10 | 1 | 1 | 0 | 1.51755 | 61.007 | 19.9 |
| 11 | 1 | 1 | 3 | 1.46684 | 63.356 | 0.3 |
| 12 | 1 | 0 | 10 | 1.43725 | 64.817 | 15.0 |
| 13 | 0 | 0 | 12 | 1.43050 | 65.161 | 3.5 |
| 14 | 1 | 1 | 6 | 1.34063 | 70.141 | 10.4 |
| 15 | 0 | 2 | 1 | 1.31040 | 72.007 | 0.4 |
| 16 | 2 | 0 | 2 | 1.29910 | 72.733 | 6.9 |
| 17 | 0 | 2 | 4 | 1.25663 | 75.612 | 3.3 |
| 18 | 2 | 0 | 5 | 1.22738 | 77.746 | 0.3 |
| 19 | 1 | 1 | 9 | 1.18753 | 80.881 | 0.6 |
| 20 | 1 | 0 | 13 | 1.17994 | 81.511 | 0.2 |
| 21 | 0 | 2 | 7 | 1.15837 | 83.363 | 0.1 |
| 22 | 0 | 0 | 15 | 1.14440 | 84.614 | 0.1 |
| 23 | 2 | 0 | 6 | 1.12073 | 86.837 | 4.1 |
| 24 | 0 | 1 | 14 | 1.11119 | 87.771 | 1.8 |

Stick Pattern

D.2

CuO: JCPDS#05-0661

| 05-0661 | | Wavelength= 1.5405 | | | | | | i | | | |
|--|--|--------------------|-----|---|---|---|------------|-----|---|---|---|
| CuO | | 2 θ | Int | h | k | l | 2 θ | Int | h | k | l |
| Copper Oxide | | 32.519* | 12 | 1 | 1 | 0 | 103.502 | 4 | 1 | 1 | 5 |
| | | 35.450* | 49 | 0 | 0 | 2 | 107.096 | 3 | 4 | 2 | 0 |
| | | 35.551* | 100 | 1 | 1 | 1 | 109.447 | <1 | 1 | 3 | 3 |
| Tenorito. syn | | 38.729* | 96 | 1 | 1 | 1 | 110.227 | 4 | 4 | 2 | 2 |
| Rad.: CuK α 1 λ : 1.5405 Filter: Ni Beta.M d-sp: | | 38.921* | 30 | 2 | 0 | 0 | 111.255 | 2 | 4 | 0 | 4 |
| Cut off: Int.: Diffract. I/lor.: 1.90 | | 46.306* | 3 | 1 | 1 | 2 | 113.526 | 2 | 1 | 1 | 5 |
| Ref: Swanson, Tatge, Natl. Bur. Stand. (U.S.). Circ. 539, I. 49 (1953) | | 51.343* | 2 | 1 | 1 | 2 | 116.891 | 1 | 5 | 1 | 1 |
| | | 53.409* | 8 | 0 | 2 | 0 | | | | | |
| | | 58.312* | 14 | 2 | 0 | 2 | | | | | |
| Sys.: Monoclinic S.G.: C2/c (15) | | 61.587* | 20 | 1 | 1 | 3 | | | | | |
| a: 4.084 b: 3.425 c: 5.129 A: 1.3676 C: 1.4975 | | 65.803* | 12 | 0 | 2 | 2 | | | | | |
| a: β : 99.47 γ : Z: 4 mp: | | 66.224* | 15 | 3 | 1 | 1 | | | | | |
| Ref: Ibid. | | 68.137* | 19 | 2 | 2 | 0 | | | | | |
| | | 72.411* | 7 | 3 | 1 | 1 | | | | | |
| Dx: 6.510 Dn: SS/FOM: F ₃₀ =18(.037. 46) | | 75.019* | 6 | 0 | 0 | 4 | | | | | |
| | | 75.228* | 7 | 2 | 2 | 2 | | | | | |
| | | 80.177* | 2 | 2 | 0 | 4 | | | | | |
| | | 82.372* | 5 | 3 | 1 | 3 | | | | | |
| | | 83.038* | 3 | 2 | 2 | 2 | | | | | |
| | | 83.344* | 2 | 3 | 1 | 2 | | | | | |
| Color: Black | | 83.601* | 4 | 4 | 0 | 0 | | | | | |
| X-ray pattern at 26 C. Sample from Johnson Matthey Company. | | 88.582* | 2 | 4 | 0 | 2 | | | | | |
| Spectroscopic analysis: faint traces of Fe and Mg. Opaque | | 89.759* | 6 | 1 | 3 | 1 | | | | | |
| mineral optical data on specimen from Cornwall, England: | | 91.677* | 2 | 1 | 3 | 1 | | | | | |
| R3R λ =211-25.7, Disp.=Std., VHN100=304-339, Ref.: IMA | | 95.642* | <1 | 2 | 0 | 4 | | | | | |
| Commission on Ore Microscopy QDF, Cu O type. C.D. Cell: | | 98.362* | 3 | 0 | 2 | 4 | | | | | |
| a=5.129, b=3.425, c=4.684, β =99.47, a/b=1.4975, | | 99.741* | 4 | 3 | 1 | 3 | | | | | |
| c/b=1.3676, S.G.=A2/a(15), PSC: mC8. Mwt: 79.55. | | 101.881 | <1 | 4 | 0 | 2 | | | | | |
| Volume[CD]: 81.16. | | | | | | | | | | | |

©1996 JCPDS-International Centre for Diffraction Data. All rights reserved.

D.3

Fe₂O₃: JCPDS#07-0322

| 07-0322 | | | | Wavelength= 1.7802 | | | | |
|---|--|--|--|--------------------|-----|---|---|---|
| FeO:Fe2O3 | | | | 2 θ | Int | h | k | l |
| Iron Oxide | | | | 21.226* | 30 | 1 | 1 | 1 |
| | | | | 35.081* | 60 | 2 | 2 | 0 |
| | | | | 41.439* | 100 | 3 | 1 | 1 |
| Magnetite | | | | 43.322* | 10 | 2 | 2 | 2 |
| Rad.: CoKa | | | | 50.535* | 50 | 4 | 0 | 0 |
| λ : 1.7802 Filter: Fe Beta.M d-sp: | | | | 62.984* | 40 | 4 | 2 | 2 |
| Cut off: Int.: Estimation l/cor.: | | | | 67.317* | 60 | 5 | 1 | 1 |
| Ref: Rooksby, X-Ray Identification and Crystal Structures of Clay | | | | 74.194* | 70 | 4 | 4 | 0 |
| | | | | 84.914* | 10 | 6 | 2 | 0 |
| | | | | 88.829* | 30 | 5 | 3 | 3 |
| | | | | 89.988* | 10 | 6 | 2 | 2 |
| Sys.: Cubic S.G.: Fd3m (227) | | | | 95.525* | 20 | 4 | 4 | 4 |
| a: 8.390 b: c: A: C: | | | | 106.107 | 20 | 6 | 4 | 2 |
| a: β : γ : Z: 8 mp: | | | | 110.258 | 50 | 7 | 3 | 1 |
| Ref: Ibid. | | | | 117.322 | 20 | 8 | 0 | 0 |
| | | | | 129.909 | 10 | 6 | 6 | 0 |
| Dx: 5.208 Dm: 5.175 SS/FOM: F ₁₈ =8(.090.25) | | | | 135.243 | 40 | 7 | 5 | 1 |
| | | | | 145.209 | 30 | 8 | 4 | 0 |
| sa: $\eta\omega\beta$: 2.42 σ_T : Sign: 2V: | | | | | | | | |
| Ref: Ibid. | | | | | | | | |
| Color: Black | | | | | | | | |
| PSC: cF56. Delete: Weissmann letter for December 1961. Mwt: 231.54. Volume[CD]: 590.59. | | | | | | | | |

©1998 JCPDS-International Centre for Diffraction Data. All rights reserved.

D.4

CuAlO₂: JCPDS# 35-1401

| 35-1401 | | Wavelength= 1.5418 | | | | | | | | | |
|---|--|--------------------|-----|---|---|----|------------|-----|---|---|----|
| CuAlO ₂ | | 2 θ | Int | h | k | l | 2 θ | Int | h | k | l |
| Copper Aluminum Oxide | | 15.890* | 10 | 0 | 0 | 3 | 112.087 | 4 | 1 | 2 | 2 |
| | | 31.090* | 40 | 0 | 0 | 6 | 112.994 | 1 | 0 | 1 | 17 |
| | | 38.720* | 47 | 1 | 0 | 1 | 115.187 | 2 | 2 | 1 | 4 |
| | | 37.881* | 100 | 0 | 1 | 2 | 128.637 | 3 | 1 | 2 | 8 |
| | | 42.318* | 23 | 1 | 0 | 4 | 138.417 | 3 | 3 | 0 | 0 |
| | | 48.351* | 9 | 0 | 0 | 9 | 140.688 | 2 | 2 | 1 | 10 |
| Rad.: CuK α λ : 1.5418 Filter: Ni Beta.M d-sp: Diffractometer | | 52.914* | 4 | 1 | 0 | 7 | 148.785 | 1 | 0 | 2 | 18 |
| Cut off: Int.: Diffract. I/ICor.: | | 57.271* | 30 | 0 | 1 | 8 | 148.234 | 1 | 0 | 1 | 20 |
| Ref: Ishizawa, N., Tokyo Institute of Technology, Tokyo, Japan, Private Communication, (1984) | | 65.321* | 26 | 1 | 1 | 0 | | | | | |
| | | 66.181* | 5 | 0 | 0 | 12 | | | | | |
| Sys.: Rhombohedral S.G.: R $\bar{3}m$ (166) | | 66.930* | 15 | 1 | 0 | 10 | | | | | |
| a: 2.8567(1) b: c: 16.943(1) A: C: 5.9310 | | 67.632* | 1 | 1 | 1 | 3 | | | | | |
| a: β : γ : Z: 3 mp: | | 72.468* | 1 | 0 | 1 | 11 | | | | | |
| Ref: Ishiguro, T. et al., Acta Crystallogr., Sec. B: Structural Science, 39, 564 (1983) | | 74.418* | 9 | 1 | 1 | 6 | | | | | |
| Dx: 5.007 Dm: 5.060 SS/FOM: F ₃₀ =45(.0159, 42) | | 77.330* | 2 | 0 | 2 | 1 | | | | | |
| Color: Dark blue | | 78.051* | 6 | 2 | 0 | 2 | | | | | |
| Prepared by solid state reaction of Cu ₂ O and Al ₂ O ₃ at 1373 K in N ₂ atmosphere. Chemical analysis (wt.%): Cu 51.8, Al 22.1, O 26.1. 3R polytype. Silicon used as an external stand. PSC: hR4. To replace 9-185. Mwt: 122.53. Volume[CD]: 119.74. | | 80.960* | 2 | 0 | 2 | 4 | | | | | |
| | | 85.284* | 3 | 1 | 1 | 9 | | | | | |
| | | 90.318* | 2 | 0 | 1 | 14 | | | | | |
| | | 92.398* | 3 | 2 | 0 | 8 | | | | | |
| | | 100.305 | 3 | 1 | 1 | 12 | | | | | |
| | | 101.009 | 3 | 0 | 2 | 10 | | | | | |
| | | 104.724 | 2 | 1 | 0 | 18 | | | | | |
| | | 109.964 | 2 | 0 | 0 | 18 | | | | | |
| | | 111.325 | 1 | 2 | 1 | 1 | | | | | |

©1996 JCPDS-International Centre for Diffraction Data. All rights reserved.

ประวัติผู้เขียน

| | |
|--------------------|---|
| ชื่อ-นามสกุล | นายเชรชฐา รัตนพันธ์ |
| วัน เดือน ปีเกิด | 11 มิถุนายน 2519 ที่บ้านโคกตาล ต.โคกตาล อ.ภูสิงห์ จ.ศรีสะเกษ |
| ที่อยู่ | 78 หมู่ที่10 บ้านโคกตาล ต.โคกตาล อ.ภูสิงห์ จ.ศรีสะเกษ |
| ประวัติการศึกษา | พ.ศ. 2525 – 2526 อนุบาล: ศูนย์พัฒนาเด็กเล็กบ้านโคกตาล ต.โคกตาล อ.ภูสิงห์ จ.ศรีสะเกษ พ.ศ. 2526 – 2532 ประถมศึกษา: โรงเรียนบ้านโคกตาล ต.โคกตาล อ.ภูสิงห์ จ.ศรีสะเกษ พ.ศ. 2532 – 2535 มัธยมศึกษา: โรงเรียนปรีอใหญ่วิทยาลัย ต.ปรีอใหญ่ อ.ขุขันธ์ จ.ศรีสะเกษ พ.ศ. 2535 – 2538 มัธยมศึกษา: โรงเรียนศรีสะเกษวิทยาลัย อ.เมือง จ.ศรีสะเกษ พ.ศ. 2538 – 2542 ปริญญาตรี: ภาควิชาฟิสิกส์ คณะวิทยาศาสตร์ มหาวิทยาลัยขอนแก่น วิทยาศาสตร์บัณฑิต (ฟิสิกส์) มหาวิทยาลัยขอนแก่น พ.ศ. 2542 – 2546 ปริญญาโท: ภาควิชาฟิสิกส์ คณะวิทยาศาสตร์ มหาวิทยาลัยขอนแก่น วิทยาศาสตรมหาบัณฑิต (ฟิสิกส์) มหาวิทยาลัยขอนแก่น วิทยานิพนธ์: “Application of parallel programming technique in 2-d club sandwich solar cell simulation” |
| ความชำนาญเฉพาะด้าน | 1.) Computer simulation, Parallel programming, Cluster computer 2.) Finite Element Analysis 3.) Materials science |
| ประสบการณ์การทำงาน | พ.ศ. 2542 – 2546 เป็นผู้ช่วยวิจัย โครงการคอมพิวเตอร์จำลองแบบเซลล์แสงแดดคลับแซนด์วิช ใน2มิติ ที่ ภาควิชาฟิสิกส์ คณะวิทยาศาสตร์ มหาวิทยาลัยขอนแก่น โดย ผศ. บำรุง สมสวัสดิ์ เป็นหัวหน้าโครงการ พ.ศ. 2546 – ปัจจุบัน ตำแหน่งผู้ช่วยนักวิจัย 3 ฝ่าย: หน่วยวิจัยสารสนเทศ การสื่อสารและการคำนวณ งาน: ห้องปฏิบัติการวิจัยการจำลองขนาดใหญ่ ศูนย์เทคโนโลยีอิเล็กทรอนิกส์และคอมพิวเตอร์แห่งชาติ (NECTEC) สำนักงานพัฒนาวิทยาศาสตร์และเทคโนโลยีแห่งชาติ (สวทช.) |

ผลงานวิจัย

พ.ศ.2553-ปัจจุบัน ชื่อโครงการ การพัฒนาเทคโนโลยีการให้ความร้อนด้วยไมโครเวฟต้นแบบในระดับอุตสาหกรรม

เป็นวิทยากรบรรยาย Finite Element Analysis

15 กันยายน 2548 ศูนย์เทคโนโลยีอิเล็กทรอนิกส์และคอมพิวเตอร์แห่งชาติ
14-15 กันยายน 2549 คณะวิศวกรรมศาสตร์ มหาวิทยาลัยขอนแก่น
28-29 สิงหาคม 2550 คณะวิศวกรรมศาสตร์ สถาบันเทคโนโลยีพระจอมเกล้าเจ้าคุณทหารลาดกระบัง
7-8 สิงหาคม 2551 ภาควิชาฟิสิกส์ คณะวิทยาศาสตร์ มหาวิทยาลัยขอนแก่น
12-14 กรกฎาคม 2554 ศูนย์กริคมมหาวิทยาลัยสงขลานครินทร์ มหาวิทยาลัยสงขลานครินทร์

Committee

20-21 กรกฎาคม 2554 The 1st Southeast Asia Conference on Thermoelectrics

อาจารย์พิเศษ

พ.ศ. 2549 สอนวิชาเขียนแบบบนคอมพิวเตอร์ ด้วยโปรแกรม Auto Cad ภาควิชาฟิสิกส์
คณะวิทยาศาสตร์ มหาวิทยาลัยอุบลราชธานี